



**HAL**  
open science

# Growth, structure and electronic properties of epitaxial graphene on rhenium, towards a two-dimensional superconducting platform.

Estelle Mazaleyrat

► **To cite this version:**

Estelle Mazaleyrat. Growth, structure and electronic properties of epitaxial graphene on rhenium, towards a two-dimensional superconducting platform.. Superconductivity [cond-mat.supr-con]. Université Grenoble Alpes, 2019. English. NNT: 2019GREAY079 . tel-02946437

**HAL Id: tel-02946437**

**<https://theses.hal.science/tel-02946437>**

Submitted on 23 Sep 2020

**HAL** is a multi-disciplinary open access archive for the deposit and dissemination of scientific research documents, whether they are published or not. The documents may come from teaching and research institutions in France or abroad, or from public or private research centers.

L'archive ouverte pluridisciplinaire **HAL**, est destinée au dépôt et à la diffusion de documents scientifiques de niveau recherche, publiés ou non, émanant des établissements d'enseignement et de recherche français ou étrangers, des laboratoires publics ou privés.

## THÈSE

Pour obtenir le grade de

### **DOCTEUR DE LA COMMUNAUTE UNIVERSITE GRENOBLE ALPES**

Spécialité : **Physique appliquée**

Arrêté ministériel : 25 mai 2016

Présentée par

**Estelle MAZALEYRAT**

Thèse dirigée par **Claude CHAPELIER**, Directeur de recherche,  
**Communauté Université Grenoble Alpes**, et  
codirigée par **Johann CORAUX**, Chargé de recherche,  
**Communauté Université Grenoble Alpes**

préparée au sein du **Laboratoire de Transport Electronique  
Quantique et Supraconductivité**, de l'**Institut de Recherche  
Interdisciplinaire de Grenoble – CEA**  
et du **Département Electronique QUantique, Surfaces et  
spinTronique** de l'**Institut Néel – CNRS**  
dans l'**École Doctorale de Physique de Grenoble**

## **Croissance, structure et propriétés électroniques du graphène épitaxié sur rhénium, vers une plateforme bidimensionnelle et supraconductrice**

Thèse soutenue publiquement le **18 décembre 2019**,  
devant le jury composé de :

**Monsieur Pierre MALLET**

Directeur de recherche, Institut Néel (CNRS), Président du jury

**Monsieur Andrew MAYNE**

Directeur de recherche, Institut des Sciences Moléculaires d'Orsay  
(CNRS) – Université Paris Sud, Rapporteur

**Madame Muriel SICOT**

Chargée de recherche, Institut Jean Lamour (CNRS) – Université de  
Lorraine, Examinatrice

**Monsieur Laurent SIMON**

Directeur de recherche, Institut de Sciences des Matériaux de Mulhouse  
(CNRS) – Université de Haute Alsace, Rapporteur

**Monsieur Ulrich STARKE**

Professeur, Max-Planck-Institut für Festkörperforschung, Examineur







# REMERCIEMENTS

---

En premier lieu, j'aimerais remercier les membres de mon jury: Andrew Mayne, Laurent Simon, Pierre Mallet, Ulrich Starke et Muriel Sicot. Je leur adresse ma gratitude pour l'intérêt qu'ils ont porté à mon travail, pour leur lecture attentive et pour leurs questions et remarques lors de la soutenance qui ont menées à d'intéressantes discussions.

Je souhaite évidemment remercier très chaleureusement mes deux co-directeurs de thèse, Claude et Johann, pour leur bienveillance, leur aide et leur soutien pendant ces trois années et demi.

Claude, j'aimerais te remercier pour ta disponibilité, ta confiance et ton écoute. Travailler avec toi a été un réel plaisir. Tu m'as beaucoup appris, et je garderai un très bon souvenir de nos échanges scientifiques et non-scientifiques. Je te souhaite de ne pas perdre ton esprit rebelle et ta curiosité, et de continuer à faire de la science comme tu l'aimes.

Johann, je te remercie pour ta grande disponibilité et pour tes qualités scientifiques et managériales, que jalourent (ou devraient jalouser) nombre de tes collègues. Tu as su me motiver et m'orienter tout au long de la thèse. Et je dois dire que ta réactivité, notamment pendant la rédaction de la thèse et des articles, m'a toujours impressionnée. Je te trouve exemplaire et j'ai vraiment eu beaucoup de chance de t'avoir comme co-directeur de thèse.

Ayant eu la chance d'effectuer ma thèse dans deux laboratoires, j'aimerais remercier les membres des deux équipes au sein desquelles j'ai travaillé.

Côté CEA, j'aimerais remercier les chercheurs et ingénieurs permanents : Vincent R. pour m'avoir en partie formée, pour ses conseils et pour sa bienveillance, Romain M., François et Jean-Pascal pour leur intérêt et leurs conseils avisés, Xavier, Marc, Christophe M., Alexandre P., Louis et Silvano. Je remercie également les ingénieurs du labo : Jean-Luc, Frédéric, Iulian et Pierre.

Parmi les "anciens" (post-)doctorants côté CEA, je voudrais saluer Alexandre A., Loïc, Salha et Dibyendu. J'adresse un grand merci plus particulièrement à Alexandre A. pour m'avoir formée sur la majeure partie des équipements que j'ai utilisés pendant ma thèse. Tu as été un très bon prof et un bel exemple à suivre, et je te souhaite le meilleur pour la suite. Je remercie également Loïc pour son aide avec le STM et ses conseils précieux. Parmi les (post-)doctorants du CEA ayant marqué mes années de thèse, je pense évidemment au "groupe initial" (pour les puristes) : Florian B., Romain A., Anthony, Thomas et Florian V. Notre groupe de grimpe et de soirées squattage chez Florian B. me manque déjà. Je remercie également celles et ceux qui sont arrivés plus tard : Tom, Cécile, Simon, Florie, Estelle et Nicolas, pour avoir perpétué les sessions grimpe/dodo en montagne pendant la canicule/soirées. Et je vous souhaite à tous une bonne continuation.

Côté CNRS, j'aimerais remercier en premier lieu (et sans grande surprise) Ana, pour le binôme soudé qu'on a formé, pour ton amitié et pour tout ce que tu m'as appris. Ton soutien a été une grande force pendant la thèse, et je te remercie d'avoir partagé avec moi les bons et les moins bons moments. Je tiens à remercier également les chercheurs permanents de l'équipe Hybrid : Laurence, Julien, Laëtitia, Nedjma et Vincent B., pour leurs conseils, leur aide et leur intérêt. Je te remercie en particulier Laurence, pour ton implication dans les différents projets qui nous lient, et pour ta

bienveillance. Je remercie également tous les "anciens" et "nouveaux" (post-) doctorants/stagiaires de l'équipe Hybrid : Alexandre A., Simone, modèle de persévérance et de patience, Goutham et Roberto, fidèles compagnons de route (et de galère), Guilliam (la danse ma passion), Kazi, Priyank (no offence) et Riadh pour les repas et sorties de labo, Brice, Sudipta, Debora, Swati, Pauline, Thanasis, Van Dung, Wei Lai, Enzo, Maria, Abhishek et Maria-Teresa. Et j'en profite pour souhaiter plein de succès à Maria dans sa thèse. Je n'oublie pas les co-bureaux qui ont égayé mon quotidien de thésarde parmi lesquels Jorge (on se voit bientôt dans les Pyrénées!), Alexis, Michael et Michal.

J'aimerais également exprimer toute ma reconnaissance et mes amitiés à Valérie et Philippe, pour leur aide technique et leur soutien. Ça a été un véritable plaisir de travailler avec vous pendant ces trois années et demi, et j'espère trouver des collègues toulousains à votre hauteur. Je remercie également Arnaud Claudel et David Jegouso pour leur bonne humeur et leur bienveillance.

Je voudrais maintenant remercier les collaborateurs avec lesquels j'ai travaillé au cours de ma thèse. Je remercie en premier lieu les membres de l'équipe parisienne du LPEM/ESPCI pour m'avoir accueillie dans leur labo. Je te remercie plus particulièrement, Sergio, pour ton implication dans le projet, tes qualités scientifiques et techniques, et ta bienveillance ; et je remercie également Thomas Vincent, Stéphane Pons et Dimitri Roditchev. En second lieu, je tiens à remercier chaleureusement mes collaborateurs lyonnais de l'ENS : merci Christophe pour ta disponibilité, les nombreux échanges qu'on a eus, et ton enthousiasme, et un grand merci également à Shagor Chowdhury pour la synthèse des molécules. Enfin, je remercie Florent Calvo et Georg Daniel Förster pour les calculs liés à la colline manquante, Bruno Gilles pour la préparation de films minces de rhénium, et Gérard Lapertot et Christophe Marin (côté CEA), et Richard Haettel (côté CNRS) pour la mise à disposition de leurs fours.

Pour terminer, je voudrais remercier ma famille et mes amis pour leur soutien et les bons moments partagés à Grenoble et ailleurs. Merci Baptiste pour ta patience et pour tout le reste.

La réalisation de structures hybrides à base de graphène, dans lesquelles le graphène est associé à d'autres matériaux, constitue une piste prometteuse pour l'étude de nombreux phénomènes. En particulier, il est possible de cette façon d'induire des propriétés dans le graphène *via* des effets de proximité. Ici, le système cible que nous avons considéré consiste en une plateforme de graphène quasi-flottant, au caractère supraconducteur induit, et qui est placée à proximité d'impuretés magnétiques. A la lecture d'articles théoriques parus récemment, il semble qu'un tel échantillon pourrait présenter des états de Yu-Shiba-Rusinov (YSR) non conventionnels.

Bien que le système cible n'ait pas encore été fabriqué, les trois ingrédients nécessaires à sa réalisation (graphène quasi-flottant, caractère supraconducteur induit et proximité à des impuretés magnétiques) ont été abordés, et ce à l'aide d'outils de la science des surfaces.

Comme cela a pu être démontré précédemment, le graphène peut être rendu supraconducteur lorsqu'il est crû directement sur un matériau supraconducteur tel que le rhénium. Des aspects structuraux liés au graphène crû sur Re(0001) ont été explorés. En particulier, nous avons montré qu'augmenter le nombre de cycles de recuit contribue positivement à la croissance de domaines de graphène étendus et de bonne qualité. La structure d'un carbure de surface du rhénium, habituellement mal comprise, a également fait l'objet d'une étude.

De plus, nous avons examiné un défaut présent dans le graphène crû sur des métaux interagissant fortement, tels que le Re(0001) et le Ru(0001). Dans la structure ondulée à l'échelle nanométrique du graphène, ce défaut apparaît sous la forme d'une dépression. Sa présence a été attribuée à des défauts d'empilement se trouvant soit dans le graphène, soit dans le substrat métallique.

En prenant le graphène supraconducteur crû sur Re(0001) comme point de départ pour la fabrication de notre système cible, nous avons recouvré le caractère quasi-flottant du graphène (perdu à cause de sa forte interaction avec le substrat de rhénium) *via* l'intercalation d'une sub-monocouche ou de quelques couches d'atomes d'or. La présence d'une forte densité de défauts, observée dans le graphène sur Re(0001) intercalé à l'or, a été attribuée au processus d'intercalation lui-même. Par ailleurs, nous avons démontré que le caractère supraconducteur du graphène, induit par le rhénium, n'est pas affecté par l'intercalation d'or. A ce stade, deux des trois conditions prévues pour la réalisation du système cible étaient remplies.

A condition d'amener des impuretés magnétiques à proximité immédiate d'un tel échantillon, des états de YSR étendus sur plusieurs nanomètres devraient être observables. Des résultats préliminaires impliquant deux composés magnétiques de type verdazyl ont été présentés. L'un de ces deux composés fut déposé sur un système modèle : le Cu(111). Avant de considérer l'usage du graphène quasi-flottant et supraconducteur comme substrat-hôte de ces composés magnétiques, des études complémentaires sur des systèmes modèles sont nécessaires. Et pour cause, nous n'avons pas encore réussi à résoudre la structure exacte des assemblées moléculaires observées sur la surface de Cu(111) ; la stabilité thermique de ces composés a été mise en cause.



The realization of graphene-based hybrid structures, where graphene is associated with other materials, offers a promising avenue for testing a variety of phenomena. In particular, one can induce properties in graphene by proximity effects. Here, the targeted graphene-based system consists of a quasi free-standing graphene platform with induced superconducting character and in close vicinity to magnetic impurities. According to recent theoretical articles, such a sample could exhibit unconventional Yu-Shiba-Rusinov (YSR) states.

Although the targeted graphene-based system was not fabricated yet, we have addressed, with the help of surface science tools, all three ingredients required for its realization (quasi-free standing graphene, induced superconducting character and proximity to magnetic impurities).

As previously demonstrated, graphene can be rendered superconducting by growing it directly on top of a superconducting material such as rhenium. Structural aspects related to graphene grown on Re(0001) were investigated. In particular, we showed that increasing the number of annealing cycles positively contributes to growing high-quality extended graphene domains. The structure of a surface rhenium carbide, which constitutes a usually ill-characterized object, was studied as well.

Additionally, a defect appearing as a depression in the nanorippled structure of graphene on strongly interacting metals such as Re(0001) and Ru(0001) was investigated and ascribed to stacking faults either in graphene or in the metal substrate.

Using superconducting graphene grown on Re(0001) as a starting point for the fabrication of the targeted graphene-based system, we recovered the quasi free-standing character of graphene (lost due to its strong interaction with the rhenium substrate) *via* intercalation of sub-monolayer to few layers of gold atoms. A high density of defects observed in gold-intercalated graphene on Re(0001) was attributed to the intercalation process itself. Besides, we demonstrated that the rhenium-induced superconducting character in graphene was not affected by gold intercalation. At this point, two of the three requirements for realizing the targeted graphene-based system were fulfilled.

Provided that we bring magnetic impurities in close proximity to such a sample, few-nanometers extended YSR states could be observed. Preliminary results involving two original magnetic verdazyl compounds were presented, one of which was deposited on a model system, namely Cu(111). Before turning to quasi-free standing superconducting graphene as a hosting material for these magnetic compounds, further investigations on model systems are needed. Indeed, we could not resolve the precise structure of the molecular assemblies covering the Cu(111) surface yet, and the thermal stability of the compounds was discussed.



# Table of contents

<b>Introduction</b>	<b>3</b>
<b>I Isolated graphene, graphene on metals and functionalization</b>	<b>5</b>
1 Isolated graphene . . . . .	6
1.a Crystallographic structure . . . . .	6
1.b Electronic structure . . . . .	7
1.c Band structure . . . . .	7
1.d Electronic transport properties . . . . .	9
1.e Raman signature of graphene . . . . .	10
2 Graphene on metals . . . . .	14
2.a Graphene growth on metals . . . . .	14
2.b Moiré superlattices . . . . .	15
2.c Hybridization between graphene $\pi$ and metal $d$ states . . . . .	17
2.d Consequences on the electronic properties . . . . .	18
3 Intercalation of thin films below graphene . . . . .	21
3.a Intercalation compounds . . . . .	21
3.b Intercalation process . . . . .	22
3.c Restoring the properties of isolated graphene <i>via</i> intercalation . . . . .	23
3.d Tuning graphene properties from below . . . . .	26
4 Functionalization of graphene from on top . . . . .	28
4.a Adatoms and molecules as dopants . . . . .	28
4.b Spin systems on graphene . . . . .	29
5 Towards probing Yu-Shiba-Rusinov states in graphene . . . . .	29
5.a Yu-Shiba-Rusinov states . . . . .	29
5.b Effect of dimensionality . . . . .	30
5.c Targeted graphene-based system . . . . .	31
<b>II Experimental techniques and methods</b>	<b>33</b>
1 Ultra-high vacuum (UHV) techniques . . . . .	34
1.a Multi-purpose UHV system . . . . .	34
1.b Reflection high energy electron diffraction . . . . .	35
1.c Surface preparations . . . . .	36
1.d Graphene growth on Re(0001) thin films . . . . .	37
1.e Molecular evaporator . . . . .	38
1.f Angle-resolved photoemission spectroscopy . . . . .	38
2 Scanning tunneling microscopy and spectroscopy . . . . .	41
2.a Working principle . . . . .	41
2.b Experimental set-ups . . . . .	42
3 Raman spectroscopy . . . . .	43
3.a Working principle . . . . .	43



3.b	Experimental set-up . . . . .	44
4	Simulations . . . . .	44
4.a	Density functional theory calculations . . . . .	44
4.b	Bond-order potential calculations . . . . .	46
<b>III Structure of graphene and a surface carbide grown on Re(0001)</b>		<b>49</b>
1	Graphene growth on Re(0001) . . . . .	51
1.a	RHEED monitoring . . . . .	51
1.b	Evolution of graphene and moiré lattice parameters . . . . .	52
1.c	Extension of graphene domains and increasing ordering . . . . .	53
2	Coexistence of graphene and rhenium carbide . . . . .	55
2.a	STM observations . . . . .	55
2.b	RHEED patterns . . . . .	56
3	Structural variants of the ordered rhenium carbide phase . . . . .	57
3.a	$(7 \times \sqrt{19})$ unit cell of rhenium carbide . . . . .	57
3.b	Grouping variants in six-fold families of equivalent domains . . . . .	58
4	Possible atomic structures of the ordered rhenium carbide phase . . . . .	60
<b>IV Depressions by stacking faults in nanorippled graphene on metals</b>		<b>63</b>
1	Moiré superlattice, vacant hills and relationship with atomic stacking . . . . .	66
1.a	Geometrical features of the moiré superlattice . . . . .	66
1.b	Atomic resolution of the vacant hill defect . . . . .	67
2	BOP simulations and comparison with STM observations . . . . .	67
2.a	BOP simulations . . . . .	67
2.b	Comparison with STM observations . . . . .	67
3	Discarded defect structures . . . . .	69
3.a	Rotated nano-grains . . . . .	69
3.b	Vacancies in the carbon lattice . . . . .	69
3.c	Vacancies in the metal lattice . . . . .	70
4	Possible defect candidates . . . . .	71
4.a	Stacking faults in the metal lattice . . . . .	71
4.b	Moiré dislocations . . . . .	71
4.c	Stacking faults in the carbon lattice . . . . .	72
5	On the possible origin of the vacant hill defects . . . . .	75
6	Electronic properties of the vacant hills . . . . .	76
6.a	Local conductance measurements . . . . .	76
6.b	DFT calculations . . . . .	76
<b>V Defective, hole-doped and superconducting quasi free-standing graphene on Re(0001) obtained by gold intercalation</b>		<b>81</b>
1	Graphene-covered Re(0001) . . . . .	83
1.a	Structural properties . . . . .	83
1.b	Electronic band structure . . . . .	84
2	Gold deposition/intercalation process . . . . .	84
3	Structural and electronic properties of gold-intercalated graphene on Re(0001) . . . . .	86
3.a	Atomic force microscopy observations . . . . .	86
3.b	Scanning tunneling microscopy and spectroscopy . . . . .	87
3.c	DFT calculations . . . . .	89
3.d	Topography-dependence in conductance measurements . . . . .	93
4	Quasi free-standing character of gold-intercalated graphene on Re(0001) . . . . .	93

4.a	Dirac cone of quasi free-standing graphene . . . . .	93
4.b	Raman modes of quasi free-standing graphene . . . . .	95
5	Defects in gold-intercalated graphene on Re(0001) . . . . .	96
6	Superconducting properties . . . . .	98
<b>VI Molecular assemblies of verdazyl radicals on Cu(111)</b>		<b>101</b>
1	Verdazyl radicals . . . . .	102
1.a	Magnetic properties . . . . .	103
1.b	Verdazyl radicals on surfaces . . . . .	105
2	Synthesis and characterization . . . . .	106
2.a	Synthesis . . . . .	106
2.b	Electron spin resonance . . . . .	108
2.c	UV-visible spectroscopy . . . . .	109
2.d	Raman spectroscopy . . . . .	109
3	Sublimation temperature and stability . . . . .	110
3.a	Protocol . . . . .	110
3.b	TMOV molecules . . . . .	112
3.c	DOBV molecules . . . . .	113
4	DOBV deposition on metals . . . . .	114
4.a	Experimental adjustments . . . . .	114
4.b	RHEED monitoring . . . . .	115
4.c	DOBV molecular assemblies on Cu(111) . . . . .	116
<b>Conclusion</b>		<b>121</b>
<b>Bibliography</b>		<b>123</b>



Graphene, an atomically thin layer of carbon atoms arranged in a honeycomb lattice, has been under the spotlight for over 15 years now, and keeps revealing its peculiar properties. The initial interest for graphene was motivated by two of its unique features: its two-dimensional character and its electronic properties. The latter derive from its peculiar band structure, which can be described in an analogy with relativistic massless particles.

In parallel to the investigation of the properties of isolated (pristine) graphene, numerous works have been devoted to the examination of graphene-based hybrid structures, where graphene is associated with other materials. Such structures can consist, for instance, in layered heterostructures where graphene is supported on a stack of different materials or sandwiched between different materials. They can also rely on the deposition of atoms or molecules on top of graphene. The use of such hybrid structures allows to tune the properties of the whole system. In particular, one can induce properties in graphene *via* proximity effects (*e.g.* the superconducting proximity effect).

The work presented in this thesis was carried out in the context of an ongoing collaboration between two laboratories located in Grenoble, CEA/IRIG (Claude Chapelier) and CNRS/Institut Néel (Johann Coraux), and is the continuation of the PhD works of Charlène Tonnoir [1] and Alexandre Artaud [2]. Within this collaboration, the focus of research has progressively shifted from relatively simple graphene-based systems to more complex structures.

When supported on a metal, graphene's interaction with its substrate can have a large impact on graphene's properties. Although there is a continuum of possibilities from low to strong interaction between graphene and its metal substrate, two (extreme) cases of graphene-substrate binding are usually acknowledged, associated with so-called weakly and strongly interacting substrates.

The influence of the substrate, and the differences observed with respect to isolated graphene will be presented in Chapter I, followed by the description of the structural, electronic and vibrational properties of intercalated graphene. Intercalation of thin films between graphene and its metal substrate will be presented as a way to (partly) recover the properties of isolated graphene, and as a way to tune its properties. Although it is a widely used technique, there are still aspects related to intercalation that remain unclear: What are the spurious effects of intercalation? In particular, are defects created upon intercalation and in which amounts? Do proximity effects stemming from the initial hosting material survive graphene intercalation? Tuning graphene's properties in hybrid systems will be covered as well by considering functionalization from on top *via* deposition of adatoms and molecules. At the end of Chapter I, the targeted graphene-based system and the motivation for realizing such a system will be presented: it consists of a quasi free-standing graphene platform with induced superconducting character and in close vicinity to magnetic impurities. It was previously shown that growing graphene on Re(0001) results in induced superconductivity in graphene [3]. This method has therefore been used for the works presented in this thesis.

Shifting from relatively simple graphene-based systems (graphene grown on Re(0001) [3]) to more complex ones consisting of intercalated graphene, on the one hand, and with molecules deposited on top, on the other hand, has required a significant effort. In particular, molecular depositions on surfaces had never been carried out before in the ultra-high vacuum system used for this PhD work.

An introduction to the experimental techniques and numerical tools used in this thesis will be given in Chapter II. The working principle of scanning tunneling microscopy and spectroscopy (STM/STS),

reflection high energy electron diffraction (RHEED), angle-resolved photoemission spectroscopy (ARPES) and Raman spectroscopy will be presented. The two numerical methods that supported the works presented in this thesis will be introduced as well, namely density functional theory (DFT) and bond-order potential (BOP) simulations.

The first two chapters presenting experimental results (Chapters III and IV) will be mainly focused on structural aspects related to graphene grown on Re(0001). In Chapter III we address the following questions: What is the influence of the number of annealing cycles when growing graphene on Re(0001)? In particular, how are the quality of graphene and the size of graphene domains affected by it? Can we provide structural models for rhenium surface carbide?

In Chapters III and IV the structure of a surface rhenium carbide and a certain type of defect have been investigated. What is the nature of the latter? There is an obvious motivation for eliminating these objects in the prospect of growing high-quality graphene, but these objects could actually also display exciting properties. They are nonetheless detrimental in view of realizing the targeted graphene-based system.

To be more specific, Chapter III will present a study of the structure of graphene and a surface carbide grown on Re(0001), completed by means of RHEED and STM. Three atomic models proposed for the surface carbide phase will contribute to the description of a usually ill-characterized structure and a semi-quantitative RHEED analysis will demonstrate the positive influence of the number of annealing cycles for growing high-quality extended graphene domains.

In Chapter IV, we investigated a defect in graphene's structure that has been repeatedly observed on metal surfaces such as Re(0001) and Ru(0001), and which appears as a depression in the nanorippled topography of graphene. The nature of this defect was studied by means of STM/STS, BOP simulations and DFT calculations, and was attributed to stacking faults either in graphene or in the metal substrate.

Now turning to the actual fabrication of the targeted graphene-based system, we present in Chapter V an extensive study of graphene on Re(0001) intercalated with sub-monolayer to few-layers of a weakly interacting metal, namely gold. Our data consistently show that graphene recovers a quasi free-standing character upon gold intercalation. We also demonstrate that a high density of defects is created during the process of intercalation, an issue often overlooked in works relying on intercalated graphene. Finally, we establish that the rhenium-induced superconducting properties of graphene are not altered by gold intercalation. As a result, two of the three requirements for realizing the targeted graphene-based system are fulfilled: graphene is quasi free-standing and superconducting.

Chapter VI presents preliminary results obtained with two original magnetic molecules which were never investigated on surfaces before. With these molecules, we wish to address several questions: Can we induce magnetic properties in graphene? How strong is the interaction with the substrate? What is the contribution of intermolecular interactions? Finally, in the light of recent theoretical articles [4, 5], what behaviour can we expect when depositing these molecules on superconducting graphene? Their sublimation temperature in vacuum and ultra-high vacuum environments was studied. Although we did not deposit these compounds on quasi-free standing superconducting graphene yet, we present preliminary results obtained on a model system, namely the (111) surface of copper. The precise structure of the molecular assemblies observed with STM could not be determined and requires further investigations.

# ISOLATED GRAPHENE, GRAPHENE ON METALS AND FUNCTIONALIZATION

## Contents

---

1	Isolated graphene . . . . .	6
	1.a Crystallographic structure . . . . .	6
	1.b Electronic structure . . . . .	7
	1.c Band structure . . . . .	7
	1.d Electronic transport properties . . . . .	9
	1.e Raman signature of graphene . . . . .	10
2	Graphene on metals . . . . .	14
	2.a Graphene growth on metals . . . . .	14
	2.b Moiré superlattices . . . . .	15
	2.c Hybridization between graphene $\pi$ and metal $d$ states . . . . .	17
	2.d Consequences on the electronic properties . . . . .	18
3	Intercalation of thin films below graphene . . . . .	21
	3.a Intercalation compounds . . . . .	21
	3.b Intercalation process . . . . .	22
	3.c Restoring the properties of isolated graphene <i>via</i> intercalation . . . . .	23
	3.d Tuning graphene properties from below . . . . .	26
4	Functionalization of graphene from on top . . . . .	28
	4.a Adatoms and molecules as dopants . . . . .	28
	4.b Spin systems on graphene . . . . .	29
5	Towards probing Yu-Shiba-Rusinov states in graphene . . . . .	29
	5.a Yu-Shiba-Rusinov states . . . . .	29
	5.b Effect of dimensionality . . . . .	30
	5.c Targeted graphene-based system . . . . .	31

---

## Abstract

In this Chapter, we present the structural, electronic and vibrational properties of isolated graphene. In particular, we discuss the influence of doping, defects and strain on the Raman signature of graphene. After briefly introducing graphene growth on metals in UHV conditions, we present the structural and electronic modifications of graphene supported on different metallic substrates with respect to isolated graphene. An overview of graphite and graphene intercalation compounds is given, followed by the description of the structural, electronic and vibrational properties of intercalated graphene. Functionalization of graphene from below (with use of intercalants) and using adatoms and molecules deposited on top are reviewed. At the end of the Chapter, the targeted graphene-based system is presented.

## 1 Isolated graphene

### 1.a Crystallographic structure

The hexagonal (honeycomb) lattice of graphene consists in a triangular Bravais lattice with two atoms (A and B) per unit cell. The term sublattice is usually used to refer to the triangular A and B lattices which constitute the Bravais lattice of graphene. The unit cell of graphene's lattice is defined by the vectors  $(\mathbf{a}_1, \mathbf{a}_2)$ . When expressed in the  $(\mathbf{e}_x, \mathbf{e}_y)$  basis, these vectors write as:

$$\mathbf{a}_1 = a\sqrt{3}\left(\frac{\sqrt{3}}{2}, \frac{1}{2}\right), \quad \mathbf{a}_2 = a\sqrt{3}\left(\frac{\sqrt{3}}{2}, -\frac{1}{2}\right) \quad (\text{I.1})$$

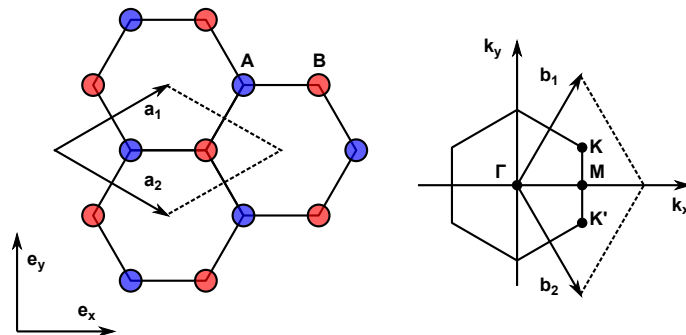
where  $a = 1.42 \text{ \AA}$  is the interatomic distance. The lattice parameter of graphene, denoted as  $a_{\text{gr}}$ , is related to the interatomic distance through  $a_{\text{gr}} = a\sqrt{3}$ .

The first Brillouin zone of graphene is hexagonal (Figure I.1, right). The reciprocal lattice vectors  $(\mathbf{b}_1, \mathbf{b}_2)$  satisfy the relationship  $\mathbf{a}_i \cdot \mathbf{b}_j = 2\pi\delta_{ij}$ , where  $\delta_{ij}$  is the Kronecker delta.  $(\mathbf{b}_1, \mathbf{b}_2)$  given in the  $(\mathbf{k}_x, \mathbf{k}_y)$  basis write as:

$$\mathbf{b}_1 = \frac{4\pi}{3a}\left(\frac{1}{2}, \frac{\sqrt{3}}{2}\right), \quad \mathbf{b}_2 = \frac{4\pi}{3a}\left(\frac{1}{2}, -\frac{\sqrt{3}}{2}\right) \quad (\text{I.2})$$

The highest-symmetry points of graphene ( $\Gamma$ , K, K' and M) are represented in Figure I.1. K and K' are non-equivalent consecutive corners of the first Brillouin zone. As we will show in Section 1.c, the low-energy physics of graphene occurs at K and K'. Their coordinates (in the  $(\mathbf{k}_x, \mathbf{k}_y)$  basis) are given hereafter:

$$\text{K} = \left(\frac{2\pi}{3a}, \frac{2\pi}{3\sqrt{3}a}\right), \quad \text{K}' = \left(\frac{2\pi}{3a}, -\frac{2\pi}{3\sqrt{3}a}\right) \quad (\text{I.3})$$



*Figure I.1: Crystallographic structure of graphene. Left: Direct lattice of graphene, made of two triangular sublattices with A- and B-type atoms. The unit cell (dashed lines) in direct space is defined by the vectors  $\mathbf{a}_1$  and  $\mathbf{a}_2$ . Right: Reciprocal lattice of graphene. The first Brillouin zone of graphene and the reciprocal unit cell (dashed lines) defined by the vectors  $\mathbf{b}_1$  and  $\mathbf{b}_2$  are shown. The highest-symmetry points ( $\Gamma$ , K, K' and M) are indicated. Figure reproduced and adapted from Ref. [6].*

## 1.b Electronic structure

We remind the electronic configuration of an isolated carbon atom:  $1s^2 2s^2 2p^2$ . The two  $1s$  electrons are core electrons. They are bound to the nucleus and do not play any role in the electronic properties of graphene. The  $2s$  and  $2p$  electrons (four electrons, in total) are valence electrons and their atomic orbitals undergo what is called an  $sp^2$  hybridization:  $2s$ ,  $2p_x$  and  $2p_y$  orbitals hybridize and give rise to three  $sp^2$  orbitals. These  $sp^2$  orbitals are linear combinations of  $2s$ ,  $2p_x$  and  $2p_y$  orbitals and are contained in the  $xy$  plane (Figure I.2, top part).

$sp^2$  orbitals strongly overlap between neighbouring carbon atoms and give rise to molecular orbitals, called bonding  $\sigma$  and anti-bonding  $\sigma^*$  orbitals. These orbitals are associated to covalent bonds which are responsible for the in-plane mechanical strength of graphene.

The remaining fourth electron of each carbon atom, which belongs to the unchanged  $2p_z$  orbital, is oriented along the  $z$  axis (axis orthogonal to the crystal plane). The small overlap of  $2p_z$  orbitals between carbon atoms results in the formation of  $\pi$  and  $\pi^*$  molecular orbitals, of energies close to the Fermi energy. These orbitals are associated with the formation of delocalized bonds, which play a major role in the electronic properties of graphene.

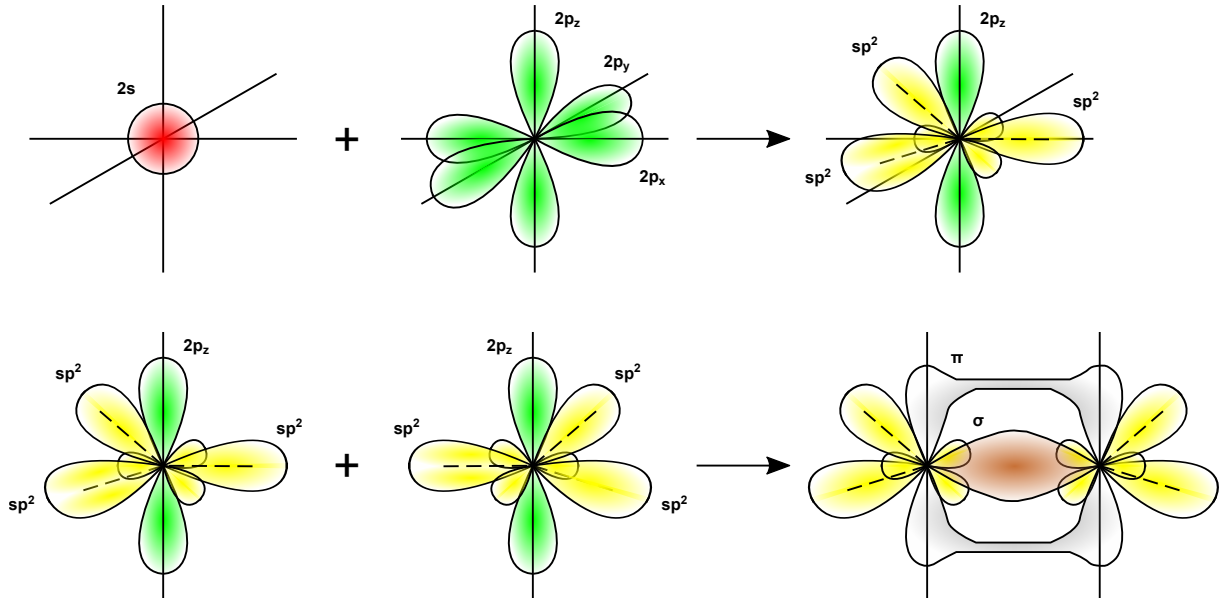


Figure I.2:  $sp^2$  hybridization and formation of  $\sigma$  and  $\pi$  bonds in graphene. **Top:** The  $2s$ ,  $2p_x$  and  $2p_y$  orbitals of carbon hybridize and give rise to three  $sp^2$  orbitals, contained in the  $xy$  plane. The unchanged  $2p_z$  orbital is oriented along the  $z$  axis. **Bottom:**  $sp^2$  orbitals of neighbouring carbon atoms strongly overlap and form  $\sigma$  bonds.  $2p_z$  orbitals of neighbouring carbon atoms slightly overlap and give rise to  $\pi$  bonds.

## 1.c Band structure

As recalled in the previous subsection, graphene has eight energy bands to fill (six  $\sigma/\sigma^*$  and two  $\pi/\pi^*$ ). For pristine graphene, only the bottom four bands (the bonding bands) are filled since there are four valence electrons available.

The electronic band structure of graphene can be derived using the tight-binding model. This approach consists in considering only the most important orbitals for the study and is valid only when the overlap between neighbouring orbitals is low, *i.e.* when we can “attach” an electron to a specific atom. Here, the low-energy  $\pi$  and  $\pi^*$  orbitals are the ones which play the most important role in the electronic properties of graphene. The overlap between neighbouring atoms is small, hence the tight binding model can be applied and gives a satisfying description of the system.



The Hilbert basis of the system is defined as:  $\{|\phi(\mathbf{r} - \mathbf{R}_i)\rangle\}_{i=1}^{\infty}$ , where  $\mathbf{r}$  is the position of the electron of the  $2p_z$  orbital and  $\mathbf{R}_i$  is the position of the atom at site  $i$ . The  $i,j$  component of the Hamiltonian of the system, which describes the interaction between the sites  $i$  and  $j$ , is defined as follows:

$$H_{ij} = \langle \phi(\mathbf{r} - \mathbf{R}_i) | H | \phi(\mathbf{r} - \mathbf{R}_j) \rangle = \int d\mathbf{r} \phi^*(\mathbf{r} - \mathbf{R}_i) H \phi(\mathbf{r} - \mathbf{R}_j), \quad (\text{I.4})$$

Using the first nearest-neighbour approximation, the  $i,j$  component of the Hamiltonian rewrites as:

$$H_{ij} = \begin{cases} -t & \text{if } i,j \text{ are first nearest-neighbours} \\ 0 & \text{otherwise} \end{cases} \quad (\text{I.5})$$

where  $-t$  is the hopping amplitude between first nearest-neighbours ( $t \simeq 2.7$  eV), *i.e.*:

$$-t = \left( \int d\mathbf{r} \phi^*(\mathbf{r} - \mathbf{R}_i) H \phi(\mathbf{r} - \mathbf{R}_j) \right)_{i,j \text{ first nearest-neighbours}} \quad (\text{I.6})$$

The total Hamiltonian of the system is computed applying the Bloch theorem for each sublattice A and B.

$$H = \begin{matrix} \bullet & & \bullet \\ & \epsilon_{\bullet} & -t - t \exp(i\mathbf{k} \cdot \mathbf{a}_1) - t \exp(i\mathbf{k} \cdot \mathbf{a}_2) \\ \bullet & \left( \begin{array}{cc} & \\ -t - t \exp(-i\mathbf{k} \cdot \mathbf{a}_1) - t \exp(-i\mathbf{k} \cdot \mathbf{a}_2) & \epsilon_{\bullet} \end{array} \right) & \bullet \end{matrix} \quad (\text{I.7})$$

The blue and red bullets illustrate the basis used to express the total Hamiltonian, which consists in Bloch waves associated to sublattices A and B.  $\epsilon_{\bullet}$  and  $\epsilon_{\bullet}$  are the onsite interaction energies of the sublattices A and B, respectively. These energies are equal since the atoms of the two sublattices are of the same nature (they are C atoms). The reference in energy is fixed so that  $\epsilon_{\bullet} = \epsilon_{\bullet} = 0$ .

The other two components of this Hamiltonian can easily be understood with the following reasoning. Let us consider the atom A (blue) which belongs to the unit cell depicted in Figure I.1. It has three first nearest-neighbour atoms, which are all type-B atoms (red). One of these atoms is part of the same unit cell as the atom A (atom immediately on its right). Therefore, it only brings a “ $-t$ ” term to the associated Hamiltonian component. The other two first nearest-neighbour atoms belong to two distinct unit cells, which both differ from the (main) unit cell of the atom A. The bottom left atom B brings a “ $-t$ ” term, multiplied by a phase term. This phase term is related to the vector that relates the main unit cell to the unit cell of the bottom left atom B, *i.e.*  $-\mathbf{a}_1$ . Therefore, the term brought by this second neighbour writes as  $-t \exp(-i\mathbf{k} \cdot (-\mathbf{a}_1)) = -t \exp(i\mathbf{k} \cdot \mathbf{a}_1)$ . By applying the same reasoning to the top left B atom, we find that the associated term is  $-t \exp(i\mathbf{k} \cdot \mathbf{a}_2)$ . Overall,  $H_{\bullet\bullet} = -t - t \exp(i\mathbf{k} \cdot \mathbf{a}_1) - t \exp(i\mathbf{k} \cdot \mathbf{a}_2)$ . The total Hamiltonian rewrites as:

$$H = \begin{pmatrix} 0 & f(\mathbf{k}) \\ f^*(\mathbf{k}) & 0 \end{pmatrix} \text{ where } f(\mathbf{k}) = -t(1 + \exp(i\mathbf{k} \cdot \mathbf{a}_1) + \exp(i\mathbf{k} \cdot \mathbf{a}_2)). \quad (\text{I.8})$$

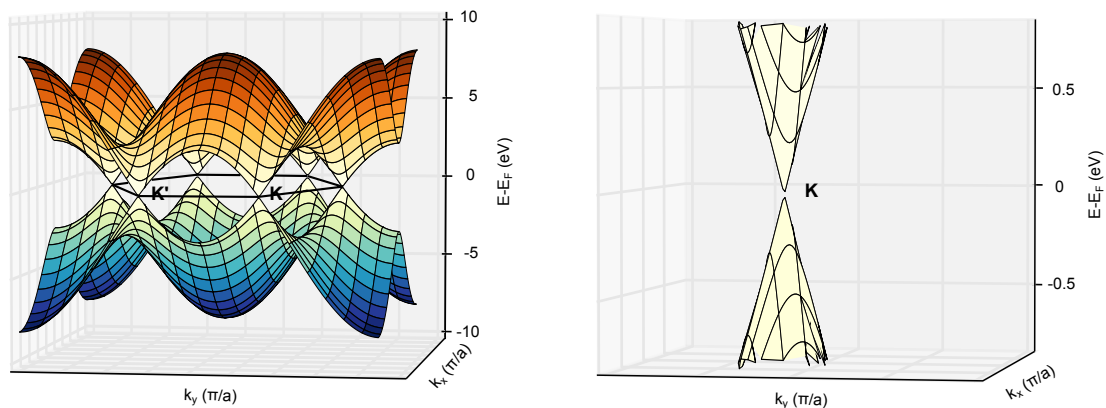
The eigenvalues of this Hamiltonian satisfy:  $E(\vec{k})^2 - |f(\vec{k})|^2 = (E(\vec{k}) - |f(\vec{k})|)(E(\vec{k}) + |f(\vec{k})|)$ , *i.e.*  $E(\vec{k}) = \pm |f(\vec{k})|$ . They write more explicitly under the following form:

$$E_{\pm}(k_x, k_y) = \pm t \sqrt{3 + 2 \cos(\sqrt{3}k_y a) + 4 \cos(\sqrt{3} \frac{k_y a}{2}) \cos(\sqrt{3} \frac{k_x a}{2})} \quad (\text{I.9})$$

The  $+$  and  $-$  signs refer to the bands lying, respectively, above and below the Fermi level. In other words, they refer to the anti-bonding  $\pi^*$  and bonding  $\pi$  bands, respectively.

In the absence of doping, the anti-bonding  $\pi^*$  band, which constitutes the valence band (represented in blue in Figure I.3, left) and the bonding  $\pi$  band, which corresponds to the conduction band of graphene

(in orange) touch exactly at the Fermi energy at the K and K' points. For this reason, graphene is often said to be a zero band gap semiconductor. The dispersion relation  $E(k)$  of graphene is linear around the K and K' points (Figure I.3, right). In the energy range where the linear dispersion is a good approximation, a Dirac Hamiltonian can in fact be used to describe the properties of the electrons. Consequently, the K and K' points are called the Dirac points and the linear behaviour of the energy for small wave vectors is referred to as the Dirac cones. In this linear regime, charge carriers in graphene behave as chiral massless quasi-particles whose velocity is the Fermi velocity  $v_F$ . This Fermi velocity is approximately 300 times less than the speed of light. This description helps explaining many of the peculiar properties of graphene. The description of some of these properties will be addressed in the following subsection.



*Figure I.3: Band structure of graphene derived from the tight-binding model in the first nearest-neighbour approximation. Left: The  $\pi$  (blue) and  $\pi^*$  (orange) bands of graphene touch at the Fermi energy at the K and K' points. The K and K' points lay at the corners of the first Brillouin zone of graphene. Right: Linear dispersion around the K (and K') points for small wave vectors.*

## 1.d Electronic transport properties

Ever since the works of Geim and Novoselov, which were published from 2005 [7] and awarded with the Nobel Prize in Physics in 2010, graphene has revealed unique thermal, mechanical and electronic properties (the latter having spurred the initial interest devoted to graphene).

Fascinating electronic transport properties have been addressed in graphene when sufficiently high quality samples could be prepared, in which mesoscopic ballistic transport occurs. Ballistic transport (as opposed to diffusive transport) refers to the electronic conduction regime where charge carriers move in quasi-classical straight trajectories, only limited by the borders of the sample. In the ballistic regime, the mean free path of electrons is such that electrons do not experience collisions in the channel length  $L$  of the considered device (where  $L$  varies between the nanometer and the micron). At low temperature, the ballistic mean free path of electrons in graphene heterostructures can reach up to  $15 \mu\text{m}$  [8], whereas it reaches “only” 10 to 100 nm in doped silicon.

Graphene also holds the record of the highest intrinsic mobility at room temperature: it amounts to  $15\,000 \text{ cm}^2 \cdot \text{V}^{-1} \cdot \text{s}^{-1}$  [9], versus  $1\,400 \text{ cm}^2 \cdot \text{V}^{-1} \cdot \text{s}^{-1}$  for silicon, and can go as high as  $10^6 \text{ cm}^2 \cdot \text{V}^{-1} \cdot \text{s}^{-1}$  at low temperature [10]. In fact, it was shown that at a technologically relevant carrier density of  $1 \cdot 10^{12} \text{ cm}^{-2}$ , the intrinsic mobility of graphene at room temperature could reach  $2 \cdot 10^5 \text{ cm}^2 \cdot \text{V}^{-1} \cdot \text{s}^{-1}$  [11]. We remind that the mobility characterizes the aptitude of charge carriers to be displaced under an electric field.

Other remarkable electronic phenomena were observed in graphene, such as the abnormal integer quantum Hall effect (abnormal IQHE) and Klein tunneling. The abnormal IQHE, also known as the half-integer quantum Hall effect, is a relativistic analogue of the IQHE [7, 12]. We remind the reader that the IQHE relies on the quantization of the energy of charged particles in a uniform magnetic field, in so-called Landau levels. In graphene, the abnormal IQHE shows up as an uninterrupted ladder of

equidistant steps in the Hall conductivity  $\sigma_{xy}$ , shifted by one-half with respect to the standard IQHE sequence, so that  $\sigma_{xy} = 4\frac{e^2}{h}(N + \frac{1}{2})$  where  $N$  is the index of the Landau level. The abnormal behaviour observed in graphene is related to subtle properties of massless Dirac fermions, in particular to the existence of both electron-like and hole-like Landau states at exactly zero energy [7].

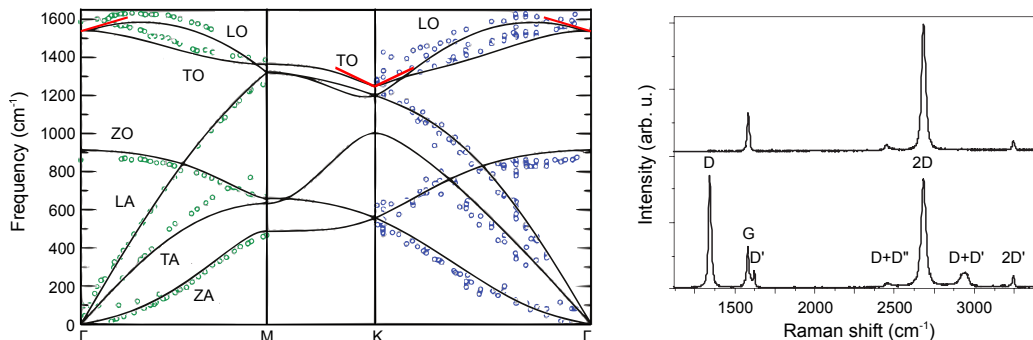
As for Klein tunneling - predicted in high-energy physics and experimentally observed for the first time in graphene - it corresponds to the unimpeded penetration of charge carriers through high and wide potential barriers. In particular, in  $n$ - $p$ - $n$  and  $p$ - $n$ - $p$  junctions, the transmission is 1 for angles close to the normal incidence. This phenomenon is related to the peculiar (relativistic) nature of charge carriers in graphene [13, 14]. Although the conical electronic band structure of graphene is important, the relativistic nature of charge carriers in graphene is rather related to the honeycomb structure, and more precisely to the relative contributions of the sublattices A and B. The electronic band structure of graphene actually results from the intersection of two branches originating from sublattices A and B. For this reason, an electron with energy  $E$  propagating in the positive direction and a hole with energy  $-E$  propagating in the opposite direction lie on the same branch. The interconnection of electrons and holes constitutes the crucial element for Klein tunneling. In condensed matter, electrons and holes are usually described by separate Schrödinger equations. In graphene, the description of charge carriers is made by using two-component wavefunctions. In an analogy with relativistic particles, a so-called pseudospin is defined, in relation to the sublattices A and B. In the absence of pseudospin-flip processes (such processes are rare as they require a short-range potential, which would act differently on A and B sublattices), an electron moving to the right which comes across a potential barrier can only be scattered to a right-moving electron state or to a left-moving hole state. If the barrier is such that graphene is for instance,  $n$ -doped, then  $p$ -doped, then  $n$ -doped again, the incoming electron will be scattered to a hole and then back to an electron with transmission 1.

### 1.e Raman signature of graphene

Raman spectroscopy is a non destructive technique which relies on the study of inelastically scattered light. For the non-specialist reader, we recommend reading the brief presentation of the technique given in Section 3 before proceeding to the present section.

As recalled in Section 1.a, graphene presents two atoms per unit cell. For this reason, it exhibits six vibrational modes: three acoustic modes, ZA, TA and LA, and three optical modes ZO, TO and LO. The letters Z, L and T refer to out-of-plane, longitudinal and transverse modes, respectively.

The dispersion relation of phonons in isolated graphene can be derived from DFT calculations [15]. The calculated dispersion relation is very close to the one observed experimentally using high resolution electron energy loss spectroscopy (HREELS), as can be seen in Figure I.4.



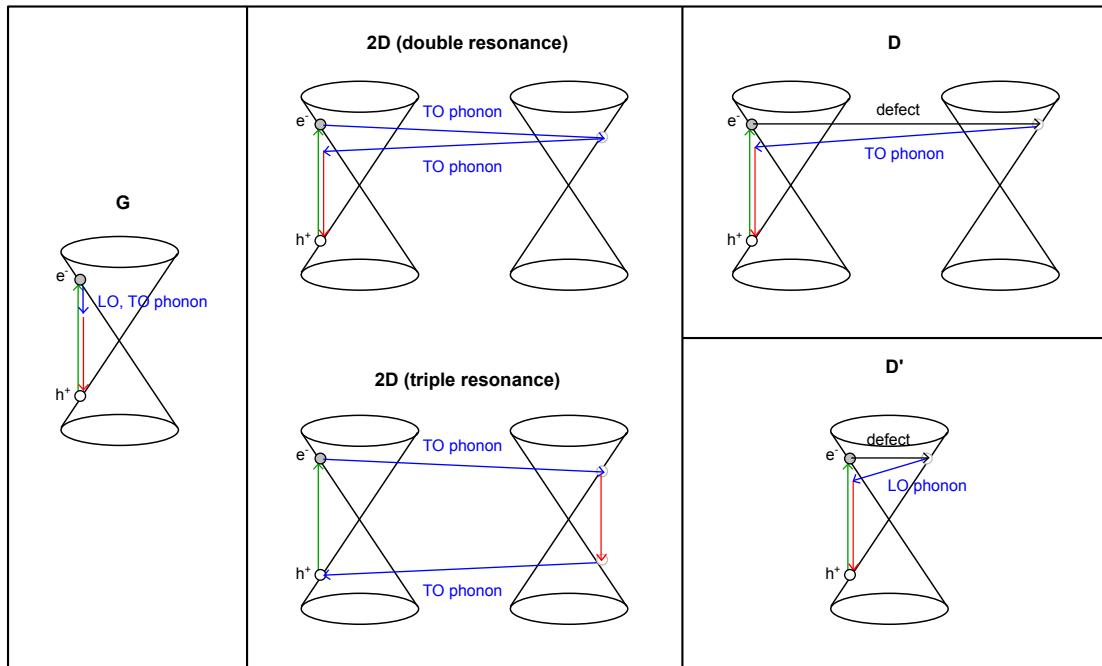
**Figure I.4: Phonon dispersion and Raman signature of graphene.** **Left:** Phonon dispersion of isolated graphene. Black lines: phonon dispersion calculated with DFT. Green and blue circles: HREELS data of Refs. [16] and [17], respectively. The red lines represent the Kohn anomalies. Figure adapted from Ref. [15]. **Right:** Raman spectra of pristine (top) and defected (bottom) graphene. The main peaks are labelled. Figure adapted from Ref. [18].

In Raman spectroscopy, graphene exhibits a specific signature and is hence easily identified. The most prominent modes of isolated graphene give rise to intense peaks in Raman spectroscopy, the so-called G and 2D bands (Figure I.4, top right).

The various Raman-active vibrational modes of graphene are sketched in Figure I.5.

The G band, observed around  $1580\text{ cm}^{-1}$ , is associated with a one-phonon first-order Raman process which originates from  $\Gamma$ , the center of the first Brillouin zone of graphene. It involves LO and TO phonons.

The 2D band is related to a two-phonon second-order Raman process involving TO phonons at K and K'. It is observed around  $2660\text{ cm}^{-1}$ . Two equivalent forms of the Raman process related to the 2D band exist: the double resonance and the triple resonance. In direct space, the process at the origin of the 2D band corresponds to the breathing mode of a six-atom carbon ring. In bilayer graphene, the 2D band splits into four bands, reflecting the evolution of the band structure [19].



**Figure I.5: Raman processes in graphene.** **Left:** One-phonon first-order G band process. **Center:** Two-phonon second-order 2D band processes: the double resonance (top), and the triple resonance (bottom). **Right:** One-phonon second-order doubly resonant process for the D band (intervalley process) (top) and for the D' band (intravalley process) (bottom). For one-phonon second-order transitions, one of the two scattering events is an elastic scattering event. Resonance points are shown as open circles near the K and K' points. Figure reproduced and adapted from Ref. [22].

In a material with metallic behaviour, an abrupt change in the screening of a lattice vibration associated with a specific wavenumber by conduction electrons gives rise to an anomalous behavior in the phonon dispersion, known as a Kohn anomaly. The Kohn anomalies of the phonon dispersion of isolated graphene, appearing as kinks in the phonon dispersion of the LO mode at  $\Gamma$  and of the TO mode at K (Figure I.4, left), are intimately related to the dispersion of the  $\pi$  bands around the high-symmetry point K. In fact, the slope of these branches (LO mode at  $\Gamma$  and TO mode at K, also referred to as the highest optical branch) provides a direct measurement of the electron-phonon coupling between these modes and the  $\pi$  bands [20]. This coupling is responsible for the strong signals observed in Raman spectroscopy. The effect of graphene's substrate on the Kohn anomalies of graphene has been investigated in Ref. [15]. Strongly interacting metallic substrates are responsible for the vanishing of the Kohn anomalies in graphene, which results in the absence of the characteristic graphene bands in Raman spectroscopy.

Other modes can be observed in the presence of structural disorder (Figure I.4, bottom right). In particular, the D band, which stems from a one-phonon second-order doubly resonant scattering process in the presence of defects, appears around  $1330\text{ cm}^{-1}$ . It involves the same phonons as the 2D band, *i.e.*

TO phonons at K and K'. An elastic scattering event, due to the presence of a defect, replaces one of the two phononic inelastic scattering events. Similarly to the D band, the D' band (which is significantly less intense than the D band) originates from a one-phonon second-order doubly resonant Raman process in the presence of defects. It involves LO phonons around  $\Gamma$  and is observed around  $1620 \text{ cm}^{-1}$ . While the D band process is an intervalley scattering process, the D' band process is an intravalley process *i.e.* it connects two points belonging to same Dirac cone at K or K'. The overtone of the D' band is called the 2D' band, and similarly to the 2D band does not require a defect for its activation. Another defect-activated (weak) feature corresponding to the combination of the D and D' modes, and known as the D+D' peak, is observed at about  $3000 \text{ cm}^{-1}$ . Finally, the band observed in defected samples at about  $2450 \text{ cm}^{-1}$  is assigned to a combination of the D mode with a phonon mode belonging to the LA branch (seen at  $\simeq 1100 \text{ cm}^{-1}$  when measured with visible light) and called the D" mode. It is therefore referred to as the D+D" mode.

The D mode, its overtone, and the combination modes involving it are strongly dispersive with the excitation (laser) energy due to the Kohn anomaly at K and the resonant scattering mechanism at the origin of such peaks [20, 21]. In fact, the D peak dispersion can be used as a way to probe the Kohn anomaly *i.e.* as a way to measure the electron-phonon coupling. By contrast, the G peak is insensitive to the excitation energy.

### Influence of defects

The effect of structural disorder on the Raman spectrum of graphene has been extensively studied [23, 24, 25, 21]. In particular, the G, 2D and D band widths increase as the density of defects increases, *i.e.* as the inter-defect distance  $L_D$  decreases [25]. Such broadening is associated with the defect-induced shortening of the Raman phonon lifetimes.

Besides, it was shown that the D to G intensity ratio,  $I_D/I_G$ , has a non-monotonic dependence with  $L_D$ : it increases with increasing  $L_D$ , reaches a maximum at  $L_D = 3\text{-}4 \text{ nm}$ , and then decreases for  $L_D > 3\text{-}4 \text{ nm}$  (Figure I.6, left). Lucchese *et al.* proposed a phenomenological model to account for such behaviour, which they attribute to competing mechanisms contributing to the Raman D band [24]. The authors defined two length scales, denoted by  $r_A$  and  $r_S$ , with  $r_A > r_S$ . Within the area defined by the shorter radius  $r_S$ , structural disorder occurs and the concerned region is called the structurally-disordered region or S-region. For distances larger than  $r_S$  but shorter than  $r_A$ , which define the so-called activated-region or A-region, the structure of the graphene lattice is preserved but the close-by defect causes an enhancement of the D band. S-regions contribute less to the D band than A-regions, as the graphene lattice is damaged in the former regions. The  $L_D$  dependence of the  $I_D/I_G$  ratio can be understood from the evolution, with increasing defect density, of the fraction areas corresponding to S- and A-regions. Indeed, for low defect density (large  $L_D$ ), the area contributing to the D band scattering process is proportional to the number of defects. As the defect density increases, the A-regions start to overlap and eventually saturate, hence the D band intensity reaches a maximum. As the defect density further increases, the S-regions dominate and the D band intensity decreases. The phenomenological model proposed by Lucchese *et al.* writes as:

$$\frac{I_D}{I_G}(L_D) = C_A f_A(L_D) + C_S f_S(L_D) \quad (\text{I.10})$$

where  $f_A$  and  $f_S$  are the fractions of the A- and S-regions, respectively, and  $C_A$  and  $C_S$  are the parameters of the model. The phenomenological model developed by Lucchese *et al.* was implemented using stochastic simulations. Although it can be generalized to any source of point defects, the measurements presented in Ref. [24] were performed on graphene subjected to  $\text{Ar}^+$  ion bombardment. For this reason, the simulations used to track the evolution of a graphene sheet under an increasing defect density considered ion bombardment as the source of defects, where the impact positions of  $\text{Ar}^+$  ions followed a random

sequence. Snapshots of the evolution of the graphene sheet for different defect concentrations are shown in Figure I.6 (right).

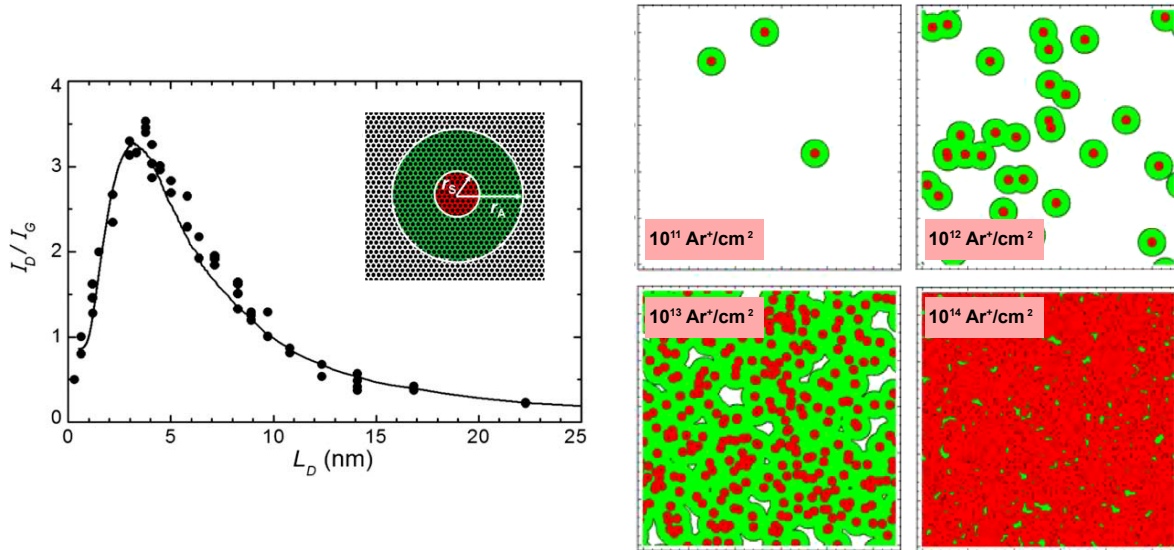


Figure I.6:  $L_D$  dependence of the  $I_D/I_G$  ratio. **Left:**  $I_D/I_G$  as a function of  $L_D$ , measured on graphene subjected to  $\text{Ar}^+$  ion bombardment (black circles), and phenomenological model (solid line). Inset: Definition of the activated A- (green) and structurally-disordered S- (red) regions. **Right:** Snapshots of (a portion of) the graphene simulation cell, showing the structural evolution of the graphene sheet for different defect concentrations. Figure adapted from Ref. [24].

Finally, the D' band intensity and width increase as the inter-defect distance decreases. Actually, when  $L_D$  reaches  $\simeq 2$  nm or less, the G and D' bands become hardly discernable from one another (the D' band appears at the right shoulder of the G band) [24]. For this reason, the position of the G band can be slightly overestimated. Other than this, the positions of graphene bands are not altered by the presence of defects.

### Influence of doping

The effect of doping on the Raman spectrum of graphene has been thoroughly investigated [26, 27, 28, 29, 30, 31]. It was shown to mainly influence the G band. In doped graphene, the Fermi energy shift induced doping has two major effects, which differently affect the position of the G band. Firstly, it changes the equilibrium lattice parameter with a consequent stiffening/softening of the phonons. This effect was extensively studied in the case of graphite intercalation compounds: electron doping ( $n$ -doping) results in an expansion of the crystal lattice, while hole doping ( $p$ -doping) results in a contraction of the crystal lattice [32]. Consequently,  $n$ -doping is responsible for a downshift of the G band while  $p$ -doping results in an upshift. Secondly, various (dynamical) effects beyond the adiabatic Born-Oppenheimer approximation modify the phonon dispersion close to the Kohn anomalies of graphene [26, 27, 29, 30]. The latter effects result in the removal of the Kohn anomaly at  $\Gamma$ , which causes a G band wavenumber increase with the doping level, regardless of the type of doping. Overall, for low doping levels ( $< 3 \cdot 10^{13} \text{ cm}^{-2}$ ), both  $n$ - and  $p$ -doping result in an upshift of the G peak [27, 29], while for high doping levels ( $> 3 \cdot 10^{13} \text{ cm}^{-2}$ ), the  $n$ -doped case reverses [26] (Figure I.7, top left).

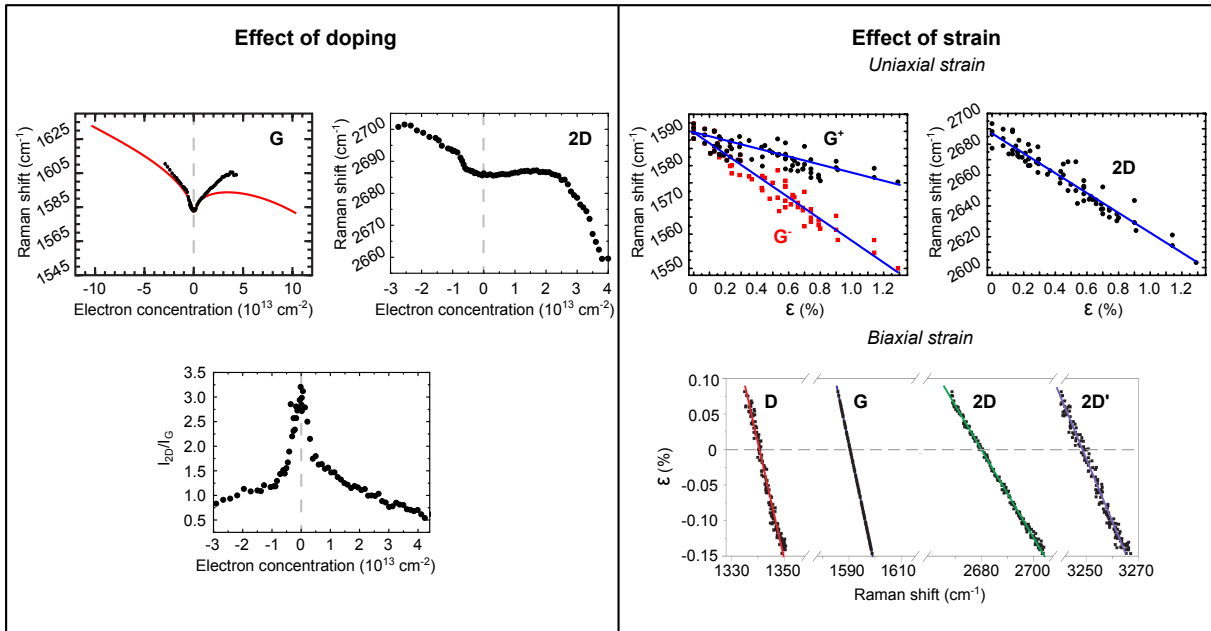
As for the 2D band, its position increases for hole doping, and decreases for high electron doping [29] (Figure I.7, top left). Besides, the 2D band intensity exhibits a strong dependence with the doping level [29, 30], which was assigned in Ref. [30] to a combination of electron-phonon and electron-electron scattering. The 2D band intensity, normalized with the G band intensity, is shown as a function of the electron concentration in Figure I.7 (bottom left).



## Influence of strain

Finally, strain also influences the Raman signature of graphene [18]. In the case of uniaxial tensile strain, it was shown that the G band splits into two bands called  $G^-$  and  $G^+$ , one polarized along the strain, the other perpendicular to it [33, 34]. Such splitting occurs due to the crystal symmetry breaking. The splitting increases and the  $G^-$  and  $G^+$  band wavenumbers decrease linearly as the uniaxial tensile strain increases (Figure I.7, top right). The 2D and 2D' band wavenumbers decrease linearly as well but do not split for small strains (Figure I.7, top right). It is important to note that the linear shifts measured for  $G^-$ ,  $G^+$  and 2D modes are different in Refs. [33] and [34] (the shift of the 2D' mode is not reported in Ref. [33]). Still, the 2D peak position is found to be the most sensitive to uniaxial tensile strain: it shifts by  $-21 \text{ cm}^{-1}$  per percent of strain in Ref. [33] and  $-64 \text{ cm}^{-1}$  per percent of strain in Ref. [34]. Indeed, uniaxial strain moves the relative positions of the Dirac cones, hence it has a significant influence on the position of the 2D mode, which originates from an intervalley (double/triple) resonance process.

In the case of biaxial (*i.e.* isotropic) strain, no G-peak splitting occurs (the crystal symmetry is preserved). For tensile biaxial strain, the D, G, 2D and 2D' bands shift to lower wavenumbers [35, 36], while they shift to higher wavenumbers for compressive biaxial strain [35] (Figure I.7, bottom right). Linear fits to the data (under compressive and tensile biaxial strain) indicate that, similarly to the case of uniaxial strain, the 2D band position is the most sensitive to biaxial strain [35, 36].



**Figure I.7: Effect of doping and strain on the Raman spectrum of graphene.** **Left:** (Top) Positions of the G and 2D bands as a function of the electron concentration, adapted from Ref. [29]. The red solid line is the calculated non-adiabatic trend reported in Ref. [26]. (Bottom)  $I_{2D}/I_G$  as a function of the electron concentration, adapted from Ref. [29]. **Right:** (Top) Positions of the  $G^-$ ,  $G^+$  and 2D bands as a function of the applied uniaxial (tensile) strain  $\epsilon$ , adapted from Ref. [34]. The solid lines are linear fits to the data. (Bottom) Positions of the D, G, 2D and 2D' modes as a function of the applied biaxial strain  $\epsilon$ , adapted from Ref. [35]. The solid lines are linear fits to the data.

## 2 Graphene on metals

### 2.a Graphene growth on metals

Graphene growth on metals has been known for decades, with first reports dating back to the 60s addressing the pollution of catalyst surfaces by graphene or thin graphite films. Since then the viewpoint has changed, as metal substrates are well-suited to the growth of high-quality large-area graphene in

well-chosen conditions, for instance in UHV (we refer the reader to a few recent specialized reviews that address growth on these substrates [37, 38, 39]). In addition, the metal may be used as both a substrate and a material hosting properties that could influence those of graphene, *via* a proximity effect.

Graphene growth in UHV consists in exposing a clean metallic surface to a carbon-containing species at sufficiently high temperature. Different growth mechanisms have been identified: after the cracking of the carbon precursor species, carbon atoms can either remain on the surface of the metal as it is the case for low carbon solubility metals like Ir, Cu, Pt and Au, dissolve inside the metal bulk such as with high carbon solubility metals like Ru, Re, Rh and Ni or form surface carbides [40], whose structure is sometimes complex and ill-characterized.

The thermally activated decomposition of the carbon precursor onto the metal, followed by the carbon adatoms diffusion on the metal surface and the formation of graphene is referred to as surface growth *via* chemical vapour deposition (CVD). In metals like Ru, Re, Rh and Ni, the high solubility of carbon in the temperature ranges of interest ( $\simeq 700$  K) [41] is such that carbon atoms preferentially dissolve into the metal bulk. Surface segregation upon cool down of carbon atoms stored inside the bulk metal can result in the formation of graphene [42].

One CVD approach consists in growing graphene on Cu foils, using quartz tubes as growth chambers. This method, which takes advantage of the etching nature of hydrogen, has allowed growing large-area high-quality graphene sheets with temperature- and pressure-controlled introduction of a mixture of methane and hydrogen [43].

Graphene growth on single-crystal Re(0001) and the competing formation of a surface carbide have been investigated in Refs. [44, 45] and will be discussed in further details in Chapter III. Rhenium is a substrate of choice in view of inducing superconductivity in graphene *via* the proximity effect [3], and superconductivity is a crucial ingredient for realizing the targeted graphene-based system which will be presented at the end of this Chapter. For this reason, in the following sections, we will illustrate as much as possible the introduced concepts with graphene on Re(0001).

## 2.b Moiré superlattices

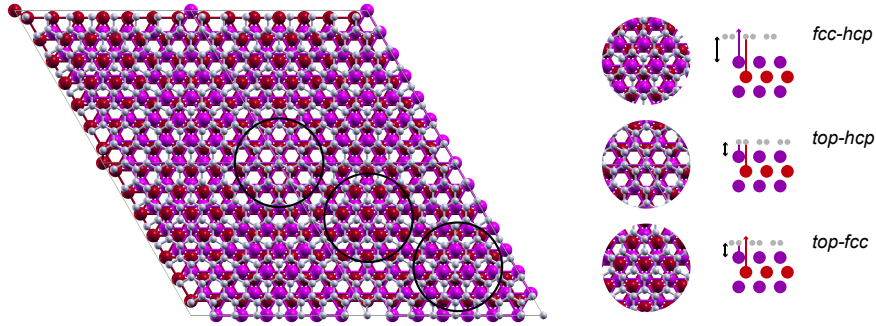
### Nanorippling and relationship with atomic stacking

When supported on a metallic substrate, the lattice mismatch and/or the disorientation between graphene and the substrate result in a periodic undulation of graphene on top of its substrate. This undulation translates into a moiré superlattice, associated with a periodicity (the moiré superperiodicity) of the order of the nanometer [46]. The moiré superlattice exhibits a hill-and-valley topography: hills correspond to regions where the graphene-substrate distance is larger, and valleys refer to the graphene regions closest to the substrate.

We briefly remind elementary geometrical features of the moiré pattern between graphene and its metallic substrate (detailed descriptions can be found in focused reports [47, 48, 49, 50]). Disregarding first the nanorippling of graphene, the relative in-plane stacking of C atoms on the metal lattice varies from site to site in the moiré pattern. Three high-symmetry stacking types are usually considered, namely *fcc-hcp*, where the two C sublattices of graphene each sit on different hollow binding sites (usually called *hcp* and *fcc*) of the substrate, *top-hcp* and *top-fcc*, where one of the C sublattices sits directly atop a metal atom and the other on a hollow site (*hcp* or *fcc*). At the location of the *fcc-hcp* stacking, *i.e.* the location of a moiré hill, we only see through the graphene lattice the Re atoms of the topmost layer. At the location of the *top-hcp* and *top-fcc* stackings (which are two inequivalent moiré valleys), respectively no Re atom and the atoms from the second Re plane are seen through. Figure I.8 shows the converged structure of graphene/Re(0001) calculated *via* DFT, assuming a coincidence of  $(8 \times 8)$  graphene unit cells on top of  $(7 \times 7)$  Re(0001) unit cells. The *fcc-hcp*, *top-hcp* and *top-fcc* regions are indicated. For these three kinds of stacking the interaction between graphene and the substrate is different as well [51, 44, 52],



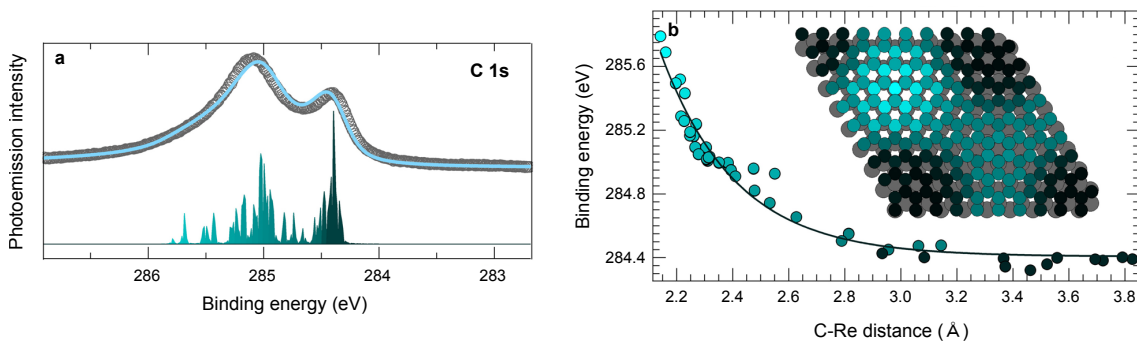
thus the graphene-metal distance is different: this is what drives the nanorippling of graphene.



**Figure I.8: Varying atomic stacking within the moiré unit cell.** **Left:** Top view of the converged structure of the  $(7 \times 8)$  graphene/Re(0001) system, adapted from Ref. [3]. Grey rhombi indicate the moiré unit cell. **Right:** Atomic stacking in *fcc-hcp*, *top-hcp* and *top-fcc* regions, from top and side views.

The relative height of the hills and valleys depends on several factors. Especially, a stronger interaction (we will later precise the nature of this interaction) between graphene and its substrate imposes lower valleys. Two extreme cases of graphene-substrate binding are commonly acknowledged: weakly interacting metallic substrates such as Ir(111) [53, 52], Pt(111) [54, 46, 55], Cu(111) [56], Al(111) [57], Ag(111) [58] and Au(111) [59]; and strongly interacting metallic substrates such as Re(0001) [3, 60, 61], Ru(0001) [51, 62, 63, 64], Rh(111) [65] and Ni(111) [66]. The latter category is characterized by a strong nanorippling of the graphene sheet [3, 63, 64] and short graphene-substrate distances [65]. For instance, when graphene is supported on Re(0001), graphene’s corrugation (taken as the maximum value of vertical separation between C atoms) amounts to 1.70 Å. The average C-Re distance is  $\simeq 2.60$  Å (taken as the vertical separation between graphene and Re layers, whose heights are averaged over all atoms in the graphene layer and in the Re layer, respectively). The minimum C-Re distance (at the location of moiré valleys) is 2.10 Å and the maximum C-Re distance (at the location of moiré hills) is 3.80 Å.

Contrary to strongly interacting substrates, weakly interacting metals are associated with a smaller graphene nanorippling and larger graphene-substrate distances [52, 55]. For instance, graphene corrugation for graphene supported on Ir(111) (Ref. [52]) amounts to  $\simeq 0.30$  Å and the average C-Ir distance is  $\simeq 3.40$  Å. The minimum and maximum C-Ir distances are 3.30 Å and 3.60 Å, respectively. The term “strong” and “weak” interaction will be further explained in the coming subsections.



**Figure I.9: Distribution of C 1s core-level binding energies and relationship with the nanorippling of graphene grown on Re(0001).** (a) C 1s core-level spectrum of graphene/Re(0001) (empty circles) together with the simulated spectrum (solid blue line) and the calculated spectral distribution corresponding to the 200 C atoms that constitute the simulation supercell. (b) Binding energy of non-equivalent C atoms as a function of the C-Re distance. The color scale reflects the continuum in binding energies of the C 1s components. Figure adapted from Ref. [44]

The C 1s core-level spectrum of graphene/Re(0001), shown in Figure I.9(a), exhibits two main components separated by  $\simeq 700$  meV. The low binding energy component can be naively assigned to

the weakly interacting regions (*i.e.* the moiré hills) while the higher binding energy component would correspond to the strongly interacting regions (*i.e.* the moiré valleys). Actually, rather than a net distinction between “weakly” and “strongly” interacting regions, the results reported in Ref. [44] point to a continuous distribution of core level binding energies in the range [284.3,285.8] eV. The C 1s core-level binding energies of the 200 C atoms present in the moiré unit cell were computed and the total C 1s spectrum was calculated, in very good agreement with the experimental data. Moreover, Miniussi *et al.* found a clear correlation between the binding energy and the C-Re distance (a smaller C-Re distance is associated with a higher binding energy), as can be seen in Figure I.9(b).

### Influence of the interfacial interaction

The structure of a graphene-substrate system is actually closely tied to its electronic properties. Gao *et al.* investigated the influence of the interfacial interaction (charge transfer) on the moiré superstructures of graphene on transition metal substrates [61]. More specifically, they studied the interplay between the strain energy and the interfacial interaction for two model systems, namely graphene/Re(0001) (Re(0001) is a “strongly” interacting metallic substrate) and graphene/Ir(111) (Ir(111) is a “weakly” interacting metallic substrate), by means of DFT calculations. They established which of the two (the strain energy or the interfacial interaction) dominates the moiré superstructure, *i.e.* determines the morphology and stability of graphene. They showed that the strong interfacial interaction in graphene/Re(0001) causes a deviation of C–C bond lengths with respect to free-standing graphene. This in turn introduces a large strain in graphene which facilitates the interaction between graphene and the Re(0001) substrate. Overall, the interfacial interaction dominates the moiré superstructure in the case of graphene/Re(0001). This behaviour is in contrast with the strain-driven moiré superstructure of graphene on Ir(111). The interaction between graphene and the metal substrate, considered as “strong” for graphene/Re(0001) and “weak” for graphene/Ir(111) will be addressed in the following subsection.

### 2.c Hybridization between graphene $\pi$ and metal $d$ states

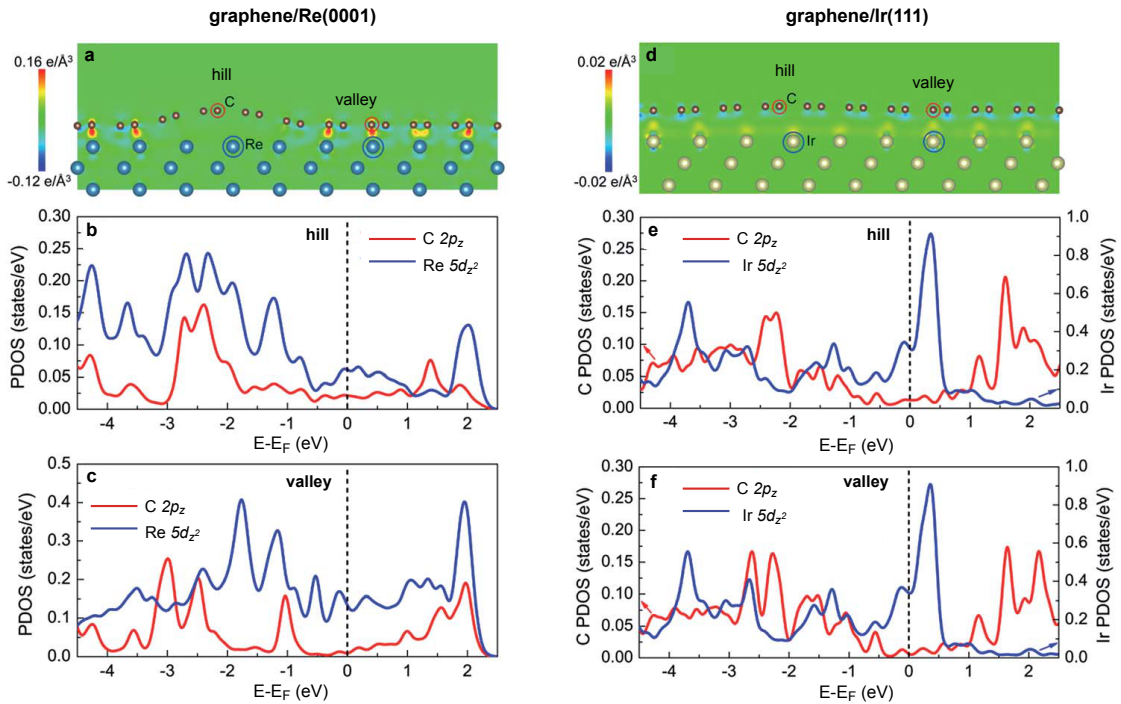


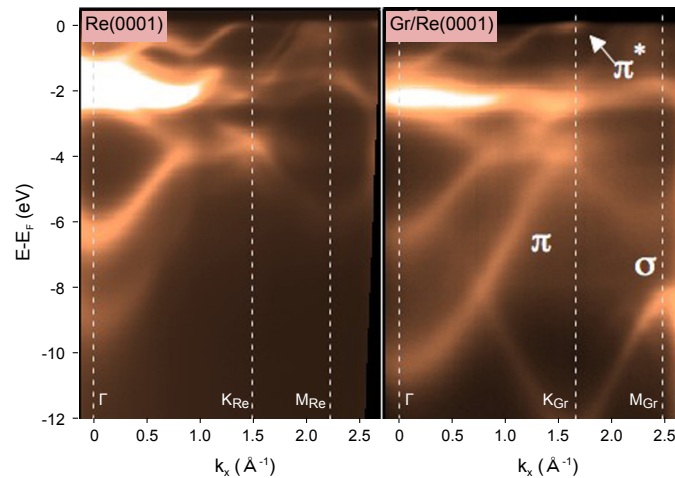
Figure I.10: **Hybridization between graphene and metal  $d$  states.** (a,d) Interfacial charge-transfer distribution between graphene and Re(0001) (a), and between graphene and Ir(111) (d). (b-f) Partial density of states (PDOS) for the C atoms ( $2p_z$  orbital), Re atoms ( $5d_{z^2}$  orbital) and Ir atoms ( $5d_{z^2}$  orbital) labelled in (a,d). Figure adapted from Ref. [61].

Several works illustrated that the interfacial interaction between graphene and transition metal substrates is closely related to the hybridization between the C  $\pi$  orbitals and the metal  $d$  orbitals, especially between the C  $2p_z$  orbital and the metal  $d_{z^2}$  orbital [67, 51, 68, 69, 70, 38]. In 2017, Gao *et al.* confirmed it, by means of DFT calculations [61]. Figure I.10 shows the charge transfer distributions between graphene and Re(0001) (Figure I.10(a)), and between graphene and Ir(111) (Figure I.10(d)). The charger transfer intensities are strong in the valley region of graphene/Re(0001), which indicates a strong interaction. On the contrary, they are rather weak in the hill region of graphene/Re(0001), and in both valley and hill regions of graphene/Ir(111). The hybridization between the C  $2p_z$  orbital and the Re(0001)  $d_{z^2}$  orbital in the hill regions is reflected by the correspondence of the partial density of states curves (peak positions) between the two orbitals (Figure I.10(b)). Such correspondence is not observed in the valley region of graphene/Re(0001), and in both valley and hill regions of graphene/Ir(111), indicating that hybridization did not occur there.

## 2.d Consequences on the electronic properties

### Band gap opening

The chemical nature of the bonds established between graphene and its metallic substrate due to the hybridization between graphene  $\pi$  and metal  $d$  states varies from one substrate to another. Strongly interacting metallic substrates are associated with a tendency to form covalent bonds with graphene, whereas the bonding between graphene and weakly interacting metallic substrates is of van der Waals-type [65, 61]. For the former category, hybridization between the metal  $d$  states and the  $\pi$  band of graphene results in a loss of graphene's electronic linear dispersion [60], as is illustrated in Figure I.11.



**Figure I.11: Band gap opening in graphene on Re(0001).** **Left:** Photoemission intensity plot along the  $\Gamma$ -K direction of Re(0001). **Right:** Photoemission intensity plot along the  $\Gamma$ -K direction of graphene/Re(0001). The highest-symmetry points  $\Gamma$ ,  $K_{\text{Re}}$ ,  $M_{\text{Re}}$ ,  $K_{\text{Gr}}$  and  $M_{\text{Gr}}$  are indicated. Figure adapted from Ref. [60].

Figure I.11 shows ARPES data measured on a clean Re(0001) surface (Figure I.11, left) and on graphene-covered Re(0001) (Figure I.11, right), along the  $\Gamma$ -K direction. The metal  $d$  states of Re extend mainly from 2.5 eV below the Fermi level to the Fermi level (Figure I.11, left). Consequently, the hybridization gap which opens where the metal  $d$  states and graphene  $\pi$  band intersect, lies close to the Fermi level. For this reason, the Dirac cones of graphene are disrupted. The data shows the presence of the  $\pi$  and  $\sigma$  electronic states of graphene. Rather than exhibiting a linear dispersion, the  $\pi$  band displays a parabolic dispersion with a maximum at the K point 3.90 eV below the Fermi level: the hybridization between the metal  $d$  states and graphene  $\pi$  band has opened a large band gap.

Contrary to strongly interacting substrates, weakly interacting metals preserve the Dirac cones of graphene. The reason is that the hybridization energies associated with the overlap of the metal  $d$  orbitals with the  $\pi$  orbitals of graphene are much higher (in absolute values) than in the case of strongly interacting metallic substrates [65, 61]. In other words, hybridization occurs in regions far from the Dirac point.

### Charge transfer

We now introduce the phenomenological capacitor model proposed in Refs. [71, 69]. This very simple model allows discussing the type ( $n$ -type or  $p$ -type doping) and amount of charge transfer in graphene on weakly interacting metals. It relies, for some part, on the work function difference between graphene and the metal substrate. Graphene and the metal substrate work functions, denoted by  $W_G$  and  $W_M$  respectively, correspond to the energy required to extract an electron from the surface of the said material and bring it to a vacuum state at rest. In other words, the higher the work function, the harder it is to extract an electron, hence the more likely it is that the material is populated with electrons.

Naively, one would assume that graphene is doped with electrons when  $W_G > W_M$ , and doped with holes when  $W_G < W_M$ . The crossover point from  $n$ -doping to  $p$ -doping would then lie at  $W_M = W_G$ . Yet, this is not what is observed experimentally. Numerically, the crossover point (calculated by means of DFT calculations) is found at  $W_M - W_G = 0.9$  eV when the distance  $d$  between graphene and the metal substrate is close to the equilibrium distance (*i.e.*  $d \simeq 3.3$  Å for weakly interacting metallic substrates) [71]. Interestingly, the crossover point reduces when the distance is increased (it reaches  $W_M - W_G \simeq 0$  eV when  $d$  equals 5 Å). In other words, the naive model holds only when there is no overlap between the graphene and metal wavefunctions. Such a behaviour points to a contribution from the graphene-metal chemical interaction.

The model proposed in Refs. [71, 69] is introduced hereafter. The work function of the graphene-covered metal is given by  $W(d) = W_M - \Delta V(d)$ , where  $\Delta V$  is the interface voltage drop generated by the graphene-metal interaction.  $\Delta V$  translates the fact that graphene's work function is renormalized when graphene is supported on a metal, due to charge reordering. This voltage drop has two contributions, it writes as  $\Delta V = \Delta V_{\text{tr}}(d) + \Delta V_{\text{c}}(d)$ , where  $\Delta V_{\text{tr}}$  is the charge transfer contribution and  $\Delta V_{\text{c}}$  is the chemical interaction contribution.

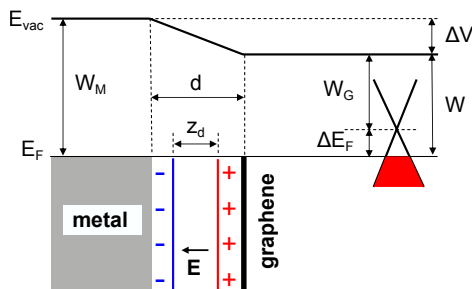


Figure I.12: Schematic illustration of the parameters used in modeling the interface dipole and potential step formation at the graphene-metal interface. Figure adapted from Ref. [71].

The charge transfer contribution  $\Delta V_{\text{tr}}$  stems from the spatial separation of positive and negative charges. Graphene and the metal substrate are modeled as a plane capacitor, *i.e.* they are viewed as charged electrodes creating a dipole electric field. This electric field results in a voltage drop  $V_{\text{tr}}$  at the interface.  $\Delta V_{\text{tr}}$  is positive when electrons are transferred from graphene to the metal, and negative when they are transferred from the metal to graphene. This model introduces an effective distance  $z_d$ , which corresponds to the distance between the charge sheets on graphene and the metal ( $z_d < d$ ). This distance is indicated in Figure I.12.

The chemical interaction contribution to the interface voltage drop,  $\Delta V_{\text{c}}$ , does not depend on the metal substrate but strongly depends on the graphene-metal distance. It is deduced from DFT results

on Cu(111). At an equilibrium separation of 3.3 Å,  $\Delta V_c \simeq 0.9$  eV, and becomes negligible when the graphene-metal distance is large.

The Fermi level shift, from which the amount of transferred charges can be deduced, is modeled as  $\Delta E_F(d) = W(d) - W_G$ . The type (*n*-type or *p*-type) of the charge transfer between graphene and the metal substrate depends on the sign of  $\Delta E_F$ . Three cases are possible:

- $W_M > W_G + \Delta V$  (case depicted in Figure I.12): the work function of the metal is so large that it compensates the voltage drop at the interface, resulting in *p*-doped graphene.
- $W_G < W_M < W_G + \Delta V$ : the work function of the metal is larger than the work function of graphene, yet not large enough to compensate the voltage drop at the interface, resulting in *n*-doped graphene.
- $W_M < W_G < W_G + \Delta V$ : the work function of the metal is smaller than the work function of graphene. *n*-doping is favoured by such configuration and is further favoured by the interface voltage drop.

We remind the reader that this model only holds for graphene on weakly interacting metallic substrates. In that case, graphene's band structure still exhibits a linear dispersion and is mainly affected by the charge transfer (rigid shift of the Dirac cones).

### Superpotential effect

When graphene is supported on a weakly interacting metal substrate, the moiré superlattice imposes a smooth periodic superpotential. As a result, the electronic band structure of graphene develops replicas of Dirac cones and mini-bandgaps. These features were observed, for instance, in graphene/Ir(111) [53, 72, 73, 74], graphene/h-BN [75] and twisted bilayer graphene [76].

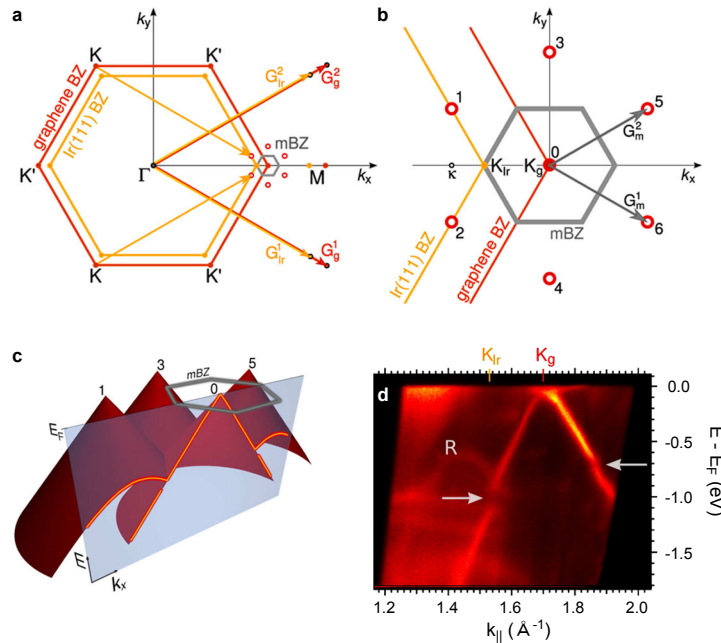


Figure I.13: (a) BZ of the Ir(111) surface and graphene lattices drawn to scale. The mini-Brillouin zone (mBZ) is indicated around the K point of graphene. Open dots denote the vertices of Dirac cones replicated by moiré reciprocal vectors,  $G_m$ . (b) Blowup of the mBZ. Central dot denotes the center of the primary Dirac cone, while 1–6 are replicas. (c) ARPES experimental plane (shaded) along the  $\Gamma$ -K-M direction cuts the primary and replica cones (only partially shown). (d) ARPES spectrum of graphene-covered Ir(111). The K points of iridium and graphene are marked as  $K_{Ir}$  and  $K_g$ , respectively. Horizontal arrows denote the mini band-gaps in the primary Dirac cone. A visible replica band is labeled as R. Figure adapted from Ref. [53].

Some of the results reported in Ref. [53] on graphene-covered Ir(111) are shown in Figure I.13. A sketch of the Brillouin zones of graphene and Ir(111) is displayed in Figure I.13(a).  $G_{Ir}$  and  $G_g$  denote the



reciprocal lattice vectors of the Ir surface and graphene, respectively. The moiré superpotential, associated with the reciprocal vectors  $\mathbf{G}_m = \mathbf{G}_g - \mathbf{G}_{Ir}$  is responsible for the replica bands centered at the points labeled 1–6 in Figure I.13(b) and opens a bandgap in the Dirac cone along the mini-BZ (mBZ) boundary. Experimentally, the ARPES plane along the  $\Gamma$ -K-M direction cuts the primary and replica cones and gives rise to a hyperbolic band whose maximum is centered at the center of the mBZ (Figure I.13(c)). This helps understanding the experimental ARPES spectrum given in Figure I.13(d): the primary cone centered around  $K_g$  displays a faint additional band labeled R for replica band, and mini band-gaps indicated with arrows.

### 3 Intercalation of thin films below graphene

Intercalation consists in the insertion of atomic or molecular layers, referred to as the intercalant, between layers of a host material. This host material can be a layered material where all layers are made of the same material, such as in the case of graphite or a heterostructure, where one or few layers of a material are adsorbed on another material, such as in the case of graphene on metals.

In order to recover the intrinsic structural, electronic and vibrational properties of isolated graphene, one method consists in intercalating a buffer layer in between graphene and its initial substrate. Before turning to that discussion, we give an overview of graphite and graphene intercalation compounds.

#### 3.a Intercalation compounds

Graphite intercalation compounds have been extensively studied for more than fifty years now [77, 78, 40]. Alkali metals (such as K, Rb, Cs and Li) used as intercalants have provided numerous graphite intercalation compounds. They have been considered, from the very beginning, as prototype materials as they are easily prepared and well known from a structural point of view [78, 40]. Nowadays, alkali metals are still often used as intercalants for graphene on metals.

Several intercalation methods have been used throughout the years, including vapor-phase reactions, liquid intercalation methods [79] and electrochemical reactions. Among these methods, the two-zone vapour transport method (which consists in a vapor-phase reaction) has remained the most popular one for intercalating graphite [78, 40]. As illustrated in Figure I.14, it consists in the following: graphite and the intercalant are kept in a bulb, with some distance separating the two, and are heated to some temperature  $T_i$  and  $T_g$  ( $>T_i$ ), respectively. The intercalation rate is controlled by the temperature difference  $T_g - T_i$  (the smaller the difference, the smaller the intercalation rate) and depends on the intercalant.

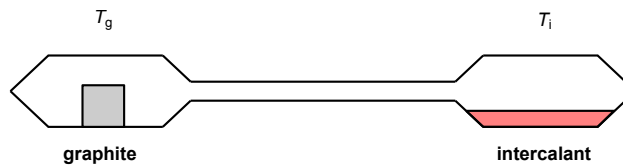
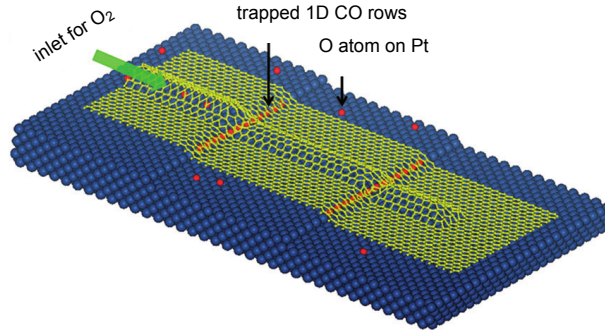


Figure I.14: Schematic diagram of the two-zone vapour transport method where  $T_g$  and  $T_i$  indicate the temperatures of the graphite and intercalant, respectively. Figure reproduced and adapted from Ref. [78].

Several interesting phenomena related to intercalation have been described. For instance, it was shown that an unstable intercalant can be stabilized *via* intercalation. This is true for  $TlBr_3$ -intercalated graphite: in principle,  $TlBr_3$  must be kept in liquid  $TlBr_3$  and does not exist by itself, but stable graphite intercalation compounds can be formed with  $TlBr_3$  [80].

Chemical reactions can also occur after intercalation is completed, below the intercalated material. Soon after the fabrication of the first graphite intercalation compounds, it was shown that when graphite is intercalated with  $FeCl_3$ ,  $FeCl_3$  can be reduced to  $FeCl_2$  using a stream of  $H_2$  at 650 K [81]. More recently, it was shown that a graphene layer adsorbed on a metal can exhibit a strong confinement effect

on the chemistry of the molecules underneath: the reaction of confined CO molecules, forming 1D rows intercalated between graphene and Pt(111), with O<sub>2</sub> molecules was visualized by means of low energy electron microscopy [82]. It was shown that intercalated CO molecules remain trapped close to the step-edges thanks to the C-Pt interaction in these locations, which acts as a barrier for outward diffusion of CO. Under O<sub>2</sub> atmosphere, wrinkles function as nanosized inlets for O<sub>2</sub> to react with the trapped CO molecules close to the step-edges (Figure I.15).



*Figure I.15: Schematic showing a reaction under the graphene cover with a wrinkle structure.* The wrinkle functions as a nanosized inlet/outlet for molecules such as O<sub>2</sub>. Pt and O atoms are represented as blue and red balls, respectively. The graphene sheet is represented in yellow.

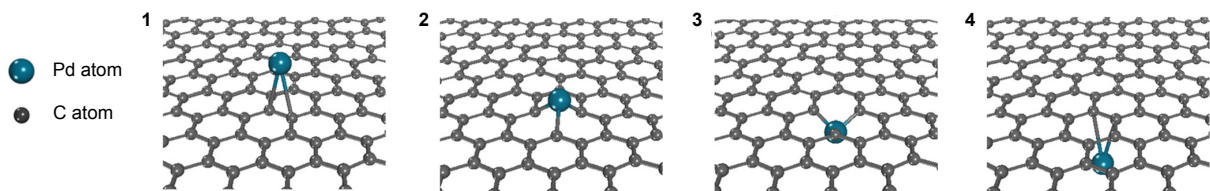
In relation with chemistry occurring under graphene cover, the terms “superefficient diffusion” (SED) have been employed to describe the very efficient diffusion of certain intercalated atoms (such as Cs atoms) below graphene and into the bulk of the metal substrate [83]. It was proposed in Ref. [83] that SED could serve as a novel efficient source of Cs atoms. Indeed, after an exposure to the atmosphere, the Cs-saturated metal substrate continued to emit Cs in UHV conditions.

Other potential applications of intercalation compounds include rechargeable batteries [84].

### 3.b Intercalation process

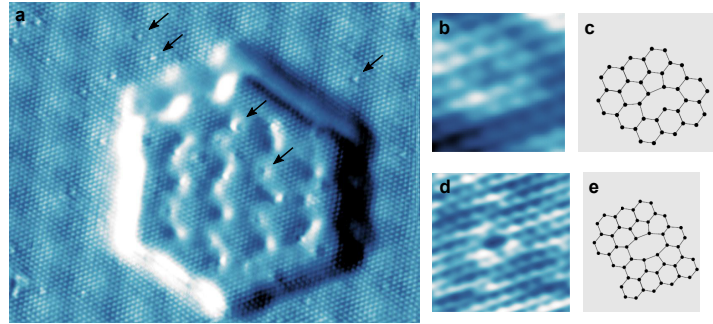
Regarding the microscopic origin of the intercalation process, we now focus on graphene intercalation compounds only, as it will be the subject of Chapter V. Pre-existing defects such as point defects in graphene [85, 86, 87, 88, 89] and graphene edges [89, 90, 91, 92] have been proposed to be potential intercalation pathways. For instance, it was shown in Ref. [89] that Co intercalates between graphene and Ir(111) at different pre-existing defect locations: while Co preferentially intercalates at the substrate step-edges below certain rotational domains of graphene on Ir(111), it is mostly found close to wrinkles below other domains.

Another mechanism, based on the material diffusion via metal-generated defects, followed by the subsequent healing of the graphene lattice, has been suggested [93, 87]. This mechanism is illustrated in Figure I.16 in the case of Pd intercalation of graphene grown on Ru(0001).



*Figure I.16: Sketch of the intercalation process of a Pd atom.* (1) The Pd atom rests on perfect graphene. (2) At high temperature (800 K), the Pd atom bonds with carbon atoms and induces an atomic defect in graphene. (3) The Pd atom passes through the defect and bonds with the substrate lattice (not drawn here). (4) The carbon atoms re-bond and graphene heals itself. Figure adapted from Ref. [93].

Finally, a Cu penetration path beneath graphene was proposed to occur via metal-aided defect formation with no or poor self-healing of the graphene sheet for the Cu intercalation of graphene on Ir(111) [94]. In other words, it was shown that Cu intercalation is harmful for graphene grown in Ir(111). An intercalated island surrounded with non-intercalated graphene on Ir(111) is shown in Figure I.17(a). Atomic defects are indicated with arrows. Close-up views centered on a carbon mono- and on a carbon di-vacancy defect are shown in Figure I.17(b,d), respectively, alongside the corresponding ball-and-stick models displayed in Figure I.17(c,e). Such atomic defects were not observed prior to Cu intercalation. To rule out any interaction with foreign species naturally present in the preparation chamber (such as H<sub>2</sub>O, H<sub>2</sub>, O<sub>2</sub> or CO) as a possible origin of point defects formation, a pristine graphene/Ir(111) sample was annealed for one hour at the temperature used for intercalating Cu (775 K). No such point defect was observed afterwards, hence supporting a metal-aided defect formation occurring during Cu intercalation.



**Figure I.17: Atomic defects formed upon Cu intercalation of graphene on Ir(111).** (a) STM image of graphene on Ir(111) intercalated with 0.2 ML of Cu. The central part of the image shows an intercalated island, while the rest of the image exhibits non-intercalated graphene on Ir(111). Arrows point to atomic defects on both types of regions. (b,d) Close-up views centered on a carbon mono- (b) and di-vacancy (d) defect. (c,e) Ball-and-stick models of a reconstructed carbon mono- (c) and di-vacancy (e). Figure adapted from Ref. [94].

### 3.c Restoring the properties of isolated graphene *via* intercalation

Intercalation has been proven to decouple graphene from metal substrates, provided that the intercalated species is weakly coupled to graphene. In particular, graphene is quasi free-standing in the following systems: graphene/Ag/Re(0001) [60], graphene/Pb/Re(0001) [95], graphene/Au/Ni(111) [107, 97, 98], graphene/Al/Ni(111) [99], graphene/Cu/Ni(111) [96, 98], graphene/Ag/Ni(111) [96, 98], graphene/Bi/Ni(111) [98], graphene/Au/SiC(0001) [100, 101, 233], graphene/Au/Ru(0001) [102, 93], graphene/In/Ru(0001) [93], graphene/Pb/Ru(0001) [103], graphene/Au/Ir(111) [104], graphene/Pb/Ir(111) [105] and graphene/Pb/Pt(111) [106].

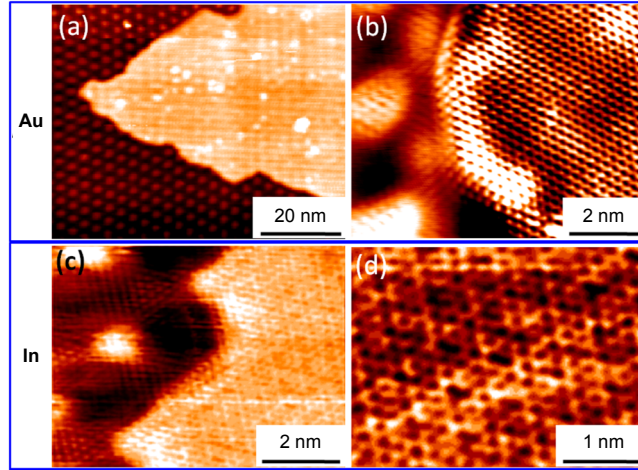
The quasi free-standing character of intercalated graphene is visible in the flattening of graphene, in its electronic band structure and in vibrational spectra: intercalation restores (at least partly) the structural, electronic and vibrational properties of isolated graphene.

#### Structural properties of intercalated graphene

Figure I.18 shows STM images taken on graphene on Ru(0001) intercalated with Au and In films [93] (Au and In are part of the weakly interacting metals). Intercalation was performed by depositing the equivalent of one or few layers of Au or In on graphene-covered Ru(0001), followed by an annealing at 500 K. Figure I.18(b,c) demonstrates that the graphene lattice is undisturbed and extends continuously across the intercalated and non-intercalated areas. Intercalated areas are flatter than non-intercalated areas which present the typical moiré pattern of graphene on Ru(0001). In intercalated areas, the honeycomb lattice of graphene is visible, as seen in atomic resolution images (Figure I.18(b,d)). In the case of graphene on Ru(0001) intercalated with Au, a shallow moiré pattern is still visible in intercalated



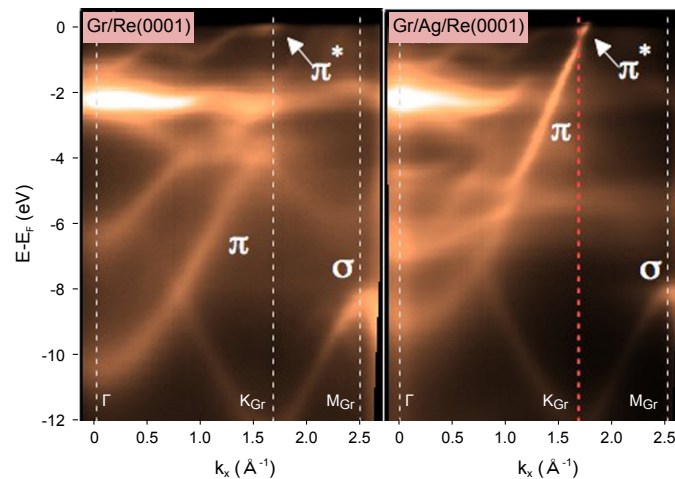
regions (Figure I.18(b)), indicating a residual (weak) graphene-Au interaction.



**Figure I.18: Flattening of graphene on Ru(0001) via intercalation of Au and In films.** **Top:** Structure of Au-intercalated graphene on Ru(0001). (a) Scanning tunneling topograph of partially Au-intercalated graphene on Ru(0001). The left part of the STM image corresponds to graphene/Ru(0001), while the right part corresponds to graphene/Au/Ru(0001). (b) Atomic resolution image across an edge of Au-intercalated graphene. Graphene on top of the intercalated film exhibits the typical honeycomb lattice of isolated graphene. **Bottom:** Structure of In-intercalated graphene on Ru(0001). (c) Scanning tunneling topograph of partially In-intercalated graphene on Ru(0001). The left part of the STM image corresponds to graphene/Ru(0001), while the right part corresponds to graphene/In/Ru(0001). (d) Atomic resolution image on In-intercalated graphene. Figure adapted from [93].

### Electronic properties of intercalated graphene

The electronic band structure of graphene supported on Re(0001) before and after the intercalation of one monolayer of Ag was measured by means of ARPES [60] (Figure I.19). The intercalation of Ag (which is a weakly interacting metal) reduces the graphene-Re interaction: the  $\pi$  state is shifted by about 1.60 eV towards the Fermi level at the  $\Gamma$  point and recovers a linear dispersion in the proximity of the Fermi level. The electron charge transfer from Ag to graphene shifts the Dirac point to an energy of 0.4 eV below the Fermi level, allowing for the observation of the  $\pi^*$  band.

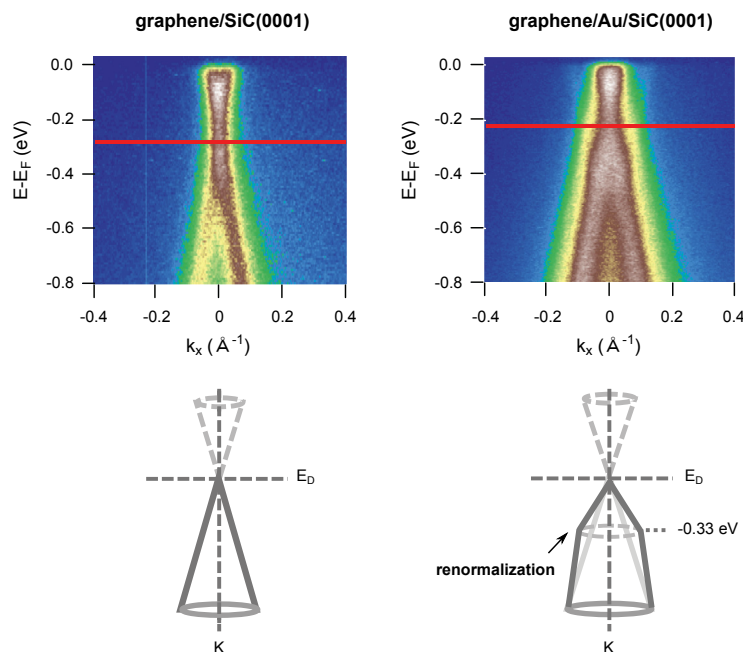


**Figure I.19: Restoring graphene's electronic properties via intercalation of a Ag layer.** **Left:** Photoemission intensity plot along the  $\Gamma$ -K direction of graphene/Re(0001). **Right:** Photoemission intensity plot along the  $\Gamma$ -K direction of graphene/Ag/Re(0001). The highest-symmetry points  $\Gamma$ ,  $K_{Gr}$  and  $M_{Gr}$  are indicated. Figure adapted from Ref. [60].

A residual small (less than 0.5 eV) band gap is observed after Ag intercalation and is attributed to hybridization between graphene and a Ag  $d$  state, indicating that graphene on the intercalated Ag layer is still not completely decoupled, electronically speaking.

Actually, in several graphene intercalation compounds, the dispersion relation close to the Dirac point was found to be strongly perturbed. In particular, a renormalization of the electronic band structure was observed in graphene/Au/Ni(111) [107] and graphene/Au/SiC(0001) [108], despite Au being a weakly interacting metal. This renormalization appears in ARPES measurements as a kink in the slope of graphene's Dirac cone, as shown in Figure I.20.

In the case of graphene on Ni(111), intercalated Au forms a continuous layer and the kink in the electronic band structure of graphene appears at -0.95 eV [107]. This kink was assigned to a substrate effect. More specifically, it was ascribed to a residual interaction with the gold monolayer, but a clear explanation is still pending. In the case of graphene on SiC(0001), gold intercalates in the form of small aggregates, in between the top graphene layer and the buffer layer, and the kink was found to appear at -0.33 eV [108] (Figure I.20). Similarly to the case of graphene/Au/Ni(111), the origin of the (stronger) renormalization observed for graphene/Au/SiC(0001) remains an open question to our knowledge.



**Figure I.20: Renormalization of graphene's linear dispersion. Top:** ARPES intensity measured around the Dirac point for (left) graphene/SiC(0001) and (right) graphene/Au/SiC(0001). **Bottom:** A renormalization is observed around -0.33 eV for graphene/Au/SiC(0001). Figure adapted from Ref. [108].

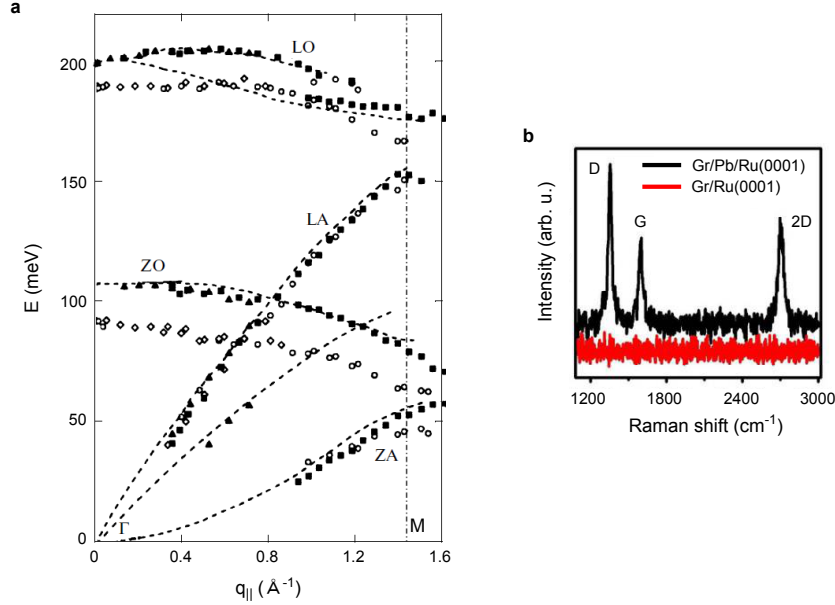
### Vibrational properties of intercalated graphene

The phonon dispersion curve of graphene on Ni(111) intercalated with Au, measured by means of HREELS, exhibits a stiffening of graphene's phonon modes with respect to graphene on Ni(111) (*i.e.* a shift in the energies of these modes towards higher energies) [109], as evident in Figure I.21(a). More specifically, we observe a stiffening of the ZO, LO and LA modes. The phonon dispersion curve of intercalated graphene is in turn closer to the one of isolated graphene or graphite.

Such a behaviour derives from the weakened graphene-substrate interaction by means of Au intercalation: the hybridization between the C  $\pi$  and Ni  $d$  states is significantly reduced, hence we observe a reversal of the energetic shift of graphene modes towards the positions observed for pristine graphene.

In Raman spectroscopy, hybridization between the  $d$  states of a strongly interacting metal substrate such as Ni(111) and graphene  $\pi$  states results in the absence of the characteristic modes

of graphene [15]. For this reason, the Raman spectrum of graphene-covered Ru(0001) is essentially featureless (Figure I.21(b)). In particular, the characteristic G and 2D peaks of graphene are absent. Decoupling graphene from Ni(111) by means of Pb intercalation restores graphene's vibrational modes, hence the G and 2D modes are visible (Figure I.21(b)). The defect-activated D mode is present as well and is ascribed to graphene edges. The authors claim that it could be due to a Pb coverage of less than 1 ML. Similar observations were made on graphene on SiC(0001) intercalated with Au [101].



**Figure I.21: Stiffening of graphene's phonon modes via intercalation and restoring of Raman modes.** (a) Dispersion curves of phonon vibrational modes in the  $\Gamma$ M direction for graphene/Ni(111) (open symbols) and graphene/Ni(111) after deposition of 6 Å of Au and subsequent annealing at 670 K (closed symbols). (b) Raman spectra of graphene/Ru(0001) before (red) and after (black) Pb intercalation. Figure adapted from [109, 101].

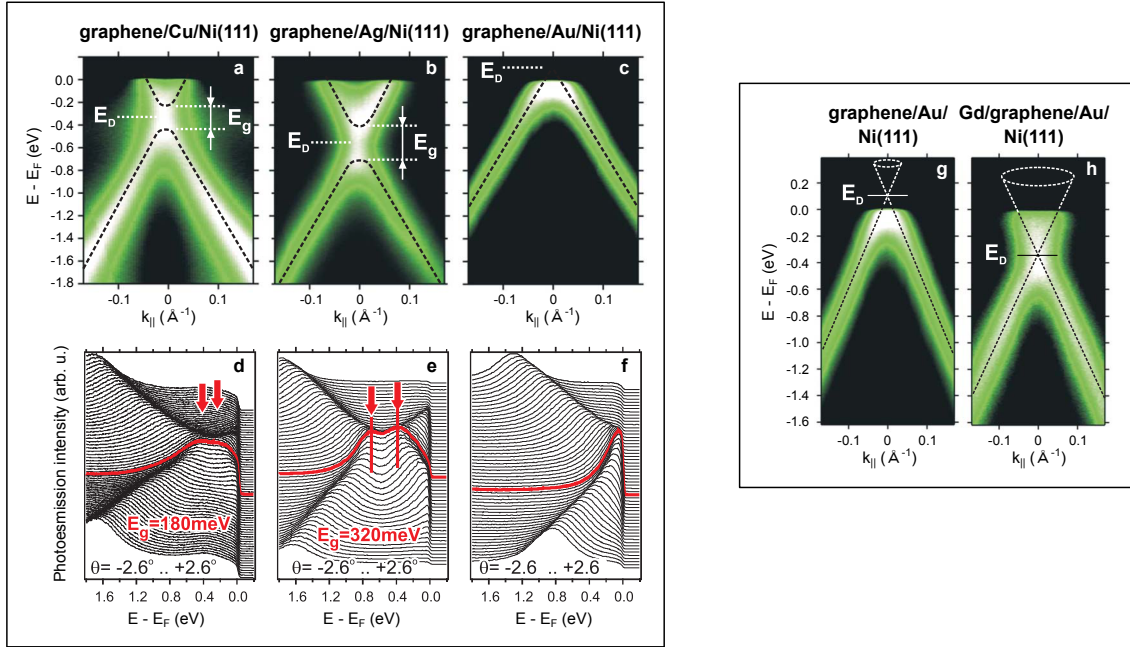
### 3.d Tuning graphene properties from below

#### Control of the doping level and bandgap

Beyond quenching the graphene-metal interaction, intercalation also offers a way to tune graphene's properties via, for instance, the control of the doping level. In particular, graphene is  $n$ -doped in the following compounds: graphene/Ag/Re(0001) [60], graphene/Pb/Re(0001) [95], graphene/Al/Ni(111) [99], graphene/Cu/Ni(111) [96, 98], graphene/Ag/Ni(111) [96, 98], graphene/Bi/Ni(111) [98], graphene/Pb/Ir(111) [105] and graphene/Pb/Pt(111) [106]; and  $p$ -doped in graphene/Au/Ni(111) [107, 97, 98], graphene/Au/Ru(0001) [102] and graphene/Au/Ir(111) [104].

Intercalation can also open bandgaps in graphene: hybridization between metal  $d$  and graphene  $\pi$  states is much less with weakly interacting metals but can still occur, as it was shown for Ag-intercalated graphene on Re(0001) [60]. Figure I.22 shows photoemission plots around the K point of graphene on Ni(111) intercalated with 1 ML of Cu, Ag and Au [96]. Graphene intercalated with Cu and Ag is  $n$ -doped (the Dirac point lies below the Fermi level) (Figure I.22(a,b)) and opens a bandgap of 180 meV and 320 meV, respectively (Figure I.22(d,e)). More precisely, the Dirac point is shifted by  $\Delta E_F = -310$  meV in graphene/Cu/Ni(111) and by  $\Delta E_F = -560$  meV in graphene/Ag/Ni(111), where  $\Delta E_F$  is defined as the difference between the Fermi energy and the middle of the gap. By contrast, Au intercalation results in slightly  $p$ -doped graphene ( $\Delta E_F = 100 \pm 20$  meV). The Dirac point (not seen in Figure I.22(c,f)) lies above the Fermi level, where the  $\pi$  bands cross.

To determine whether Au intercalation opens a bandgap, the authors of Ref. [96] deposited Gd atoms on top of Au-intercalated graphene on Ni(111). Gd deposition results in  $n$ -doping, hence the Dirac point is shifted below the Fermi level and becomes visible in ARPES. As evident in Figure I.22, the linear dispersion around the K point of graphene is preserved and no bandgap is visible. Actually, a quantitative analysis revealed that, if a bandgap has opened, it must be less than 20 meV. In other words, one can consider that graphene's electronic properties are restored.



**Figure I.22: Effect of intercalation on the doping level and bandgap of graphene.** **Left:** Photoemission plots around the K point of graphene on Ni(111) intercalated with 1 ML of (a,d) Cu, (b,e) Ag and (c,f) Au. Cu and Ag intercalations result in  $n$ -doped graphene and open substantial bandgaps (180 meV and 320 meV, respectively), while Au intercalation results in slightly  $p$ -doped graphene. **Right:** Photoemission plots around the K point of graphene on Ni(111) intercalated with 1 ML of Au, before (g) and after (h) deposition of Gd. Gd  $n$ -doping reveals the gaplessness of Au-intercalated graphene on Ni(111). Figure adapted from Ref. [96].

A similar methodology was employed in Ref. [102] to determine whether Au-intercalated graphene on Ru(0001) presents a bandgap. The authors showed that, similarly to Au-intercalated graphene on Ni(111), the intercalation of 1 ML of Au results in a slight  $p$ -doping of graphene (the Dirac point is  $\simeq 150$  meV above the Fermi level). Upon deposition of potassium atoms, the Dirac point is shifted below the Fermi level and a large bandgap ( $\simeq 200$  meV) is visible. The opening of a bandgap is ascribed to Au and not K, on the ground that the bandgap does not increase with higher K coverage. Hybridization between graphene and Au states is excluded as there are no gold states near the Dirac point. Instead, the authors claim that the appearance of the bandgap is related to the broken symmetry of the two carbon sublattices, induced by the lattice mismatch between graphene and Au. It should be noted that K deposition on Au-intercalated graphene on Ni(111) opens a bandgap while Gd deposition (discussed before) does not, as reported in Ref. [96]. This was attributed to different adsorption geometries [96]. Whether the bandgap observed for Au-intercalated graphene on Ni(111) with K adatoms increases with increasing K coverage was not discussed in Ref. [96], hence the argument proposed in Ref. [102] to exclude a K-related bandgap cannot be confirmed or infirmed. Still, the opening of a bandgap in Au-intercalated graphene on Ru(0001) is surprising, as pointed out in Ref. [102].

### Inducing spin-orbit coupling in graphene

In recent years, the possibility to induce spin-orbit (SO) coupling in graphene via an intercalated species has attracted much attention. Indeed, the intrinsic spin-orbit coupling in graphene is rather weak, hence

externally inducing spin-orbit coupling in graphene would allow to use graphene in active elements of spintronics, such as the Das-Datta spin field effect transistor [110]. Yet, despite the recent efforts in tackling spin-orbit coupling in intercalated graphene, some questions are still under debate.

Calleja *et al.* investigated Pb-intercalated graphene on Ir(111) islands through STM/STS measurements [105]. Their spectroscopy measurements show regularly spaced sharp resonances, similar to Landau levels, continuously shifted in energy as the tip moves away from the intercalated regions. These spatially dependent resonances were ascribed to a strong and spatially modulated SO coupling induced in graphene by the intercalated Pb monolayer. Large spin-orbit coupling effects were later detected in the same system through spin-resolved photoemission spectroscopy [111]. What remains pending is an explanation for the energy dependence of the resonance peaks observed by Calleja *et al.* with the index level  $n$ . Their data clearly show a linear dependence  $E_n \propto n$  whereas, unlike the conventional two-dimensional electron gas, the Landau level energies of massless Dirac fermions are expected to display a square-root dependence with the index level  $n$ .

In a recent paper, Klimovskikh *et al.* studied Pb-intercalated graphene on Pt(111) by means of low energy electron diffraction, angle- and spin-resolved photoelectron spectroscopy [106]. They claimed that an energy gap of 200 meV has opened in the band structure of graphene at the Dirac point and that a spin-splitting of 100 meV is detected in the conduction band. The opening of these gaps was ascribed to SO effects. Dedkov and Voloshina strongly criticized the treatment and analysis of spin-resolved photoelectron spectroscopy data in a comment to the authors [112]. They firmly questioned the interpretations and conclusions reported in Ref. [106]. Klimovskikh *et al.* replied and provided further statistical analysis to support the main conclusion of their article [113].

Finally, Marchenko *et al.* reported a giant Rashba splitting ( $\simeq 100$  meV) in Au-intercalated graphene on Ni(111) detected by angle- and spin-resolved photoelectron spectroscopy [97]. Based on *ab initio* calculations, they attributed the giant SO splitting to dilute Au atoms in hollow sites that are in closer vicinity to the graphene sheet compared to a continuous intercalated Au monolayer. The authors reconciled previous measurements showing a smaller SO splitting ( $\simeq 13$  meV) [107] with the more recent ones by remarking that coexisting intercalated areas with and without extra individual Au atoms result in the simultaneous presence of high- and low-splitting phases. Finally, Krivenkov *et al.* released a paper attributing the giant SO splitting previously detected in Au-intercalated graphene on Ni(111) to intercalated Au nanoclusters [114]. By deriving the band structure of graphene in the case of a single intercalated Au atom (the relaxed structure was determined by means of DFT calculations), they found a giant Rashba-type SO splitting ( $\simeq 60$  meV) and a gap opening ( $\simeq 60$  meV). They concluded that structures very similar to that obtained for the single Au atom case develop upon intercalation of graphene on Ni(111). Finally, recent DFT calculations [115] could not explain the giant Rashba splitting reported in Ref. [97].

## 4 Functionalization of graphene from on top

### 4.a Adatoms and molecules as dopants

It has been demonstrated that one can dope graphene with adatoms rather than from below (intercalation). For instance, hole doping is possible by depositing Au, Sb or Bi atoms on graphene supported on SiC(0001) [116]. While Bi and Sb deposition only reduces the natural  $n$ -type doping induced by the SiC(0001) substrate by shifting the Dirac point in the direction of the Fermi level, Au shifts the Dirac point into the unoccupied states therethore inducing  $p$ -type doping. ARPES measurements showed that the conical shape of the electronic band structure remains unperturbed (in particular, no bandgap opens upon adsorption of Au, Sb and Bi atoms) [116].

Small gas molecules and hydrocarbons have also been used to dope graphene, with both  $n$ -type ( $\text{NH}_3$  [117], polyethyleneimine [118], dimethylantracene [119]) and  $p$ -type dopants ( $\text{H}_2\text{O}$  [120],  $\text{O}_2$  [121],



diazonium salts [118], dibromoanthracene [119]).

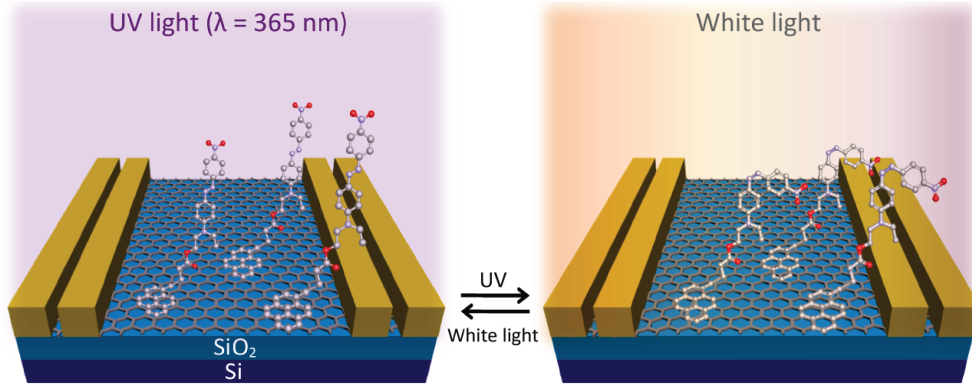


Figure I.23: Schematic depiction of the reversible photoisomerization process of DR1P on graphene by UV and white light illuminations. Oxygen, carbon and nitrogen atoms are represented in red, white and purple, respectively. Figure adapted from Ref. [122].

Charge transfer by use of an adsorbed species plus an external stimulation has been demonstrated as well. For instance, light-driven reversible modulation of doping in graphene has been realized with azobenzene chromophores [122]. The molecule used to functionalize graphene was the photochromic molecule Disperse red 1 (DR1). This particular dipolar chromophore contains donor and acceptor groups connected by  $\pi$ -conjugation with an azobenzene group. Kim *et al.* synthesized a pyrene-tethered DR1, denoted as DR1P. DR1P (shown in Figure I.23) is tethered to the surface of graphene via  $\pi$ - $\pi$  interactions between pyrene and graphene. As the *trans* state of azobenzene converts to the *cis* state under UV light, significant geometrical changes occur (Figure I.23). The reversible process is performed with white light illumination. Going from *cis* to *trans* or from *trans* to *cis* changes the dipole moment of the molecule, which in turn changes the extent of doping. By means of Raman spectroscopy and electrical measurements, Kim *et al.* demonstrated that the charge carrier concentration can be modulated by  $\simeq \pm 1 \cdot 10^{12} \text{ cm}^{-2}$  (up to  $\simeq 18\%$  of carrier concentration in DR1P/graphene) while preserving the high mobility of graphene.

#### 4.b Spin systems on graphene

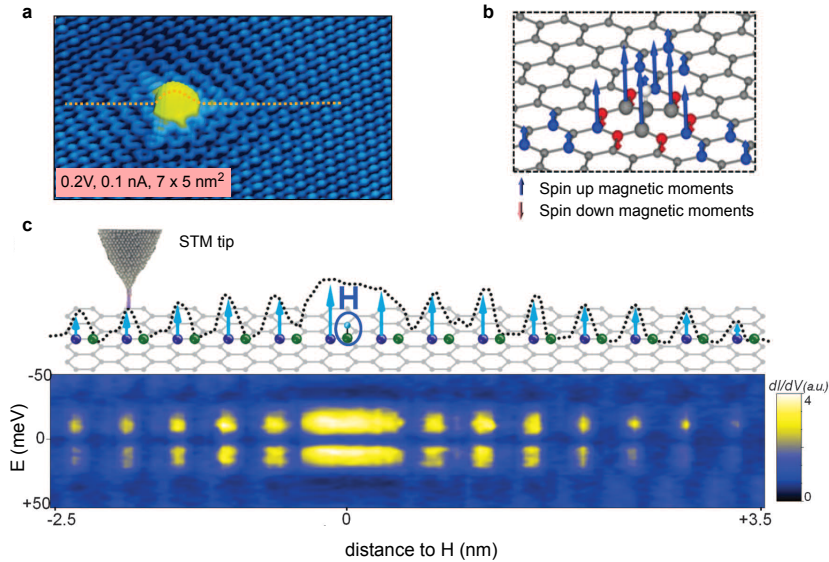
Different approaches for inducing magnetic properties in graphene from on top have been proposed: for instance, one relies on the deposition of hydrogen adatoms [123] and another on the formation of carbon vacancies in the graphene lattice [124].

By means of STM/STS measurements, González-Herrero *et al.* showed that the adsorption of a single hydrogen atom on graphene induces a magnetic moment characterized by a spin-split state at the Fermi energy [123]. This spin-split state lies essentially on the carbon sublattice lacking the deposited hydrogen atom. The spatial extension of the spin-polarized state is shown in Figure I.24(c), and reaches several nanometers. This suggests that long-range magnetic interactions mediated by direct exchange should take place. By manipulating the deposited hydrogen atoms with the STM tip (not shown here), the authors showed that one can tailor the magnetism of selected graphene regions.

## 5 Towards probing Yu-Shiba-Rusinov states in graphene

### 5.a Yu-Shiba-Rusinov states

The presence of a magnetic impurity on top of a superconducting material can give rise to so-called Yu-Shiba-Rusinov (YSR) states [125]. YSR physics can be viewed as the analogue of the Kondo effect for a superconducting material. The Kondo effect, which manifests itself as an increase of resistance at



**Figure I.24: Spatial extension of the spin-polarized electronic state induced by H atoms in graphene.** (a) STM topograph of a single H atom on graphene. (b) Calculated magnetic moments induced by H chemisorption (the length of the arrows codes the relative magnitudes of the magnetic moments). (c) Top: Schematic of the graphene structure along the dashed line indicated in (a). Green (purple) balls indicate the positions of carbon atoms belonging to the same (opposite) sublattice with respect to the locus of H chemisorption. The dotted line shows the evolution of the height of the measured occupied peak, and the arrows show the relative magnetic moment contribution of each carbon atom. Bottom: Conductance map [ $dI/dV(x,E)$ ] along the dashed line indicated in (a). All experimental data were acquired at 5 K. Figure adapted from Ref. [123].

low temperature, was first reported in 1934 [126]. It was only in 1964 that this anomalous behaviour (we normally expect a decrease in resistance at low temperature) was explained and attributed to magnetic impurities [127]. The screening of magnetic impurities by conduction electrons of the metal - which can be described by a local antiferromagnetic exchange coupling - is responsible for spin-flip contributions to the resistance, accounting for the increase of resistance below a certain temperature called the Kondo temperature. In a superconducting material, no quasiparticle is available in the superconducting gap to screen the magnetic impurity. Indeed, the superconducting character is carried by pairs of electrons of opposite wavevectors and spins known as Cooper pairs [128]. The local competition between superconductivity and magnetism results in a pair-breaking effect: the exchange interaction between the magnetic impurity and the surrounding Cooper pairs tends to align the spins of the electrons forming the Cooper pairs, hence it tends to break the Cooper pairs.

Because of this pair-breaking effect, the energy associated with a quasiparticle excitation is lowered by a quantity

$$E_b = \Delta \frac{1 - (\pi JS \rho_0)^2}{1 + (\pi JS \rho_0)^2} \quad (\text{I.11})$$

where  $\Delta$ ,  $J$ ,  $S$  and  $\rho_0$  correspond to the superconducting gap, the exchange coupling constant, the spin ( $S \gg 1$ ) and the normal-state density of states at  $E_F$ , respectively. For intermediate coupling ( $JS \leq 1/\pi\rho_0$ ),  $E_b$  falls in the superconducting gap. In STS measurements, this translates in a pair of peaks observed inside the superconducting gap. Although predicted in 1968, the first experimental observation of YSR states dates from 1997: pairs of weak peaks appearing inside the superconducting gap of Nb were observed when the STM tip was placed on top of Mn and Gd adatoms [129].

## 5.b Effect of dimensionality

In 2015, the (significant) influence of dimensionality on the extension of YSR states was investigated by means of STM/STS measurements [130]. Ménard *et al.* experimentally evidenced YSR states with spatially oscillating particle-hole asymmetry extending tens of nanometers away from individual Fe atoms embedded in a 2H-NbSe<sub>2</sub> crystal. 2H-NbSe<sub>2</sub> is a layered superconductor with two-dimensional character.

The enhanced spatial extension with respect to the one observed, for instance, by Yazdani *et al.* (of the order of the Å) [129], was attributed to the two-dimensional character of the superconducting material [130].

### 5.c Targeted graphene-based system

YSR states in graphene have been theoretically investigated, assuming a superconducting proximity effect [4, 5]. It seems that depending on the type of impurity we expect or not in-gap states. For a single magnetic impurity in the honeycomb, Lado and Fernández-Rossier showed that no in-gap state is expected unless the exchange coupling constant  $J$  takes unrealistically large values [5]. This result is a direct consequence of the vanishing density of states of graphene at the Fermi energy. For a hydrogenated graphene, the situation is strikingly different: in-gap states appear at weak coupling and their positions (in energy) follow a linear evolution with  $J$  (rather than the quadratic dependence followed by conventional YSR states) [5]. Finally, the parity switching point of YSR states arising from hydrogenated graphene displays another unconventional property. The parity switching point is the point at which  $J$  is large enough so that the YSR states appearing on both sides of the Fermi energy join and cross the Fermi energy (in conventional YSR states, the critical exchange coupling constant  $J_c$  equals  $1/\pi S\rho_0$  ( $E_b = 0$  in Equation I.11)). In hydrogenated graphene, Lado and Fernández-Rossier showed that  $J_c$  depends on the superconducting gap  $\Delta$  [5]. In practice, one could tune the parity switching point with temperature ( $\Delta$  depends on the temperature).

These theoretical predictions rise several questions: what behaviour can we expect for molecules holding a spin deposited on graphene, or for spin impurities embedded in the substrate in close vicinity to graphene? We believe that it would be interesting to probe the unusual properties of YSR states with various types of magnetic impurities.

Provided that the two-dimensional character still has the same significant influence on the spatial extension of YSR states in graphene as for conventional YSR states [130], three ingredients are necessary to observe few nanometers-extended YSR states in graphene:

- a superconducting material (such as rhenium) in close proximity to graphene, that will induce superconductivity in graphene *via* proximity effect,
- graphene with two-dimensional character, *i.e.* quasi-free standing graphene,
- and magnetic impurities deposited in the vicinity of graphene, for instance a molecular magnet, a magnetic defect in graphene, or magnetic impurities embedded in the substrate.

As previously demonstrated in Ref. [3], growing graphene on a Re(0001) substrate results in induced superconductivity in graphene. However, this comes with a major drawback: Re(0001) being a strongly interacting metal, the two-dimensional character of pristine graphene is lost. Although the targeted graphene-based system was not fabricated yet, results related to all three ingredients will be addressed in this thesis.





## EXPERIMENTAL TECHNIQUES AND METHODS

**Contents**

---

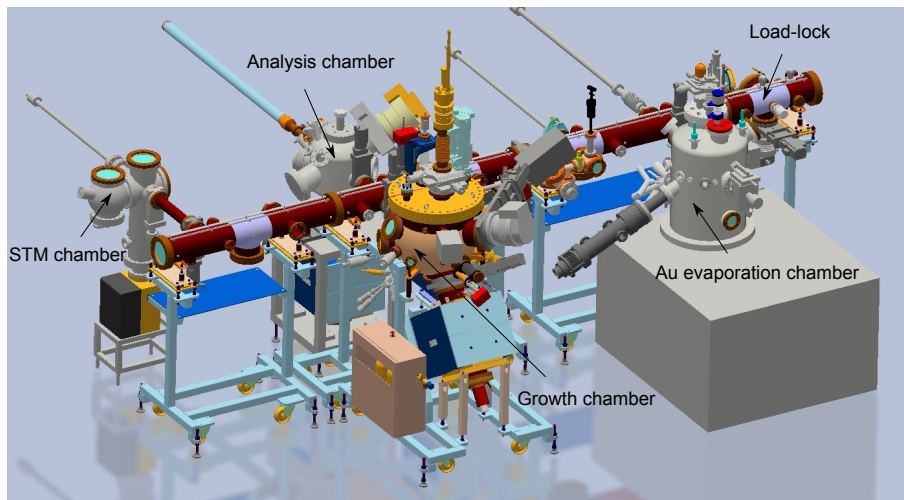
1	Ultra-high vacuum (UHV) techniques . . . . .	<b>34</b>
1.a	Multi-purpose UHV system . . . . .	34
1.b	Reflection high energy electron diffraction . . . . .	35
1.c	Surface preparations . . . . .	36
1.d	Graphene growth on Re(0001) thin films . . . . .	37
1.e	Molecular evaporator . . . . .	38
1.f	Angle-resolved photoemission spectroscopy . . . . .	38
2	Scanning tunneling microscopy and spectroscopy . . . . .	<b>41</b>
2.a	Working principle . . . . .	41
2.b	Experimental set-ups . . . . .	42
3	Raman spectroscopy . . . . .	<b>43</b>
3.a	Working principle . . . . .	43
3.b	Experimental set-up . . . . .	44
4	Simulations . . . . .	<b>44</b>
4.a	Density functional theory calculations . . . . .	44
4.b	Bond-order potential calculations . . . . .	46

---

# 1 Ultra-high vacuum (UHV) techniques

## 1.a Multi-purpose UHV system

The samples presented in this thesis were mainly prepared in a multi-purpose UHV system located in Néel Institute (Grenoble) encompassing four chambers connected to one another *via* a tunnel also held under UHV (Figure II.1). The base pressure in the system is  $\approx 10^{-10}$  mbar. On one side of the tunnel, a fast load-lock chamber kept with limit pressure at  $10^{-8}$  mbar is used to introduce new samples and probes used for scanning tunneling microscopy (STM). The samples are mounted onto either Mo plates or Zr-Ta-Mo alloy plates which are adapted to either single crystals or thin films. The plates are jacketed onto 1-inch-large molybdenum blocks (so-called molyblocks). The transfer of the samples (i.e. the transfer of the molyblocks) from one chamber to another is performed using magnetic and mechanical transfer rods. The temperature of the surfaces is monitored with a Keller infra-red pyrometer.



*Figure II.1: Multi-purpose UHV system.* The UHV system encompasses four chambers: the STM chamber, the analysis chamber, the growth chamber and the Au evaporation chamber. The chambers are connected *via* a tunnel. The samples are introduced using a fast load-lock chamber and transferred from one chamber to another using transfer rods.

One of the UHV chambers, called the growth chamber, was extensively used for the preparation of the samples. This chamber is equipped with a valve and a gas line that are used for graphene growth *via* decomposition of  $C_2H_4$  and for high temperature  $O_2$  cleaning. This chamber is also equipped with  $Ar^+$  ion sputtering. Argon is introduced in the chamber with a separated valve and gas line, and bombardment is performed using a Gen 2 (Tectra GmbH) plasma source. The purity of the introduced gases can be checked with a quadrupole mass spectrometer. In the growth chamber, the sample plates (without the molyblocks) are transferred onto a heating stage using a magnetic wobblestick. The temperature of the surface is monitored both with a thermocouple located close to the plate, and with the pyrometer. The molecular evaporator is also located in this chamber. Finally, an electron gun facing a phosphor screen is used to perform reflection high-energy electron diffraction (RHEED) measurements.

A second UHV chamber, also equipped with RHEED, includes two electron-beam evaporators, one of which was used for gold evaporation. The deposition rates are monitored using a quartz microbalance which can be positioned at the sample location. In this chamber, the annealing of the samples is performed using a resistivity-heated Ta filament. The third chamber, called analysis chamber, was mainly used for the annealing of Re(0001) single crystals since its heating furnace allows to reach the highest temperatures in the system, up to  $\approx 1570$  K. The fourth chamber hosts the STM. Similarly to the growth chamber, the sample plates are positioned in the STM using a wobblestick.

## 1.b Reflection high energy electron diffraction

RHEED is a surface science technique that relies on the diffraction of high-energy electrons in grazing incidence. It provides information on the structure of a solid sample surface. Figure II.2 sketches a typical RHEED set-up.

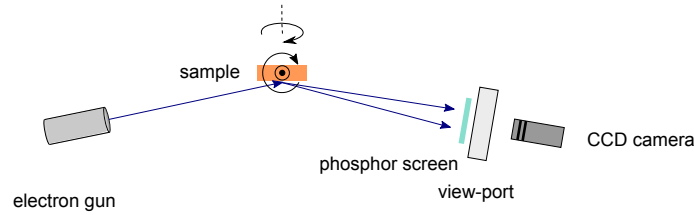


Figure II.2: **Sketch of a typical RHEED set-up.** High-energy electrons hit the sample in grazing incidence and are scattered at the sample surface. The impact positions of the diffracted electrons on a phosphor screen are recorded using a CCD camera. They provide insight on the lattice parameters of the surface species.

An electron gun provides high-energy electrons (typically a few 10 keV). These high voltage-accelerated electrons are focused using electrostatic lenses on the sample under a  $1^\circ$  to  $4^\circ$  incidence. The grazing incidence ensures a low penetration of the electrons in the solid i.e. only a region very close to the surface is probed: electrons are diffracted along a few atomic layers by the atoms of the probed lattice. Then, the orientation of the diffracted beams is determined *via* their trace on a phosphor screen. A CCD camera, mounted on the view-port of the chamber records the diffraction patterns.

The study of the reciprocal lattice (by RHEED or any other diffraction technique) allows retrieving meaningful information on the direct lattice. RHEED being a surface-sensitive technique, it provides information on 2D direct lattices. The reciprocal lattice of a 3D crystal is a 3D lattice made of points. In the limit of an infinite  $c$  lattice parameter perpendicular to the surface (Figure II.3), the 3D crystal becomes a set of (infinitely-separated) 2D crystals. Conversely, the distance between lattice points in reciprocal space,  $2\pi/c$ , vanishes. The reciprocal lattice points hence effectively form rods perpendicular to the surface.

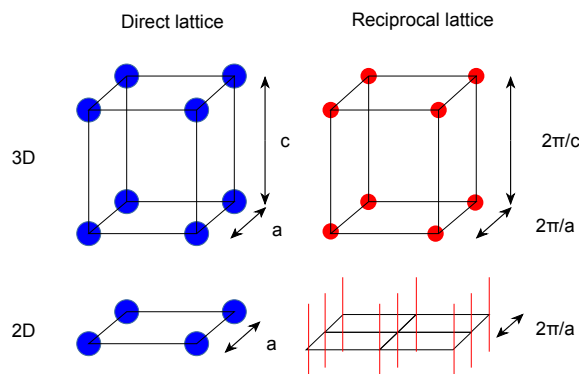
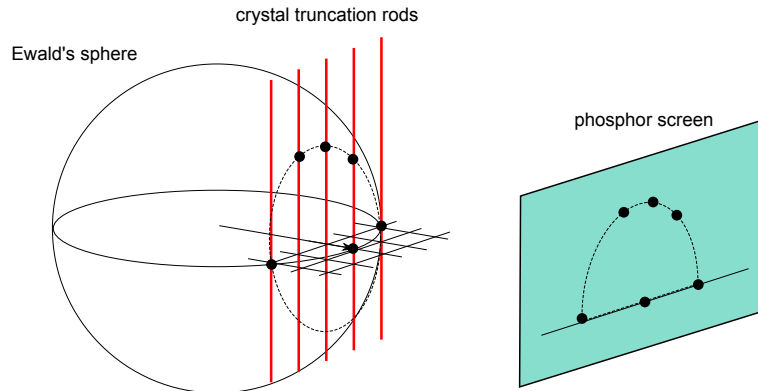


Figure II.3: **Examples of direct lattices and corresponding reciprocal lattices.** For a cubic 3D crystal, the reciprocal lattice is made of points. For a 2D crystal it is made of rods perpendicular to the surface. Figure reproduced from Ref. [131].

The construction of diffraction patterns in RHEED relies on two simple conditions:

1. The diffraction is elastic, i.e. the scattered wave vector  $\vec{k}_f$  has the same norm as the incident wave vector  $\vec{k}_i$ :  $||\vec{k}_f|| = ||\vec{k}_i|| = k_i$ . As a result, the possible wave vectors  $\vec{k}_f$  have their extremity on a sphere of radius  $k_i$ , called the Ewald's sphere.
2. For the interference with the probed lattice to be constructive, the difference  $\vec{q} = \vec{k}_f - \vec{k}_i$  must be a vector of the reciprocal lattice (Bragg's law).

These two conditions having to be simultaneously complied with, the geometric locus of solutions corresponds to the intersection between the Ewald's sphere and the reciprocal lattice rods (see Figure II.4).



*Figure II.4: Construction of a diffraction pattern in RHEED.* The apparatus is assumed to be perfect (Ewald's sphere infinitely thin), and so is the probed surface (crystal truncation rods infinitely thin). The dark spots indicate the intersection points between the rods and the sphere, and give rise to the associated diffraction spots on the phosphor screen. Figure reproduced and adapted from Ref. [131].

In the ideal case, a diffraction pattern should be made of points (intersection between a sphere and rods). Nevertheless this is not what is observed and for several reasons. On the one hand, the electron beam is not perfectly collimated and electrons are not perfectly monokinetic. Instead they distribute along a certain energy range, centered around a mean value  $E_i$ . This energy inhomogeneity translates into a certain thickness of the Ewald's sphere. On the other hand, the surface is not perfect: it presents terraces and steps and the crystal lattice comprises defects. The reciprocal lattice of the probed surface is therefore not made of infinitely thin rods. The Ewald's sphere and the rods of the reciprocal lattice having finite thicknesses, a RHEED pattern is not made of points but is rather made of streaks.

When the electron beam's axis is aligned to well-defined crystal atomic directions, which defines an azimuth, the central so-called specular streak (corresponding to the rod passing through the center of reciprocal space) is surrounded by symmetric streaks (corresponding to the  $+1/-1$ ,  $+2/-2$ , etc, -order rods of the reciprocal lattice). Lattice parameters in direct and reciprocal spaces being inversely proportional, the further (closer) from the central streak a given streak is, the smaller (larger) the lattice parameter associated to it in direct space.

For further information on the analysis of RHEED patterns, the reader is invited to refer to the PhD thesis of Alexandre Artaud [2] who developed a dedicated Python program used in the present thesis.

### 1.c Surface preparations

Single crystal surface preparations were mainly performed in the growth and analysis chambers. The surface state was checked using both RHEED and STM measurements. More specifically, the preparation recipes were optimized in order to obtain RHEED patterns free of any sign of surface reconstruction and STM images showing  $\geq 100$  nm-wide terraces, with no or few surface pollutions. Finally, high sputtering ion energies can lead to sub-surface Ar implantation during the sputtering step, and result in the observation in STM of few tens of nm-large protrusions, called "Ar bubbles". The ion energies used for the preparations of the single crystals were adjusted so that no Ar bubble is found. The preparation recipes of Re(0001), Pt(111) and Cu(111) single crystals, which were extensively used during this thesis, are presented hereafter.

**Re(0001) single crystals**

The monitoring of the surface temperature of Re(0001) single crystals is performed with the emissivity of the pyrometer set to 0.3.

- The surface is bombarded with Ar<sup>+</sup> with 2 keV ion energy for 45 min, then 1.5 keV for 30 min, then 1 keV for another 30 min.
- A flash annealing of the surface up to  $\approx 1570$  K is performed. This first sputtering-annealing cycle cleans the surface quite effectively but it leads to the implantation of Ar<sup>+</sup> ions below the surface. As a result, the next cycles are performed with lower ion energies.
- The surface is bombarded with Ar<sup>+</sup> with 1.5 keV ion energy for 30 min, then 0.5 keV for 30 min.
- A flash annealing of the surface up to  $\approx 1570$  K is performed.

The two last steps are repeated as many times as required.

**Pt(111) single crystal**

The monitoring of the surface temperature of Pt(111) single crystal is performed with the emissivity of the pyrometer set to 0.15.

- The surface is bombarded with Ar<sup>+</sup> with 1 keV ion energy for 20 min.
- The surface is annealed up to 1070 K for 2 min.
- The temperature is decreased down to 770 K. As the temperature decreases, the oxygen valve is opened in order to reach  $P_{O_2} \approx 10^{-7}$  mbar and to stay 3 min at 770 K under this oxygen pressure.
- The oxygen valve is closed and a flash desorption of the excess oxygen up to 1070 K is performed.

**Cu(111) single crystal**

The monitoring of the surface temperature of Cu(111) single crystal is performed with the emissivity of the pyrometer set to 0.1.

1. The surface is bombarded with Ar<sup>+</sup> with 0.8 keV ion energy for 30 min.
2. The surface is annealed up to 620 K-670 K for 10 min.

**1.d Graphene growth on Re(0001) thin films**

The preparation of rhenium thin films and graphene growth on rhenium thin films are presented hereafter. For further details on this topic, we refer the reader to the PhD theses of Amina Kimouche [132] and Charlène Tonnoir [1].

Rhenium films with 40 nm- to 50 nm-thickness were used as substrates. Following a change of oven in the laboratory where the films were grown (SIMAP Grenoble, Bruno Gilles), the Re deposit recipe was slightly adapted compared to that used in earlier works involving Néel Institute and CEA-IRIG [3]. In this paragraph, parameters used in previous Re deposits (*i.e.* before the oven was changed, at the time when Amina Kimouche and Charlène Tonnoir were doing their PhDs) are indicated in parentheses. Rhenium films were grown by Bruno Gilles in a dedicated UHV system using an electron-beam evaporator at a rate of 15 Å/min (8 Å/min) at 1200 K (1050 K). Pieces of  $\alpha$ -Al<sub>2</sub>O<sub>3</sub>(0001) wafers, annealed under UHV at 650 K (570 K) for 5 h (4 h) beforehand, were used as growth substrates. Then, the thin film samples were transported in atmospheric conditions into the UHV system presented in Section 1.a, where they were first annealed to 1070 K for 30 min. To grow graphene, the sample surface was exposed to

$10^{-7}$  mbar of ethylene at 1260 K for a few minutes, and subsequently cooled down to 970 K within few tens of minutes. This procedure yielded single-layer graphene covering the whole sample surface [3].

The graphene-on-Re 40 nm-thick film sample presented in Chapter V (Raman spectrum on Gr/Re) was prepared with the “old” Re deposit parameters, and corresponds to the “AK49” sample prepared by Amina Kimouche. Scanning tunneling microscopy and spectroscopy measurements obtained on this sample are presented in Ref. [3].

### 1.e Molecular evaporator

The molecular evaporator - the mounting and calibrating of which is detailed later - used for the depositions of molecules on surfaces presented in this thesis is a Kentax two-cell evaporator designed especially for materials with a low sublimation temperature. This evaporator was purchased and installed during summer 2017 by myself, another PhD student (Ana Cristina Gómez Herrero), and two engineers (Philippe David, Valérie Guisset).



*Figure II.5: Kentax two-cell molecular evaporator.* The crucible is filled with molecules and inserted in the molecular evaporator. Left and right images were taken from the user manual provided by Kentax [133].

The molecule-containing quartz crucibles are placed in the molecular evaporator as seen in Figure II.5 and are resistively heated with tungsten coils. Even though the two cells of the evaporator have independent tungsten coils, both crucibles are cooled down using water during operation, so that the unused cell is not heated by the neighboring coils.

A shutter (not visible in Figure II.5) allows to control the opening and closing of the crucibles outlets. The initial geometry of the shutter (provided by Kentax) was not ideal. Indeed, it comprised three holes allowing the individual opening of the two crucibles outlets (one crucible outlet is opened while the other one remains closed) and the opening/closing of both crucible outlets – the opening of both crucibles outlets allowing co-deposition of the two molecule-containing crucibles. This configuration was not satisfying, as it implied crossing the position of the other crucible outlet when opening/closing the crucible outlet of interest. It eventually led to the crossed contamination of the crucibles: the shutter is usually rotated during operation, allowing for the molecules adsorbed on the shutter surface facing the heated crucible (when the heated crucible is closed) to contaminate the other crucible when the shutter is rotated. For this reason, we replaced the initial shutter and opted for a two-hole geometry.

### 1.f Angle-resolved photoemission spectroscopy

Before describing the experimental set-up which was used for measuring the photoemission maps shown in Chapter V, we briefly remind the working principle of angle-resolved photoemission spectroscopy (ARPES).

#### Working principle

ARPES is a technique based on the photoelectric effect, which allows mapping the occupied electronic states of solid samples in reciprocal space. The idea is the following: an electron sitting on an energy

level absorbs energy from an incoming photon and is ejected in vacuum. The detection of the outgoing photoemitted electron (also called “photoelectron”) allows retrieving information on its initial state.

The energy conservation writes as follows:

$$h\nu = E_{\text{kin}} - E_{\text{b}} + \Phi \quad (\text{II.1})$$

where  $h\nu$ ,  $E_{\text{kin}}$ ,  $E_{\text{b}}$  and  $\Phi$  are the energy of the incoming photon, the kinetic energy of the photoemitted electron, the binding energy ( $E_{\text{b}} < 0$ ) of the electron sitting on its initial state, and the electron work function (*i.e.* the energy required to remove an electron from sample to vacuum), respectively.

The component parallel to the surface of the crystal wave-vector is conserved and is related to the kinetic energy of the photoemitted electron through the following formula:

$$k_{\parallel} = \sqrt{\frac{2m}{\hbar^2} E_{\text{kin}}} \sin(\Theta) \quad (\text{II.2})$$

where  $m$  is the electron free mass and  $\Theta$  the emission angle of the photoelectron.

The three step model, a simple phenomenological model introduced by Berglund and Spicer [134], is the most commonly used model to describe the photoemission process. As one would guess, in this model, the photoemission process is decomposed into three steps: 1. the optical excitation of an electron in the bulk, 2. the travel of this excited electron to the surface and 3. its escape into vacuum. The optical excitation is related to the photoelectric effect: an electron in the bulk of the probed material absorbs energy of an incoming photon. During its travel towards the surface, the excited electron can experience inelastic collisions, in which case it will eventually contribute to the diffuse background of the photoemission spectrum. On the contrary, if the excited electron travels a distance less than the electron mean free path (of the order of a few Å), the information on its initial state will be preserved and eventually contribute to the useful part of the signal. Finally, to escape into vacuum, the excited electron must overcome the surface potential.

Measuring the kinetic energy  $E_{\text{kin}}$  and emission angle  $\Theta$  of photoemitted electrons, and combining Equations II.1 and II.2 allows accessing the dispersion relation  $E_{\text{b}}(k_{\parallel})$ . Note that the perpendicular component of the wave-vector  $k_{\perp}$  is not conserved across the sample surface due to the lack of translational symmetry along the surface normal. In general, this means that ARPES experiments do not allow a complete determination of the total crystal wave-vector  $k$ . Nonetheless, two-dimensional materials are characterized by a negligible dispersion along the  $z$  axis (*i.e.* along the surface normal), hence the dispersion relation is almost exclusively determined by  $k_{\parallel}$ .

The expression of the photoemission intensity within the three step model involves matrix elements which depend on several parameters, including the energy and polarization of the photon source, and falls out of the scope of this work.

In practice, to explore the electronic valence band (binding energies of the order of 1-10 eV), ultra-violet (UV) light is used as a photon source. UV light emission is provided using either rare gas-discharge lamps or synchrotron beamlines. The sample position and tilt angle are precisely adjusted so that the beam is well focused on the sample. The azimuthal angle of the sample is fixed in order to select the desired direction in reciprocal space. ARPES measurements are collected at different polar angles over an angular range set by the energy and wave-vector range that needs to be explored. Photoelectrons are emitted from the surface and collected by an electron analyzer. The latter captures an image recording the electron kinetic energy  $E_{\text{kin}}$  as function of the emission angle  $\Theta$  of the collected photoelectrons. The coordinates of the image are then converted into binding energy  $E_{\text{b}}$  and wave-vector  $k_{\parallel}$ .



### Experimental set-up

ARPES experiments were performed in LPEM, ESPCI (Paris) with the help of Sergio Vlaic. I was welcomed within his group for a one-month measurements campaign. A sketch of the UHV system encompassing the ARPES chamber and a preparation chamber is shown in Figure II.6. Samples were prepared and characterized *in situ* with ARPES, prior to any exposure to air.

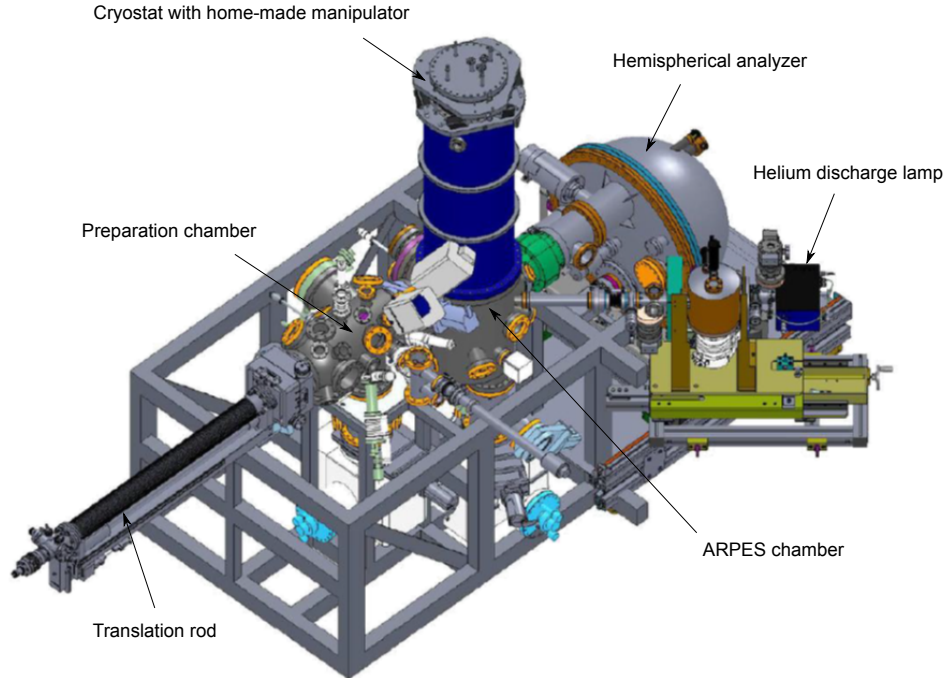


Figure II.6: **ARPES experimental set-up.** The UHV system encompasses two chambers: the ARPES chamber and the preparation chamber.

Surface preparation and graphene growth were performed in the preparation chamber. The sample was placed onto a heating stage whose position was precisely controlled using a four-axis manipulator. The preparation chamber is equipped with a valve and a gas line that were used for graphene growth *via* decomposition of  $C_2H_4$ . This chamber is also equipped with  $Ar^+$  ion sputtering. Argon was introduced in the chamber with a separated valve and gas line, and bombardment was performed using an ion gun. The temperature of the surface was monitored with a pyrometer. A LEED-Auger apparatus was used to check the structural and chemical state of the surface at different stages of the sample's preparation. LEED was also used as a way to retrieve the orientation of the high symmetry directions of the sample with respect to a known direction. Such information was of interest to later align the sample in the ARPES chamber.

The ARPES chamber is equipped with  $He_I$  and  $He_{II}$  lamps as sources (spectral lines at 21.22 eV and 40.81 eV photon energies). The sample was placed on a six-axis home-made manipulator mounted on a liquid helium flow cryostat. Photoemitted electrons were detected using a hemispherical analyser. The measurements presented in Chapter V were performed using p-polarized (90% degree of polarization) photons, at an estimated sample temperature of 100 K. The electronic band structure and high-symmetry points of the sample's surface were identified by collecting ARPES measurements at different polar angles over an angular range of more than  $60^\circ$ .

## 2 Scanning tunneling microscopy and spectroscopy

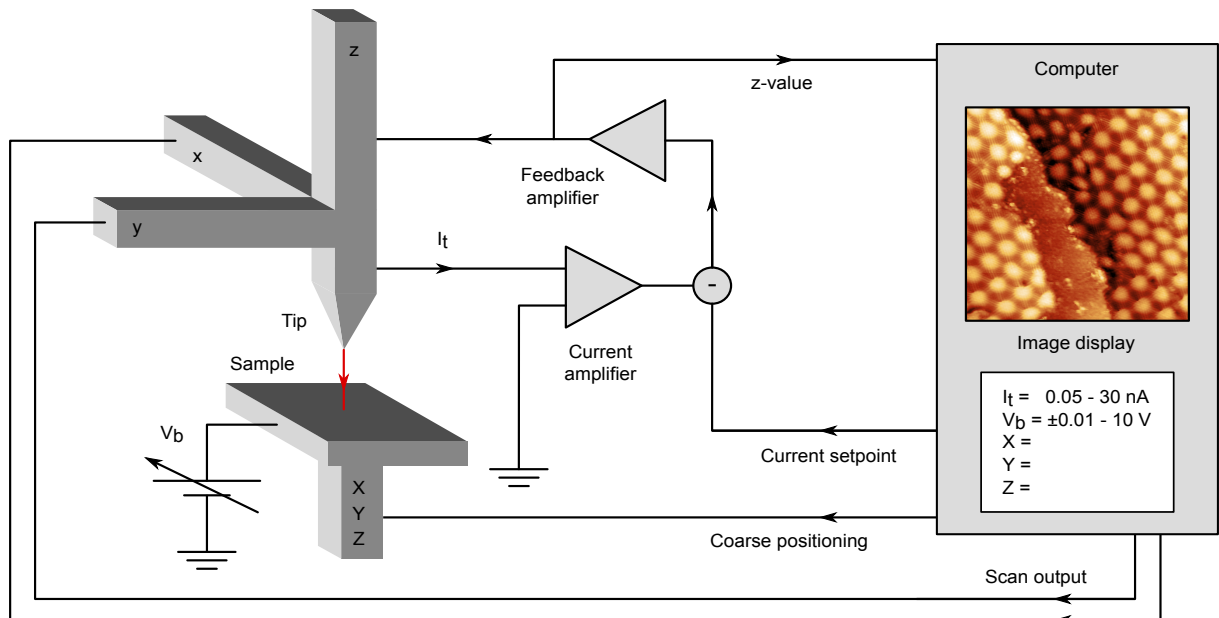
### 2.a Working principle

#### Scanning tunneling microscopy

Scanning tunneling microscopy (STM) is a scanning probe microscopy technique with which atomic resolution can be reached. STM relies on a purely quantum phenomenon which gave it its name: the tunnel effect. This effect is observed when one considers two conductors separated by a very thin insulator. Classically, electrons cannot jump from one conductor to the other by applying a difference of potential because the circuit is open. However, when adopting a quantum point of view and considering the wave functions that describe the electrons of both conductors, one can show that provided that the two conductors are close enough (typically, 1 nm apart), there is a non-zero probability for electrons to jump from one conductor to the other. In scanning tunneling microscopy, the idea is to reproduce such metal-insulator-metal junction using the tip of a metal probe (hereafter called the STM tip) and a conducting sample separated by vacuum. When the distance between the tip and the sample is small enough, the wave functions on either side of the insulator overlap. The current stemming from quantum tunneling depends exponentially on the tip-sample distance  $d$ :

$$I_t \propto \exp(-2\kappa d), \text{ with } \kappa = \sqrt{\frac{2m\phi}{\hbar^2}} \quad (\text{II.3})$$

with  $m$  the electron free mass, and  $\phi$  the work function of the tip and sample (for simplicity the work functions of the tip and of the sample are assumed to be equal). For a metal,  $\phi \sim 5$  eV, so  $\kappa \sim 1 \text{ \AA}^{-1}$ . As a result, a variation of  $d$  of only 1  $\text{\AA}$  leads to an order of magnitude variation of  $I_t$ . This exponential dependence explains the very high vertical resolution of scanning tunneling microscopes.



*Figure II.7: Basic principle of a scanning tunneling microscope:* a tip is scanned using three piezoelectric actuators ( $x, y, z$ ) above a sample positioned by inertial motors ( $X, Y, Z$ ). During the scan, a voltage bias  $V_b$  is set between the sample and tip, so a tunnel current  $I_t$  can be measured. A feedback loop compares the measured current to a setpoint value, so their difference drives the  $z$  piezoelectric actuator to maintain a constant tip-sample distance. The imposed  $z$  displacement is displayed as a topograph on the control computer. Figure adapted with permission from Ref. [2].

The constant-current imaging mode (Figure II.7) consists in scanning the surface along the  $x$  and  $y$  directions while maintaining - using a feedback loop - a constant tunnel current  $I_{set}$  called the current

set-point. The adjustments of the vertical position  $z$  during scanning allow retrieving the (apparent) topography of the probed surface  $z(x, y)$ , which is assumed to be chemically uniform so far. One can also use a constant-height imaging mode: the tip scans the surface maintaining a constant tip position  $z$ . In this case, the feedback loop is open (or slowed down) and the variations of the tunnel current  $I_t(x, y)$  are acquired. The images presented in this thesis are acquired using the constant-current imaging mode.

### Scanning tunneling spectroscopy

In addition to their remarkable spatial resolution, scanning tunneling microscopes give access to the local electronic density of states of the probed sample.

The tunneling current flowing between the tip and the sample, derived from the Fermi golden rule, writes as [135, 136]:

$$I(V_b) = \frac{2\pi e}{\hbar} |M|^2 \int_{-\infty}^{+\infty} d\epsilon N_t(\epsilon) N_s(\epsilon + eV_b) [f_t(\epsilon) - f_s(\epsilon + eV_b)] \quad (\text{II.4})$$

where  $|M|^2$  is the mean value of  $|M(\epsilon_t, \epsilon_s)|^2$ . The indices  $t$  and  $s$  stand for tip and sample, respectively. The matrix element  $M(\epsilon_t, \epsilon_s)$  corresponds to the coupling (i.e. the overlap) between the electronic wavefunctions of the tip and of the sample at the energies  $\epsilon_{t,s}$ . It is usually assumed to be independent in energy when the applied voltage  $V_b$  is small compared to the Fermi energy  $E_F$ . This explains why  $|M(\epsilon_t, \epsilon_s)|^2$  is usually replaced by  $|M|^2$ .  $N_{t,s}(\epsilon)$  is the density of states and  $f_{t,s}(\epsilon)$  the Fermi-Dirac distributions of the electrons, in the tip and sample.

In the low temperature limit and considering an applied voltage  $V_b$  small compared to the Fermi energy, the Fermi-Dirac distributions become step functions with  $f(\epsilon) = 1$  for  $\epsilon < E_F$ , and 0 otherwise. As a result,  $f_t(\epsilon) = 1$  for  $\epsilon < E_F$ , and 0 otherwise, and  $f_s(\epsilon + eV_b) = 1$  for  $\epsilon < E_F - eV_b$ , and 0 otherwise. Assuming  $E_F = 0$  and assuming that the tip has an energy-independent density of states (which is reasonable considering that we use metallic tips), Equation II.4 simplifies as:

$$I(V_b) = \frac{2\pi e}{\hbar} |M|^2 N_t \int_{-eV_b}^0 d\epsilon N_s(\epsilon + eV_b) \quad (\text{II.5})$$

Finally, deriving Equation II.6 leads to:

$$\frac{dI}{dV}(V_b) = \frac{2\pi e}{\hbar} |M|^2 N_t N_s(eV_b) \quad (\text{II.6})$$

### Topographic and electronic contributions

In topographic measurements, when using the constant-current imaging mode,  $I_t(V_b)$  is acquired and the adjustments of the vertical position  $z$  during the scanning relate to the topography of the probed surface  $z(x, y)$ . However, electronic contributions can never be discarded. As seen in Equation II.5, the tunnel current is directly proportional to the integrated density of states of the sample. When  $V_b$  is raised, the integration runs on some additional states that contribute to the tunnel current. As a result, It is increased and it will result in the STM image in a higher apparent height. This is commonly referred to as an electronic density of states effect, and it should always be taken into account when deriving topographic figures from STM images.

## 2.b Experimental set-ups

The STM and STS measurements presented in this thesis were performed using three different set-ups:

- A commercial room-temperature STM working in UHV: Omicron UHV-STM 1, with chemically etched W tips.
- A home-made STM/STS set-up installed in an inverted dilution refrigerator (*sionludi*) working with a  $^3\text{He}/^4\text{He}$  mixture at temperatures down to 50 mK, with Pt-Ir tips.
- A home-made STM/STS set-up implemented inside a  $^4\text{He}$  refrigerator that can operate down to 1.5 K if we pump on it.

Thermal drift and miscalibrations are corrected. The differential conductance spectra were obtained using a standard lock-in technique. The modulation amplitude and frequency will be given in the concerned sections. Representative spectra of regions of interest are obtained averaging a few 10 to 100 spectra in the said regions.

### 3 Raman spectroscopy

#### 3.a Working principle

The Raman effect relates to inelastic light scattering. Inelastic scattering may occur, for instance, in the presence of lattice vibrations. These vibrations are sensitive to various effects, which make them a very insightful probe for various physical properties. For instance, lattice defects activate otherwise forbidden vibration modes and strain is readily detected as it alters the vibration energies (*via* the anharmonicity of the interatomic potentials). Changes in the electronic properties also modify the vibration energies (*via* the electron-phonon interaction). In this regard, the study of graphene has greatly benefited from Raman spectroscopy investigations [18]. In practice, the incident light in a Raman spectroscopy set-up is nowadays provided by a laser source. It interacts with the sample and the inelastically scattered light is collected. Raman processes, illustrated in Figure II.8, can be described as follows:

1. An incident photon of pulsation  $\omega_i$  disturbs the system.
2. It creates an electron-hole (e-h) pair, i.e. it excites an electron up to a virtual or real electronic state.
3. This electron-hole pair absorbs (anti-Stokes) or emits (Stokes) a phonon of pulsation  $\Omega$ : the crystal lattice vibrates.
4. The absorption or emission of a phonon modifies the energy of the electron-hole pair (e'-h').
5. The electron e' decays by emitting a photon of pulsation  $\omega_d$ .

If the energy of the incident photon ( $\hbar\omega_i$ ) corresponds to a real electronic state, the process is said to be resonant because it is much more efficient. If not, the state is virtual and the process is non-resonant. The possible configurations are summed up in Figure II.8.

Resonant Raman scattering should not be confused with fluorescence. When the incident photon energy is higher than one of the electronic states of the system, the electron can decay non-radiatively down to this electronic state, and fluoresce (decay down to the fundamental state) from it. This phenomenon is different from Raman scattering because the electron transits *via* a real intermediate state whereas Raman process is a scattering process. Fluorescence is responsible for broad peaks and makes difficult the assigning of the peaks associated to Raman processes (Raman peaks can be “buried” within the fluorescence signal and/or appear shifted if the fluorescence-related background is not well taken into account, hence not well subtracted). In practice, the incident laser wavelength is chosen so that fluorescence is minimal.

In a Raman spectrum, the intensity of the scattered light is plotted as a function of a quantity called the Raman shift  $\delta$ . The Raman shift corresponds to the wave number associated to the difference

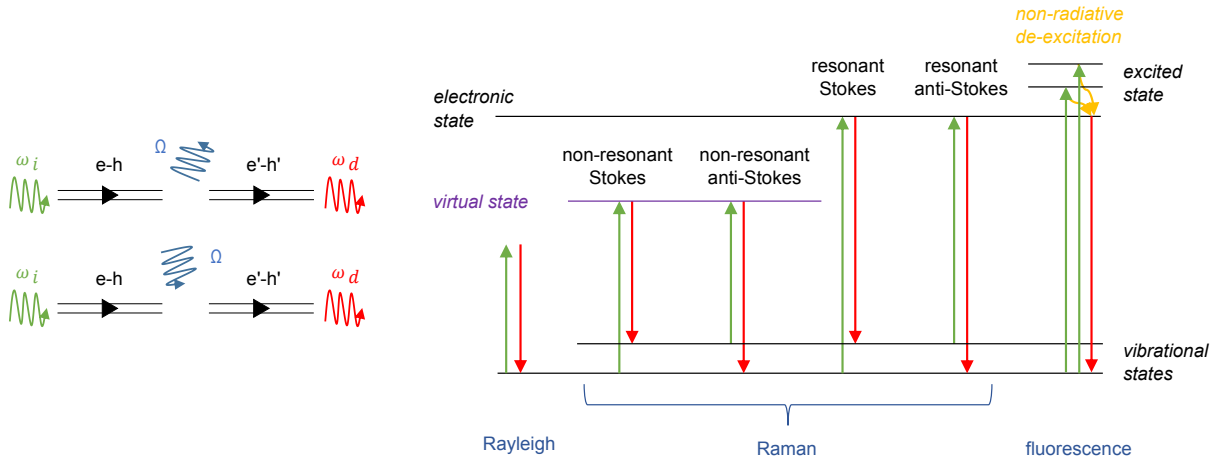


Figure II.8: Sketches of the Raman process and of the phenomena at play in Raman spectroscopy. **Left:** Sketch of the Raman process. The electron-hole pair emits (Stokes) or absorbs (anti-Stokes) a phonon. **Right:** Rayleigh scattering corresponds to elastic scattering. The green and red arrows correspond to the incident and scattered light, respectively. Figure reproduced and adapted from Ref. [137].

of energy between the incident photon and the scattered one, i.e.  $\hbar\omega_i - \hbar\omega_d$ . Said differently, the Raman shift is proportional to the energy of the exchanged phonon. The peak corresponding to elastic scattering (Rayleigh scattering) is the central peak. The peaks corresponding to Raman scattering (Stokes and anti-Stokes) are located on either side of this peak. In practice, the Rayleigh peak is filtered with a high-pass optical filter, because its high intensity is too high (several orders of magnitude higher) with respect to that corresponding to Raman scattering, and the dynamical range of the detector would not allow to detect the latter. In our case, we disregarded the anti-Stokes peaks.

The fundamental selection rule in Raman spectroscopy states that the total phononic wave vector exchanged during a Raman process is zero:  $\vec{q}_{tot} = \vec{0}$ . It is important to note that this does not mean that all the phonons exchanged during a Raman process have a zero wave vector. One can imagine two-phonon processes with opposite wave vectors, so that  $\vec{q}_{tot} = \vec{q} + (-\vec{q}) = \vec{0}$ . For one-phonon processes, this selection rule imposes that only the phonons around the  $\Gamma$  point are to be probed. For acoustic branches, having energies close to zero near the  $\Gamma$  point, the Raman shift is inappreciable (the difference of energy is zero). As a result, only optical phonons are probed.

### 3.b Experimental set-up

Raman spectroscopy measurements were acquired with a 532 nm Nd:YAG laser using a commercial confocal WITEC spectrometer at room temperature under ambient conditions. The signal is collected through 50 $\times$  or 100 $\times$  objectives, dispersed by either a 600 lines/mm or a 1800 lines/mm grating and integrated for a certain amount of time. The acquisition details of each acquired spectrum will be given in the concerned sections.

## 4 Simulations

### 4.a Density functional theory calculations

Calculations performed in the framework of density functional theory (DFT) are shown in Chapters IV and V. In this section, we recall the basic principle of DFT, how it is used in practice and its limitations.

Nowadays, DFT is the computational method most used to perform ground-state electronic structure calculations of atoms, molecules and solid state materials. Instead of expressing solutions of the Schrödinger equation in terms of wave-functions, the properties of a particular system are determined using functionals

(*i.e.* functions of another function) of the (spatially-dependent) charge density  $\rho$ , hence the name density functional theory. The motivation for finding methods, such as DFT, which do not consist in determining the wave-functions of the system of interest stems from the very high computational cost of wave-function-based methods, such as the Hartree-Fock method.

We now discuss in more details what terms are involved in the Schrödinger equation and how DFT tackles them. The Hamiltonian operator of a quantum system consists of a sum of three terms: the kinetic energy operator, the external potential energy operator (related to the interaction of the electrons with an external potential) and the electron-electron interaction energy operator. The kinetic energy operator includes a kinetic energy operator related to the ions and a kinetic energy operator related to the electrons. These two contributions are separated using the Born-Oppenheimer approximation, assuming that, because the mass of an electron is much lower than the mass of an ion, electrons react instantly to any ion displacement. The movement of the ions is treated separately and classically, and its effect on the movement of electrons is re-introduced in the Hamiltonian of the system as a Coulomb potential (interaction between the electrons and the nuclei). In materials simulation the external potential includes the Coulomb potential and any additional external potential applied to the system. Hohenberg and Kohn showed that every term of the Schrödinger equation can be written as a unique functional of the charge density and that solving the Schrödinger equation consists in minimizing the energy with respect to the charge density functional [138].

At this point, the energy functional  $E[\rho]$  writes as:

$$E[\rho] = T[\rho] + V_{ext}[\rho] + V_{ee}[\rho] \quad (\text{II.7})$$

where  $T[\rho]$  is the kinetic energy functional,  $V_{ext}[\rho]$  is the external potential functional (which usually simply includes the electron-ion Coulomb interaction), and  $V_{ee}[\rho]$  is the electron-electron potential functional.

Kohn and Sham proposed the following approach to approximate the kinetic energy and the electron-electron potential functionals. They introduced a fictitious system of  $N$  non-interacting electrons, described by a single determinant wavefunction of  $N$  one-electron orbitals. In this approach, the Schrödinger equation rewrites as a set of one-electron Schrödinger-like equations, known as the Kohn-Sham equations [139] and the energy functional  $E[\rho]$  rearranges as:

$$E[\rho] = T_S[\rho] + V_{ext}[\rho] + V_H[\rho] + E_{xc}[\rho] \quad (\text{II.8})$$

where  $T_S[\rho]$  is the Kohn-Sham kinetic energy functional,  $V_H[\rho]$  is the classical Coulomb potential (or Hartree energy) functional and  $E_{xc}[\rho]$  is the exchange-correlation functional. Both  $T_S[\rho]$  and  $V_H[\rho]$  are written as functions of the auxiliary orbitals associated with the (fictitious) system of non-interacting electrons. The exchange-correlation functional can be viewed as a correction which includes all the many-particle interactions which are omitted in  $T_S[\rho]$  and  $V_H[\rho]$ .

One major difficulty in DFT lies in the choice of the exchange-correlation functional (the exact exchange-correlation functional is only known for the free electron gas case). One of the simplest approximations of the exchange-correlation functional is the local-density approximation (LDA), where the functional depends only on the density at the coordinate where the functional is evaluated [139]. This crude approximation provides very good results. However, because it is based on a homogeneous electron gas, LDA tends to simulate the system more homogeneous than it really is, underestimating interatomic distances and overestimating binding energies. Corrections have been proposed, such as the generalized gradient approximation (GGA), which takes into account both the density and its gradient [140].

In practice, DFT calculations are performed as follows. The total energy of the system is calculated using Equation II.8, assuming an initial atomic structure. Variations of the total energy upon atomic displacements are calculated, which provides access to the forces applied to the atoms. The equilibrium

atomic structure is determined by minimizing the total energy and cancelling out the forces applied on atoms.

One of DFT limitations lies in its inability to produce accurate excited-states properties. Although the bandgap is a ground-state property, in DFT, it is determined from the band structure hence it is usually inaccurate.

The DFT calculations presented in this thesis were performed by Laurence Magaud (Institut Néel, Grenoble) using the Vienna Ab initio Simulation Package (VASP) code [141]. VASP is developed in the Technical University of Vienna, in Austria, and relies on a basis of plane waves. The electron-ion interaction is described using the projected augmented wave (PAW) formalism [142]. This formalism enables handling relatively large systems such as surfaces or interfaces. Several ways of expressing the exchange and correlation term within the GGA framework are possible. In this thesis, the PBE functional (named after its authors: Perdew, Burke and Ernzerhof) was used [143]. Since the van der Waals interaction plays an important role in the systems we studied, Grimme corrections were introduced [144]. Finally, because VASP only deals with periodic systems, simulating surfaces implies periodic boundary conditions in the vertical direction of space. These boundary conditions require the use of vacuum slabs in between units of interest in the vertical direction of space, to ensure that no spurious interaction between neighbouring units occurs.

## 4.b Bond-order potential calculations

When very large supercells must be tackled, as it will be the case in Chapter IV, DFT becomes too expensive in terms of computational time. A different approach, which allows tackling thousands of atoms, consists in using parametrized interatomic potentials such as bond-order potentials (BOP), to describe the system of interest and solve the classical equations of atomic motion. The framework for this type of approach is molecular dynamics: atoms and molecules are allowed to interact for a fixed period of time. The forces exerted on atoms and their potential energies are calculated using parametrized atomistic potentials (in the present case, BOP).

BOP are pair potentials (*i.e.* they describe interactions between pairs of atoms), and describe analytically the strength of the interatomic bonds in function of their environment. For this reason, BOP can describe several different bonding states of an atom. In chemistry, a higher bond order generally means a shorter bond length and a stronger bond, whereas a lower bond order means a longer bond length and a weaker bond. For instance, the triple bond  $C \equiv O$  has a bond order of 3 and is stronger and shorter than the double bond  $C = O$ , which has a bond order of 2.

The Morse potential inspired the form of BOP: in the original paper of Brenner [145], the binding energy  $E_b$  for the hydrocarbon potential is given as a sum of bonds with repulsive  $V_R$  and attractive  $V_A$  pair terms.

$$E_b = \sum_i \sum_{j(>i)} [V_R(r_{ij}) - \overline{B}_{ij} V_A(r_{ij})] \quad (\text{II.9})$$

where  $B_{ij}$  is the bond order. It represents the many-body coupling between the bond from atom  $i$  to atom  $j$  and the local environment of atom  $i$ . To a first approximation,  $B_{ij}$  can be expressed as a function of the local coordination  $Z$  as  $B_{ij} \propto Z^{-\delta}$ , where  $\delta$  depends on the particular system. The repulsive and attractive terms have a form which resembles the Morse potential:

$$V_R(r_{ij}) = f_{ij}(r_{ij}) D_{ij}^{(e)} / (S_{ij} - 1) e^{-\sqrt{2S_{ij}} \beta_{ij} (r - R_{ij}^{(e)})} \quad (\text{II.10})$$

$$\text{and } V_A(r_{ij}) = f_{ij}(r_{ij}) D_{ij}^{(e)} / (S_{ij} - 1) e^{-\sqrt{2/S_{ij}} \beta_{ij} (r - R_{ij}^{(e)})} \quad (\text{II.11})$$

where the function  $f_{ij}$  restricts the pair potential to nearest neighbours. When the  $S_{ij}$  parameter equals 2, the pair terms reduce to the usual Morse potential, where the adjustable parameters  $D_{ij}^{(e)}$ ,  $R_{ij}^{(e)}$  and  $\beta_{ij}$

correspond to the equilibrium well depth, the equilibrium bond distance and the width potential. BOP are empirically parametrized for the system of interest, usually against DFT results.

A BOP parametrized for graphene on Ru(0001) will be introduced in Chapter IV. The BOP simulations presented in Chapter IV were performed by Georg Daniel Förster (LEM, Châtillon) and Florent Calvo (LIPhy, Grenoble).





# STRUCTURE OF GRAPHENE AND A SURFACE CARBIDE GROWN ON RE(0001)

## Contents

---

1	Graphene growth on Re(0001) . . . . .	51
1.a	RHEED monitoring . . . . .	51
1.b	Evolution of graphene and moiré lattice parameters . . . . .	52
1.c	Extension of graphene domains and increasing ordering . . . . .	53
2	Coexistence of graphene and rhenium carbide . . . . .	55
2.a	STM observations . . . . .	55
2.b	RHEED patterns . . . . .	56
3	Structural variants of the ordered rhenium carbide phase . . . . .	57
3.a	$(7 \times \sqrt{19})$ unit cell of rhenium carbide . . . . .	57
3.b	Grouping variants in six-fold families of equivalent domains . . . . .	58
4	Possible atomic structures of the ordered rhenium carbide phase . . . . .	60

---

## ***Abstract***

We scrutinize the structure of graphene and a surface carbide grown on the (0001) surface of Re(0001), by means of RHEED and STM. We demonstrate with a semi-quantitative RHEED analysis that increasing the number of annealing cycles during graphene growth on Re(0001) contributes positively to growing high-quality extended graphene domains. This finding is consistent with STM images taken after different numbers of annealing cycles. The observation by STM of coexisting graphene and ( $7\times\sqrt{19}$ ) surface carbide is reported for the first time. The numerous surface carbide domains, with well-defined crystallographic orientations, are examined and grouped in six-fold families of equivalent domains. Possible atomic arrangements for one of these families are proposed. The atomic models are constructed using trimers of carbon atoms adsorbed in a specific stacking sequence, in agreement with previous XPS measurements.

## **Introduction**

Graphene growth on strongly interacting metallic substrates such as Re(0001) [44, 45, 3, 60, 61], Ru(0001) [51, 62, 63, 64], Rh(111) [65] and Ni(111) [66] has the advantage of selecting one crystallographic orientation of graphene with respect to its substrate. This is related with a tendency to form covalent bonds between graphene and the substrate [65, 61], as opposed to graphene grown on weakly interacting metallic substrates such as Ir(111) [53, 52], Pt(111) [54, 46, 55], Cu(111) [56], Ag(111) [58] and Au(111) [59], where van der Waals bonding is dominant [52, 65, 61]. Graphene growth on the latter kind of substrates results in domains with a large number of possible crystallographic orientations with respect to the substrate [54, 46, 56, 146, 147, 148, 55, 49].

Yet, growing graphene on strongly interacting substrates is not an easy task. On Rh(111), Ru(0001) and Re(0001), there is a subtle competition between the formation of different carbon phases, graphene and metal carbides [45, 149, 150, 151]. The relative stability of the two differs according to the temperature. In some cases, even in temperature ranges where graphene is more stable, graphene nucleation requires a high carbon chemical potential (a high carbon adatom concentration) [149]. In the case of a Re(0001) substrate that we address here, the growth conditions favouring the growth of graphene correspond to rather narrow windows of growth parameters (substrate temperature, hydrocarbon gas pressure and exposure time) [45].

Although obviously considered as detrimental in the context of graphene growth, surface metal carbides are important ingredients in a number of catalysis processes, as it was shown in the case of ammonia synthesis and decomposition, hydrogenolysis, isomerization, methanation, and hydroprocessing [152, 153]. Besides, they often consist of well-ordered surface structures with crystallographic unit cells at the scale of nanometers, which makes them efficient nanopatterns driving the self-organization of metallic clusters of interest for nanomagnetic or nanocatalysis applications [154, 155, 107].

Only few works devoted to surface carbides formed on the (0001) surface of rhenium have been reported so far [156, 45, 150]. The ( $7\times\sqrt{19}$ ) carbide overlayer was previously identified in LEED measurements [156, 45], but never observed directly with a local probe method.

In this study, we investigate the structure of graphene and the ( $7\times\sqrt{19}$ ) surface carbide grown on Re(0001) by means of RHEED and STM. We find that increasing the number of annealing cycles during graphene growth contributes positively to growing high-quality extended graphene domains. The coexisting graphene and ( $7\times\sqrt{19}$ ) surface carbide are observed for the first time by STM. The various orientations of the surface carbide domains are addressed and grouped in six-fold families of equivalent domains, each family having a specific atomic arrangement. Three atomic models are proposed for the carbide structure of one of these families, in agreement with previous XPS measurements [45].

# 1 Graphene growth on Re(0001)

A rhenium single-crystal cut with a (0001) surface was used as substrate and prepared following the recipe given in Chapter II. Graphene growth was performed using the hybrid temperature-programmed growth-chemical vapour deposition (TPG-CVD) method described in Ref. [45], which consists in a succession of rapid annealing cycles under  $C_2H_4$  atmosphere. Here, the Re(0001) surface was exposed to an ethylene pressure of  $P_{C_2H_4} = 5 \cdot 10^{-7}$  mbar, at room temperature. The temperature of the surface was increased within 2 min up to 970 K, followed by a cooling down to 520 K within 10 min. This step is called a TPG cycle and was repeated ten times. Then, a final (eleventh) annealing cycle was performed in absence of  $C_2H_4$ . Figure III.1 shows the evolution of the temperature (measured with a pyrometer set on the sample) as a function of time.

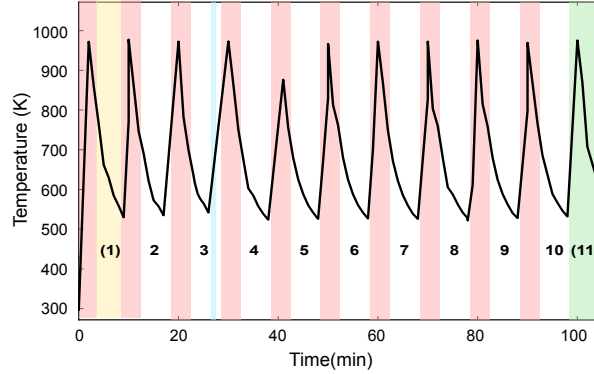


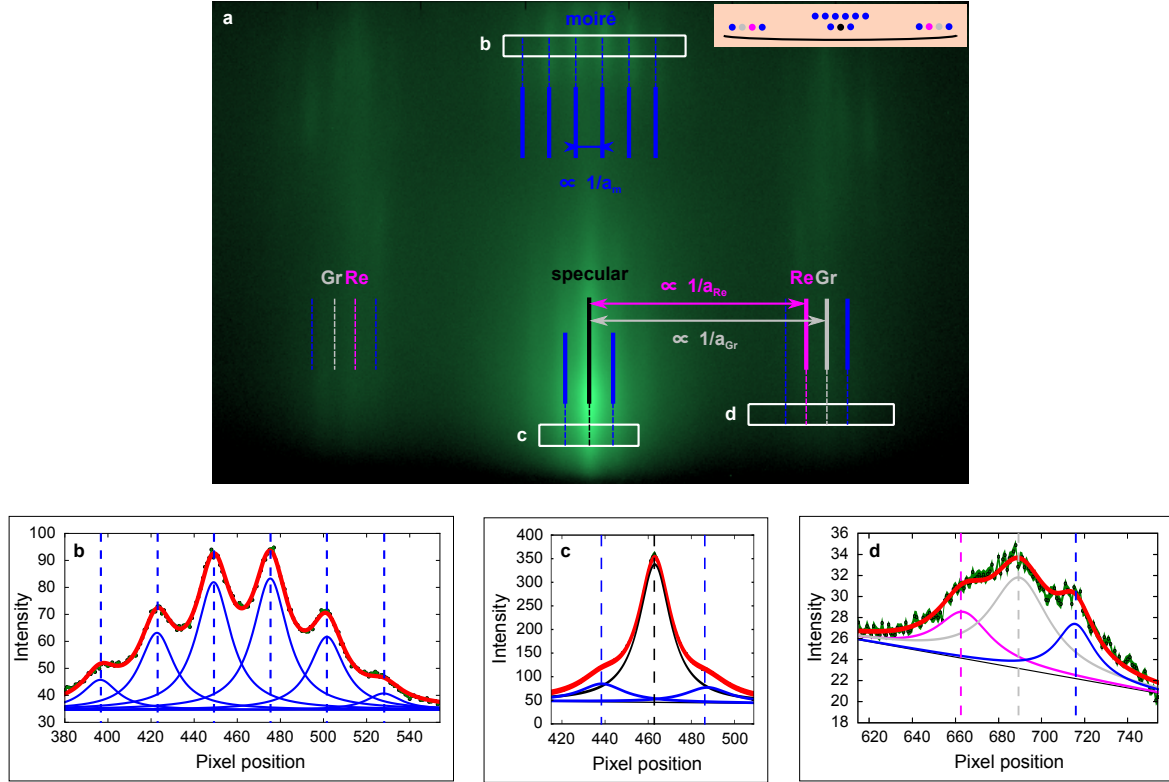
Figure III.1: **Sample temperature as a function of time, during graphene TPG cycles.** The RHEED patterns falling during the last TPG cycle (green rectangle), the TPG-fast annealings (red rectangles), the Ti sublimation cycle (blue rectangle) and the first TPG cycle (yellow rectangle) were excluded from the analysis.

## 1.a RHEED monitoring

During graphene growth, a movie of RHEED patterns was recorded using a CCD camera. The RHEED movie was acquired with an electron beam energy of 10 keV. Only the first ten TPG cycles (out of a total of eleven TPG cycles) were recorded. As a result, the last TPG cycle, which occurred after the  $C_2H_4$  valve was closed, is absent from the data set (see green rectangle in Figure III.1). The RHEED patterns of the first ten cycles which fall during TPG annealings (indicated with rectangles in red in Figure III.1) are systematically discarded from the analysis as they cannot be properly fitted. Indeed, the TPG annealings blind the CCD camera (the sample heating filament becomes very intense and saturates the CCD camera). During the third TPG cycle, a Ti sublimation cycle (indicated with a blue rectangle in Figure III.1) occurred and caused the deflection of the electron beam. All the RHEED patterns taken during Ti sublimation are excluded from the analysis. Finally, cycle 1 (indicated with a yellow rectangle in Figure III.1) is excluded from the analysis, as it will be explained later on. In the end, only the RHEED patterns which do not fall in a coloured rectangle are used to extract structural information on the sample. These RHEED patterns fall in the TPG cycles 2 to 10 (numbered in Figure III.1).

Figure III.2(a) shows a typical graphene-covered Re(0001) RHEED pattern along the  $[01\bar{1}0]$  incident azimuth, taken during the movie. The lattice mismatch and the strong electronic coupling between graphene and rhenium result in a periodic undulation of graphene on top of rhenium. This long wavelength beating (in real space) is known as a moiré superlattice [44, 3]. Streaks associated with the moiré superlattice are indicated in blue in Figure III.2(a). The positions and full widths at half maximum (FWHM) of graphene, Re and moiré streaks during the RHEED movie (*i.e.* during the TPG cycles) are extracted using the lorentzian fittings sketched in Figure III.2. Rectangular regions of interest are selected on the RHEED patterns, represented with white rectangles in Figure III.2(a). The intensity is integrated

over about 100 pixels (height of the rectangles) along the direction parallel to the diffraction streaks, in order to improve the signal-to-noise ratio. During the first cycle, no satisfying fit can be obtained in rectangle d. As a result, cycle 1 is excluded from the analysis. The left-hand part of the RHEED pattern is not used for the analysis, as it requires, in order to have satisfying fits, a change of the fit function in between cycle 4 and cycle 5. This change results in artificial shifts in the extracted data. Anyway, it was checked that the evolution of lattice parameters and FWHM is qualitatively the same whether we use the left-hand and right-hand parts of the RHEED pattern, or the right-hand part and the specular part.



*Figure III.2: Periodic features observed in RHEED on graphene-covered Re(0001).* (a) RHEED pattern of graphene-covered Re(0001) along the  $[01\bar{1}0]$  incident azimuth. Coloured lines indicate the specular (black), Re (pink), graphene (grey) and moiré (blue) streaks. Regions of interest are indicated with white rectangles. Inset shows a schematic top view of the reciprocal space with all observed rods and a cut of the Ewald's sphere (black line). (b-d) Line profiles (green) are extracted from the rectangular cuts by line averaging along the vertical direction and are fitted with lorentzian peaks on a constant (b) or linear (c,d) background.

The specular streak position is extracted from the fit of the three central streaks (white rectangle c). The fit is performed using three equally spaced lorentzians (Figure III.2(c)). The moiré streak position and moiré FWHM are extracted from the fit of the central moiré streaks (white rectangle b) in the top part of the RHEED pattern. The fit is performed using six equally spaced lorentzians with a single FWHM (Figure III.2(b)). The fits in b and c regions are very good: the curves corresponding to the sum of all lorentzians (red) match well the experimental points (green). The graphene and Re streaks positions and graphene and Re FWHM are extracted from the fit of the group of streaks observed in the right-hand part of the RHEED pattern (white rectangle d). The fit is performed using three equally spaced lorentzians (Figure III.2(d)). Individual bad fits were discarded. This only applied for the region d of the RHEED pattern. The regions b and c were sufficiently low-noise not to require removing individual bad fits.

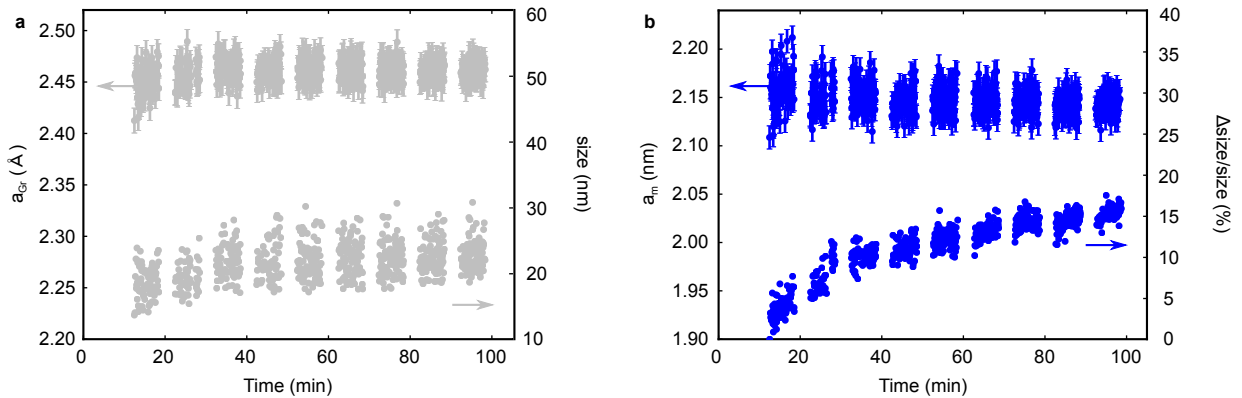
### 1.b Evolution of graphene and moiré lattice parameters

The Re lattice parameter was assumed constant and equal to  $a_{Re} = 2.76 \text{ \AA}$ . This assumption is reasonable both at the scale of a single TPG cycle and at the scale of all the TPG cycles. For the former, since

the linear thermal expansion coefficient of bulk Re is  $6.2 \cdot 10^{-6} \text{ K}^{-1}$  [157], and the temperature difference within a single TPG cycle is  $\Delta T = 970 - 520 = 450 \text{ K}$ , one can show that lattice expansion/compression amounts to 0.3%. Given that our fit procedure has a precision of  $\simeq 1\%$ , set by the signal-to-noise ratio, this effect can be neglected. For the latter, we assume that any local change in Re lattice parameter will be compensated elsewhere in the lattice and the average value of Re lattice parameter will remain the same.

The graphene lattice parameter was computed as  $a_{\text{Gr}} = (d_{\text{Re}}/d_{\text{Gr}}) \times a_{\text{Re}}$ , where  $d_{\text{Gr}}$  ( $d_{\text{Re}}$ ) is the distance between the graphene (rhenium) streak and the specular (central) streak. As seen in Figure III.3(a), no significant change in graphene lattice parameter is found during graphene growth and its average value, 2.46 Å, is close to the values found in the literature.

The moiré superlattice parameter, shown in Figure III.3(b) as a function of time, was computed similarly to what was presented for graphene. The moiré superlattice parameter seems to decrease from cycle 2 to cycle 4 but the data dispersion is important, preventing to make a definitive statement. It otherwise seems constant from cycle 5 to 10. If true, the small decrease of moiré superlattice parameter from cycle 2 to 4 could for instance mean that the lattice parameter mismatch between graphene and Re increases, *i.e.* that the graphene lattice parameter decreases. It was proposed that the progressive filling of vacancies during graphene growth and the thermally activated diffusion of small vacancies to the edges of graphene islands where they are annihilated, reduce the tensile strains, which results in a decrease of graphene lattice parameter. Such a mechanism was originally described in Ref. [158], where large strains were observed during graphene growth on Ir(111). It was later attributed to the contraction (observed in LEED) of the moiré supercell during graphene growth, in the graphene/Re(0001) sample presented in Ref. [45]. In our case, if the contraction of the moiré superlattice parameter from cycles 2 to 4 were true, it would still be much less than the 3% contraction observed in Ref. [45]. This could indicate that the size of graphene islands is higher in our sample, which makes them less sensitive to deformations effects at their edges. Overall, the moiré superlattice parameter is, in our study, approximately equal to 2.14 nm, which is close to the values found in the literature.



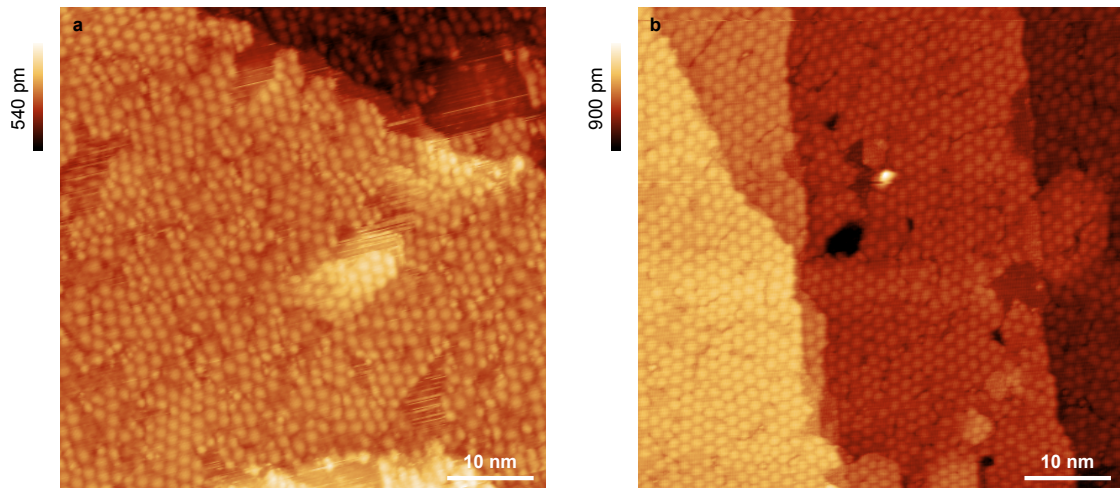
**Figure III.3: Evolution of graphene and moiré lattice parameters and domain sizes.** (a) Graphene lattice parameter and size of structurally coherent graphene domains, as a function of time. (b) Moiré superlattice parameter and size of structurally coherent moiré domains, as a function of time.

### 1.c Extension of graphene domains and increasing ordering

We now turn to a discussion on the size of graphene islands. Within the kinematic theory of diffraction and in the case of crystalline domains without strain fields, the FWHM of the scattering rods of a certain species is inversely proportional to the domain size of the said species. Strictly speaking, this theory only gives a qualitative description of RHEED measurements, but for the sake of simplicity we will restrain from invoking complex effects accounted for by a dynamical diffraction theory.

The FWHM of the Re streak (not shown) is unchanged from cycle 2 to cycle 10 and amounts to  $\simeq 0.40 \text{ \AA}^{-1}$ . In principle, assuming that Re domains extend over  $\simeq 100 \text{ nm}$ , we would expect a FWHM around  $0.006 \text{ \AA}^{-1}$  (as a first approximation, we can consider that the size of structurally coherent domains equals  $2\pi/\text{FWHM}$ ). The observed broadening is in fact also attributed to other effects, the coherence length of the electron beam and instrumental effects. More specifically, we consider that every observed streak (associated with a FWHM  $W$ ) is the convolution of a streak whose FWHM is related to the domain size of the material (and limited by the coherence length of the electron beam)  $w$  with a contribution of instrumental origin ( $\omega$  FWHM). We assume the following relationship:  $W^2 = w^2 + \omega^2$  (1), where  $\omega = \alpha \times w$ . The  $\alpha$  parameter is set by the coherence length  $l_c$  of the electron beam [131], which amounts to approximately  $20 \text{ nm}$ . Precisely, we assume that the FWHM  $w$  related to Re domain sizes equals  $2\pi/l_c$  (*i.e.*  $0.03 \text{ \AA}^{-1}$ ), as the  $\simeq 100 \text{ nm}$  size of the structurally-coherent Re(0001) domains is larger than the coherence length of the electron beam. It comes  $\alpha \simeq 13$  ( $0.40 \text{ \AA}^{-1}/0.03 \text{ \AA}^{-1}$ ). From  $w$  determined using relationship (1), we assess the size of graphene and moiré structurally coherent domains as  $2\pi/w$  (this estimate of the size only applies when the size is smaller than  $l_c$ ). Moiré domain sizes are shown in relative units. Indeed, the moiré streaks used for the analysis correspond to the intersection of the Ewald's sphere with moiré truncation rods in the second Laue zone. There, the coherence length of the electron beam is different from the one in the first Laue zone. Consequently we cannot rely, for moiré streaks, on the width of the first Laue zone Re streaks as a reference.

As seen in Figure III.3(a), the size of graphene domains increases from cycle 2 to 4 and is then constant until cycle 10. It goes from  $19 \text{ nm}$  on average during the second TPG cycle to  $22 \text{ nm}$  during cycles 4 to 10, which corresponds to a 20% increase. In fact, above cycle 4, we may consider that the graphene size exceeds the coherence length of the electron beam, and cannot be assessed – we hence provide here a lower limit estimate of the domain size. The increasing size of graphene domains is in agreement with the commonly accepted growth scenario. At the beginning of graphene growth, graphene forms small islands. Then, graphene islands progressively increase in size and no additional graphene island is formed – the nucleation regime is over, presumably because the distance between graphene islands becomes lower than the surface diffusion length of the carbon adspecies serving as building blocks during growth.



**Figure III.4: Increasing ordering among graphene domains revealing by STM.** Scanning tunneling topographs of graphene-covered Re(0001) after (a) one TPG cycle, and (b) two TPG cycles. (a)  $I_t = 4 \text{ nA}$ ,  $V_t = 0.01 \text{ V}$ ,  $T = 300 \text{ K}$ . (b)  $I_t = 2 \text{ nA}$ ,  $V_t = 1 \text{ V}$ ,  $T = 300 \text{ K}$ .

As for the size of moiré domains, the increase is clear and runs from cycle 2 to cycle 10, with an overall increase amounting to 15% (Figure III.3(b)). The increasing size of moiré domains is consistent with the increasing size of graphene domains although it does not saturate *i.e.* it does not increase beyond the coherence length of the electron beam. Structurally coherent moiré domains are therefore smaller



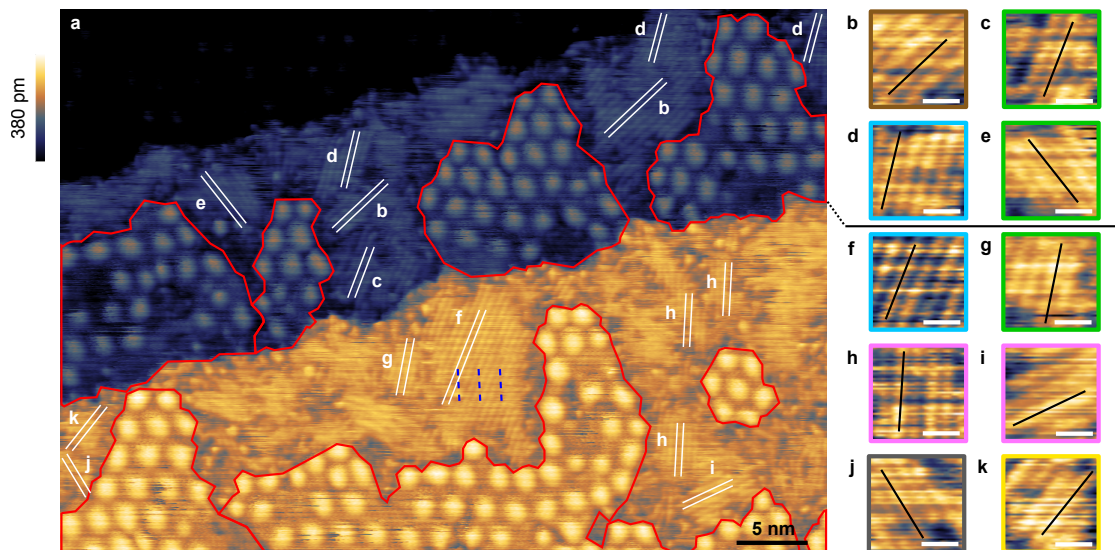
than structurally coherent graphene domains. In other words, graphene domains present distinct moiré structures separated by domain walls across which the structural coherence of graphene is preserved. An increasing ordering among graphene domains occurring during the TPG cycles is evident when comparing Figure III.4(a) and Figure III.4(b) which show STM images taken after one and two TPG cycles, respectively. Graphene is less defective and exhibits a lower variety of moiré superlattice orientations after two TPG cycles (Figure III.4(b)) than after one TPG cycle (Figure III.4(a)). The re-organization of the graphene lattice, which may include the incorporation of small size-selective carbon clusters within graphene and the healing of point defects such as C monovacancies probably contributes to the increasing size of moiré domains observed in RHEED, together with the contribution stemming from the overall increasing size of graphene domains. Our measurements are consistent with LEED measurements reported in Ref. [45], where the diffraction spots associated with the moiré periodicity were found to increase in intensity at each TPG cycle. Here we provide a semi-quantitative analysis of the increased ordering in graphene.

Overall, graphene domain sizes extracted with RHEED measurements seem consistent with the STM observations: structurally coherent graphene domains cover 15-20 nm in the early stages of graphene growth. In conclusion, we have shown that increasing the number of TPG cycles contributes positively to growing high-quality extended graphene domains.

## 2 Coexistence of graphene and rhenium carbide

A second sample was prepared as follows. First, a TPG-CVD method was performed, consisting of five cycles between 520 K and 870 K (four cycles under an ethylene pressure of  $P_{\text{C}_2\text{H}_4} = 1 \cdot 10^{-7}$  mbar and one in absence of  $\text{C}_2\text{H}_4$ ). Then, the sample was annealed for 1 h at 870 K.

### 2.a STM observations



**Figure III.5: Direct imaging of coexisting graphene and surface carbide domains.** (a) Scanning tunneling topograph of a Re(0001) surface with coexisting graphene and surface carbide phases.  $I_t = 2$  nA,  $V_t = 1$  V,  $T = 300$  K. Solid red and white lines indicate graphene grain boundaries and the parallel atomic rows of the rhenium carbide phase, respectively. Blue dashed lines highlight the modulation of apparent height observed for one specific variant of the carbide phase. (b-k) Close-up views (scale bars = 1 nm) of the ten carbide phase variants identified in (a), where (b-e) are the variants identified in the lower terrace, and (f-k) are the variants identified in the upper terrace. Black lines highlight the atomic rows. Variants are grouped together in families of specific atomic arrangements, with matching frames' colors.



Figure III.5(a) shows an STM image with coexisting graphene patches (easily recognizable from their moiré patterns) and another surface structure, appearing as domains of parallel rows separated by about 0.5 nm. As we will see, the latter structure is assigned to a rhenium carbide.

Graphene domains extend over a few nanometers to few tens of nanometers and cover  $\simeq 40\%$  of the surface. They exhibit local variations in the moiré superlattice parameter ( $\simeq 1.7\text{-}2.5$  nm) and orientation. Grain boundaries between graphene crystallites and their edges are indicated as red lines in Figure III.5(a). The disorder observed in the graphene lattice can be explained by the formation under kinetic control of small size-selective carbon clusters, which act as obstacles to graphene growth [159]. Small-size rounded shapes are visible across the surface and in particular at the edges of graphene domains, supporting the claim that carbon clusters have confined the extension of graphene domains and locally strained and disrupted the graphene lattice.

The observed disorder could also be related to the competitive formation of rhenium carbide. The carbide forms domains (highlighted with solid white lines in Figure III.5(a)), with different well-defined crystallographic orientations, and sizes that are generally smaller than those of the graphene domains. The carbide surface coverage, 30% in the preparation conditions we have chosen, is only slightly lower than the graphene coverage. We thus expect a strong contribution to the diffraction patterns measured with RHEED, which indeed exhibit other streaks than those of graphene and its moiré pattern (Figure III.6, see next subsection).

Disordered structures corresponding neither to graphene nor to the ordered rhenium carbide phase are observed across the surface. They are attributed to a disordered rhenium carbide phase. Finally, structures of intermediate order, such as merging atomic rows with different orientations (see bottom right corner of Figure III.5(a)), are visible.

## 2.b RHEED patterns

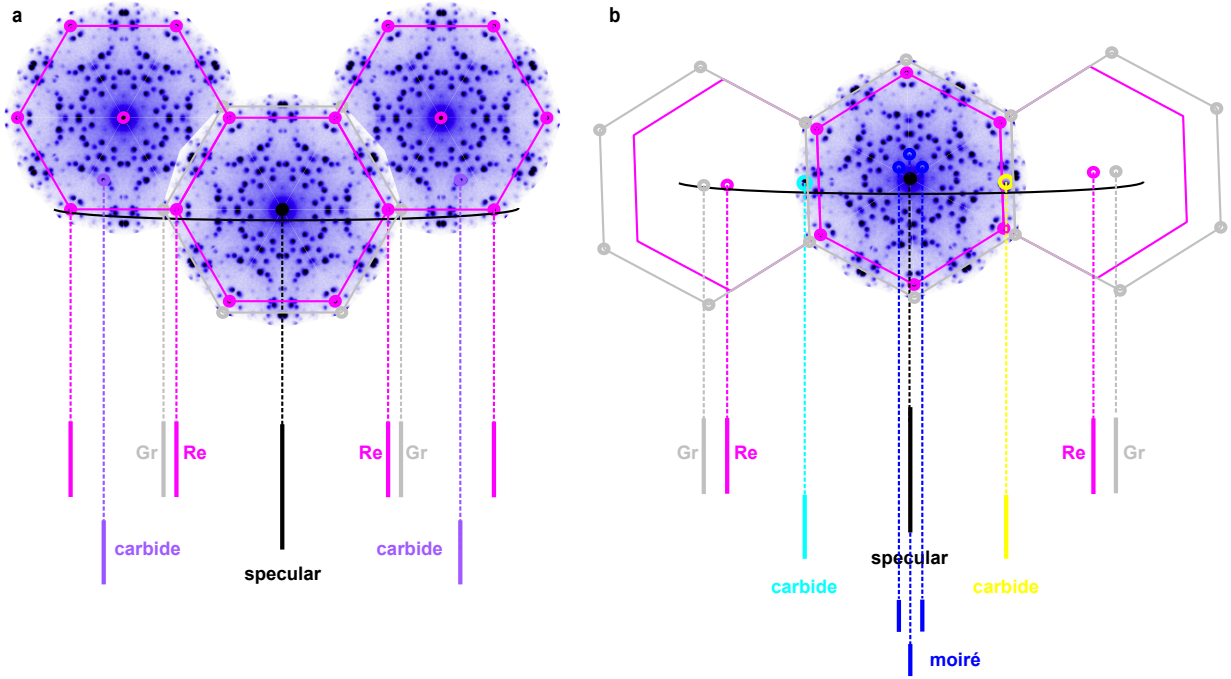
Figure III.6(a,b) shows RHEED patterns taken along the  $[11\bar{2}0]$  and  $[01\bar{1}0]$  incident azimuths, respectively. These RHEED patterns were acquired with an electron beam energy of 17 keV (Figure III.6(a)) and 19 keV (Figure III.6(b)). Both RHEED patterns exhibit other streaks than graphene, rhenium and moiré streaks, which are expected for graphene-covered Re(0001). The additional streaks (purple, light blue and yellow streaks) are assigned to the  $(7 \times \sqrt{19})$  surface carbide phase. We make use of LEED measurements performed on the  $(7 \times \sqrt{19})$  rhenium carbide phase [45] for the assignment of the latter streaks. The LEED patterns shown in Figure III.6 were adapted from Ref. [45]: the bottom left distortion-free region of the LEED pattern measured by Miniussi *et al.* was used to reconstruct a full distortion-free LEED pattern. The RHEED pattern shown in Figure III.6(b) was taken slightly out of the highest-symmetry azimuth. As a result, we observe different contributions from two streaks assigned to surface carbide (light blue and yellow streaks) in the left- and right-hand parts of the RHEED pattern. The RHEED pattern presented in Figure III.6(a) does not show such asymmetry.

## 3 Structural variants of the ordered rhenium carbide phase

### 3.a $(7 \times \sqrt{19})$ unit cell of rhenium carbide

We address the various orientations of the ordered rhenium carbide phase. Ten variants were identified in Figure III.5(a) and close-up views are shown in Figures III.5(b-k). The rhenium carbide phase is described, using the Park-Madden notation, by the following matrix:

$$\begin{pmatrix} \vec{b}_1 \\ \vec{b}_2 \end{pmatrix} = \begin{pmatrix} 7 & 0 \\ 2 & 5 \end{pmatrix} \begin{pmatrix} \vec{a}_1 \\ \vec{a}_2 \end{pmatrix}$$



**Figure III.6: Periodic features observed in RHEED on coexisting graphene-covered Re(0001) and surface carbide.** RHEED patterns of coexisting graphene and surface carbide phases along the (a)  $[11\bar{2}0]$  and (b)  $[01\bar{1}0]$  incident azimuths. Vertical coloured lines indicate the specular (black), Re (pink), graphene (grey), moiré (dark blue) and surface carbide (purple, light blue and yellow) streaks. LEED measurements performed on surface carbide [45] and Re and graphene reciprocal space are represented above the RHEED patterns. For both highest-symmetry directions, a cut of the Ewald’s sphere is indicated with a black horizontal line. The streaks observed in RHEED are assigned in correspondence with LEED measurements and graphene and Re reciprocal space. LEED measurements are reproduced and adapted from Ref. [45].

where  $\vec{b}_1, \vec{b}_2$  are the unit cell vectors of the overlayer, and  $\vec{a}_1, \vec{a}_2$  are the unit cell vectors of the Re(0001) lattice. The matrix relating rhenium carbide to the Re(0001) lattice was initially reported in Ref. [156], although there was no mention of a carbide phase yet. The structure, observed in LEED, was attributed to carbon. It was later assigned to a surface carbide by Miniussi *et al.*, in Ref. [45], and similar LEED measurements were presented. The overlayer forms a  $(7 \times \sqrt{19})$  structure. A ball-and-stick model of all possible configurations of the  $(7 \times \sqrt{19})$  unit cell of rhenium carbide, is depicted in Figure III.7. Both sides of a Re(0001) step-edge are presented, as the “type” of terrace (type A or B, see below) is of importance when determining the equivalence of unit cells. Re is a hcp crystal, *i.e.* a stacking of close-packed atomic planes along the  $[0001]$  direction, labelled as ABABAB... On both sides of an atomic step-edge are found an A plane and a B plane. This different labelling accounts for the two-fold symmetry relating an A plane to a B plane. It essentially consists in a  $180^\circ$ -rotation applied to the substrate that inverts the hcp and fcc hollow sites, as seen in Figure III.7. Within a terrace, equivalent configurations are constructed using  $120^\circ$ -rotations. Through a step-edge, the equivalence is preserved via mirror symmetry along a highest-symmetry direction of the Re(0001) lattice. We find that each terrace presents two sets of three equivalent configurations, whose unit cells are drawn in Figure III.7 with, respectively, thick and thin white lines (thin lines are only partially visible as they are partially covered with thick lines). Each set has an equivalent set in the other terrace (there is a two-by-two correspondence). In total, two groups of six equivalent domains (three domains per terrace) are found. These two groups “superimpose” perfectly when the second topmost plane of Re is disregarded. In other words, they form the same reconstructions, although they are not equivalent in terms of binding sites.

This pair of seemingly identical six-domain groups results in a six-domain LEED pattern, as reported in Refs. [45, 156]. It was described in Ref. [45] as the superposition of three domains rotated by  $120^\circ$  from each other, each having two subdomains related by an in-plane rotation of  $\simeq 12^\circ$ . The observation of

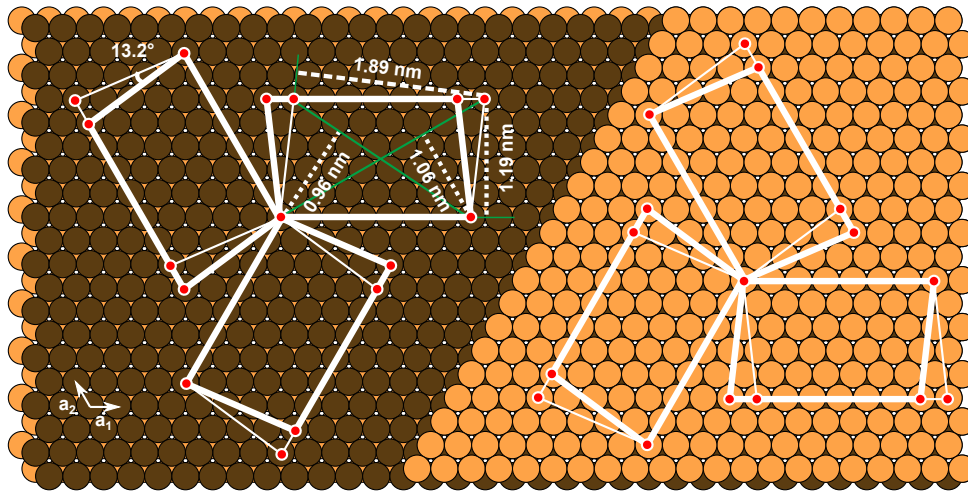


Figure III.7: **Ball-and-stick model of all possible configurations of the  $(7 \times \sqrt{19})$  unit cell of rhenium carbide, on both sides of a Re(0001) step-edge.** For each terrace, there are two sets of three equivalent configurations. The equivalence of configurations is indicated by the thickness of the unit cells. The periodicities associated with the  $(7 \times \sqrt{19})$  unit cell are indicated.  $\vec{a}_1$  and  $\vec{a}_2$  are the unit cell vectors of the Re(0001) lattice.

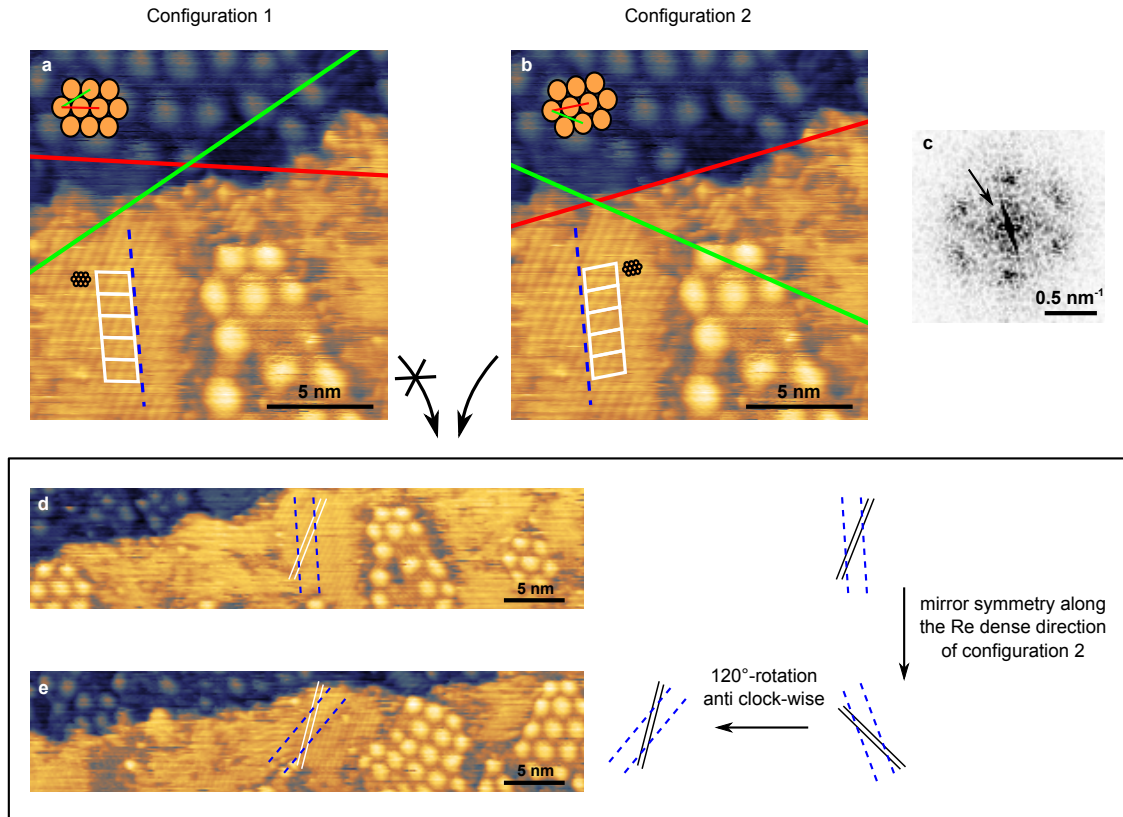
so-called LEED subdomains is related to the mirror symmetry along the highest-symmetry directions of the Re(0001) lattice.

### 3.b Grouping variants in six-fold families of equivalent domains

With all the possible configurations of the unit cell in mind, we can now group the ten variants identified in Figure III.5(a) in six-fold families of equivalent domains, each family having a specific atomic arrangement. To do so, we must first find a clear indication of the Re(0001) substrate orientation, as the mirror operation should only be performed along one of the two highest-symmetry directions of the Re(0001) lattice, namely the  $[11\bar{2}0]$  and  $[01\bar{1}0]$  directions (which will be referred to, from now on, as the Re “dense” and “not-so-dense” directions, respectively). The substrate atomic step-edge observed in Figure III.5(a) could be a low energy one, aligned along one of the two highest-symmetry directions of the Re(0001) lattice. This would implicitly tell the in-plane orientation of the surface. However, we cannot exclude that impurities attached to the step-edges or a too low preparation temperature (1570 K here) prevent the substrate from adopting exclusively lowest-energy configuration step-edges. We prefer to make use of another information that will lift this ambiguity: the modulation in apparent height along the atomic rows of one variant of the carbide phase forms lines with a well-defined orientation (blue dashed lines in Figure III.5(a)) and is, as we will see, insightful in this respect.

We assign this modulation in apparent height to the rhenium carbide unit cell itself. Indeed, the blue dashed lines are separated by 1.8 nm in the STM image, close to the 1.89 nm periodicity associated with the large dimension of the  $(7 \times \sqrt{19})$  unit cell (Figure III.7) – an explanation for the origin of the lower apparent height along the blue dashed lines will be provided later in the text. Assuming that the carbide unit cell in this particular region is oriented along the blue dashed lines, the Re(0001) lattice oriented such as in Figure III.7 is  $6.6^\circ$ -rotated ( $13.2^\circ/2$ ) with respect to the blue dashed lines (see the  $13.2^\circ$ -angle in Figure III.7). It is rotated either clock-wise or anti clock-wise, both cases being considered in Figures III.8(a) and III.8(b), respectively. The resulting (different) orientations of the Re(0001) lattice are represented in Figures III.8(a,b). Green and red lines represent the highest-symmetry directions of the resulting Re(0001) lattice, closest to the step-edge orientation. If the case depicted in Figure III.8(a) (configuration 1) is the right configuration, then the step-edge is not well-oriented along any of the highest-symmetry directions, neither a dense direction (red line) nor a not-so-dense direction (green line). Conversely, the case depicted in Figure III.8(b) (configuration 2) is consistent with a step-edge oriented along the dense direction (the red line is oriented along the step-edge).

To determine which of the two configurations (1 or 2) is the right configuration we make use of a large scale image that presents the upper terrace already shown in Figure III.5(a) and another terrace covered with rhenium carbide and showing, locally, a similar modulation in apparent height as the one observed for the variant “f” in Figure III.5(a). These two regions are shown in Figure III.8(d,e). We find that only the configuration 2 (Figure III.8(b)) is consistent with the observation of both these two regions. It appears that these regions are equivalent upon a combination of  $120^\circ$ -rotation and mirror symmetry along the dense direction of the Re(0001) lattice. It was not possible to find a similar set of geometrical transformations that would relate the two regions with the configuration 1. In other words, the configuration 2 is the right configuration, hence the step-edge is oriented along the dense direction of the Re lattice.



**Figure III.8: Comparison of the two possible unit cell configurations for the variant presented in Figure III.5(f).** (a,b) Close-up views of the scanning tunneling topograph shown in Figure III.5(a). The Re(0001) lattice is either  $6.6^\circ$ -rotated (a) clock-wise or (b) anti clock-wise with respect to the unit cells orientation (blue dashed lines). For each configuration (1 and 2), unit cells are represented with solid white lines and are rotated to match the direction of lower apparent height (blue dashed line). The resulting (different) orientations of the Re(0001) lattices are represented, at scale, close to the unit cells, and in closer views in the top left corners of (a) and (b). Green and red lines represent the highest-symmetry directions of the resulting Re(0001) lattices. (c) Fast Fourier transform of the larger-scale image shown in Figure III.5(a), revealing the first moiré harmonics and the step-edge-related harmonic (line pointed with an arrow). Bottom part: (d,e) Scanning tunneling topographs of the two regions showing carbide atomic rows associated with a modulation of apparent height. A sketch of the operations relating the two regions and obtained using the configuration 2 is shown.

As a side note, we would like to point out that the highest-symmetry directions of the moiré and Re(0001) lattices do not align. The fast Fourier transform shown in Figure III.8(c) reveals the first moiré harmonics and an oblique line (pointed with an arrow) related to the step-edge direction. We know from the previous argument that the step-edge is oriented along the dense direction of the Re(0001) lattice. Since the moiré lattice is misaligned with respect to the step-edge, the moiré and Re(0001) lattices do not align. The misalignment of the moiré lattice with respect to the Re(0001) lattice amounts to  $12^\circ$  (the coincidence with the  $12^\circ$ -angle mentioned earlier and measured by Miniussi *et al.* is fortuitous). This misalignment is not a surprise, since a variety of orientations and strains were already found in this system [44, 3, 49] and is in fact related to the small energy difference between distinct coincidence (moiré)

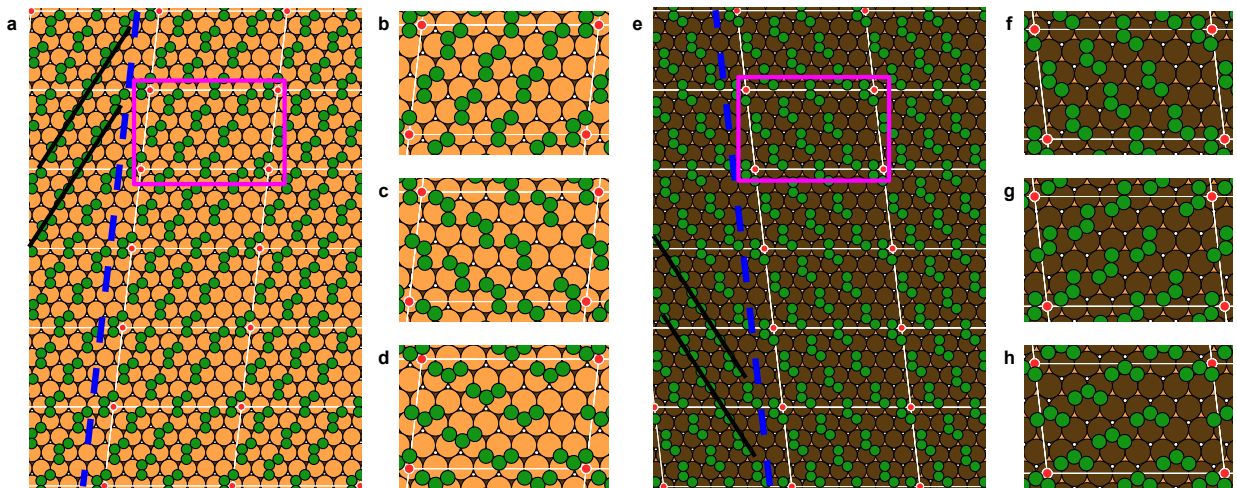


structures of graphene on the metal surface. Kinetic hindrance to the alignment of a given graphene domain towards the lowest-energy coincidence structure is a possible interpretation too. With STM we hence expect to image graphene domains with different kinds of orientations/strains across the surface.

Now that the Re lattice crystallographic directions are unambiguously identified, families of specific atomic arrangements are constructed as follows. Variants are grouped via  $120^\circ$ -rotations within a terrace, and via mirror symmetries along the highest-symmetry directions of the Re(0001) lattice between terraces. Overall, we find six families of equivalent atomic arrangements, each associated with a different color matching the frames' color of the variants depicted in Figure III.5(b-k).

## 4 Possible atomic structures of the ordered rhenium carbide phase

We now turn to the possible atomic structures of rhenium carbide. We focus on the family of variants comprising the variant that exhibits a modulation of apparent height (referred to as family 1 from now on, and indicated with light blue frames in Figure III.5), as it is the only family for which the atomic rows' orientation with respect to the unit cell is known.



*Figure III.9: Possible atomic structures associated with family 1 of rhenium carbide, assuming that the upper terrace is an A plane.* (a) Ball-model on the upper terrace (A plane). (b) Close-up view at the rectangle shown in (a). (c,d) Close-up views with carbon trimers individually rotated to match the two other possible hcp-fcc-hcp sequences. (e) Ball-model on the lower terrace (B plane). (f) Close-up view at the rectangle shown in (e). (g,h) Close-up views with carbon trimers individually rotated to match the two other possible hcp-fcc-hcp sequences. (a,e) The solid black lines and the blue dashed lines indicate the atomic rows of family 1 and the associated modulation of apparent height observed in STM, respectively.

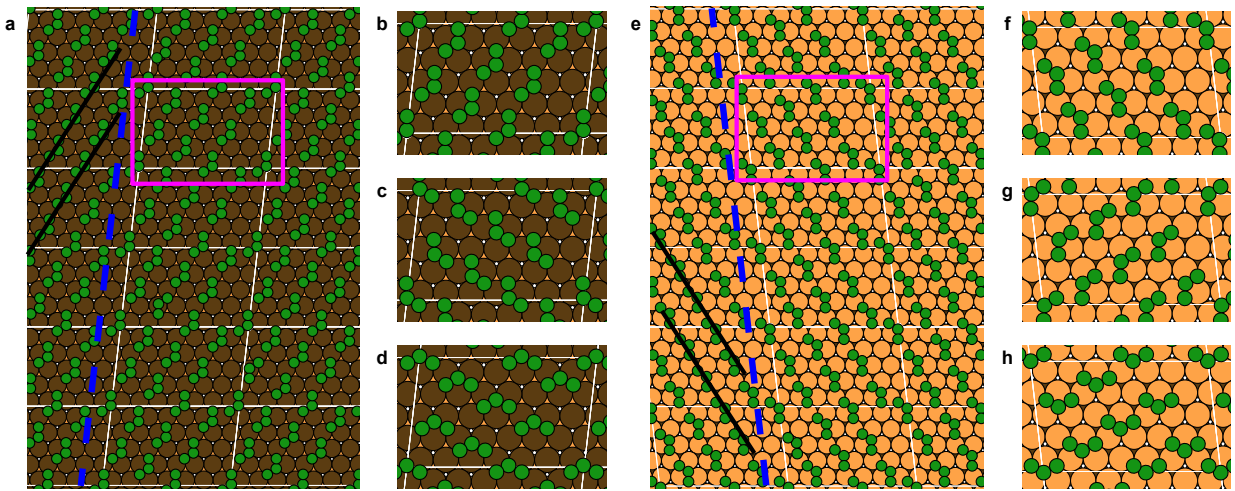
Although the STM image presented in Figure III.5(a) reveals an atomic-scale contrast, it does not directly unveil the atomic arrangement of rhenium carbide. Figures III.9 and III.10 present possible atomic arrangements for family 1. Atomic arrangements were constructed using trimers of carbon atoms adsorbed in adjacent sites in an hcp-fcc-hcp sequence. This choice is driven by the finding of a specific core level shift observed in the Re  $4f_{7/2}$  spectra, that could only be rationalised by invoking carbon trimers arranged in this precise sequence [45].

Figure III.9(a) shows a ball-model for family 1 assuming that the upper terrace (which features the observed modulation in apparent height) is an A plane (orange plane). Carbon trimers arranged in an hcp-fcc-hcp sequence form parallel rows, aligned along the direction indicated with solid black lines. These rows are presumably responsible for the atomic-scale contrast observed in Figure III.5(a) (parallel rows highlighted with solid white lines, separated by  $\simeq 0.5$  nm). The trimer rows present a “lack” of trimers along the direction indicated with a blue dashed line. This “lack” of trimers is due to the orientation’s

breaking of trimer rows, which is necessary to comply with the unit cell of rhenium carbide. It presumably accounts for the lower apparent height along the blue dashed lines indicated in Figure III.5(a). The absence of a modulation in apparent height for the variant “d” observed in the lower terrace (which is the other variant belonging to family 1) is attributed to the lower spatial extension of the said variant, in the three locations where it is visible (see Figure III.5(a)).

Figures III.9(c,d) present similar ball models for family 1 as the one presented in Figure III.9(a) but with carbon trimers individually rotated to match the two other possible hcp-fcc-hcp sequences. We emphasize that in figures III.9(c,d), carbon trimers are individually rotated. The unit cell is not rotated, hence the rows of carbon trimers are still oriented along the solid black lines indicated in Figure III.9(a). Still, the ball-model presented in Figure III.9(a) (and in the close-up view shown in Figure III.9(b)) is more likely to be responsible for our observations, as carbon trimers are individually aligned along the orientation of the rows.

Figures III.10(a-d) depict ball-models for family 1 assuming that the upper terrace is now a B plane (brown plane). Similar observations can be made.



*Figure III.10: Possible atomic structures associated with family 1 of rhenium carbide, assuming that the upper terrace is a B plane.* (a) Ball-model on the upper terrace (B plane). (b) Close-up view at the rectangle shown in (a). (c,d) Close-up views with carbon trimers individually rotated to match the two other possible hcp-fcc-hcp sequences. (e) Ball-model on the lower terrace (A plane). (f) Close-up view at the rectangle shown in (e). (g,h) Close-up views with carbon trimers individually rotated to match the two other possible hcp-fcc-hcp sequences. (a,e) The solid black lines and the blue dashed lines indicate the atomic rows of family 1 and the associated modulation of apparent height observed in STM, respectively.

The ratio of the numbers of carbon atoms lying on a fcc site with respect to carbon atoms lying on an hcp site (within a unit cell) amounts to 0.5, in good agreement with the intensity ratio between the two C 1s core level components measured for rhenium carbide (0.57) in Ref. [45].

## Conclusions

We have investigated the structure of graphene and a surface carbide grown on the (0001) surface of Re(0001), using RHEED and STM. The number of TPG annealing cycles is found to positively contribute to growing high-quality extended graphene domains. STM images of coexisting graphene domains and surface carbide domains attributed to the  $(7 \times \sqrt{19})$  overlayer are reported for the first time. The various orientations of the surface carbide domains are addressed, and variants are grouped in six-fold families of equivalent domains, each family having a specific atomic arrangement. Three atomic models are constructed for one of these families, with structural constraints based on previous XPS measurements [45]. These models account for the STM and electron diffraction measurements. In particular, they reproduce

the atomic-scale contrast in the form of parallel atomic rows, and the modulation in apparent height at the scale of the ( $7 \times \sqrt{19}$ ) unit cell observed in STM images. We plan on verifying the stability of the three atomic models proposed for surface carbide *via* DFT calculations. DFT should also inform us on a possible hierarchy (in energy) among the models.

# DEPRESSIONS BY STACKING FAULTS IN NANORIPPLED GRAPHENE ON METALS

## Contents

---

1	Moiré superlattice, vacant hills and relationship with atomic stacking . . . . .	<b>66</b>
1.a	Geometrical features of the moiré superlattice . . . . .	66
1.b	Atomic resolution of the vacant hill defect . . . . .	67
2	BOP simulations and comparison with STM observations . . . . .	<b>67</b>
2.a	BOP simulations . . . . .	67
2.b	Comparison with STM observations . . . . .	67
3	Discarded defect structures . . . . .	<b>69</b>
3.a	Rotated nano-grains . . . . .	69
3.b	Vacancies in the carbon lattice . . . . .	69
3.c	Vacancies in the metal lattice . . . . .	70
4	Possible defect candidates . . . . .	<b>71</b>
4.a	Stacking faults in the metal lattice . . . . .	71
4.b	Moiré dislocations . . . . .	71
4.c	Stacking faults in the carbon lattice . . . . .	72
5	On the possible origin of the vacant hill defects . . . . .	<b>75</b>
6	Electronic properties of the vacant hills . . . . .	<b>76</b>
6.a	Local conductance measurements . . . . .	76
6.b	DFT calculations . . . . .	76

---



## Abstract

A broad variety of defects has been observed in two-dimensional materials. Many of these defects can be created by top-down methods such as electron irradiation or chemical etching, while a few of them are created along bottom-up processes, in particular during the growth of the material, in which case avoiding their formation can be challenging. This occurs *e.g.* with dislocations, Stone-Wales defects, or atomic vacancies in graphene. Here we address a defect that has been observed repeatedly since 2007 in epitaxial graphene on metal surfaces like Ru(0001) and Re(0001), but whose nature has remained elusive thus far. This defect has the appearance of a vacant hill in the periodically nanorippled topography of graphene, which comes together with a moiré pattern. Based on atomistic simulations and STM/STS, we argue that such defects are topological in nature and that their core is a stacking fault patch, either in graphene, surrounded by loops of non-hexagonal carbon rings, or in the underlying metal. We discuss the possible origin of these defects in relation with recent reports of metastable polycyclic carbon molecules forming upon graphene growth. Like other defects, the vacant hills may be considered as deleterious in the perspective of producing high quality graphene. However, provided they can be organized in graphene, they might allow novel optical, spin, or electronic properties to be engineered.

The study presented in this Chapter is the result of a collaborative work initiated and led by Alexandre Artaud (CEA/Institut Néel, Grenoble), with Georg Daniel Förster (LEM, Grenoble), Florent Calvo (LIPhy, Grenoble) and Laurence Magaud (Institut Néel, Grenoble) [160]. My contribution consisted mainly in sample preparation and low temperature STM/STS measurements (Figure IV.10), as well as the corresponding data analysis and taking part in discussing the outcomes of DFT calculations.

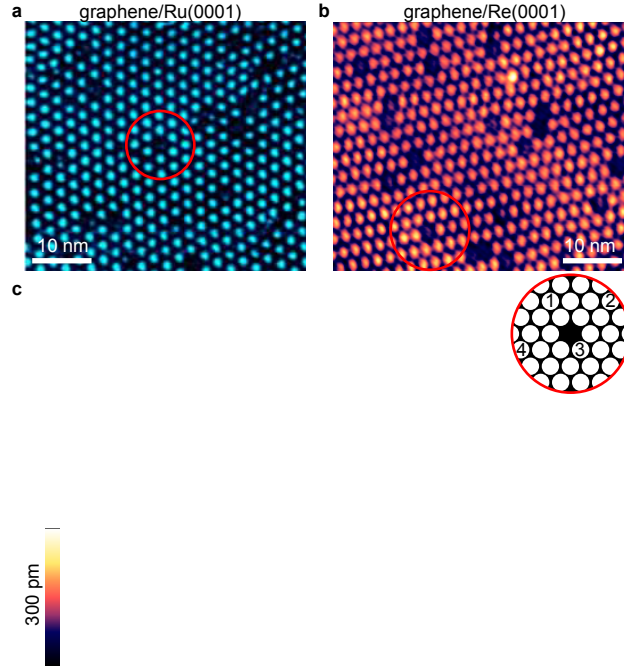
## Introduction

As recalled in Chapter I, epitaxial ultrathin films often form superstructures due to the lattice mismatch or disorientation with their substrate. Two-dimensional (2D) materials like graphene [161, 162, 54, 46], boron nitride [163, 164], or transition metal dichalcogenides [165, 166] are no exception. Some of these superstructures are called moiré patterns, in an analogy with optics. In the case of 2D materials, the strong internal bonds together with low bending rigidity are responsible for a natural rippling, whose in-plane period is the moiré pattern lattice parameter, *i.e.* a few nanometers given the typical lattice mismatch with the substrate. Borrowing now the language of geology, the moiré patterns of 2D materials are associated with a hill-and-valley topography.

The relative height of the hills and valleys depends on several factors. Especially, a stronger interaction between the 2D material and the substrate imposes lower valleys, as extensively discussed in the case of graphene on metals [51, 52]. The distinctive bending and binding at hills and valleys have numerous consequences on the properties of graphene (and, presumably, of other epitaxial 2D materials, too). For instance, the electronic band structure of graphene develops replicas of Dirac cones and mini-bandgaps [53], its work function is larger at the location of the hills [167], its chemical reactivity is different at hills and valleys [168, 169, 170]. Disorder in the hill-and-valley topography may thus have important consequences on these properties.

One specific kind of disorder is often encountered in graphene on metals, namely a depression in the pattern of hills spawned by the moiré (Figure IV.1). This defect, which we call a “vacant hill”, is seen in most scanning tunneling micrographs, whatever the measurement conditions [62, 171, 172, 173, 174, 175, 176, 177, 178, 179], of graphene grown on one of the prominent metal surfaces used to produce large-area high quality graphene, Ru(0001) [63, 174]. The same defect is observed in graphene grown on Re(0001) [3, 150], and possibly as well on Rh(111) [180, 87], two similar systems in terms of graphene-metal interaction strength [44]. However, to the best of our knowledge, it has not been

seen on other metal surfaces.



**Figure IV.1: Depressions in the pattern of hills, in graphene/Ru(0001) and graphene/Re(0001).** Scanning tunneling topographs of graphene prepared on (a) Ru(0001) and (b) Re(0001), revealing a significant density of defects (circled in red) in the moiré lattice. (c) Three-dimensional view of (b), highlighting the hill-and-valley nanorippled surface associated with the moiré lattice, and the defects appearing as vacant hills. (b,c) Graphene growth was performed on a rhenium thin film, following the procedure described in Section 1.c. A closed-path ‘1-2-3-4’ around one vacant hill is schematized in the inset. (a) is reproduced from Ref. [179].

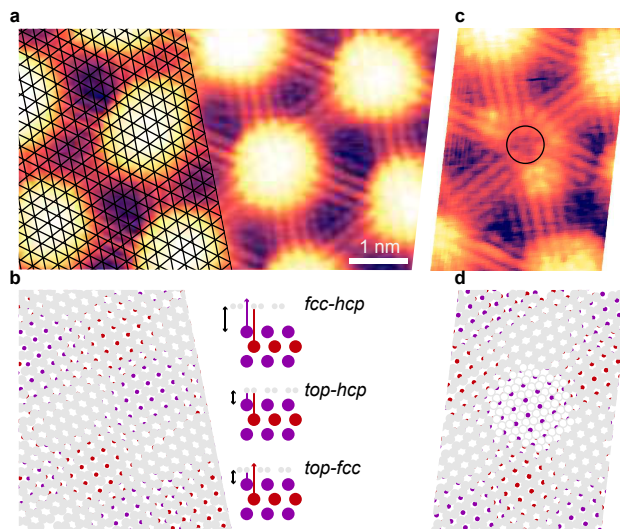
Much like with any other defect, reducing the density of vacant hills is desirable for many applications. This is presumably needed to achieve pure band-like electronic and phononic properties, or to increase the degree of ordering in 2D lattices of nanoparticles self-organized on the graphene/Ru(0001) or graphene/Rh(111) moirés [175, 181, 182, 183, 184, 185, 186, 187, 188]. Additionally, vacant hills seem also to be entry points for the intercalation of oxygen between graphene and Ru(0001) [179]. This is obviously a shortcoming in the prospect of fully impermeable membranes or protective coatings. Yet such pathways have already been exploited to decouple graphene from its substrate and to create highly stretched graphene nanobubbles with strong, Landau-level-like intrinsic electronic resonances [179].

The question that we focus on here has remained open since the first STM images of graphene/Ru(0001) were published in 2007 [62, 171], and a few years later in graphene/Rh(111) [180] and graphene/Re(0001) [3]: What is the nature of the vacant hill? The answer to this question is missing because the available observations are unable to reveal the atomic structure. Our strategy is to consider different classes of atomic structures involving deviations to the perfect atomic lattices of the metal surface or graphene. Such a survey has been so far out of reach of DFT calculations in reason of the prohibitive computing time required to address already a few of the candidate structures. Instead, we use molecular dynamics simulations based on a parametrized BOP to explore a variety of structures, and DFT calculations too in the case of simple structures. The confrontation of the simulation results to high resolution STM/STS data leads to the conclusion that at the center of the vacant hills, the stacking of carbon atoms on the substrate differs from that found at a regular hill. The vacant hill may then be seen as a stacking fault where bonding to the substrate is stronger. Possible structures feature a stacking fault either in the metal surface or in the graphene lattice. In the latter case, loops of defects stitch the stacking fault to the surrounding graphene, and these loops comprise non-hexagonal carbon rings. In this sense, the vacant hills are topological defects and their electronic properties naturally differ from those of regular hills.

# 1 Moiré superlattice, vacant hills and relationship with atomic stacking

## 1.a Geometrical features of the moiré superlattice

Before addressing the vacant hill defect in itself, we briefly remind elementary geometrical features of the moiré pattern between graphene and a metal surface (for further details, we refer the reader to Section 2.b and to focused reports [47, 48, 49, 50]). Three high-symmetry stacking types are usually considered, namely *fcc-hcp* (location of a moiré hill), *top-hcp* and *top-fcc* (location of two inequivalent moiré valleys). For these three kinds of stacking the interaction between graphene and the substrate is different [51, 44, 52], thus the graphene-metal distance is different: this is what drives the nanorippling of graphene. The *fcc-hcp*, *top-hcp* and *top-fcc* regions are illustrated in Figure IV.2(c).



**Figure IV.2: Atomic-resolution of the moiré superlattice and the vacant hill defect, and relationship with atomic stacking.** (a,c) Atomic-resolution scanning tunneling topographs of graphene on Re(0001), revealing the moiré pattern (a) and a vacant hill defect (c). Part of (a) is overlaid with a grid whose vertices match the positions of C atoms of one of the two graphene sublattices. (b,d) Positions of the C atoms (grey balls) extracted from (a,c). In (d), the white balls with grey contour are the positions of C atoms extrapolated from the surrounding graphene lattice, *i.e.* in the absence of the vacant hill defect. The atomic positions in the two topmost Re layers have been refined to match the moiré pattern in (a,c) (hills appear in blue). The C/Re stackings for the three characteristic sites of the moiré, the two valleys (*top-hcp*, *top-fcc*) and the hill (*fcc-hcp*), are sketched with three side views.

These considerations help to rationalize the atomic resolution STM observations (Figure IV.2(a)) of the moiré pattern for graphene on Re(0001). Graphene growth was prepared on a Re(0001) single crystal. Re(0001) single crystal preparation and graphene growth procedures are described in Section 1.c and Section 1, respectively. For graphene growth, only two temperature-programmed growth-chemical vapour deposition (TPG-CVD) cycles were performed.

On top of the STM image shown in Figure IV.2(a), a grid whose vertices mark the positions of C atoms belonging to one of the two sublattices of graphene was overlaid [189, 49, 190]. To produce a geometrical construction of the moiré matching Figure IV.2(a), the two C sublattices were displayed and the periodicity and rotation of the two topmost planes of metal atoms were adjusted, both planes being simply in-plane shifted according to the hexagonal compact stacking in Re(0001). The result is shown in Figure IV.2(b). At the location of the *fcc-hcp* stacking, *i.e.* the location of a moiré hill, we only see through the graphene lattice the Re atoms of the topmost layer. At the location of the *top-hcp* and *top-fcc* stackings (which are two inequivalent moiré valleys), respectively no Re atom and the atoms from the second Re plane are seen through. Note that the present discussion can be directly transposed to the case of graphene on Ru(0001).

### 1.b Atomic resolution of the vacant hill defect

We now turn to atomic resolution imaging at the location of a vacant hill. A typical image is shown in Figure IV.2(c). It resembles the one published in Ref. [150]. Here we attempt to determine the positions of C atoms, just like what was achieved for graphene on Re(0001) in the absence of defects. Away from the defect site this task is rather straightforward. In contrast, at the defect location we are faced with the usual shortcomings of STM imaging: the details that we observe are both of topographic and electronic nature, and without *a priori* knowledge on the structure of the defect, determining the atomic positions is ambiguous. We therefore temporarily refrain to devise on the detailed nature of the defect. This is why in Figure IV.2(d), the carbon atoms are represented as open symbols at the location of the defect: these symbols correspond to an extrapolation of the perfect graphene lattice. We note, once more, that if graphene were perfect and the Re unperturbed there, then the C/Re stacking would be of *fcc-hcp* type (Re atoms of the topmost substrate plane seen through).

## 2 BOP simulations and comparison with STM observations

### 2.a BOP simulations

Using numerical simulations to model defects in the metal and graphene substrates, where the atomic structure of the regular lattice is altered over typically 1 nm, requires large calculation supercells (several thousands of atoms) without which spurious boundary effects would be likely present and difficult to evaluate. This is prohibitive for most DFT approaches. We use instead BOP calculations that allow thousands of atoms to be treated. A BOP potential has in fact been carefully parametrized for the Ru-C system [188] against the results of DFT calculations [65], and it was found to satisfyingly reproduce the structural parameters of the nanorippled graphene/Ru(0001) moiré. Interestingly, (0001)-terminated Ru and Re have strong electronic similarities, with in both cases *d* bands in the 2–4 eV range below the Fermi level [195, 60, 95]. This is possibly a reason why  $sp^2$ -hybridized carbon behaves very similarly on Ru(0001) and Re(0001): on both surfaces, similar small size-selective polycyclic clusters tend to form [196, 197, 159] and graphene is nanorippled with almost identical minimum and maximum graphene-metal distances [51, 44, 3, 61]. Hence, while an optimized BOP potential is not yet available for Re-C, we expect it to be very similar to the one presently used for Ru-C.

The bond-order potential parametrized for graphene on Ru(0001) combines the original BOP of Brenner for carbon [145] and the embedded-atom model of Li *et al.* [212] for ruthenium. Two versions of the BOP were originally designed, with and without dispersion corrections. Geometric properties predicted by DFT being in slightly better agreement with the latter, this version was chosen in the present work.

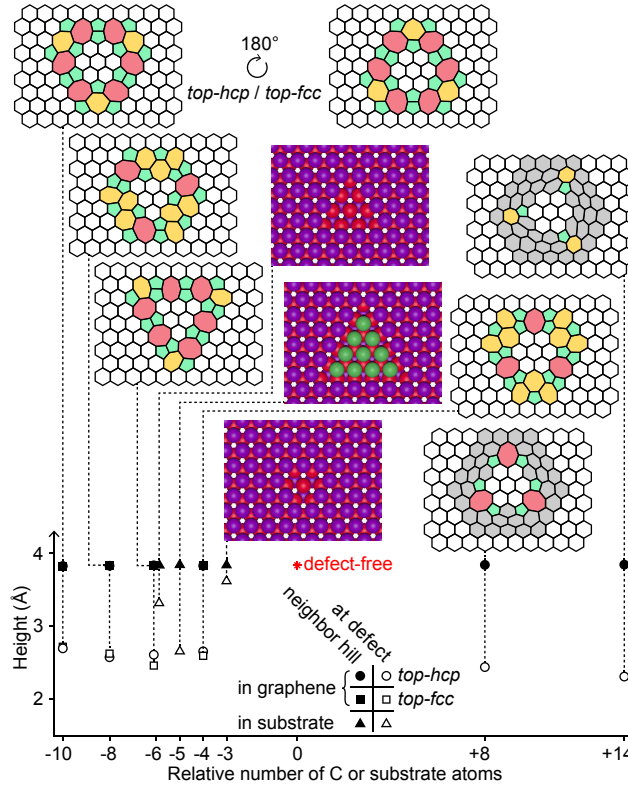
Lateral periodic boundary conditions were applied with a box dimension chosen such that the lateral graphene lattice constant is imposed at 2.497 Å [65]. The simulations were then conducted on the 12 on 11 moiré commensurability, where 12 graphene unit cells match 11 unit cells of the Ru(0001) surface lattice, thus setting the *hcp* lattice constant *a* of the metal to be 2.724 Å, letting the other lateral constant as free to accommodate better upon geometry optimization. Only three layers of ruthenium in ABA stacking were explicitly considered in all calculations.

The systems considered were vacant hills with different structure ( $1 \times 1$  supercell) possibly surrounded by regular hills (up to  $4 \times 4$  supercells in total), or a maximum number of 10416 atoms. After a short molecular dynamics trajectory at 300 K, the geometry of the entire system was locally minimized, and its structural details scrutinized.

### 2.b Comparison with STM observations

For all the structures simulated with a bond-order potential, the height of graphene with respect to the average height of the uppermost Ru(0001) metal plane (averaged away from the defect location) was

calculated both at the location of the defect and at the location of the neighbor hills. This allows a comparison with the apparent topography observed in STM images – the contribution from the electronic density of states to the apparent topography will be addressed later in the Chapter. Figure IV.3 shows a summary of the obtained results, with close-up views of the considered structures. We will often refer to this figure in the following sections.



**Figure IV.3: Summary of the results obtained using BOP simulations.** Height of graphene with respect to the average height of the uppermost Ru(0001) metal plane (averaged away from the defect location) at the location of a defect (open symbols) and of the neighbor hills (filled symbols), as function of the relative number of C or substrate atoms compared to the defect-free graphene or substrate. Two structures (*top-hcp*, *top-fcc*) have been considered for four of the defects in graphene (-10, -8, -6, -4 C atoms), rotated by 180° with one another.

location	$\Delta N$	supercell size stacking	$\times 1$		$\times 2$			$\times 3$			$\times 4$		
			$h_d$	$E_{ads}$	$h_d$	$h_n$	$E_{ads}$	$h_d$	$h_n$	$E_{ads}$	$h_d$	$h_n$	$E_{ads}$
none	0		3.84	12.5	3.84	3.84	12.5	3.84	3.84	12.5	3.84	3.84	12.5
graphene	-4	<i>top-fcc</i>	2.59	20.3	2.59	3.81	13.4	2.59	3.83	11.9	2.59	3.83	11.4
		<i>top-hcp</i>	2.65	20.9	2.65	3.80	13.5	2.65	3.82	12.1	2.65	3.83	11.5
graphene	-10	<i>top-fcc</i>	2.66	29.4	2.71	3.77	15.5	2.71	3.81	13.0	2.71	3.82	12.0
		<i>top-hcp</i>	2.71	29.3	2.70	3.79	15.3	2.70	3.82	12.8	2.70	3.83	12.0
graphene	-8	<i>top-fcc</i>	2.62	26.8	2.62	3.78	14.7	2.62	3.81	12.6	2.62	3.82	12.0
		<i>top-hcp</i>	2.57	26.2	2.57	3.78	14.6	2.57	3.81	12.6	2.57	3.82	12.0
graphene	-6	<i>top-fcc</i>	2.45	22.3	2.45	3.83	13.8	2.45	3.83	12.2	2.45	3.83	11.6
		<i>top-hcp</i>	2.60	21.6	2.60	3.82	13.7	2.60	3.83	12.1	2.60	3.83	11.6
graphene	+8	<i>top-hcp</i>	4.40	24.9	3.91	2.87	12.3	3.61	3.00	11.8	2.44	3.84	10.4
graphene	+14	<i>top-hcp</i>	3.89	16.9	3.85	3.19	15.4	3.11	2.91	12.8	2.30	3.84	9.0
metal	-3	<i>top-fcc</i>	3.62	12.2	3.62	3.83	11.5	3.62	3.84	11.1	3.62	3.84	11.0
metal	-6	<i>top-fcc</i>	3.37	11.3	3.32	3.85	11.3	3.32	3.84	11.1	3.32	3.84	10.9
metal	-5	<i>top-fcc</i>	2.65	13.2	2.65	3.85	11.7	2.65	3.84	11.3	2.65	3.84	11.1

**Table IV.1:** Hill height  $h_d$  (in Å) at the location of a defect on a *fcc-hcp* region of the moiré, and at the location of the neighbor (regular) hill ( $h_n$ ), together with adsorption energy  $E_{ads}$  (in meV). For each defect, the number of C or metal atoms relative to the defect-free structure ( $\Delta N$ ) is given. Different supercell sizes have been considered, whose size is expressed as multiples of a (11×11)-on-(12×12) moiré unit cell corresponding to graphene/Ru(0001).

The structures optimized *via* BOP simulations consist in defective graphene/Ru(0001) structures, with defects such as vacancies in the carbon/metal lattice and stacking faults in the carbon/metal lattice. Structures involving stacking faults in the carbon lattice comprise closed loops of non-hexagonal carbon rings surrounding the stacking fault.

Table IV.1 lists several quantities extracted from the BOP simulations for the defects considered in Figure IV.3.: the heights of graphene with respect to the average height of the topmost metal plane, at the location of the defect and at the location of the neighbor moiré hill, and the adsorption energy (energy difference between the potential energy of the system with graphene in interaction with the metal surface, and the energies of graphene and the metal optimized at a finite distance for which they do not interact), as a function of the size of the supercell used for the calculations.

Changing the size of the supercell puts in evidence that defects interact when they are close from one another, especially when they are first neighbors. The interactions translate in height variations from 1% to several 10% depending on the kind of defect, being especially large in the case of defects with an excess of C atoms.

### 3 Discarded defect structures

#### 3.a Rotated nano-grains

One important observation can be made to get further insight into the nature of the vacant hill. Within the circle drawn in Figure IV.2(c), we discern three to four hollow spots. These spots may correspond to the centers of carbon rings or to one of the two carbon sublattices, which can appear as hollow sites depending on the local graphene/metal stacking [51, 49]. Within the resolution of our image, the spacing between these spots is compatible with the graphene lattice parameter, and the spots seem to align along directions parallel to zigzag C rows in the surrounding graphene. Whether these spots lay or not on the vertices of the network of highest-symmetry lines of the surrounding graphene cannot be determined given the resolution of our STM image. For these few defect-related spots the triangulation procedure that we used to extract the position of C atoms of the defect-free graphene lattice [190] becomes unreliable.

This observation suggests that at the center of the defect, the carbon lattice is unrotated with respect to the surrounding graphene, although it is possibly in-plane shifted. This rules out an interpretation of the defect as a rotated nano-grain such as the ones observed in epitaxial graphene grown on silicon carbide [191].

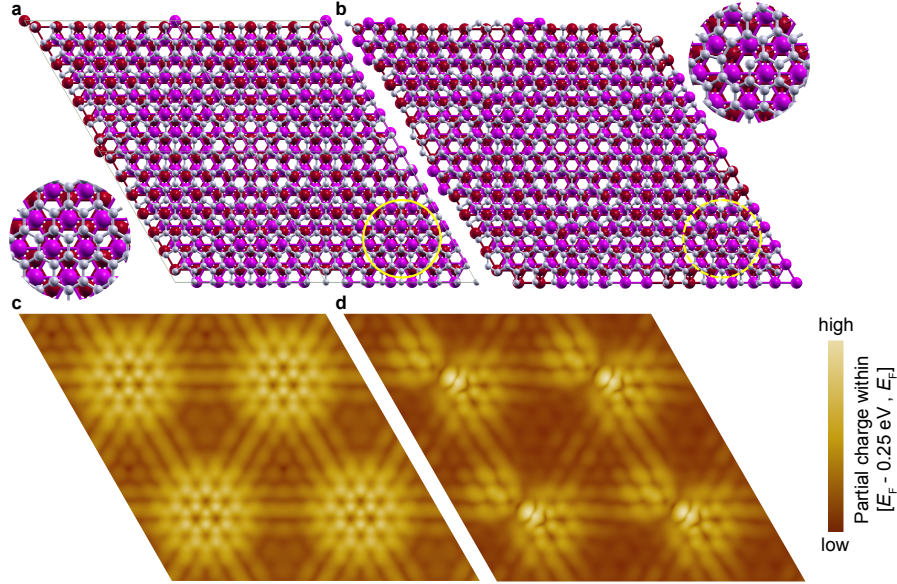
#### 3.b Vacancies in the carbon lattice

Vacancies in the carbon or metal lattices could be another interpretation. Atomic vacancies in the carbon lattice are for instance known to increase graphene's reactivity, leading to the formation of carbon-metal bonds and a decreased distance between graphene and the metal [192, 193, 158]. This behavior however depends on the region (*e.g.* *top-hcp*, *top-fcc*, *fcc-hcp*) where the carbon vacancy is located: on a *fcc-hcp* (hill) region, there is no metal atom directly underneath the defect, and our first principle simulations (DFT) reveal that the graphene height is not significantly altered there (Figure IV.4).

The atomic structure of a supercell made of  $(7 \times 7)$  Re(0001) unit cells in coincidence with  $(8 \times 8)$  graphene unit cells was relaxed, with and without a single C atom vacancy at the center of the moiré hill where the stacking is *fcc-hcp*. More precisely, a single C atom sitting on a *hcp* site was removed. The vacancy structure has a strong energy cost of 15.5 eV. The optimized structures are shown in Figure IV.4(a,b). In the presence of the vacancy, the *fcc-hcp* remains a hill, with height variations between atoms surrounding the defect of the order of 1 Å.

In Figure IV.4(c,d), we show cross-sections, taken just above the highest C atom, of the square modulus of the wave function integrated between 0.25 eV below the Fermi level ( $E_F$ ) and  $E_F$ .





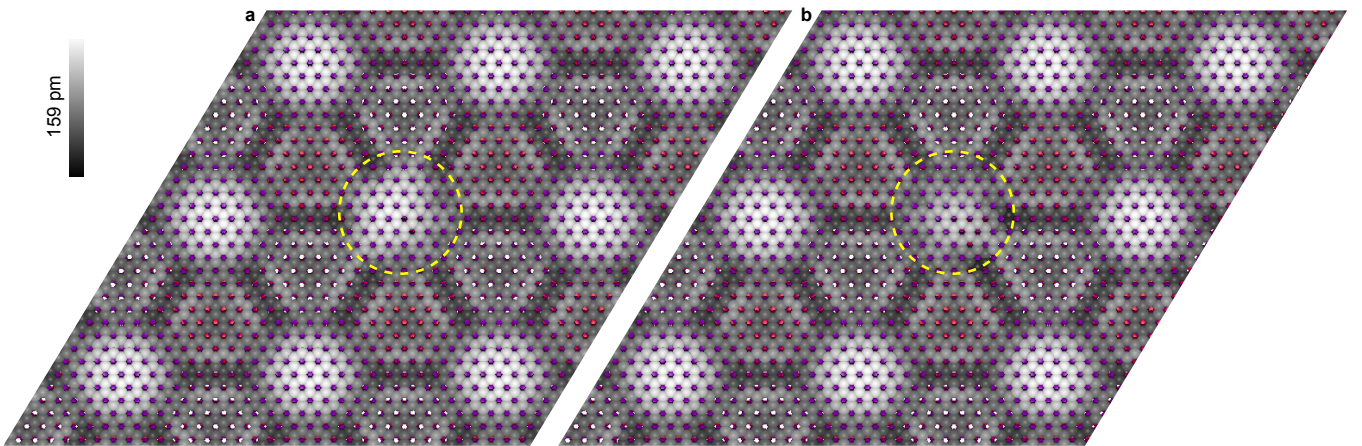
*Figure IV.4: Vacancies in the carbon lattice, tackled by DFT simulations.* (a,b) Top view of the optimized structures of a graphene/Re(0001) moiré unit cell with and without a single C atom vacancy located at the moiré hill. Two zooms on a *fcc-hcp* site are shown (left: defect-free, right: with C vacancy). (c,d) Cross-sections of the wave function integrated between  $E_F - 0.25$  eV and  $E_F$ , with and without the vacancy.

These cross sections are known to qualitatively reproduce the STM observations [3]. Cross-sections are strikingly different from the STM images of the vacant hill. We conclude that the presence of a C vacancy does not generate a vacant hill.

### 3.c Vacancies in the metal lattice

Vacancies in the metal lattice have been invoked in another epitaxial 2D material with vacant hills, namely MoS<sub>2</sub> grown on Au(111) [194]. In these vacant hills no atomic defect was found in the 2D material, and their measured low electronic density of states was ascribed to the presence of a nanometer-scale atomically-deep vacancy island in the Au(111) substrate.

We consider two possible vacancy islands in the metal surface, triple- and sextuple-vacancies with triangular shape. Figure IV.5 displays top-views of the carbon topography optimized *via* BOP simulations, for triple- (Figure IV.5(a)) and sextuple- (Figure IV.5(b)) vacancies in the metal substrate.



*Figure IV.5: Vacancies in the metal lattice, tackled by BOP simulations.* Top-views of the carbon topography, with C atoms shown as balls whose grey shade codes the height of the C atoms above 2.3472 Å from the average height of the topmost metal plane, for triple- (a) and sextuple- (b) vacancies in the metal substrate.

Simulations reveal no vacant hill at the location of the vacancies. We note that the local graphene/metal stacking corresponds to *top-fcc* at the location of the vacancy, but with a much larger distance than in the valley with the same stacking in defect-free graphene. The distance is close to 3.5 Å, very close to the height of regular moiré hills. At the moiré hills, where graphene is expected to be decoupled from the substrate [51, 3], the local density of states is enhanced (see corresponding discussion at the end of this Chapter), implying that the apparent height as assessed with STM may be an over-estimation of the true height. In the case of the metal vacancies discussed in the present paragraph (for which the distance is also large), one would thus expect a protrusion in the STM image, and not a depression (“vacant hill”) as we observe.

The triple- and sextuple-vacancies structures are presented in Figure IV.3 without displaying the top graphene layer, with the corresponding graphene heights at the location of the defects and at the location of the neighbor hills. Vacancies in the metal substrate do not constitute possible candidates for the vacant hill defect.

## 4 Possible defect candidates

We now turn to the description of the structures identified as possible candidates of the vacant hill defect, namely stacking faults in the metal and carbon lattices, and moiré dislocations. The latter kind of defect could be at the origin of (at least some of) the vacant hills reported in Ref. [179].

### 4.a Stacking faults in the metal lattice

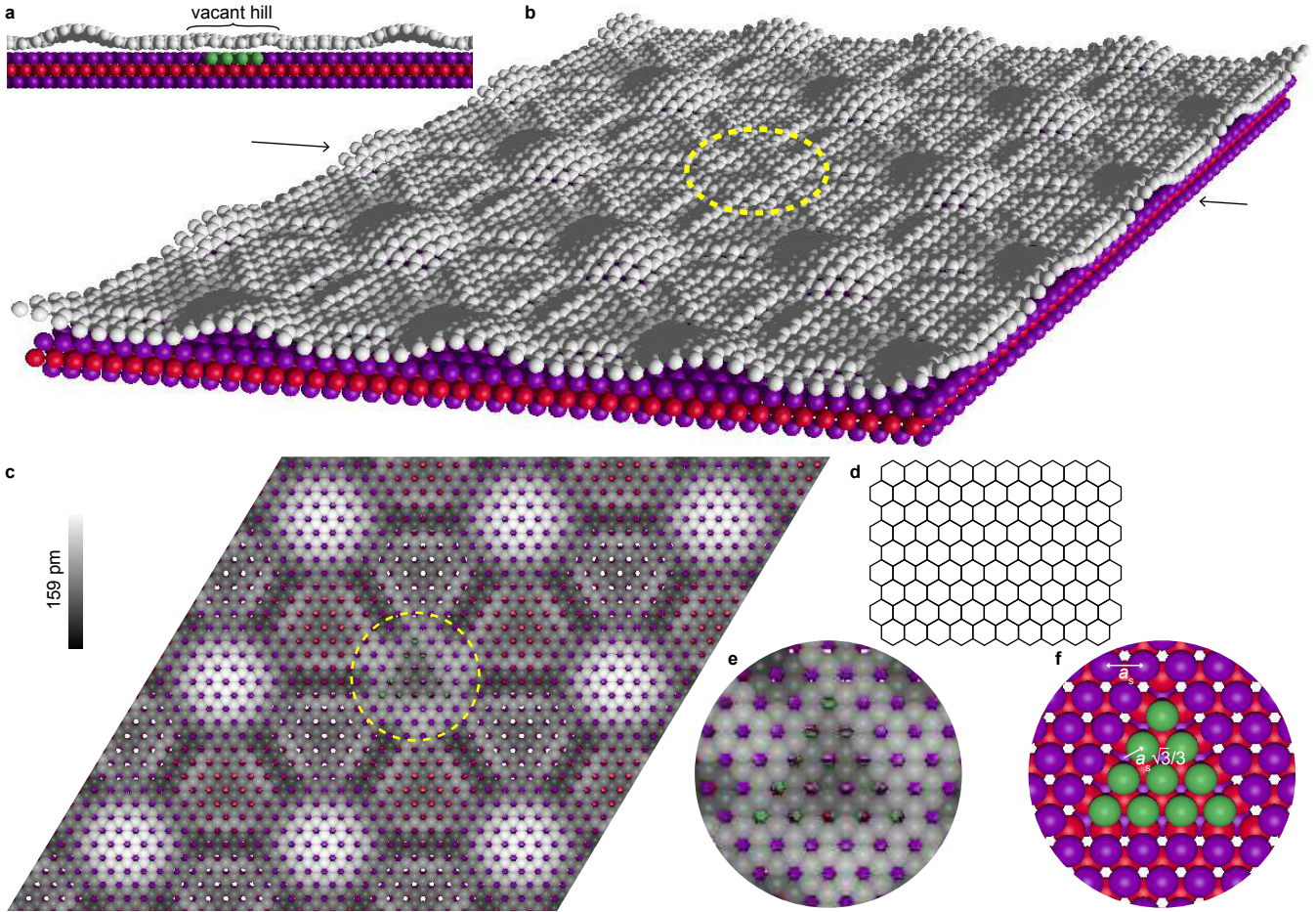
A straightforward configuration with the same stacking (*top-fcc*), but with the metal surface closer to graphene, is a stacking fault nanoisland in the metal uppermost layer. In this defect (points with -5 substrate atoms in Figure IV.3), the metal atoms (shown as green balls in Figure IV.6) are positioned on *fcc* hollow sites of the metal, *i.e.* they are laterally shifted by  $a_s/\sqrt{3}$  ( $a_s$  being the substrate’s lattice parameter) along a  $\langle 1\bar{1}00 \rangle$  direction. The optimized structure of such a defect is represented in Figure IV.6(a-c) from different viewpoints. Closer views on the optimized structure, with and without displaying the top graphene layer are shown in Figure IV.6(e,f). The simulations find a clear local energy minimum for a vacant hill (Figure IV.6), which appears deeper by about 1.2 Å compared to regular hills. There we expect a similar conductance as in the moiré valleys. This configuration is the first possible structure that we propose for the vacant hill, and we anticipate that stacking fault islands with slightly different shapes or sizes are also potential candidates.

The effects of such defect configurations can now be discussed in relation with STM observations of vacant hills in graphene on Ru(0001). These observations found no defect in the carbon lattice, implying that the vacant hill corresponds to a defect in the Ru(0001) substrate [179]. It was suggested that these defects are metal vacancies, for instance induced by ion beam bombardment during the preparation of the sample surface [179]. We however expect that at the temperature used to grow graphene, the metal surface reconstructs in a vacancy-free, staircase of atomically-flat terraces. Besides, we have just discussed that our simulations do not support a scenario with vacancies, and rather point to stacking faults. Interestingly, stacking fault formation has been reported previously in Ru(0001) upon graphene growth, in this case in the form of a lattice of stacking faults [198].

### 4.b Moiré dislocations

It should be noted that graphene as studied in Ref. [179] has rotational disorder, while we have carefully selected highly-ordered graphene samples in the present work. To prove this, closed Burgers circuits like the ‘1-2-3-4’ circuit in the inset of Figure IV.1(c) can be drawn around any vacant hill observed in Figure IV.1(a,b), ruling out the presence of dislocations in the moiré lattice. Moiré dislocations would





**Figure IV.6: Stacking faults in the metal lattice, tackled by BOP simulations.** Vacant hill model with a stacking fault in the metallic substrate. (a) Side-view ball model of the optimized nanorippled topography of graphene on Ru(0001), with two hills and one vacant hill. The amplitude of the out-of-plane displacement of C atoms has been multiplied by two. (b) Three-dimensional view corresponding to (a). Two arrows mark the cut used in (a). (c) Top-view of the carbon topography, with C atoms shown as balls whose grey shade codes the height of the C atoms above 2.347 Å from the average height of the topmost metal plane. (d) Honeycomb graphene lattice exclusively composed of hexagonal rings at the location of the vacant hill. (e,f) Closer view (yellow dotted circle in (b,c)) on a vacant hill, with and without displaying the top graphene layer, showing that carbon atoms atop the faulted substrate atoms (green balls) bring graphene closer to the substrate.

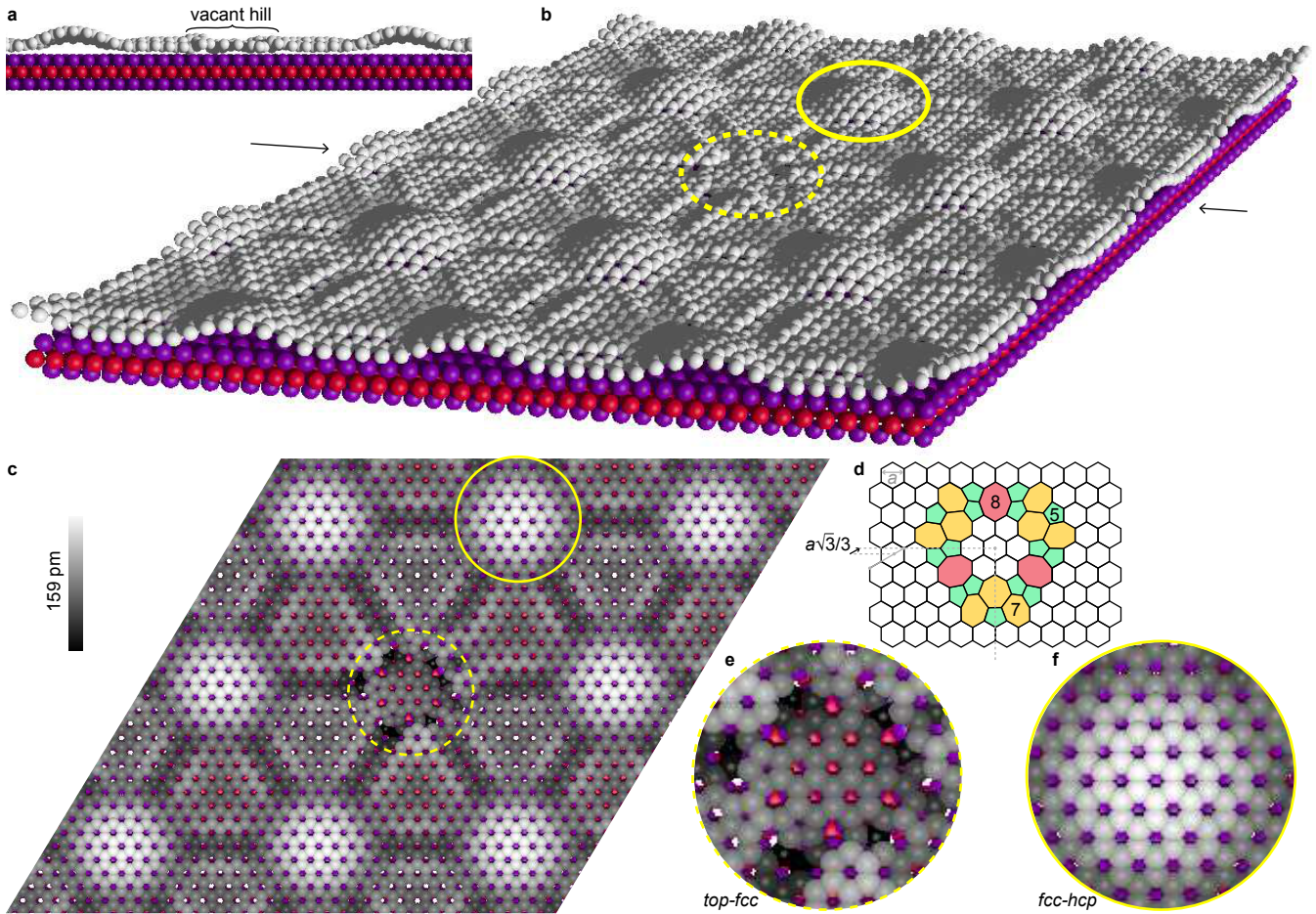
necessarily be observed in the presence of dislocations in the carbon lattice [189], and these atomic-scale dislocations accompany rotational disorder in a 2D material like graphene [199, 189].

Dislocations are surrounded by mechanical deformations, which alter the regular stacking configuration between the C and metal substrate atoms at the origin of the hill-and-valley topography of the moiré pattern. It is then conceivable that some of these deformations cause a vacant hill where the otherwise expected *fcc-hcp* stacking is strongly perturbed, even in the absence of a metal stacking fault underneath, and this could be the origin of (at least some of) the vacant hills reported in Ref. [179]. This is the second possible structure that we propose for the vacant hill.

#### 4.c Stacking faults in the carbon lattice

We now discuss a third possible kind of structure for the vacant hill, in which the C atoms' positions are laterally shifted with respect to the regular lattice. In other terms, this nano-grain is a graphene stacking fault, with a *top-fcc* and *top-hcp* stacking on top of the substrate instead of the regular *fcc-hcp* stacking, the substrate being unaltered (to a first approximation) by the presence of the defect. The boundary between such a stacking fault and the surrounding graphene necessarily consists of non-hexagonal rings, forming a loop of defects.

Here again we use BOP calculations to assess the stability and topography of several such candidate structures. These structures differ by the kind of nano-grain boundaries around the stacking fault at the center of the vacant hill. The stacking fault is a lateral shift of the graphene lattice by  $a/\sqrt{3}$  ( $a$  being graphene's lattice parameter) along armchair directions, with opposite orientations for the *top-fcc* and *top-hcp* stacking types (see an example in Figure IV.7(d)).



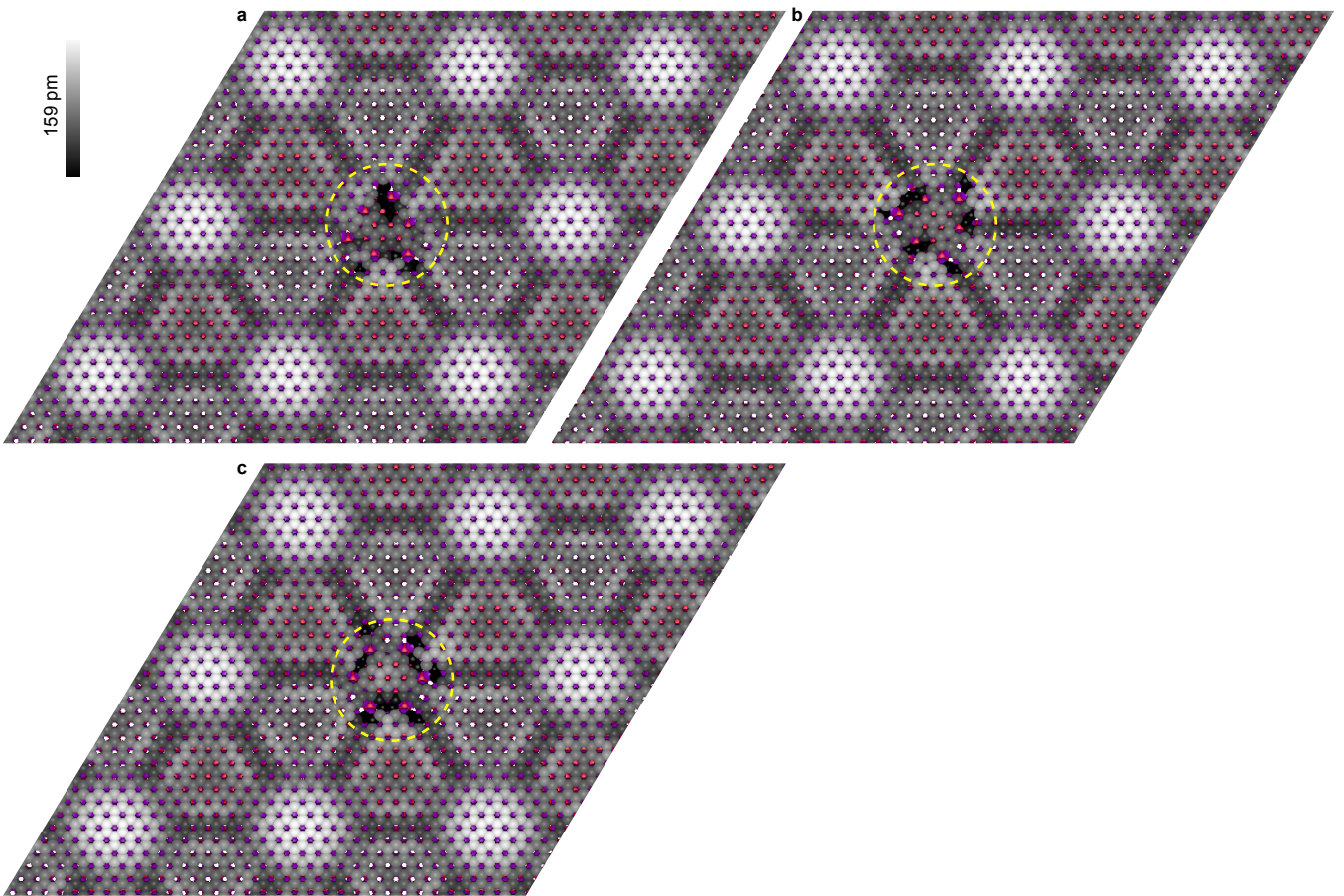
**Figure IV.7: Stacking faults in the carbon lattice, tackled by BOP simulations.** Vacant hill model with a stacking fault in graphene itself. (a) Side-view ball model of the optimized nanorippled topography of graphene on Ru(0001), with two hills and one vacant hill. The amplitude of the out-of-plane displacement of C atoms has been multiplied by two. (b) Three-dimensional view corresponding to (a). Two arrows mark the cut used in (a). (c) Top-view of the carbon topography, with C atoms shown as balls whose grey shade codes the height of the C atoms above 2.347 Å from the average height of the topmost metal plane. (d) Details of the C structure of the defect, revealing a lateral shift along the armchair direction of the core of the defect relative to the surrounding defect-free graphene. The grain boundary consists of pentagons, heptagons, and octagons. (e,f) Closer views of (c) (yellow solid and dotted circles in (b,c)), showing the *top-fcc* (*fcc-hcp*) stacking of C on Ru at the location of a vacant hill (regular hill) where the second (first) Ru plane is seen through the carbon rings, in red (purple).

Strain (shear, stretch, compression) and non-hexagonal rings can accommodate these lateral shifts. As discussed below, strain alone is not sufficient, while non-hexagonal rings alone are. The localized nature of the vacant hill, as opposed to the stiffness of the graphene lattice that *a priori* favors extended strain gradients [200, 201], suggests that non-hexagonal rings are likely to play a key role. Noteworthy, chains of non-hexagonal carbon rings with two pentagons and one octagon as repeating units [202, 203], or tilted Stone-Wales defects (two pentagons and two heptagons) [204], have already been observed between two-laterally shifted graphene domains. These chains represent discontinuities in the translational order parameter field of the graphene lattice and are therefore one-dimensional topological defects. We then explored the stability of a variety of looped grain boundaries constructed with fragments of these two kinds of topological defects.



To limit the number of possible configurations we focus on those with the highest symmetry and a small core made of six or seven hexagonal rings. The optimized structure of such a defect with a six-hexagon-core and a C density closest (-4 C atoms in Figure IV.7) to the case of defect-free graphene is represented in Figure IV.7(a-c) from different viewpoints and is sketched without the substrate in Figure IV.7(d). The graphene nanograin is surrounded by non-hexagonal rings, here pentagons, heptagons, and octagons. The depression that is observed is a clear energy minimum for the system. This finding confirms that a stacking fault, here in the graphene lattice, naturally gives rise to a vacant hill in the moiré pattern (clearly apparent when comparing Figure IV.7(e,f)).

Top-views of the carbon topography for graphene stacking faults with -6, -8 and -10 C atoms are shown in Figure IV.8. Details of the graphene nanograins, surrounded by loops of non-hexagonal C rings are shown in Figure IV.3, with the corresponding graphene heights at the location of the defects and at the location of the neighbor hills.

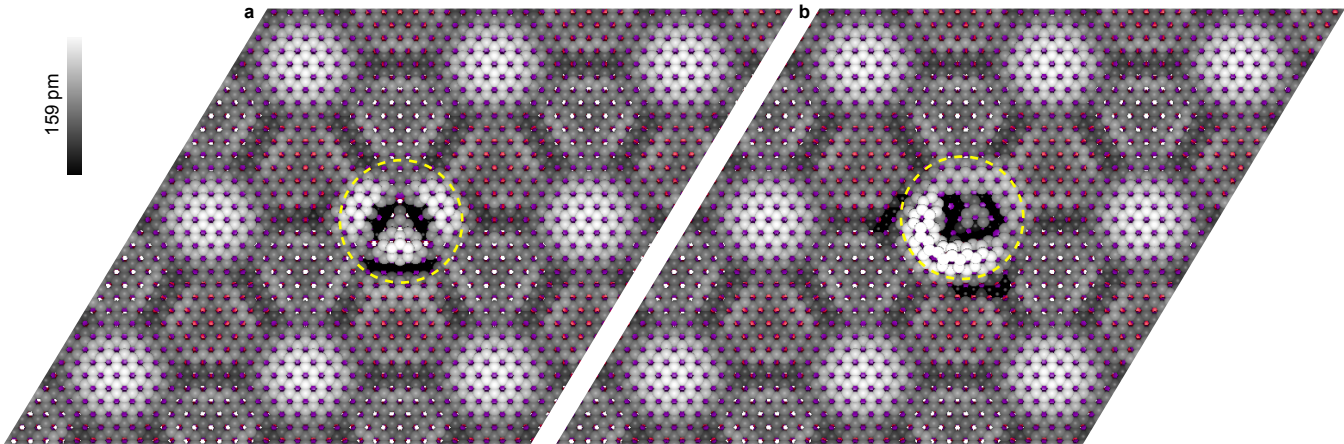


**Figure IV.8: Stacking faults in the carbon lattice with defect C atoms, tackled by BOP simulations.** Top-views of the carbon topography, with C atoms shown as balls whose grey shade codes the height of the C atoms above 2.347 Å from the average height of the topmost metal plane, for graphene nanograins surrounded by loops of non-hexagonal C rings, corresponding to (a) -6, (b) -8, and (c) -10 C atoms compared to defect-free graphene.

In Figure IV.3 we show alternative candidate structures for the vacant hill defect, with two shapes of nanograins and different kinds of boundaries. Each of these structures can be stacked in a *top-hcp* or *top-fcc* manner on the substrate, *i.e.* they are related by a 180°-rotation of the metal substrate. These two *alter ego* structures differ by a few 100 meV in binding energy, with a hierarchy that depends on the distance between the defects (Table IV.1). It is then hard to judge whether one or the other configuration is preferentially expected.

The BOP simulations predict that the vacant hill is deeper than the neighbor regular hill by typically 1 Å, and this holds for a rather broad range of C densities lower than that of defect-free graphene.

In the case of an excess of C atoms, the graphene topography seems much more complex than in the experimental observations. Top-views of the carbon topography for graphene stacking faults with +8 and +14 C atoms are shown in Figure IV.9(a,b), respectively. Graphene topography consists in strong, localized protrusions and depressions (above 1 Å). This is better visualized in Figure IV.9 than in Figure IV.3, where the height assessment we use, at the very center of the defect, does not account for the peculiar topography. We conclude that the (strongly) distorted hexagonal rings of excess-C-structures do not seem relevant ingredients to obtain looped grain boundaries forming vacant hills.



**Figure IV.9: Stacking faults in the carbon lattice with excess C atoms, tackled by BOP simulations.** Top-views of the carbon topography, with C atoms shown as balls whose grey shade codes the height of C atoms above 2.3472 Å from the average height of the topmost metal plane, for graphene nanograins surrounded by deformed hexagonal C rings plus non hexagonal rings, corresponding to (a) +8, and (b) +14 C atoms compared to defect-free graphene.

It is tempting to discuss the relative energies of the system with different kinds of defects, to try to identify the most probable structure for the vacant hill. Unfortunately, comparing the total energies of systems comprising a different number of atoms is meaningless. In addition, experimental observations of *e.g.* Stone-Wales defects indicate that defect formation during graphene growth is not forbidden even in case of high, few-electron volt formation energies [205]. As we will soon see, there are however other arguments, related to the origin of the vacant hill defect, that are more insightful in this respect.

Before we turn to this discussion, we would like to mention the observations of related defects in free-standing single-layer WSe<sub>2</sub>, that may also be seen as a stacking fault surrounded by loops of non hexagonal rings [206]. These defects are obtained after electron-beam irradiation, that leads to departure of Se from the material. It seems that WSe<sub>2</sub> is more tolerant than graphene to the presence of dangling bonds.

## 5 On the possible origin of the vacant hill defects

Unlike the defects reported in WSe<sub>2</sub> [206], the defects of interest here have formed upon epitaxial growth of graphene. The cores of the vacant hill structures that we discussed above are polycyclic clusters. Alone, these cores remind the size-selective clusters that are specifically observed on Rh(111), Ru(0001), and Re(0001) at early stages of graphene growth [180, 197, 196, 207, 159]. In a recent study we established that these clusters are stacked in a *top-fcc* configuration on the Re(0001) surface, and that they are metastable species whose occurrence is kinetically controlled [159]. It is then tempting to consider the clusters as natural sources of stacking faults in the system, and different viewpoints can be considered whether the stacking fault constituting the vacant hill is in the metal surface or in graphene.

Except where, by chance, a growing graphene patch meets a preformed metastable cluster with locally the same *top-fcc* stacking, the cluster and the graphene patch will be faulted with respect to one another.

As we have shown above, this results in the persistence of certain clusters until advanced stages of graphene growth are reached [159]. The open question at this point is how the cluster is eventually incorporated in the surrounding graphene lattice. This incorporation could occur by the formation of loops of non-hexagonal rings surrounding the graphene nanograin, or by a lateral displacement of the cluster dragging a patch of the topmost metal layer via the strong bonds between the C atoms at the cluster's periphery and the metal surface [159], thereby generating a stacking fault in the metal. Note that the latter process is expected to yield metal adatoms from the surface, which could for instance attach to the closest metal step edges.

At other sites of the moiré pattern, for instance the *top-hcp* site, the incorporation of metastable clusters could be less difficult (no stacking fault is observed in general at these locations). Whether at such sites the metastable cluster (forming a stacking fault) is dissolved before the graphene patch can cover this site, or alternatively, loops of non-hexagonal rings allow to stitch the defect and are subsequently healed, remains unclear at this stage.

Using a lower C adatom concentration during growth or higher temperatures reduces the density of vacant hills, from several  $10^4 \mu\text{m}^{-2}$  to few  $10^3 \mu\text{m}^{-2}$  [178]. Note that on Rh(111), Ru(0001), and Re(0001), too high temperatures that may allow to fully eliminate the vacant hills become problematic due to the tendency of carbon to dissolve in the bulk [208] or to form a surface carbide [149, 45, 209]. Overall, the vacant hills seem to be traces of the kinetic limitation towards the disappearance of metastable carbon clusters.

## 6 Electronic properties of the vacant hills

### 6.a Local conductance measurements

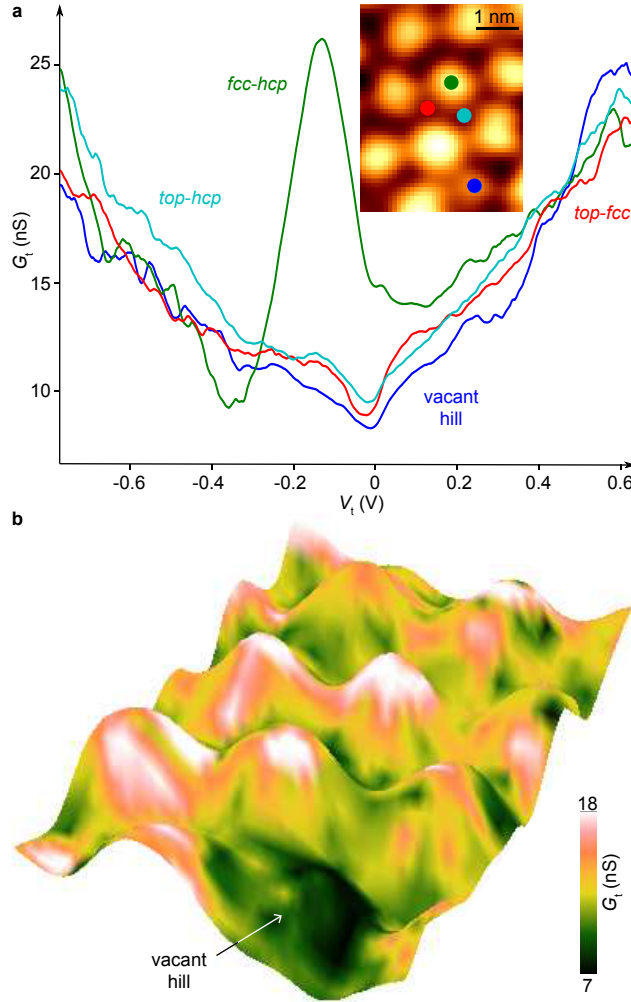
With the help of low temperature STS, we now address the electronic properties of graphene/Re(0001) at different locations in the moiré pattern and at the location of vacant hills. Graphene growth was performed on a thin Re(0001) film on sapphire, following the procedure described in Section 1.c. The differential conductance spectra were acquired at 4 K, using a standard lock-in technique with a 5 mV modulation of the tip-sample bias voltage ( $V_t$ ) at 480 Hz.

We find a strong correlation between the local (apparent) height and the local tunneling conductance ( $G_t$ ) versus tip-sample bias ( $V_t$ ): the conductance is strongly enhanced 100 meV below the Fermi level, forming a marked peak at the location of the hills (*fcc-hcp*) (Figure IV.10(a)). This peak is absent at the valleys of the moiré (*top-hcp* and *top-fcc*), while at these sites a dip is observed at the Fermi level. The correlation is visualised on Figure IV.10(b), where the apparent topography is overlaid with the corresponding conductance  $G_t(V_t = -0.1 \text{ eV})$  map. More specifically, the apparent topography is overlaid with an interpolated conductance map. Interpolation ensured that the grid of the conductance map matches the grid of the apparent topography (it artificially decreased the grid spacing of the conductance map).

The conductance spectra at the location of the vacant hill are very similar to those measured at the valleys (*top-hcp* and *top-fcc*) of the moiré, which themselves are hardly discernable from one another. This finding is consistent with our interpretation of the defect as a stacking fault corresponding to either a *top-hcp* or a *top-fcc* stacking, where the graphene-metal distance is similar to that in the moiré valleys.

### 6.b DFT calculations

To rationalize these observations we turn to the results of DFT calculations. We cannot address the vacant hill itself, since, as mentioned earlier, the supercell that would be required to obtain reliable results would be too large to be tackled. Instead we discuss the spatial variations, within a defect-free moiré unit cell, of the local density of states, a quantity that contributes to the experimental tunneling conductance.



**Figure IV.10: Moiré-site and vacant hill dependent variations of the conductance measurements.** (a) Conductance  $G_t(V_t)$  spectra measured at the location of a vacant hill, and of the *fcc-hcp* (hill), *top-fcc* (valley) and *top-hcp* (valley) sites of the moiré. Inset: STM topograph and the four locations where  $G_t(V_t)$  spectra have been measured. (b) Apparent topography measured with STM in a region comprising a vacant hill, represented with a three-dimensional rendering and overlaid with the corresponding local differential conductance map measured below the Fermi level at  $V_t = -0.1$  eV.

The system is described by a slab that contains five Re layers, one graphene layer, and a 10 Å-thick empty space on top. Atoms in the third Re plane were fixed while all the other atoms were let free to relax. The in-plane size of the supercell used for the calculation was set by assuming a coincidence of  $(8 \times 8)$  graphene unit cells on top of  $(7 \times 7)$  Re(0001) unit cells, corresponding to the experimental observations. A single  $k$  point, the supercell K point, was used to get a precise description of the graphene low energy states. After convergence, residual forces were less than  $0.025$  eV/Å.

Graphene strongly perturbs the charge distribution at the Re(0001) surface, as can be noticed when comparing the cross sections of the partial charge integrated below the Fermi level, at the graphene/Re(0001) and Re(0001)/vacuum interfaces (respectively top and bottom atomic layers in Figure IV.11(a)). The out-of-the-surface extension of the Re wave-functions is indeed strongly reduced at the valleys of the moiré, due to the hybridization between graphene and Re(0001) orbitals that is the strongest there.

Due to this spatially-varying hybridization, the density of states of the C and Re atoms are themselves varying. In the case of Re atoms, the variation is essentially related to the position in the moiré, while in the case of C atoms, it is additionally related to the kind of sub-lattice. Figure IV.12 shows the density of states of individual C and Re atoms in *fcc-hcp*, *top-fcc* and *top-hcp* regions. Regarding C atoms, the density of states in the *fcc-hcp* and *top-hcp* regions was computed for four C atoms: three equivalent C atoms forming a triangle pointing downwards for *fcc-hcp* and upwards for *top-hcp*, plus one C atom located exactly at the center of the said regions. Whether the C atom is on a *top* or *hcp* or *fcc* site with



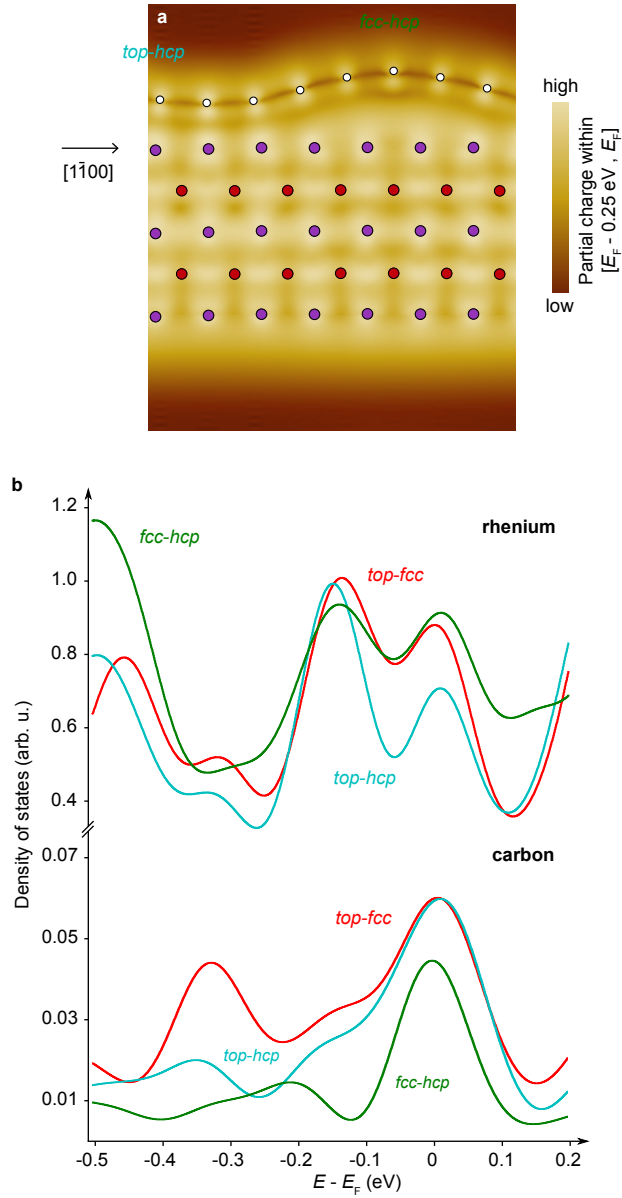
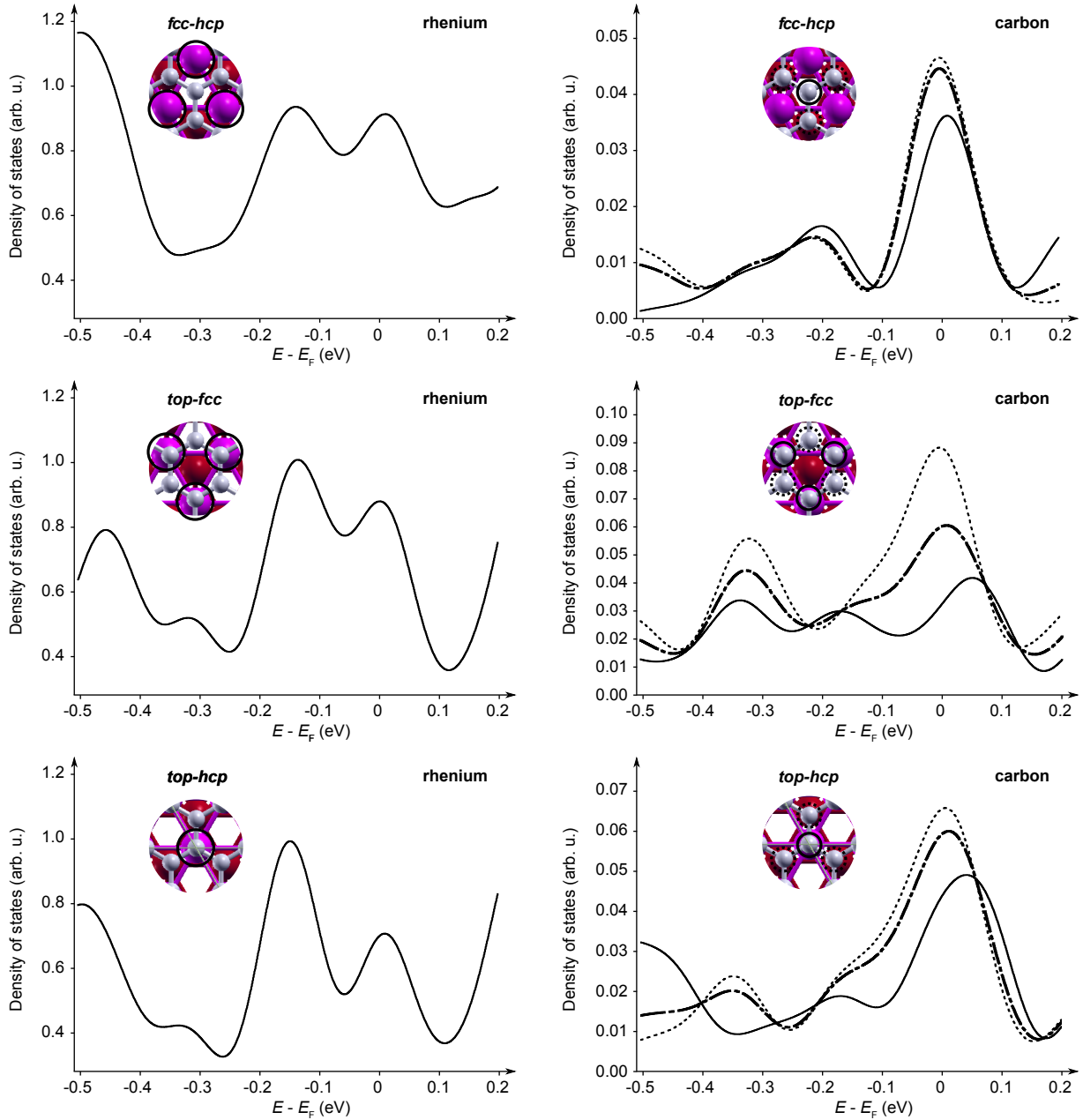


Figure IV.11: DFT results obtained for  $(7 \times 8)$  graphene/Re(0001). (a) Cross-section of the partial charge integrated between the  $E_F$  and  $E_F - 0.25$  eV, along the  $[1\bar{1}00]$  direction, deduced from the DFT calculations on defect-free graphene/Re(0001). (b) Electronic density of states (electron energy  $E$ ) of individual Re atoms (top curves) and averaged over a few C atoms (four and six respectively, bottom curves) at the hills ( $fcc-hcp$ ) and valleys ( $top-fcc$ ,  $top-hcp$ ) of the moiré, from DFT calculations.

respect to Re atoms makes a large difference in the density of states. As for the density of states of C atoms in the  $top - fcc$  region, we considered six C atoms: three equivalent C atoms forming a triangle pointing upwards and three equivalent C atoms forming a triangle pointing downwards. Again, we observe a significant variation for the two inequivalent sites.

The density of states computed at the hills and valleys of the moiré is shown in Figure IV.11(b). For C atoms, it is averaged over four atoms in  $fcc - hcp$  and  $top - hcp$  regions, and over six atoms in the  $top - fcc$  region (the atoms on which the average densities of states are calculated are the ones shown in Figure IV.12). Assigning one or the other extrema in these spectra to the ones observed in the experimental conductance is *a priori* risky, since their energy position depends on the degree of approximation that is used for the simulations.

The Re density of states (averaged over three atoms in  $fcc - hcp$  and  $top - fcc$  regions and taken on one Re atom only in the  $top - fcc$  region, see Figure IV.12) is globally larger than the one of C atoms, but the larger distance to the STM tip is expected to compensate this difference, at least partly. Two



**Figure IV.12: Density of states of individual Re and C atoms at the hills (*fcc-hcp*) and valleys (*top-fcc*, *top-hcp*) of the moiré.** Top: Electronic density of states (electron energy  $E$ ) of individual Re and C atoms in the *fcc-hcp* region. The density of states was calculated on three equivalent Re atoms (left), and on four (three equivalent + one) C atoms (right). Middle: Electronic density of states (electron energy  $E$ ) of individual Re and C atoms in the *top-fcc* region. The density of states was calculated on three equivalent Re atoms (left), and on six (three equivalent + three equivalent) C atoms (right). Bottom: Electronic density of states (electron energy  $E$ ) of individual Re and C atoms in the *top-hcp* region. The density of states was calculated on one Re atom (left), and on four (three equivalent + one) C atoms (right). Electronic density of states are plotted with solid and dotted lines. The type of line used to circle a specific atom shown in one of the insets matches the type of line used to plot the density of states on this specific atom. For C atoms, we also show for each atomic stacking the average density of states with a dash-dotted line.

maxima are observed for Re and C, both at the hills (*fcc-hcp* region) and the valleys (*top-fcc* and *top-hcp* regions) around the Fermi level and about  $[-0.2, -0.1]$  eV below it (and keeping in mind that the absolute energy values should be taken with caution).

Concerning Re atoms, the lowest-energy maximum is the most intense of the two, and the intensity difference with the other maximum is more severe in the case of the valleys. Concerning C atoms, the higher-energy maximum is the most intense, and the intensity difference with the other maximum is more severe in the case of the hills. Overall, the density of states including the C and Re contributions may hence exhibit marked maxima at the hills (at the higher-energy value), and on the contrary no marked



maximum at the valleys (the C and Re contributions somewhat averaging out). These simple arguments elude (possibly important) corrections introduced by the tunneling matrix elements. Yet they suggest that the marked maxima could correspond to the peak measured in the tunneling conductance at the location of hills (Figure IV.10(a)), and conversely that no specific feature is observed experimentally at the valleys or the vacant hills.

## Conclusions

Using scanning tunneling microscopy/spectroscopy, parametrized bond-order potential calculations and density functional theory electronic structure calculations, we have addressed one of the prominent local defects encountered in epitaxial graphene grown on several metal surfaces such as Re(0001), Ru(0001), and possibly Rh(111) as well. The nature of this defect, which has been observed ever since 2007, had not been discussed in details until now. The defect appears as a vacant hill in the nanorippled pattern that is associated with the moiré pattern of graphene. This locally, lower-than-expected height and the corresponding lower tunneling conductance both point to a stacking fault, a kind of C-metal stacking that is otherwise encountered at the valleys of the moiré pattern. Microscopy shows that this vacant hill is incorporated within the surrounding graphene lattice. We discussed the possible structures of the stacking fault, either in the metal surface or in graphene itself, in the latter case in relation with closed loops of non-hexagonal carbon rings surrounding the stacking fault. Our bond-order potential calculations predict a depression in graphene for both kinds of stacking faults, consistently with our observations. We finally proposed that the vacant hills are related to the formation of metastable, kinetically blocked polycyclic clusters forming alongside the growth of graphene.

In the prospect of producing high-quality graphene, there is an obvious motivation to eliminate the vacant hill defects as much as possible. Ru(0001), Re(0001), and Rh(111) substrates, with which these defects are formed, actually stand out of the broad library of possible graphene substrates because they naturally select a single orientation of graphene, virtually free of other kinds of defects like twin boundaries. Graphene detached from Ru(0001) has already proven high electric transport performance [210], and we expect that reducing or even eliminating the vacant hills would further improve these performances. Considering metastable polycyclic carbon clusters as a plausible source for the vacant hills, avoiding their formation by *e.g.* the use of *ad hoc* molecular precursors seems a promising route.

With the predicted electronic properties of graphene anti-dot lattices in mind [211], we may change our perspective on the vacant hill defects and now also consider them as exciting objects in themselves. Noting that the moiré pattern also naturally selects the location of the stacking faults (vacant hills), controlling the number of vacant hills and their 2D organization might allow to engineer unique electronic states with no equivalent in pristine graphene.

DEFECTIVE, HOLE-DOPED AND  
 SUPERCONDUCTING QUASI FREE-STANDING  
 GRAPHENE ON RE(0001) OBTAINED BY GOLD  
 INTERCALATION

---

**Contents**

1	Graphene-covered Re(0001) . . . . .	<b>83</b>
	1.a Structural properties . . . . .	83
	1.b Electronic band structure . . . . .	84
2	Gold deposition/intercalation process . . . . .	<b>84</b>
3	Structural and electronic properties of gold-intercalated graphene on Re(0001) . . . . .	<b>86</b>
	3.a Atomic force microscopy observations . . . . .	86
	3.b Scanning tunneling microscopy and spectroscopy . . . . .	87
	3.c DFT calculations . . . . .	89
	3.d Topography-dependence in conductance measurements . . . . .	93
4	Quasi free-standing character of gold-intercalated graphene on Re(0001) . . . . .	<b>93</b>
	4.a Dirac cone of quasi free-standing graphene . . . . .	93
	4.b Raman modes of quasi free-standing graphene . . . . .	95
5	Defects in gold-intercalated graphene on Re(0001) . . . . .	<b>96</b>
6	Superconducting properties . . . . .	<b>98</b>

---

## Abstract

Graphene grown on Re(0001) is known to be strongly interacting with its substrate. To benefit from the proximity of the superconducting substrate, while recovering a free-standing character for graphene and thus two-dimensional properties, we have explored the intercalation of an ultra-thin layer of a weakly interacting metal, Au, in between graphene and Re(0001). Using RHEED, LEED, STM/STS, AFM, ARPES, Raman spectroscopy and DFT calculations, we establish that as opposed to the strongly hybridized graphene-on-Re(0001), gold-intercalated graphene on Re(0001) presents a quasi free-standing character. The weak graphene-Au interaction is evidenced by a reduced graphene corrugation, an enhanced distance between graphene and the underlying metal, a linear electronic dispersion and characteristic graphene's Raman modes. We demonstrate that gold-intercalated graphene on Re(0001) is slightly *p*-doped, in agreement with previous measurements on related systems. The high density of defects in gold-intercalated graphene on Re(0001) ( $10^{14} \text{ cm}^{-2}$ ) is attributed to the formation of defects upon intercalation. The observation of two electronic resonances in the conductance spectrum of gold-intercalated graphene on Re(0001) is rationalized by means of DFT calculations: one resonance is ascribed to the quasi-free standing character of graphene, and the other to the presence of Au. Finally, we show that gold intercalation does not alter the rhenium-induced superconductivity in graphene.

## Introduction

Epitaxial growth of large-area graphene with low defect density on various metal substrates has been a very active subject of research in the past few years. Two extreme cases of graphene-substrate binding are commonly acknowledged: weakly interacting metallic substrates such as Ir(111) [53, 52], Pt(111) [54, 46, 55], Cu(111) [56], Al(111), Ag(111) [58] and Au(111) [59]; and strongly interacting metallic substrates such as Re(0001) [3, 60, 61], Ru(0001) [51, 62, 63, 64], Rh(111) [65] and Ni(111) [66]. For the latter category, hybridization between the metal *d* states and the  $\pi$  band of graphene results in a loss of graphene's electronic linear dispersion [60], associated with a strong nanorippling of the graphene sheet [3, 63, 64] and short graphene-substrate distances [65]. These features are related with a tendency to form covalent bonds between graphene and the substrate [65, 61]. Contrary to strongly interacting substrates, weakly interacting metals preserve the Dirac cones of graphene [53, 55], with larger graphene-substrate distances [61] and a smaller graphene nanorippling [52]. The bonding between graphene and the substrate is of van der Waals-type [52, 65, 61]. The reason is that the hybridization energies associated with the overlap of the metal *d* orbitals with the  $\pi$  orbitals of graphene are much higher (in absolute values) than in the case of strongly interacting metallic substrates [65, 61]. In other words, hybridization occurs in regions far from the Dirac point.

Intercalation of a buffer atomic layer of certain elements in between graphene and its substrate is an efficient way to recover the intrinsic structural and electronic properties expected for isolated graphene. Obviously, the intercalated species should passivate the metallic substrate. In particular, graphene shows structural and electronic properties that are strongly reminiscent of isolated graphene (hence it is coined "quasi free-standing") when the metallic intercalant has full higher-energy *d* sub-shell, as shown with graphene/Ag/Re(0001) [60], graphene/Pb/Re(0001) [95], graphene/Au/Ni(111) [97, 98], graphene/Cu/Ni(111) [98], graphene/Ag/Ni(111) [98], graphene/Al/Ni(111) [99], graphene/Au/SiC(0001) [100, 101] and graphene/Pb/Ru(0001) [103].

Intercalation is however not neutral, and may have desired or spurious effects on graphene. The possibility to adjust the electronic doping of graphene from "under the carpet" has been widely explored, and both *p* and *n* doping were demonstrated accordingly [105, 104, 213, 96, 97, 102, 106, 60, 95]. The magnitude and sign of the doping is expected to depend on the work function of the metal, on the graphene-metal distance, and on the interfacial potential change resulting from the graphene-metal

interaction [71]. Consistent with this picture, using metal intercalants both electron and hole doping was demonstrated for graphene on various metal substrates including Ir(111) [105, 104, 213] and Ni(111) [96, 97], while only hole doping was reported on Ru(0001) [102] and only electron doping was reported on Pt(111) [106] and Re(0001) [60, 95].

Another effect of intercalation, when the metal intercalant is a heavy element, is a spin-orbit effect. Electronic bands with spin-splitting due to this proximity effect, amounting to 10-100 meV, have been reported with Au [107] and Pb [106, 111] intercalants. Strong spatial variations of proximity spin-orbit effects at the edge of intercalated islands were proposed to generate sharp Landau levels in graphene [105]. The origin of these effects is not fully clarified, and may relate to the structure of the intercalated layer [114, 115].

More deleterious is the possible creation of defects upon intercalation [93, 87, 94]. The energy barriers for defect creation seem *a priori* too high to be generated at room temperature, thus intercalation is at first thought rather expected to occur via graphene edges [91, 92] or pre-existing defects [85, 87]. Yet, predictions that metal atoms or clusters (naturally present in an intercalation experiment) can strongly reduce energy barriers for defect creation in graphene [214], prompt whether new defects could be created alongside intercalation.

Here, we investigate the intercalation of Au sub-monolayers and few layers in between graphene and Re(0001), a substrate of choice in view of inducing superconductivity in graphene [3]. Using electron diffraction (RHEED and LEED), STM/STS, AFM, ARPES, Raman spectroscopy, and DFT calculations, we find that graphene becomes quasi free-standing thanks to Au intercalation, reducing its corrugation, increasing its distance with the metal surface, recovering a conical electronic dispersion, an electronic resonance, and Raman-active vibration modes. We also establish that graphene becomes hole-doped, in contrast to other graphene-on-Re(0001) systems studied so far [60, 95], and we demonstrate that intercalation induces a significant density of point defects in graphene, amounting to  $10^{14}$  cm<sup>-2</sup>. Finally, we show that the rhenium-induced superconducting gap is not altered by gold intercalation.

## 1 Graphene-covered Re(0001)

Before addressing the intercalation of gold between graphene and Re(0001), we briefly describe graphene-covered Re(0001). Two separate UHV systems were used for sample preparation: one was equipped with a room-temperature UHV-STM and the other was used for ARPES experiments. Temperatures were measured with pyrometers assuming an emissivity of 0.3. The deviation from the actual sample temperature may vary with the transmission coefficient of the UHV viewport and the measurement angle for instance, and these parameters were different in the two UHV systems. We estimate an uncertainty on temperature measurements of  $\pm 50$  K.

Graphene growth on Re(0001) single-crystal was performed using the TPG-CVD method described in Chapter III. Graphene growth consisted of eleven TPG cycles, between 520 K and 970 K for the STM-equipped UHV system and between 520 K and 1100 K for the ARPES-equipped UHV system, followed by a cooling down to 520 K within 10 min for both systems. The ten first TPG cycles were performed under ethylene atmosphere, with  $P_{C_2H_4} = 5 \cdot 10^{-7}$  mbar, and the last one was performed with the C<sub>2</sub>H<sub>4</sub> valve closed.

### 1.a Structural properties

In Figure V.1(a), the typical hill-and-valley topography of graphene/Re(0001) moiré is visualized with STM. The moiré signature appears also in the planar cut of reciprocal space measured with LEED, as satellite spots around the Re(0001) and graphene first order spots (Figure V.1(b)). When grown on a Re(0001) single-crystal, graphene consists of domains of typically few tens of nanometers in size, overall covering 70% of the surface. A small fraction of the surface (15%) is covered by a rhenium carbide (for

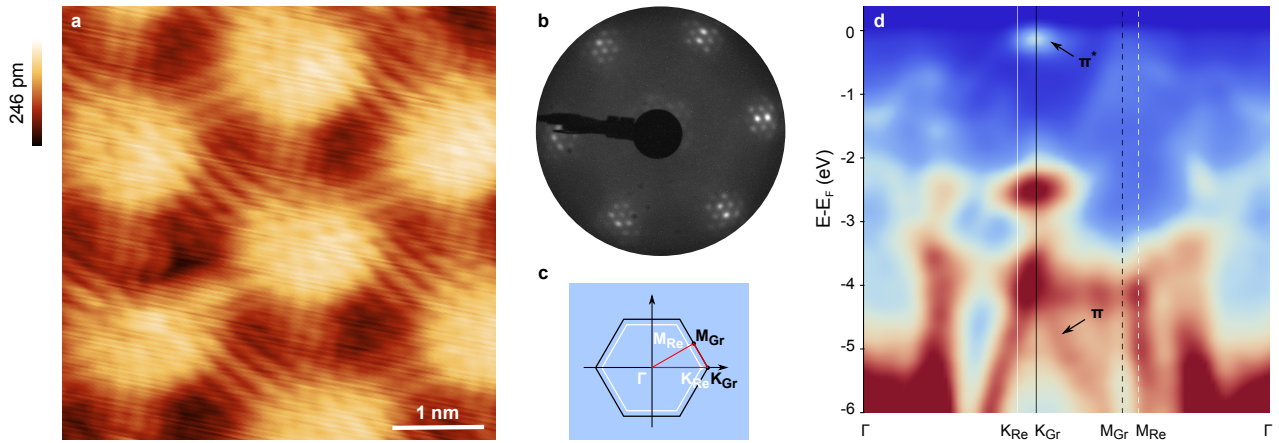


Figure V.1: **Graphene-covered Re(0001)**. (a) Scanning tunneling topograph of graphene/Re(0001), revealing the moiré with atomic resolution.  $I_t = 5$  nA,  $V_t = 20$  mV,  $T = 300$  K. (b) LEED pattern of graphene/Re(0001), measured with 80 eV electrons. (c) Reciprocal space sketch showing the  $\Gamma$ -K-M- $\Gamma$  direction (in red). The highest-symmetry points of graphene ( $K_{Gr}$ ,  $M_{Gr}$ ) and Re(0001) ( $K_{Re}$ ,  $M_{Re}$ ) are indicated. (d) Photoemission intensity plot along the  $\Gamma$ -K-M- $\Gamma$  direction of graphene/Re(0001), with an HeII source (40.8 eV photon energy). The highest-symmetry points of graphene ( $K_{Gr}$ ,  $M_{Gr}$ ) and Re(0001) ( $K_{Re}$ ,  $M_{Re}$ ) are marked on the map.

further details on the ordered rhenium carbide phase we refer the reader to Chapter III). When grown on rhenium thin films, graphene coverage reaches 90% of the surface.

We turn to the diffraction data obtained with RHEED, which is well-suited to address structural changes, in our case those occurring upon intercalation, in real-time. A typical graphene-covered Re(0001) RHEED pattern taken with  $[01\bar{1}0]$  incident azimuth is shown in Figure V.2(a). The diffraction signals from Re, graphene, and the moiré appear as streaks, which are marked with different colours in Figure V.2(a'). Assuming that the lattice parameter of Re is equal to its bulk value *i.e.*  $a_{Re} = 2.76$  Å, the graphene lattice parameter,  $a_{Gr} = (d_{Re}/d_{Gr}) \times a_{Re}$ , where  $d_{Gr}$  ( $d_{Re}$ ) is the distance between the graphene (rhenium) streak and the specular (central) streak, is 2.47 Å, close to the values found in the literature. Additional streaks, associated to rhenium carbide, are observed in between graphene streak and the specular streak.

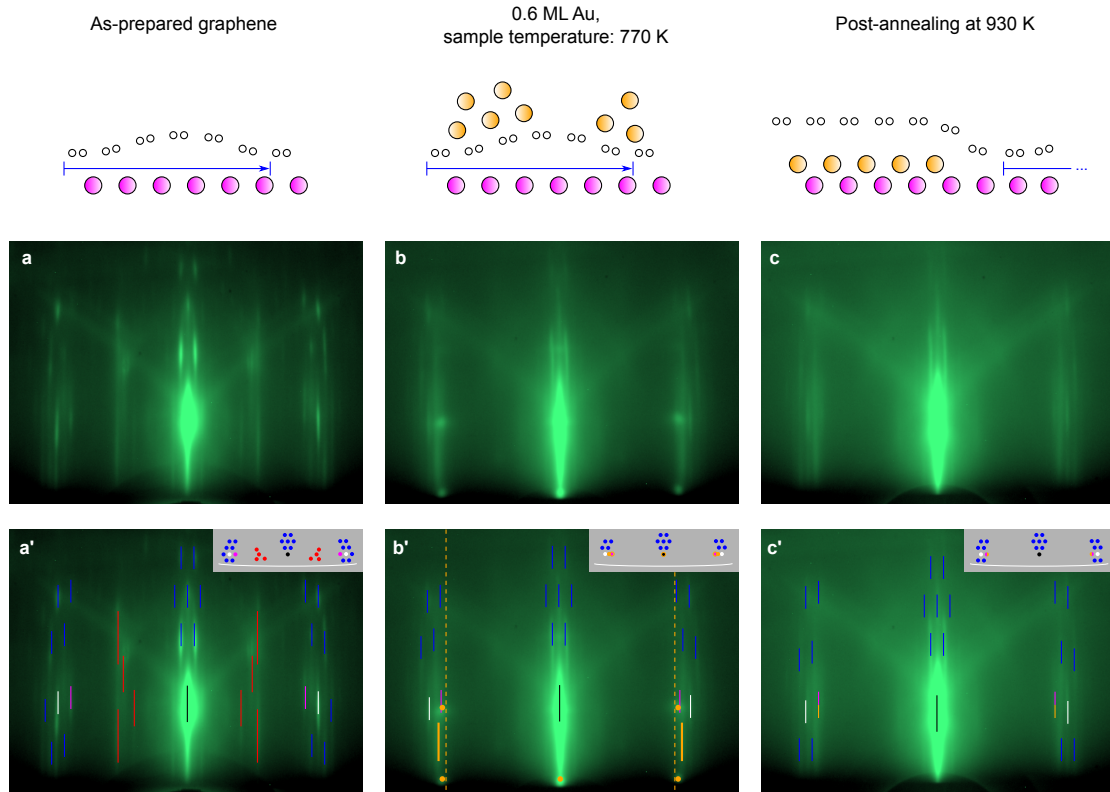
## 1.b Electronic band structure

Figure V.1(d) shows an ARPES cut of the electronic band structure below the Fermi level along the  $\Gamma$ -K-M- $\Gamma$  direction. Our data is consistent with the electronic band structure reported by Papagno *et al.* [60], and is coherent with the one reported in Ref. [95]. The observed  $\pi$  and  $\pi^*$  bands do not correspond to the case of free-standing graphene. The hybridization of the metal  $d$  states with the  $\pi$  state of graphene is responsible for the shift of the  $\pi$  state below the Fermi level. The shift amounts to 3.3 eV, suggesting a strong electron donation from the metallic substrate to graphene. The parabolic dispersion of the  $\pi$  state is less marked in our experimental band structure than in Ref. [60]. This dispersion points to a strong difference in the C-Re interaction for the two C sub-lattices, in contrast with the linear dispersion of isolated graphene. In the valleys of the moiré indeed, strong covalent-like bonds are formed between the Re atoms in the topmost metal plane and C atoms in one of the two C sub-lattices, while the other C atoms do not form such bonds [61, 3]. These bonds correspond to a strong C-Re hybridization, which presumably accounts for the electronic states observed in the ARPES map within the graphene bandgap (Figure V.1(d)).

## 2 Gold deposition/intercalation process

The deposition rate of Au was estimated using either a quartz microbalance or Auger spectroscopy. Gold deposition and intercalation were performed as follows. First, gold deposition on graphene-covered

Re(0001) was performed using either a Au evaporator or via pulsed-laser deposition, at room temperature. Then, a subsequent annealing at 970 K and 670 K in the two different systems was performed. The intercalation process occurred during the subsequent annealing and was monitored by either RHEED or LEED. An alternative method was used and gave similar results: Au deposition was performed with the sample held at 770 K, and a subsequent annealing at 930 K led to Au intercalation.



**Figure V.2: Gold deposition/intercalation process monitored by RHEED.** Top: Ball model of graphene-covered Re(0001) along the deposition/intercalation process of Au. Graphene, rhenium and gold atoms are schematically represented as white, pink and yellow balls, respectively. The moiré superperiodicity is indicated with blue arrows. Bottom: Periodic features observed with RHEED on (a,a') graphene-covered Re(0001) surface, (b,b') after depositing 0.6 ML of Au at 770 K and (c,c') after subsequent annealing at 930 K. RHEED patterns were taken along the  $[01\bar{1}0]$  incident azimuth. Coloured lines indicate the specular (black), Re (pink), graphene (white), moiré (blue), rhenium carbide (red) and Au (yellow) streaks. The bulk lattice parameter of Au(111) is indicated with dashed yellow lines. Insets show schematic top views of the reciprocal space with all observed rods and a cut of the Ewald's sphere (white line).

Figure V.2 shows the evolution of the RHEED pattern taken along the  $[01\bar{1}0]$  incident azimuth during the deposition/intercalation process of 0.6 monolayer (ML) of Au (1 ML denotes a full coverage of the Re(0001) surface with pseudomorphic single layer of Au). Gold deposition was performed with the sample held at 770 K, followed by a subsequent annealing at 930 K. After gold deposition at 770 K (Figure V.2(b-b')), some of the moiré streaks have disappeared, as well as the carbide streaks. This is an indication that gold has been deposited onto the surface. Besides, diffraction spots and streaks (yellow) appear after Au deposition. The spotty diffraction signals, which correspond to a smaller-than-bulk in-plane Au lattice parameter, are indicative of the presence of three-dimensional objects on the surface after Au deposition. An obvious reason is that at least part of the deposited Au is in the form of clusters. This is to be expected given the very different surface energies of Au and graphene, which should promote Au dewetting on graphene [215]. The small lattice parameter is indicative of a nanoscopic size of the clusters [216, 217, 218, 219]. The (yellow) streaks rather point to the presence of a two-dimensional layer of gold. These streaks are much broader than those of graphene and Re(0001) prior to Au deposition, indicative of a significant structural disorder. They are located in between the rhenium and graphene streaks, meaning that the gold layer has an intermediate lattice parameter, in between the values of

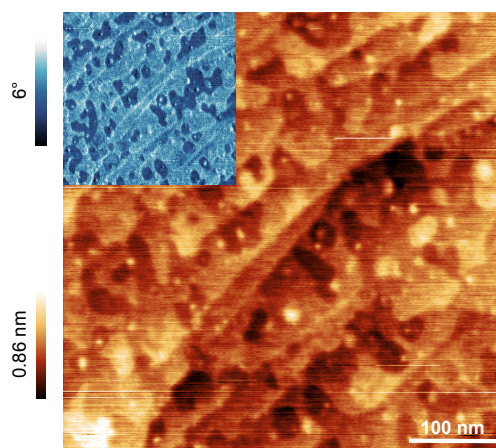
graphene and rhenium. This lattice parameter is not only smaller than the Au(111) bulk value (2.88 Å), but also smaller than rhenium's lattice parameter (2.76 Å). This suggests that Re has no particular influence on the structure of Au at this stage. It is likely that Au remains on top of graphene, having a smaller lattice parameter due to small size effects (low coordination of a large fraction of Au atoms) [216, 217, 218, 219] or due to the interaction with graphene, whose lattice parameter is typically 14% smaller than that of Au(111). Overall, the deposition at 770 K seems to mainly promote gold ripening: dewetted 3D gold clusters form on the graphene and carbide surfaces.

The subsequent annealing at 930 K (Figure V.2(c,c')) leads to the disappearance of gold spots. In the meantime, the Au-related streaks narrow, and their positions shift to match that of the Re streaks. In other words, Au is now pseudomorphic to Re(0001) and structurally less disordered than prior to annealing. A straightforward interpretation is that Au is intercalated between graphene and Re(0001), and that the latter imposes its lattice parameter to the Au layer. This is what is also observed in most metal-intercalated systems studied so far [87, 220]. In the real-time evolution of the RHEED pattern, it is clear that the Au streak and Au spots eventually shift to match the Re, and not the graphene streak. Note that the 0.6 ML amount of Au deposited on the surface is not sufficient to fully cover the Re(0001) surface, hence we expect a coexistence, in the RHEED patterns, of graphene/Re and graphene/Au/Re contributions. In the case of graphene/Au/Re, the weak interaction (see below) is expected to strongly weaken the periodic lattice distortions associated with the moiré, so the moiré streaks should vanish. The fact that we do not observe a total disappearance of these streaks is presumably due to a smaller Au surface coverage (60%) compared to the graphene coverage (70%), which leaves pristine graphene/Re(0001) regions even after full intercalation of the deposited Au.

### 3 Structural and electronic properties of gold-intercalated graphene on Re(0001)

#### 3.a Atomic force microscopy observations

Atomic force microscopy (AFM) images were taken using a Veeco AFM and an Olympus tip scanned over the surface in tapping mode with a drive frequency of 274 kHz. An AFM image of the surface is presented in Figure V.3.



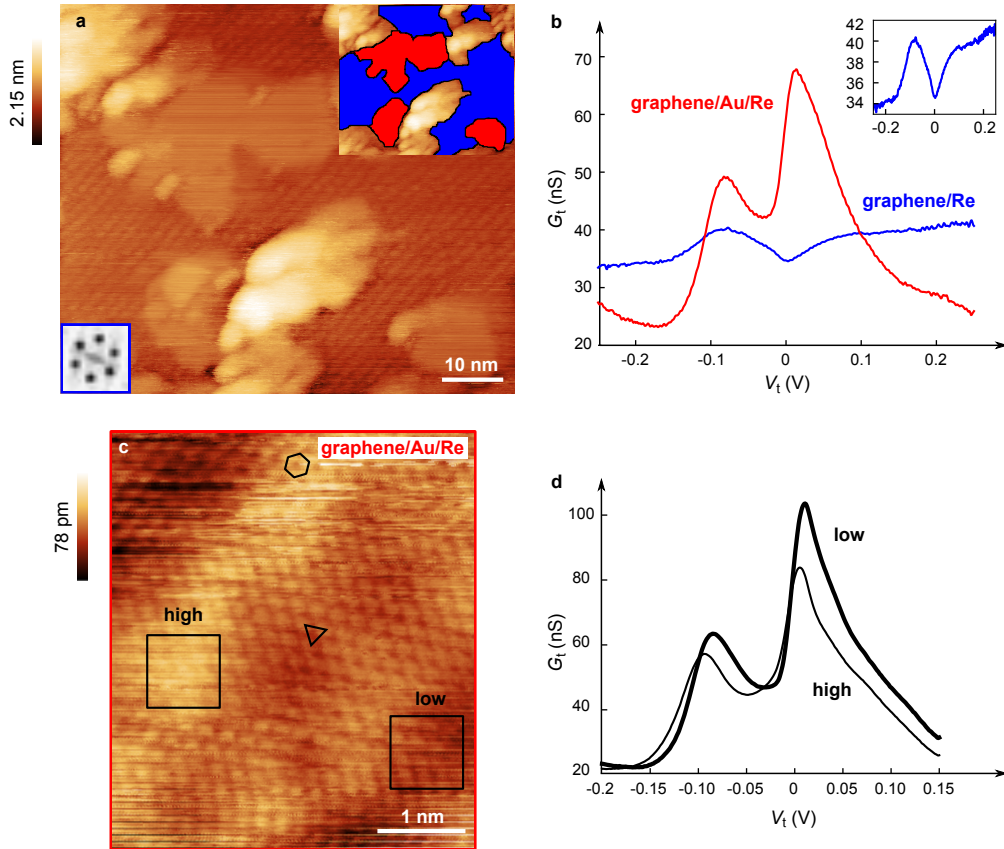
*Figure V.3: Atomic force microscopy image of graphene on Re(0001) intercalated with 0.6 ML of Au. The topographic AFM image shows height inhomogeneities. Inset: Corresponding phase contrast image, putting in evidence two types of regions (lower and higher phase) of different chemical nature.*



Both topographic and phase contrast images are shown. An underlying staircase of descending, atomically-high step edges from the substrate is observed. The width of the terraces between step edges is typically 30 to 100 nm. Superimposed on this staircase, atomically-high or -deep islands are seen. As we will confirm soon after, the lower islands correspond to graphene/Re(0001) (without intercalated Au) while the other regions correspond to graphene/Au/Re(0001) (intercalated). The phase contrast image (inset of Figure V.3) reveals that the lower islands also have a lower phase. The phase difference points to distinctive dissipative behaviour of the AFM's tapping tip in relation to a different kind of adsorbed layer on top of the surface (the microscope is operated at ambient pressure). A similar behaviour has been observed in the past on a related system, graphene/SiC with inhomogeneities in the number of graphene layers across the surface [221], and could point to a different interaction between different “kinds” of graphene (for instance in more or less strong interaction with the substrate) and airborne adsorbates. This is in agreement with the absence or presence of Au in, respectively, lower and higher regions.

To summarize, (i) the flat areas appearing with a low phase are graphene-covered rhenium regions, with no gold either on top or below the graphene sheet, (ii) the flat areas appearing with a higher phase are gold-intercalated graphene on rhenium regions, and (iii) the small spots appearing with a higher phase are non-intercalated clusters of gold.

### 3.b Scanning tunneling microscopy and spectroscopy



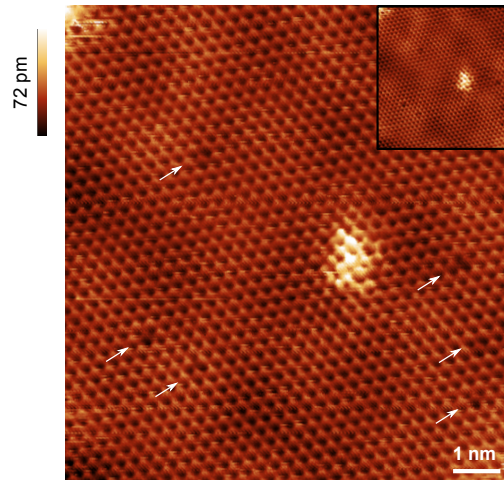
**Figure V.4: Scanning tunneling microscopy and spectroscopy performed on gold-intercalated graphene on Re(0001).** (a) Scanning tunneling topograph of graphene on Re(0001) after the deposition and intercalation of 0.6 ML Au, revealing three types of regions: the moiré pattern characteristic of graphene on Re(0001), gold-intercalated graphene on Re(0001), and regions with gold clusters on top of graphene.  $I_t = 5$  nA,  $V_t = -250$  mV,  $T = 100$  mK. Insets: (Top right) Scanning tunneling topograph overlaid with blue and red masks corresponding to graphene/Re and graphene/Au/Re regions, respectively. (Bottom left)  $(12 \text{ nm}^{-1} \times 12 \text{ nm}^{-1})$  Fast Fourier transform of a moiré region elsewhere on the surface, revealing the first moiré harmonics. (b) Conductance  $G_t(V_t)$  spectra measured for graphene/Re and graphene/Au/Re. Inset: Close-up view of the conductance  $G_t(V_t)$  spectrum of graphene/Re. (c) Scanning tunneling topograph with atomic resolution on gold-intercalated graphene on Re(0001), showing three-fold and six-fold periodicity.  $I_t = 5$  nA,  $V_t = -250$  mV,  $T = 100$  mK. (d) Conductance  $G_t(V_t)$  spectra measured in high and low regions of graphene/Au/Re.



Figure V.4(a) shows a typical STM image of graphene/Re(0001) partially intercalated with Au. It exhibits three types of regions: (i) graphene/Re(0001) regions featuring the characteristic moiré superlattice with a superperiodicity in the nanometer range - here, the moiré superlattice appears as a pattern of lines due to the convolution with the shape of the tip; the fast Fourier transform (bottom left inset of Figure V.4(a)) performed on a moiré region elsewhere on the surface more clearly highlights the characteristic hexagonal pattern, (ii) gold-intercalated graphene/Re(0001) regions forming 20-40 nm-large areas which appear much flatter (no visible moiré pattern at this scale) than graphene/Re(0001), and (iii) gold clusters on top of graphene having a high aspect ratio and presumably imaged multiple times by the tip for this reason (we will disregard these structures in the following). The first two types of regions, namely graphene/Re(0001) and graphene/Au/Re(0001), are highlighted in blue and red, respectively, in the top right inset of Figure V.4(a). Au-intercalated regions are 0.2-0.4 nm higher than non-intercalated regions, which corresponds to 1-2 intercalated gold monolayers.

A close-up STM view with atomic resolution of a gold-intercalated region is presented in Figure V.4(c). The top part of the image shows a six-fold periodicity with indiscernible contrast for the two carbon sub-lattices. The three-fold periodicity observed in the rest of the image can be attributed to a tip change and/or the sliding [222, 223] or vertical displacement of the top graphene layer [224, 225]. Although no clear periodic long wavelength pattern is observed in Figure V.4(c) (in other words, no moiré superlattice is observed), local variations of the apparent height, by as much as 80 pm (*i.e.* about two times less than in the graphene/Re(0001) moiré), are visible. The disorder observed in Figure V.4(c) might be due to stacking faults in the intercalated Au layer (with respect to the Re substrate) or strain in graphene associated with the intercalation process [92].

Figure V.5 shows a STM topograph with atomic resolution taken in a different intercalated region. A shallow moiré superlattice with a superlattice parameter of  $\simeq 2.3$  nm and a similar corrugation (80 pm) as the local variations in apparent height observed in Figure V.4(c), is visible. The observed periodicity is very close from that of the graphene/Re(0001) moiré, confirming that intercalated Au is pseudomorphic to Re(0001). The weak graphene corrugation is a signature of the much smaller graphene-Au interaction, compared to the graphene-Re interaction.



**Figure V.5: Scanning tunneling topograph with atomic resolution of defective graphene on Re(0001) intercalated with 0.6 ML Au.** Defects in the graphene lattice (C monovacancies) are highlighted with white arrows.  $I_t = 10$  nA,  $V_t = -1$  V,  $T = 100$  mK. Inset: Same scanning tunneling topograph. The moiré pattern is better visualized.

The local conductance was measured at different locations on the STM image shown in Figure V.4(a). Differential conductance spectra were acquired with a 10.6 mV modulation of the tip-sample bias voltage ( $V_t$ ) at 215 Hz. Representative spectra are displayed in Figure V.4(b). A marked conductance peak is

observed in graphene-covered Re(0001) regions around -0.1 eV. In gold-intercalated regions, a resonance is also found at -0.1 eV. This resonance is stronger and it is accompanied by a second one, centered closer to the Fermi level. The -0.1 eV resonance was previously observed in graphene/Re(0001) at the location of moiré hills (cf Chapter IV) and was attributed to an enhanced density of states in rhenium and carbon at the location of moiré hills, as evidenced by DFT calculations (DFT results will be briefly reminded in the next subsection). The enhanced density of states at the location of moiré hills results in an enhanced conductance in spectroscopy measurements. At the location of moiré valleys, such an enhanced conductance is not observed, probably due to the hybridization between the graphene and the metal states.

In the data shown in Figure V.4(a,b), the distance separating two spectroscopy measurements is 1.5 nm, hence we do not resolve the moiré-site dependent variations of the local density of states reported in Chapter IV. The persistence of the -0.1 eV resonance in gold-intercalated regions seems to indicate that graphene at the location of moiré hills and gold-intercalated graphene are somehow similar, *i.e.* they both exhibit a quasi free-standing character.

### 3.c DFT calculations

To discuss the possible origin of the extrema observed in the scanning tunneling spectroscopy data we make first-principles calculations of the local density of states. Four Re layers, one pseudomorphic Au layer, and a graphene layer were considered. A 10 Å-thick empty space was placed on top of graphene to avoid cross-talking between neighbour supercells in the periodic-boundary-conditions-simulations. The positions of the Re atoms in the third layer were fixed, while all other atoms were let free to move. The in-plane dimensions of the supercell correspond to a coincidence structure with  $(8 \times 8)$  graphene unit cells on top of  $(7 \times 7)$  Au/Re(0001). The low-energy states of graphene were simulated using a single  $k$  point, the corner (K) of the supercell. The system was converged until forces were less than 0.025 eV/Å. Match between the experimental and calculated energy positions is expected within no better than a few 100 meV given the deviation from the (necessarily) simple and ideal model that we used for the simulations.

Figure V.6 presents side views of the converged structures obtained for graphene/Re(0001) (calculated in Chapter IV) and graphene/Au/Re(0001). In the latter system, graphene is much flatter than in the former system: graphene corrugation amounts to 33 pm (*versus* 170 pm for the former system), consistent with the STM measurements (80 pm). We extract an average graphene-Au distance of 3.24 Å. This value is indicative of decoupled graphene. Overall, the intercalation of a Au layer between graphene and Re(0001) results in the lifting of the moiré valleys (the minimum C-metal distance goes from 2.10 Å to 3.12 Å).

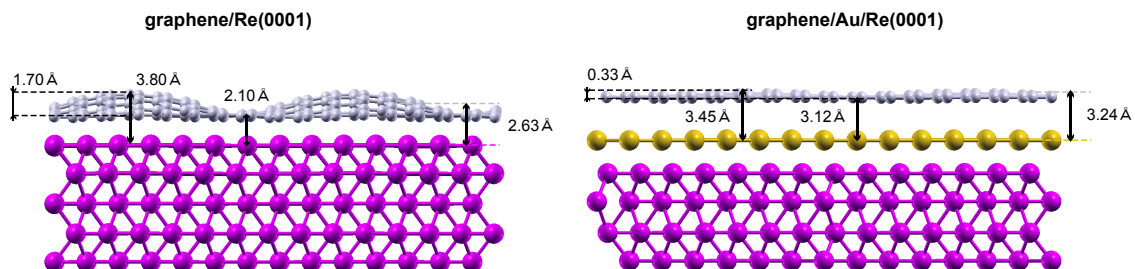
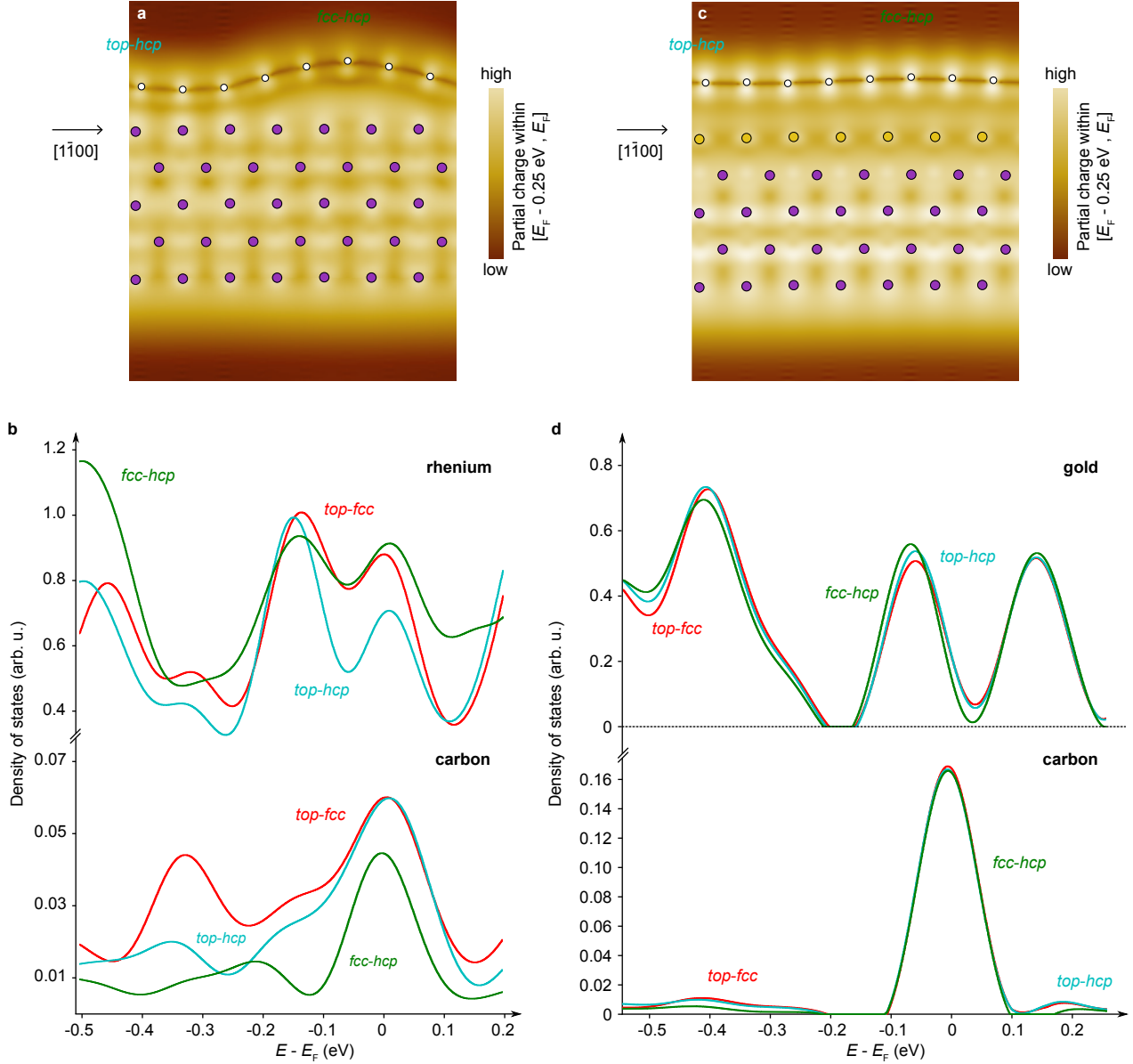


Figure V.6: Side views of the converged structures obtained for graphene/Re(0001) and graphene/Au/Re(0001). Graphene, rhenium and gold atoms are represented as white, pink and yellow balls, respectively. Graphene corrugation (taken as the maximum value of vertical separation between C atoms), the average C-metal distance (taken as the vertical separation between graphene and the topmost metal layer, whose heights are averaged over all atoms in the graphene layer and in the topmost metal layer, respectively), and the minimum/maximum C-metal distances (taken as the vertical separation between the lowest/highest C atom and the topmost metal layer) are indicated.

Figure V.7 recalls the DFT results reported in Chapter IV for graphene/Re(0001) (Figure V.7(a,b)) alongside the ones obtained here for graphene/Au/Re(0001) (Figure V.7(c,d)). When comparing the cross

sections of the partial charge integrated below the Fermi level for graphene/Re(0001) (Figure V.7(a)) and graphene/Au/Re(0001) (Figure V.7(c)), one can notice that, for graphene/Au/Re(0001), the hybridization between graphene and the orbitals of the terminal metallic layer (Au) does not depend on the local atomic stacking, as opposed to the spatially-varying hybridization with Re observed for graphene/Re(0001). The hybridization observed for graphene/Au/Re(0001) (Figure V.7(c)) is weak, similar to the one observed in hills of the moiré of graphene/Re(0001) (Figure V.7(a)), further indicating a somehow similar quasi free-standing character of graphene in both systems.



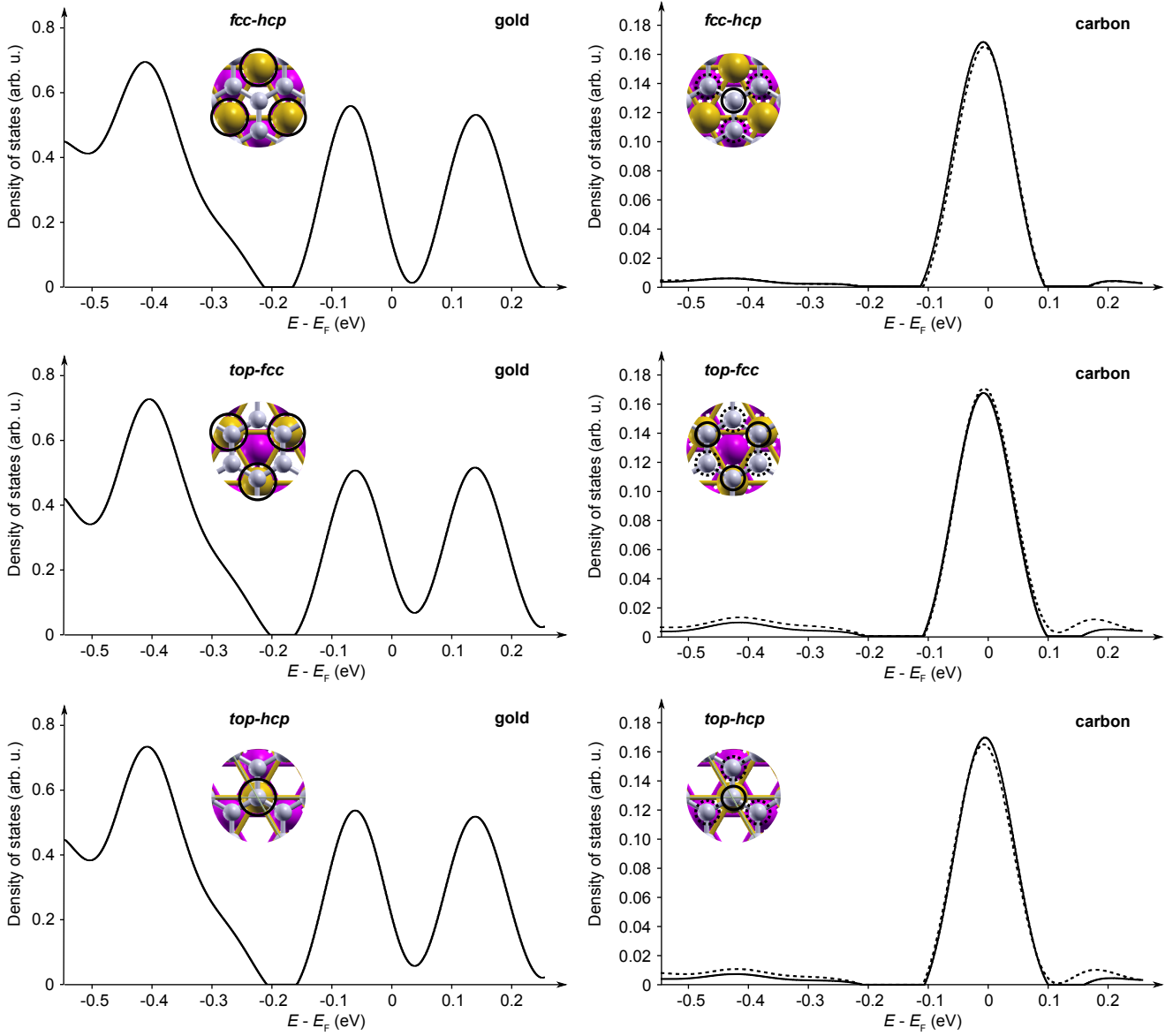
**Figure V.7: DFT results obtained for graphene/Re(0001) and graphene/Au/Re(0001)** (a) Cross-section of the partial charge integrated between the Fermi level ( $E_F$ ) and  $E_F - 0.25$  eV, along the  $[1\bar{1}00]$  direction, deduced from the DFT calculations on graphene/Re(0001). Graphene and rhenium atoms are schematically represented as white and pink balls, respectively. (b) Electronic density of states (electron energy  $E$ ) averaged over a few Re atoms (one and three respectively, top curves) and averaged over a few C atoms (four and six respectively, bottom curves) at the hills (*fcc-hcp*) and valleys (*top-fcc*, *top-hcp*) of the moiré, from DFT calculations. (c) Cross-section of the partial charge integrated between  $E_F$  and  $E_F - 0.25$  eV, along the  $[1\bar{1}00]$  direction, deduced from the DFT calculations on graphene/Au/Re(0001). Graphene, rhenium and gold atoms are schematically represented as white, pink and yellow balls, respectively. (d) Electronic density of states (electron energy  $E$ ) averaged over a few Au atoms (one and three respectively, top curves) and averaged over a few C atoms (four and six respectively, bottom curves) at the hills (*fcc-hcp*) and valleys (*top-fcc*, *top-hcp*) of the moiré, from DFT calculations.

Figure V.7(b) shows the density of states computed at the hills and valleys of the moiré of graphene/Re(0001) for Re atoms (top curves) and C atoms (bottom curves). The enhanced conductance observed in graphene/Re(0001) at -0.1 eV at the location of moiré hills (*fcc-hcp* region) was previously assigned to the marked peak in the density of states on C, located around the Fermi level (see Chapter IV, absolute energy values should be considered with caution). The absence of an enhanced conductance in the valleys (*top-hcp* and *top-fcc* regions) of graphene/Re(0001) despite the presence of a similar peak in the density of states on C, was attributed to a Re contribution, balancing out the contribution stemming from C atoms. Such compensation does not occur in hills (*fcc-hcp* region), hence the -0.1 eV resonance is observed.

We now turn to the density of states deduced from DFT calculations on graphene/Au/Re(0001). Similarly to the behaviour observed for the partial charge, the spatial variation of the density of states on Au atoms (Figure V.7(d), top curves) and C atoms (Figure V.7(d), bottom curves) is negligible. In particular, we find no significant variation in the energy positions of the observed maxima with respect to the local atomic stacking. This will be discussed later, in relation with the apparently contradictory behaviour observed in conductance measurements performed in different locations of gold-intercalated graphene on Re(0001) (Figure V.4(c,d)).

In fact, the density of states on C atoms, which is averaged over a few non-equivalent C atoms at the location of moiré hills (*fcc-hcp* region) and moiré valleys (*top-fcc* and *top-hcp* regions), shows no significant variation down to the atomic scale. Figure V.8 shows the density of states on the individual C and Au atoms considered for the calculation of the density of states in *fcc-hcp*, *top-fcc* and *top-hcp* regions. Regarding Au atoms, the density of states in the *fcc-hcp* and *top-fcc* regions corresponds to the density of states calculated on three equivalent Au atoms (forming a triangle pointing upwards for the *fcc-hcp* region and downwards for the *top-fcc* region). The density of states on Au atoms in the *top-hcp* region corresponds to the density of states on the Au atom located exactly at the center of the said region. No atomic scale variation is observed for Au atoms. Regarding C atoms, the density of states in the *fcc-hcp* and *top-hcp* regions was computed considering four C atoms: three equivalent C atoms forming a triangle pointing downwards for *fcc-hcp* and upwards for *top-hcp*, plus one C atom located exactly at the center of the said regions. The density of states on C atoms in the *fcc-hcp* and *top-hcp* regions shown in Figure V.7 consists in the average density of states on all four C atoms. For both regions, the density of states calculated for the three equivalent atoms and for the fourth atom are very similar. As for the density of states on C atoms in the *top-fcc* region, we considered six C atoms: three equivalent C atoms forming a triangle pointing upwards and three equivalent C atoms forming a triangle pointing downwards. Again, the density of states in the two inequivalent sites are hardly discernable from one another. The density of states on C atoms in the *top-fcc* region shown in Figure V.7 consists in the average density of states on all six C atoms. This uniform behaviour, down to the atomic scale, further supports a weak graphene-Au interaction.

We now go back to considering average densities of states (Figure V.7). Regarding the density of states on C atoms, one marked peak around the Fermi level is found in the calculations (with no additional feature). In agreement with the conclusion previously drawn for graphene-covered Re(0001), we suggest that this peak is at the origin of the enhanced conductance observed at -0.1 eV in gold-intercalated graphene on Re(0001). The lower magnitude of the conductance peak measured in graphene/Re(0001) regions compared to graphene/Au/Re(0001) (Figure V.4(b)) can be attributed to two effects. Firstly, the magnitude of the peak around the Fermi level in the C density of states (which is related to the presence of the -0.1 eV resonance in conductance measurements) is twice smaller for graphene/Re(0001) than for graphene/Au/Re(0001). Secondly, the spectroscopy measurements presented in Figure V.4(b) do not resolve the moiré-site dependence of the conductance. Consequently, the averaging of the conductance across the different (electronically very different) sites of the moiré pattern of graphene/Re(0001) result in a decreased magnitude of the -0.1 eV resonance, with respect to the one observed for the homogeneously decoupled graphene/Au/Re(0001).

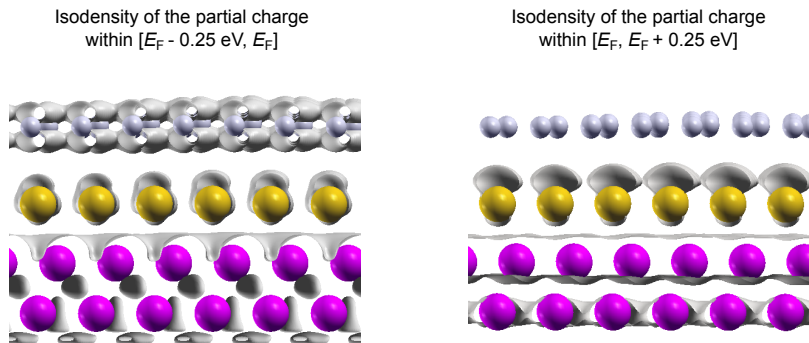


**Figure V.8: Density of states of individual Au and C atoms at the hills (*fcc-hcp*) and valleys (*top-fcc*, *top-hcp*) of the moiré.** Top: Electronic density of states (electron energy  $E$ ) of individual Au and C atoms in the *fcc-hcp* region. The density of states was calculated on three equivalent Au atoms (left), and on four (three equivalent + one) C atoms (right). Middle: Electronic density of states (electron energy  $E$ ) of individual Au and C atoms in the *top-fcc* region. The density of states was calculated on three equivalent Au atoms (left), and on six (three equivalent + three equivalent) C atoms (right). Bottom: Electronic density of states (electron energy  $E$ ) of individual Au and C atoms in the *top-hcp* region. The density of states was calculated on one Au atom (left), and on four (three equivalent + one) C atoms (right). Electronic density of states are plotted with solid and dotted lines. The type of line used to circle a specific atom shown in one of the insets matches the type of line used to plot the density of states on this specific atom.

Regarding the density of states on Au atoms, two marked maxima at about -0.08 eV and 0.15 eV are observed. We suggest that the higher-energy maximum is responsible for the intense close-to-Fermi resonance, which is only present in gold-intercalated graphene, as shown in Figure V.4(b). The lower-energy maximum is absent from conductance measurements. To rationalize the presence of only one of the two maxima of the Au density of states in conductance measurements, we compare the electronic isodensity of partial charge integrated in the energy ranges covered by the said maxima ( $[-0.25, 0]$  eV and  $[0, 0.25]$  eV, respectively). For both energy ranges, the isodensity related to Au atoms remains mainly located close to the Au atoms. They extend only marginally above the Au layer, towards the graphene sheet (Figure V.9). By contrast, we observe a significant difference between the isodensity related to C atoms in the two energy ranges: the isodensity related to C atoms forms lobes extending above and below the graphene sheet in the lower-energy range ( $p_z$  orbital, see



Figure V.9 left), while in the higher-energy range there is virtually no extension of the C isodensity beyond the radius of C atoms (Figure V.9, right). We propose that graphene is transparent in the higher-energy range, which results in making conductance measurements very sensitive to the underlying Au atoms, similarly to what was observed in Refs. [226, 227, 228, 229, 230, 231]. For this reason, only the higher-energy feature in the Au density of states is observed in conductance measurements.



*Figure V.9: Electronic isodensity in the energy ranges covered by the lower- and higher-energy maxima of Au density of states.* Graphene, rhenium and gold atoms are schematically represented as white, pink and yellow balls, respectively. **Left:** Electronic isodensity integrated between  $E_F - 0.25$  eV and  $E_F$ . **Right:** Electronic isodensity integrated between  $E_F$  and  $E_F + 0.25$  eV.

Overall, the two resonances observed in conductance measurements performed on gold-intercalated graphene on Re(0001) at -0.1 eV and close to the Fermi level are assigned to maxima appearing close to the Fermi level in the C density of states, and around 0.15 eV in the Au density of states, respectively.

### 3.d Topography-dependence in conductance measurements

The local conductance was measured in different locations of the gold-intercalated graphene region shown in Figure V.4(c). Figure V.4(d) shows representative spectra taken in the “high” and “low” regions of gold-intercalated graphene indicated in Figure V.4(c). They exhibit the two resonances mentioned earlier (the -0.1 eV resonance and the close-to-Fermi resonance). Both resonances are found at lower energies in the high regions compared to the low regions: the shift amounts up to 30 meV. At first sight, this seems in contradiction with the DFT results. Indeed, the density of states on both C and Re atoms for the graphene/Au/Re(0001) system exhibit a negligible variation of the energy positions of the maxima with respect to the local atomic stacking.

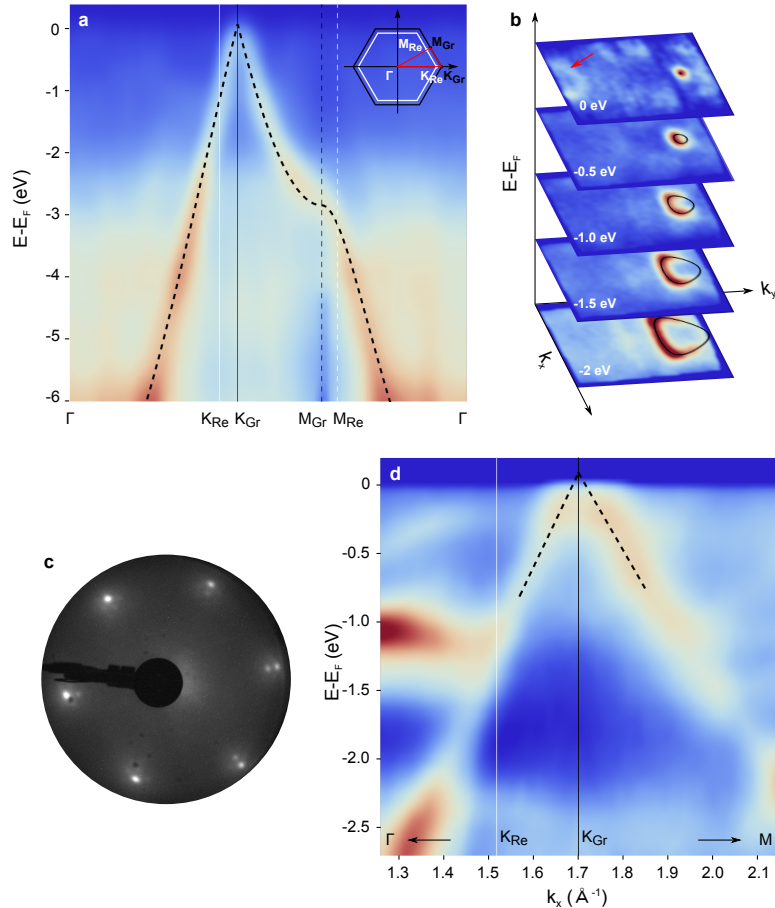
The shift observed in conductance measurements is ascribed to a spatial variation of the  $p$ -doping. Contrary to what is observed in Figure V.5, the local variations of the apparent height in Figure V.4(c) do not form a periodic moiré pattern. As mentioned before, the disorder observed in Figure V.4(c) could be related to stacking faults in the intercalated Au layer (with respect to the Re substrate) or strain in graphene associated with the intercalation process [92]. For this reason, we do not expect DFT calculations to reproduce the spatial variations observed in this disordered region.

In any case, graphene is found to be less  $p$ -doped in high regions than in low regions. According to Ref. [71], we expect a higher  $p$ -doping when the C-Au distance is higher hence the variations in apparent height do not directly translate variations in the C-Au distance. We propose two possible explanations for the observed variations. Firstly, it could be that the high regions correspond to regions with clustered Au atoms. Indeed, it was shown that in such cases graphene is pulled closer to the Au nanocluster, hence the C-Au distance is decreased [114]. In that scenario, high regions would correspond to regions where the C-Au distance is smaller, and low regions would correspond to regions where the C-Au distance is higher.

Secondly, we propose that spatial variations in the stretching of C atoms could be at the origin of the spatial variation of the  $p$ -doping [232].

## 4 Quasi free-standing character of gold-intercalated graphene on Re(0001)

### 4.a Dirac cone of quasi free-standing graphene



**Figure V.10: ARPES measurements on graphene on Re(0001) intercalated with 1.2 ML of Au.** (a) Photoemission intensity plot along the  $\Gamma$ -K-M- $\Gamma$  direction of Gr/(1.2 ML Au)/Re(0001). Inset: Reciprocal space sketch showing the  $\Gamma$ -K-M- $\Gamma$  direction (in red). (b) Energy slices of the photoemission intensity, evidencing the trigonal warping of graphene  $\pi$  state. The presence of a parabolic state at  $\Gamma$  with a minimum at about -0.2 eV is indicated with a red arrow. A first-nearest neighbour tight-binding fit is performed on graphene  $\pi$  state on both (a) and (b) plots (black solid lines) [234]. (a) and (b) plots were acquired with an HeII source (40.8 eV photon energy). (c) LEED pattern of graphene/Re(0001) intercalated with 1.2 ML Au, measured with 80 eV electrons. (d) Photoemission intensity plot (zoom around the K points) along the  $\Gamma$ -K-M direction (neither  $\Gamma$  nor M are reached), with an HeI source (21.2 eV photon energy). A linear fit is performed on the branches of graphene  $\pi$  state (black dashed lines). The Dirac point is found at the intersection of the black dashed lines.

Photoemission measurements were performed on graphene/Re(0001) intercalated with 1.2 ML of Au, to maximize the surface fraction of intercalated graphene. No moiré satellite spots are visible in LEED after intercalation, in contrast to the case of the 0.6 ML of Au deposition addressed previously (compare Figures V.10(c) and V.2(c,c')). As we have discussed, intercalation quenches the moiré pattern, so our observation points to a close-to-total intercalation of graphene/Re(0001) with Au. Figure V.10(a) displays the electronic band structure along the  $\Gamma$ -K-M- $\Gamma$  direction of graphene on Re after the intercalation of Au, with an HeII source. The  $\pi$  band shows a clear linear dispersion, with a crossing (Dirac) point above the Fermi level. No  $\pi^*$  band is observed. These observations are reminiscent of others made with related systems [60, 97, 98, 233, 101, 103], and suggest that graphene recovers (compared to graphene/Re(0001))

a free-standing character. A first-nearest neighbour tight-binding fit was performed on the  $\pi$  state of graphene (see Figure V.10(a)), following the model described in Ref. [234]. The refined fit parameters are:  $\epsilon_{2p} = 65$  meV,  $\gamma_0 = -2.98$  eV and  $s_0 = 0.028$ , where  $\epsilon_{2p}$ ,  $\gamma_0$  and  $s_0$  are the on-site energy parameter, the tight-binding hopping parameter and the overlap parameter, respectively. The fitting procedure shows that the Dirac point is above the Fermi level, *i.e.* graphene is slightly  $p$ -doped. This finding is consistent with experimental observations on related systems, namely graphene-on-metal systems intercalated with Au, graphene with adsorbed Au adatoms and graphene/Au(111), made with ARPES [107, 116, 101, 102, 97], quasiparticle interferences [104, 235] and STS [236] measurements, as well as theoretical calculations [71, 237, 232]. In contrast, on graphene/Re(0001), Ag [60] and Pb [95] intercalation resulted in  $n$ -doping of graphene.

Figure V.10(d) shows a close-up view of the electronic band structure around the K point, with an HeI source. A linear fit was performed on the branches of graphene  $\pi$  state (black dashed lines). The Dirac point is found at the intersection of the black dashed lines,  $66 \pm 40$  meV above the Fermi level, in good agreement with the tight-binding fit mentioned before. We observe no sign of moiré replica bands or minigaps along the  $\pi$  band related to the moiré superpotential which were observed in other systems [53, 72, 73, 74, 75, 76]. This once more shows that the interaction between graphene and Au is very weak. Whether a graphene-substrate interaction-related kink is present along the  $\pi$  band, that would arise due to the Au layer [107], cannot be established. The trigonal warping of the  $\pi$  band is clearly observed starting from 1 eV below the Fermi level in the  $(k_x, k_y)$  cuts of the band structure shown in Figure V.10(b).

Besides the Dirac cone, the band structure of gold-intercalated graphene on Re(0001) presents a parabolic state at  $\Gamma$  with a minimum at about -0.2 eV. This state was not observed before Au intercalation. It can be seen in Figure V.10(b) on the energy slice taken at the Fermi level, indicated with a red arrow. This state may correspond to an electronic state in Au. The Shockley surface state of Au(111) was shown to survive underneath graphene in gold-intercalated graphene on Ir(111) [104], shifted by  $\simeq 100$  meV to lower binding energy compared to the value of -505 meV observed for Au(111) single-crystals [238]. This shift was attributed to the finite intercalated Au film thickness ( $\simeq 20$  ML of Au). The presence of graphene may also have contributed to the energy shift, as it was demonstrated for the Cu(111) Shockley state [239]. Here, the electronic state measured in ARPES is shifted by  $\simeq 300$  meV with respect to the Shockley state of Au(111) single-crystals, which can be attributed to the presence of graphene and, more importantly, to the reduced thickness of the intercalated Au film (1 ML) compared with Ref. [104]. We propose that the state observed in ARPES corresponds to the maximum appearing at about -0.08 eV in Au density of states (Figure V.7), for which we previously gave an explanation of its absence from conductance measurements.

## 4.b Raman modes of quasi free-standing graphene

The observation of quasi free-standing electronic properties in graphene/Au/Re(0001) suggests that the characteristic G and 2D vibration bands of graphene could be observable in Raman spectroscopy. Indeed, unlike in the case of graphene/Re(0001) [60] or graphene/Ru(0001) [62, 63, 64], the  $\pi \leftrightarrow \pi^*$  electronic transitions are compatible with the Raman processes. The expected weak interaction between Au and graphene should not alter the Kohn anomalies of the phonon dispersion of isolated graphene, appearing as kinks in the phonon dispersion of the LO mode at  $\Gamma$  and of the TO mode at K, which are involved in the Raman G and 2D modes of graphene, respectively [15].

Figure V.11 shows Raman spectra of graphene on Re(0001) before and after the intercalation of 0.6 ML, 1.2 ML and 2.6 ML of Au. In the explored wavenumber range ( $800\text{-}3200$   $\text{cm}^{-1}$ ), the background related to luminescence from the substrate is rather high. A quadratic background was substrated from all four spectra, to recover comparable baselines.

We start with a short discussion on the Raman spectrum measured on graphene/Re(0001) (without intercalant). For this particular measurement, graphene growth was performed on a rhenium thin film.



The sample, called “AK49”, was prepared by Amina Kimouche and measured in Raman spectroscopy by Alexandre Artaud. For information on graphene growth on Re thin films, we refer the reader to Chapter II. As mentioned before, this procedure yields single-layer graphene covering the whole sample surface. No specific Raman signal is observed, and in particular no G or 2D band is detected (Figure V.11(a)). This is consistent with the large electronic bandgap found in the ARPES data (Figure V.1(b)) between the  $\pi$  and  $\pi^*$  electronic bands, due to which no electronic transition with sufficiently low energy is available in graphene to make the Raman processes active [18].

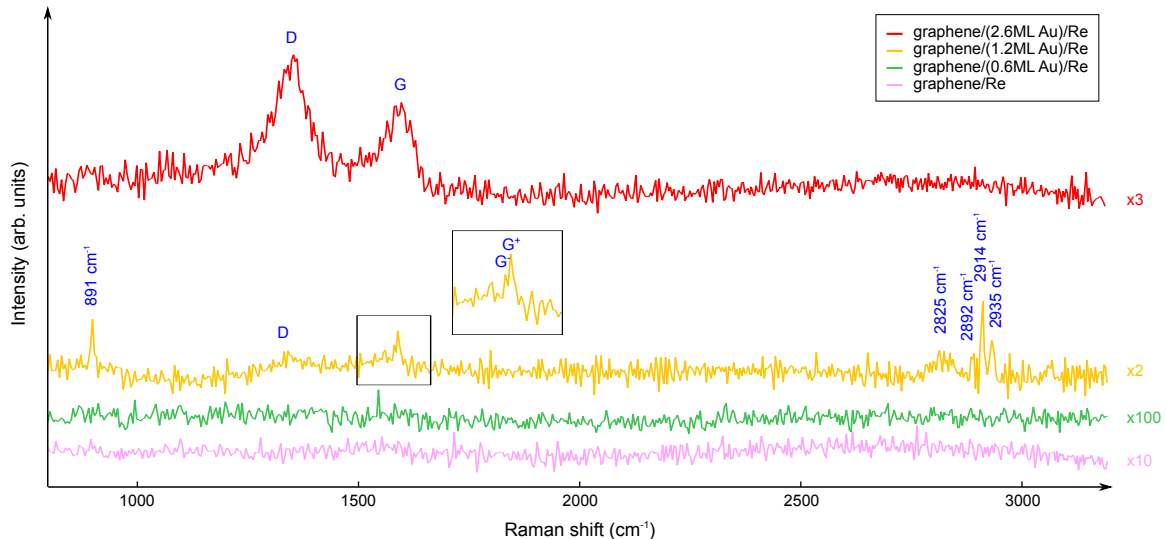


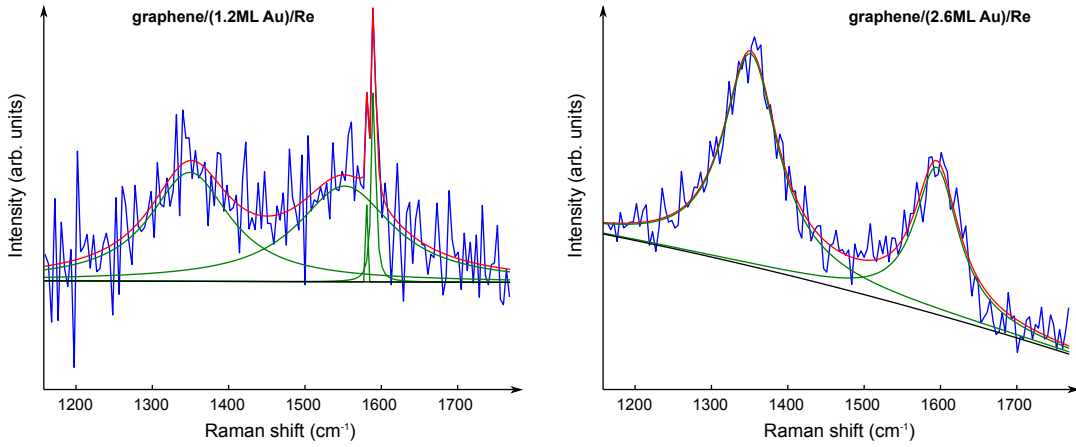
Figure V.11: Background-subtracted Raman spectra of graphene on Re(0001) before and after the intercalation of 0.6 ML, 1.2 ML and 2.6 ML of Au. Raman spectroscopy measurements were performed with a 532 nm and 1.2 mW/ $\mu\text{m}^2$  laser excitation. Spectra are offset for clarity.

The G and 2D bands are not observed either after the intercalation of 0.6 ML of Au, at odds with our expectations for graphene decoupled from its substrate (*via* the Au intercalant). We conclude that the background level is too high and the graphene vibration modes are too weak for this fraction of intercalated graphene.

For larger amounts of intercalated Au (1.2 and 2.6 ML), we do observe some of the typical graphene vibration bands. Graphene vibration bands are fitted with Lorentzians in a reduced wavenumber range (1160–1770  $\text{cm}^{-1}$ ). A linear and a quadratic background is subtracted for graphene on Re(0001) intercalated with 1.2 and 2.6 ML of Au, respectively (Figure V.12). The G peak appears at 1595  $\text{cm}^{-1}$  in (2.6 ML Au)-intercalated graphene on Re. It is split into two peaks in (1.2 ML Au)-intercalated graphene on Re, referred to as  $G^-$  and  $G^+$  in Figure V.11, pointing to a lifting of the degeneracy of the  $E_{2g}$  mode due to uniaxial strain [33, 34]. The splitting is reproducible: it is observed in many different regions of the sample. The two bands  $G^-$  and  $G^+$  are positioned at 1580  $\text{cm}^{-1}$  and 1589  $\text{cm}^{-1}$  respectively. The measured positions of the G peaks in (1.2 ML Au)- and (2.6 ML Au)-intercalated graphene on Re are compatible with the slight *p*-doping measured in ARPES, as we expect little to no upshift of the G peak [28, 29] with respect to undoped graphene (1585–1590  $\text{cm}^{-1}$ ). Besides, the position of the G peak might be slightly overestimated in (2.6 ML Au)-intercalated graphene on Re, since, as it will be discussed later, it is likely that the broad feature appearing at 1595  $\text{cm}^{-1}$  is composed of both the G and  $D'$  peaks.

Our measurements reveal no 2D band, the overtone of the D band that is active even without defects. Indeed, from the D band wavenumber (around 1350  $\text{cm}^{-1}$ , see later) the 2D band’s wavenumber would be 2700  $\text{cm}^{-1}$ . We attribute the absence of the 2D band to a broadening and concomitant reduction of intensity of the 2D peak due to defects [24, 25] (as we will see later, the level of defects is quite high in our intercalated samples). We expect that these effects lead to a 2D band below the background level, hence not detected in practice.

The D peak, which stems from a double-resonance scattering process in the presence of defects, appears at  $1349\text{ cm}^{-1}$  and  $1351\text{ cm}^{-1}$  for (1.2 ML Au)- and (2.6 ML Au)-intercalated graphene on Re, respectively. These values are consistent with Refs. [21] and [240], where the D peak was measured around  $1345\text{ cm}^{-1}$  and  $1350\text{ cm}^{-1}$ , respectively, at our excitation energy.



**Figure V.12: Fitting of the Raman spectra of graphene on Re(0001) after the intercalation of 1.2 ML and 2.6 ML of Au.** **Left:** Raman spectrum of graphene on Re(0001) after the intercalation of 1.2 ML of Au. The D,  $G^+$  and  $G^-$  peaks are fitted with lorentzians, on a quadratic background. A fourth lorentzian is used to account for the specific background at the location of the  $G^+$  and  $G^-$  peaks. **Right:** Raman spectrum of graphene on Re(0001) after the intercalation of 2.6 ML of Au. The D and G peaks are fitted with lorentzians, on a linear background.

## 5 Defects in gold-intercalated graphene on Re(0001)

We now turn to a discussion on the level of defects in intercalated graphene. The width of the Raman bands informs on the quantity of defects in our samples. We choose to focus on (2.6 ML Au)-intercalated graphene on Re, as the signal-to-noise ratio is higher and hence allows a quantitative analysis. Cançado *et al.* introduced two methods for assessing the inter-defect distance  $L_D$  based on the analysis of the D and G peaks [25]. First, we extrapolate the width of the D band we measured with a 532 nm laser excitation ( $87 \pm 6\text{ cm}^{-1}$ ) to the range explored by Cançado *et al.*, assuming a linear dependence with wavenumber [21]. The G band width ( $70 \pm 7\text{ cm}^{-1}$ ) being non-dispersive, does not need to be extrapolated. These widths are higher than the highest values reported in Ref. [25] for graphene subjected to  $\text{Ar}^+$  ion bombardment, suggesting that  $L_D$  is below 2 nm.

To obtain a better estimate of  $L_D$  we turn to the second method described by Cançado *et al.*, which was also proposed by Lucchese *et al.* in Ref. [24]. The relative intensity of the G and D bands  $I_D/I_G$  can be used to assess the fraction area around defects where the scattering processes responsible for the D mode occur [24, 25]. In turn, this provides an estimate of  $L_D$ . Here again we must extrapolate the  $I_D/I_G$  value of  $1.4 \pm 0.1$  that we measured with a 532 nm source to the range covered in Ref. [25]. Using the wavelength- $I_D/I_G$  linear dependence determined in Refs. [21, 241], we deduce  $L_D \simeq 1\text{ nm}$ .

Finally, using the quadratic form proposed by Ferrari *et al.* [23, 18], we derive  $L_D \simeq 1.5 \pm 0.1\text{ nm}$ .

All three estimates of the distance between defects seem consistent and correspond to a  $10^{14}\text{ cm}^{-2}$  defect density. Obviously, these estimates apply only to Raman-active defects. For such a high level of defects, one can consider that the broad feature appearing at  $1595\text{ cm}^{-1}$  is actually composed of both the G and D' peaks [24, 25]. The D' peak is a disorder-induced peak located around  $1620\text{ cm}^{-1}$ . Interestingly, our estimate is close to the ones we deduce, using the same three methods, in related systems, namely graphene/Ru(0001) intercalated with Pb [103] and graphene/SiC(0001) intercalated with Au [101].

What the source and nature of the defects are is a natural question. Graphene on Re(0001) already contains a certain amount of defects prior to intercalation [159]. These defects are first the boundaries

that surround single-crystal graphene grains with size of the order of few tens of nanometers. Other kinds of defects may be point defects, *e.g.* C vacancies. The intercalation process itself may induce defects such as monovacancies or divacancies in graphene [94], *via* for instance a strong interaction between Au monomers and graphene [214]. A Cu penetration path beneath graphene was proposed to occur via metal-aided defect formation with no or poor self-healing of the graphene sheet for the Cu intercalation of graphene/Ir(111) [94]. Point defects in graphene [85, 86, 87, 88, 89] and graphene edges [89, 90, 91, 92] have also been proposed to be potential intercalation pathways. Another mechanism, based on the material diffusion via metal-generated defects, followed by the subsequent healing of the graphene lattice, has been suggested [93, 87].

Figure V.5 shows an atomically-resolved STM image taken on a Au-intercalated graphene region, revealing a damaged graphene sheet at the atomic scale. Carbon monovacancies are indicated with white arrows. Other defects similar to the one visible in the center of the STM image are observed in intercalated regions. They may correspond to defects in the intercalated Au layer. Our STM observations support a typical distance of the order of 1 nm between point defects in intercalated graphene (see Figure V.5). We propose that these defects were created upon intercalation.

We observe other Raman bands, at 891, 2825, 2892, 2914 and 2935  $\text{cm}^{-1}$  in graphene/(1.2 ML Au)/Re (Figure V.11(c)). The phonon dispersion curve of rhenium was calculated in Ref. [242]. The energy of the highest energy rhenium phonon is  $\simeq 23$  meV, hence a first-order scattering process involving this phonon would result in a 190  $\text{cm}^{-1}$  Raman shift. It is therefore excluded that any of the five bands mentioned before corresponds to a first-order or a second-order scattering process involving rhenium phonons. These peaks could instead relate to the minority rhenium carbide phase coexisting with graphene. The highest-energy band could also correspond to the D+D' feature in graphene, that is linked to the presence of defects [25, 18].

## 6 Superconducting properties

Figure V.13 shows normalized conductance spectra measured at low bias voltage (with a 10  $\mu\text{V}$  modulation of the tip-sample bias voltage ( $V_t$ ) at 220 Hz) and at 65 mK on graphene-covered Re(0001) and gold-intercalated graphene on Re(0001). The conductance spectra are hardly discernible from one another and can be well fitted with the standard Bardeen-Cooper-Schrieffer (BCS) model. The same superconducting gap  $\Delta = 280 \pm 10$   $\mu\text{eV}$  is observed uniformly on the surface, on both intercalated and non-intercalated regions. In other words, intercalation of gold in between graphene and Re(0001) does not alter the rhenium-induced superconductivity in graphene.

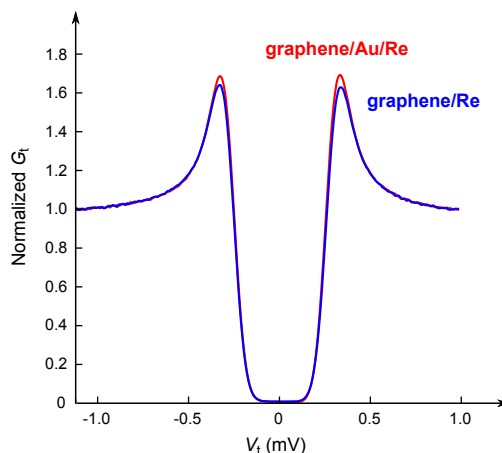


Figure V.13: Normalized conductance  $G_t(V_t)$  spectra measured on graphene/Re and graphene/Au/Re.  $T = 65$  mK.

The superconducting gap measured here is slightly different from the one reported in Ref. [3] ( $330 \pm 10 \mu\text{eV}$ ) on a graphene-covered Re(0001) thin film. The value reported in Ref. [3] is rather high compared with the superconducting gap measured on bare Re thin films ( $\simeq 255 \mu\text{eV}$  [243]). It was attributed to the presence of C atoms dissolved into the bulk of the Re thin film, as a result of the bulk saturation/segregation process at the origin of graphene growth. For graphene grown on Re(0001) single-crystal (our sample), the substrate can be viewed as an infinite reservoir of rhenium atoms, hence we do not expect to saturate the Re bulk with dissolved C atoms. The superconducting gap we measure is therefore closer to the value measured for bare Re.

## Conclusions

We have investigated the structural, electronic and vibrational properties of graphene on Re(0001) intercalated with Au, by means of RHEED, LEED, AFM, STM/STS, ARPES, Raman spectroscopy measurements, and DFT calculations. Our data consistently show that graphene recovers a free-standing character after Au intercalation, in sharp contrast with the strongly hybridized graphene-on-Re(0001). This is apparent in the electronic band structure, in the flattening of the graphene topography, in the disappearance of the moiré-related streaks in diffraction measurements, and in the vibrational spectra of graphene. The weak corrugation observed in STM, as well as the absence of minigaps and replicas in ARPES indicate a weak graphene-Au interaction. The vibrational spectra allowed us to assess the density of defects in the systems, which is high, with a typical distance between phonon scattering centers of the order of 1 nm. This value indicates that a high density of defects is created in graphene during the process of intercalation. Obviously, this is a serious issue often overlooked in works relying on intercalated graphene. This is expected to translate in a limitation of the homogeneity of graphene's physical (electronic, vibrational) and chemical (reactivity and impermeability) properties. Electronic features in the conductance spectrum of graphene/Au/Re(0001) are well reproduced by DFT calculations. The -0.1 eV resonance is related to the quasi free-standing character of graphene/Au/Re(0001). A second feature, located close to the Fermi level, is related to the presence of Au. Finally, the rhenium-induced superconducting properties of graphene are not altered by gold intercalation.



# MOLECULAR ASSEMBLIES OF VERDAZYL RADICALS ON Cu(111)

## Contents

---

1	Verdazyl radicals . . . . .	<b>102</b>
1.a	Magnetic properties . . . . .	103
1.b	Verdazyl radicals on surfaces . . . . .	105
2	Synthesis and characterization . . . . .	<b>106</b>
2.a	Synthesis . . . . .	106
2.b	Electron spin resonance . . . . .	108
2.c	UV-visible spectroscopy . . . . .	109
2.d	Raman spectroscopy . . . . .	109
3	Sublimation temperature and stability . . . . .	<b>110</b>
3.a	Protocol . . . . .	110
3.b	TMOV molecules . . . . .	112
3.c	DOBV molecules . . . . .	113
4	DOBV deposition on metals . . . . .	<b>114</b>
4.a	Experimental adjustments . . . . .	114
4.b	RHEED monitoring . . . . .	115
4.c	DOBV molecular assemblies on Cu(111) . . . . .	116

---

## Abstract

Two verdazyl radical compounds synthesized by chemist colleagues were considered as potential candidates for realizing spin molecular systems on quasi-free standing superconducting graphene. As these compounds were never investigated before on surfaces, we undertook a study of their sublimation temperature in vacuum and ultra-high vacuum environments. Although we did not deposit these compounds on quasi-free standing superconducting graphene yet, we present in this Chapter preliminary results obtained on a model system, namely Cu(111). The precise structure of the molecular assemblies observed by means of STM could not be determined and requires further investigations. The thermal stability of the compounds of interest is discussed.

## Introduction

Stable free radicals have always been of fundamental interest to chemists either as spin probes [244, 245], as key components of magnetic materials [246] or as polymerization inhibitors or mediators [247]. Here, the use of stable free radicals was intended, as explained in Chapter I, to build molecular spin systems on quasi-free standing superconducting graphene. Although we could not succeed in preparing such a sample - where quasi free-standing superconducting graphene would be, for instance, gold-intercalated graphene on Re(0001), and magnetic molecules would be deposited on top - in this Chapter we present preliminary results obtained with stable free radicals deposited on a model system, namely the (111) surface of copper.

A very limited number of stable organic radicals have been reported so far in the literature, among which one can find triphenylmethyl, nitroxide and various heterocyclic radicals (Figure VI.1). Verdazyl radicals belong to the latter category. The type of verdazyl and its properties mainly depend on the nature of the atom introduced in the ring at position 6: type I (saturated carbon atom), type II (carbonyl or thiocarbonyl function) and type III (phosphorus or boron atom) (Figure VI.1) [248]. In this Chapter we will present preliminary results involving type II verdazyl radicals deposited on Cu(111).

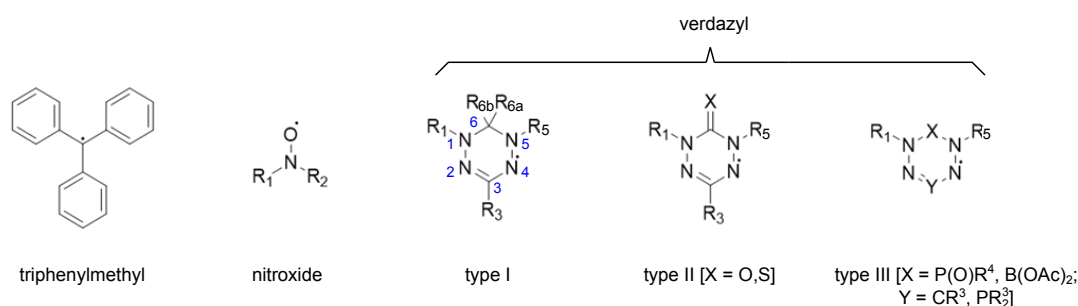


Figure VI.1: **Different types of stable organic radicals.** The positions 1, 2, 3, 4, 5 and 6 in the ring of verdazyl radicals are indicated in blue. Courtesy of Shagor Chowdhury.

## 1 Verdazyl radicals

Oxoverdazyl radicals (type II, X = oxygen) are particularly attractive due to their robustness and relatively straightforward synthesis. They are known to be stable under ambient conditions due to the delocalization of the spin density over the four nitrogen atoms (Figure VI.2). Such species are also sterically protected by the R groups introduced at the positions 1, 3, and 5. Their stability has nevertheless been shown to depend on the nature of the R group introduced at position 3 [249]. Oxoverdazyl radicals can moreover be readily identified with different analysis techniques including absorption spectroscopy with signals observed in the visible range. The resonance forms of oxoverdazyl radicals are shown in Figure VI.2.



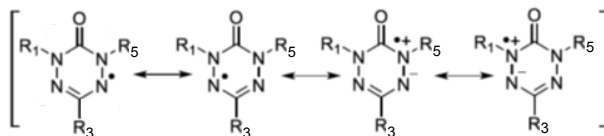


Figure VI.2: Resonance forms of oxoverdazyl radicals. Courtesy of Shagor Chowdhury.

One of the advantages of verdazyl radicals is that they constitute functionalizable compounds. The substituents can be chosen in order to improve the adhesion of the molecule on a particular surface, to promote magnetic properties [250] or to promote intermolecular interactions [248] in view of controlling the assembly of 2D molecular systems.

## 1.a Magnetic properties

### Intramolecular coupling

The linking of radicals *via* covalent bonds has long been a popular approach to spin coupling in molecular radical systems [251]. In the case of di- and polyradicals, the intramolecular exchange is generally stronger when the individual spin centers and the molecular substructure which links them are all  $\pi$ -conjugated [250]. For instance, the intramolecular interaction is higher when the spin centers are linked through aromatic groups. In fact, for such molecules, it has been established that the nature of the intramolecular interaction (ferromagnetic or antiferromagnetic) can be predicted: two radicals linked “meta on a benzene” generally lead to ferromagnetically coupled radicals (Figure VI.3, left), while para-linked systems lead to antiferromagnetically coupled systems (Figure VI.3, right) [250] – the terms meta and para are used to denote the relative locations of the substituents on a di-substituted aromatic ring: in a meta configuration, the two substituents appear on atoms of the aromatic ring separated by one atom, while in a para configuration, the two substituents are located on opposite atoms of the aromatic ring (Figure VI.3). This chief result is also known as the alternation rule: the spin flips everytime the electron jumps from one site to another.

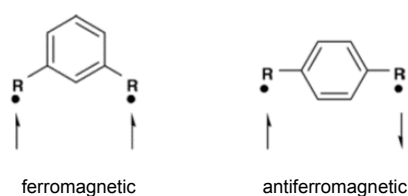


Figure VI.3: Spin preferences for diradicals linked “meta on a benzene” and “para on a benzene”. Figure adapted from Ref. [250].

In the case of verdazyl radicals, several di- and polyradicals were synthesized, with linkers at either one of the nitrogen atoms of the ring or the C3 carbon atom [250]. When the adjoining atom exhibits small spin density, the linked radicals are expected to be weakly coupled. Consequently, the respective small and substantial spin densities at C3 and on the N atoms are expected to result in, respectively, weak and strong intramolecular interactions [250].

In 2007, Gilroy *et al.* reported a study of the magnetic properties of two benzene-bridged diradicals, which will be referred to as compound A1 and compound B, respectively [249]. As can be seen in Figure VI.4, compound A1 is a para-bridged diradical, while compound B is the meta analogue of compound A. Gilroy *et al.* showed that compound A1 is weakly antiferromagnetically coupled while compound B is weakly ferromagnetically coupled, in agreement with the alternation rule [249]. Compound

A2 is, as compound A1, a para-bridged diradical. Its magnetic properties were reported in Ref. [252]: the two radicals within compound A2 are strongly antiferromagnetically coupled. This behaviour is in agreement with the alternation rule and shows that changing the N,N'-substituents to a verdazyl diradical can significantly modify the intramolecular interaction. We will discuss again compounds A1 and A2 later in the Chapter, since, as we will see, they are very similar to one of the compounds (DOBV) synthesized by our chemist colleagues.

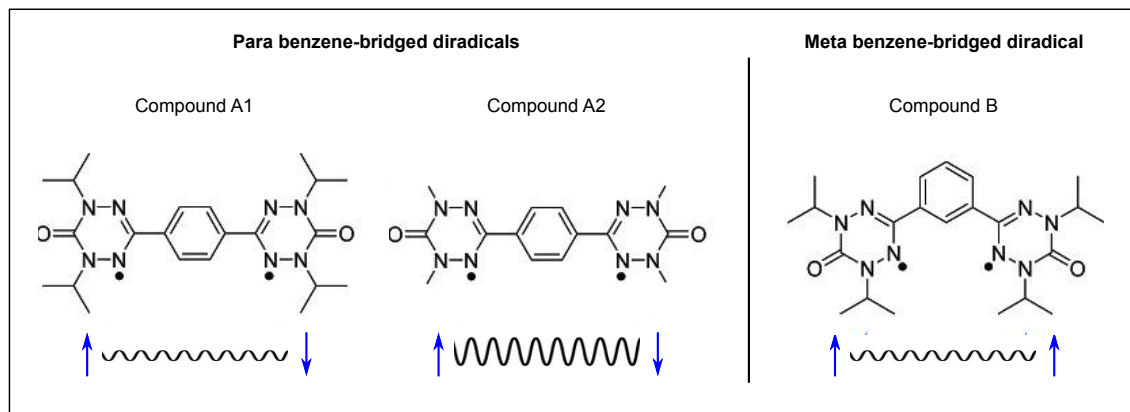


Figure VI.4: **Benzene-bridged diradicals studied in Refs. [249, 252] and associated intramolecular coupling.** Compounds A1 and A2 (left) are para-bridged diradicals and are, respectively, weakly and strongly antiferromagnetically coupled, while compound B (right) is the meta analogue of compound A1 and is weakly ferromagnetically coupled. Figure adapted from Ref. [249].

### Intermolecular coupling

We now turn to intermolecular interactions between verdazyls. Although we expect different packing structures when deposited on surfaces, we describe hereafter some of the verdazyl systems that have been characterized from a structural point of view at the solid state (powder) and whose intermolecular magnetic interactions have been investigated. We choose to focus on the verdazyls closest to the verdazyls synthesized by our chemist colleagues, with help of the review given in Ref. [249]:

- At the solid state, the 1,3,5-triphenylverdazyl compound adopts a layered structure in which aromatic substituents are pseudo-aligned with verdazyl rings [253] (Figure VI.5(a)). The C3 phenyl substituents are partially superimposed over/under the central verdazyl ring of adjacent molecules along the  $z$ -axis and the closest intermolecular contacts in these structures are some C–N contacts between 3.8 and 4.0 Å, *i.e.* beyond the van der Waals contact distance for these atoms. There is no N–N contact within 4 Å. The magnetic properties of 1,3,5-triphenylverdazyl were reported in Refs. [254, 255, 256]. Intermolecular interactions are consistent with one-dimensional (1D) antiferromagnetic chains parallel to the  $x$ -axis. Below  $\simeq 1.7$  K, the measured increased susceptibility is ascribed to spin canting: rather than being perfectly co-parallel, the spins of the 1D chains are tilted by a small angle about their axis.
- The 1,3,5-triphenylverdazyl analogue with an oxygen atom in position 6 (1,3,5-triphenyl-6-oxoverdazyl) is depicted in Figure VI.5(b). It also adopts a layered structure at the solid state (a side-view is shown in Figure VI.5(b)) [257]. Similarly to 1,3,5-triphenylverdazyl, the magnetic properties of 1,3,5-triphenyl-6-oxoverdazyl can be modelled as a Heisenberg antiferromagnetic chain down to  $\simeq 5$  K [257]. Below this temperature, the ordering is still antiferromagnetic but canted giving rise to weak ferromagnetism. This compound is similar to one of the compounds (TMOV) synthesized by our chemist colleagues (see later in the Chapter), hence we can expect similar properties. The major difference with TMOV lies in the presence of the N-phenyl substituents at

positions 1 and 5. It was shown that these groups are significantly twisted with respect to the verdazyl plane, which may explain the rather large interplanar separation of 3.65 Å within the molecular stacks [257].

- Finally, compound A2 (shown in Figure VI.4 and whose intramolecular coupling has been previously discussed) adopts a herringbone-type packing pattern in the solid state (Figure VI.5(c)) and exhibits a strong intermolecular antiferromagnetic exchange coupling [252].

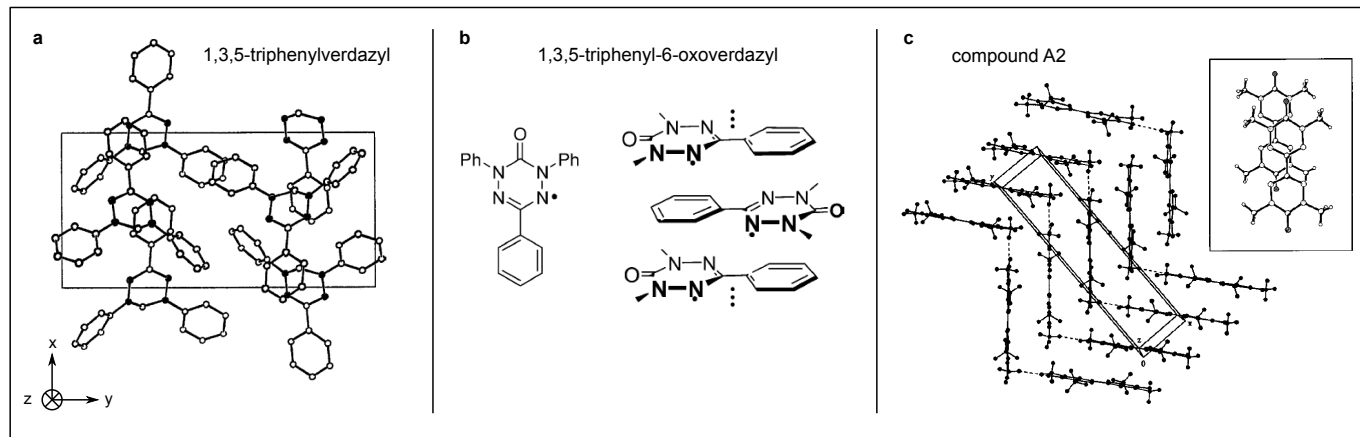


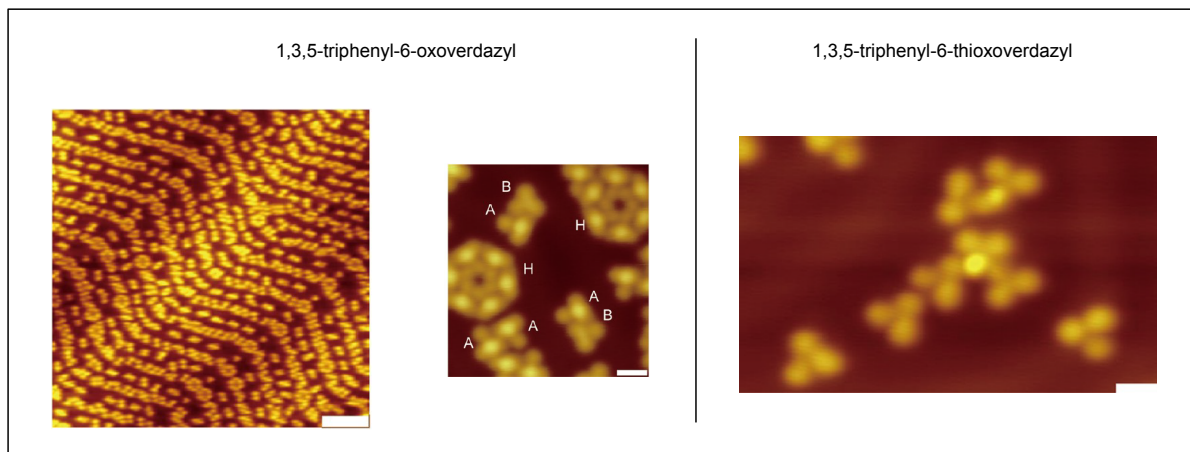
Figure VI.5: **Packing patterns of a few verdazyl radicals in the solid state.** (a) 1,3,5-triphenylverdazyl packing pattern. Figure adapted from Ref. [253]. (b) Packing pattern of the 1,3,5-triphenyl-6-oxoverdazyl. Figure taken from Ref. [249]. (c) Packing pattern of compound 2. Figure taken from Ref. [249].

## 1.b Verdazyl radicals on surfaces

To our knowledge, there is only one example in the literature where verdazyl radicals have been deposited on a surface in UHV conditions, namely 1,3,5-triphenyl-6-oxoverdazyl and 1,3,5-triphenyl-6-thioxoverdazyl on a Au(111) single-crystal [258]. The latter verdazyl compound is the analogue of the former (previously mentioned and whose packing pattern at the solid state is shown in Figure VI.5(b)) with a sulfur atom in position 6 instead of an oxygen atom. STM images of both compounds adsorbed on Au(111) are shown in Figure VI.6. In the large scale image showing 1,3,5-triphenyl-6-oxoverdazyl molecules adsorbed on Au(111), the herringbone pattern typical of Au(111) surface reconstruction is visible and clearly influences the adsorption sites of the molecules. In the small scale image, two types of assemblies are found: circular assemblies correspond to hexamers of the molecules, and dimers of molecules appear as assemblies of two molecules rotated by 180° with respect to each other. These dimers are composed of type-A and type-B molecules: the former type exhibits a protrusion in its center, while the latter does not. Liu *et al.* assigned type-A molecules to H-attached 1,3,5-triphenyl-6-oxoverdazyl molecules (an hydrogen atom is attached to the oxygen atom of the molecule), and type-B molecules to pristine 1,3,5-triphenyl-6-oxoverdazyl molecules [258].

For type-B molecules, a zero bias peak was measured by means of low temperature scanning tunneling spectroscopy and was attributed to a Kondo resonance stemming from the unpaired electron delocalized over the verdazyl ring. For type-A molecules, no zero bias peak was visible. Liu *et al.* proposed that the H-attached atom is responsible for the transfer of an electron to the verdazyl ring, which causes the disappearance of the delocalized unpaired electron, accounting for the absence of a Kondo resonance.

An STM image of 1,3,5-triphenyl-6-thioxoverdazyl molecules adsorbed on Au(111) is shown in Figure VI.6. The absence of a zero bias peak in scanning tunneling spectroscopy measurements was attributed to an electron transfer to the verdazyl ring upon adsorption on Au(111): a Au-S bond forms and is



*Figure VI.6: Verdazyl radicals deposited on Au(111). Left:* Large and small scale STM images of 1,3,5-triphenyl-6-oxoverdazyl molecules on Au(111) (scale bars: 200 Å (left) and 20 Å (right)). Hexamers, type-A and -B dimers are indicated with H, A and B letters, respectively. *Right:* Small scale STM image of 1,3,5-triphenyl-6-thioverdazyl on Au(111) (scale bar: 20 Å). Figure adapted from Ref. [258].

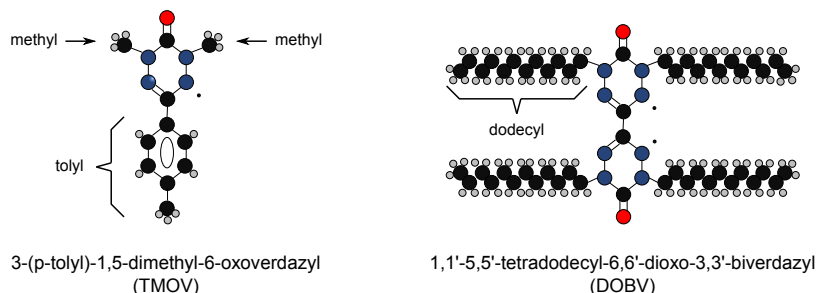
responsible for the disappearance of the radical character of the molecule, hence no Kondo resonance is to be expected. DFT calculations are in agreement with the proposed models.

## 2 Synthesis and characterization

The synthesis and chemical analysis of the verdazyl radicals presented in this Chapter were entirely performed by our chemist colleagues Christophe Bucher and Shagor Chowdhury (ENS, Lyon).

### 2.a Synthesis

Over the years, a broad range of synthesis methods have been developed for the synthesis of verdazyl radicals leading to a wide variety of unique structures [248]. The objective here was to synthesize a series of novel verdazyl compounds that could be deposited and self-assembled on graphene. Among the several compounds synthesized by our chemist colleagues, we focus here on the compounds 3-(p-tolyl)-1,5-dimethyl-6-oxoverdazyl and 1,1'-5,5'-tetradodecyl-6,6'-dioxo-3,3'-biverdazyl (Figure VI.7), as they correspond to the two compounds with which we performed deposition tests on surfaces.



*Figure VI.7: Targeted compounds: 3-(p-tolyl)-1,5-dimethyl-6-oxoverdazyl (TMOV) and 1,1'-5,5'-tetradodecyl-6,6'-dioxo-3,3'-biverdazyl (DOBV). Oxygen, nitrogen, carbon and hydrogen atoms are sketched as red, blue, black and grey balls, respectively.*

As always with organic chemistry nomenclature, the name of a molecule is constructed so that the main chemical group of the molecule appears at the end of the name. Here, the main group constituting both compounds is the verdazyl ring. The substituents linked to that main group are indicated with their associated positions (the numbering of positions in the verdazyl ring is given in Figure VI.1). The

compound 3-(*p*-tolyl)-1,5-dimethyl-6-oxoverdazyl is an oxoverdazyl radical (with the oxygen atom in position 6 of the verdazyl ring) which presents a tolyl substituent (benzene ring with a methyl group) in position 3 and two methyl substituents in positions 1 and 5. The tolyl substituent (indicated in Figure VI.7) is in a para configuration (hence the denomination **p**-tolyl), meaning that the methyl group of the tolyl substituent is connected at the atom opposite to the atom connecting the tolyl group to the rest of the molecule. The compound 1,1'-5,5'-tetradodecyl-6,6'-dioxo-3,3'-biverdazyl is a biverdazyl *i.e.* it contains two verdazyl rings (in both cases, oxoverdazyl rings). Each verdazyl ring features long alkyl chains (dodecyl groups) at positions 1 and 5. These substitution patterns have been considered to promote their physisorption on graphene and enhance their 2D-organization on the surface.

The TMOV compound has been obtained following the procedure depicted in Figure VI.8 [259]. One major advantage of this specific procedure is that it avoids the use of toxic triphosgene which is frequently used in the synthesis of verdazyl compounds. As depicted in Figure VI.8, the synthesis starts with a condensation between the commercially available carbohydrazide (1) with *p*-tolualdehyde to obtain the hydrazine (2) in 70% yield. Then the alkylation of both nitrogens was achieved using dimethylsulfate as a reactant (resulting in the intermediate compound (3)) followed by a methanolysis and ring closure reaction to produce the tetrazinanone intermediate (4). The last step consists in the oxidation of the tetrazinanone with benzoquinone to obtain the targeted verdazyl radical (5).

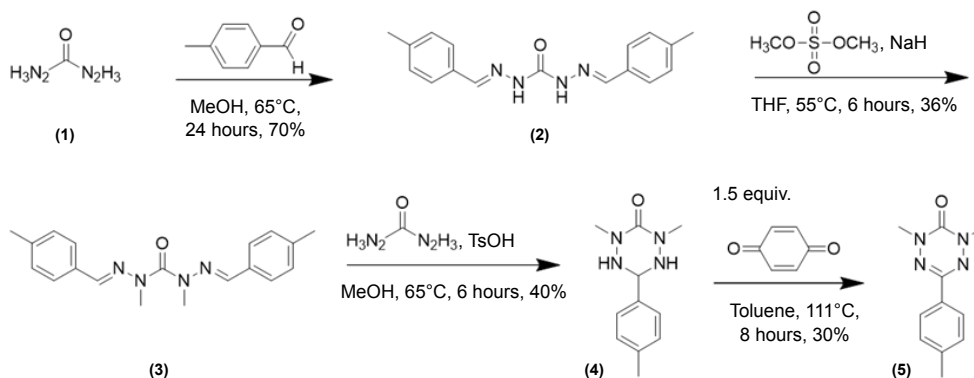


Figure VI.8: Synthesis of 3-(*p*-tolyl)-1,5-dimethyl-6-oxoverdazyl (TMOV).

The other targeted radical, the symmetric DOBV compound, has been obtained in quite good yield following a different approach (Figure VI.9) involving *N,N'*-dialkylcarbohydrazide [260] as a key starting material (1). Condensation of the latter with glyoxal (HCOCOH) led to the intermediate (2) which was in fine oxidized to obtain the desired bi-verdazyl compound (3).

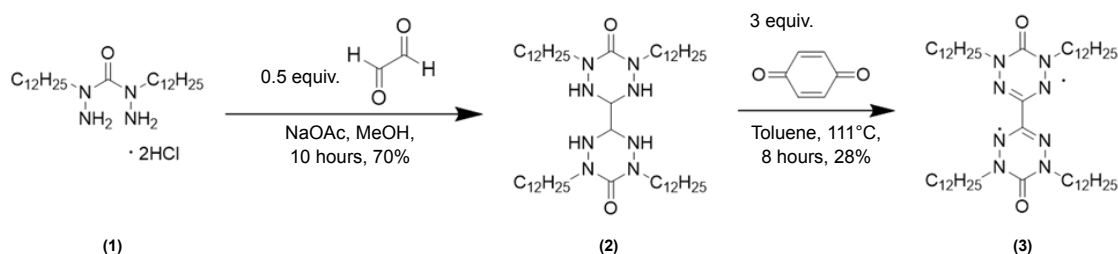


Figure VI.9: Synthesis of 1,1'-5,5'-tetradodecyl-6,6'-dioxo-3,3'-biverdazyl (DOBV).

The chemical analysis of the synthesized compounds, performed by Christophe Bucher and Shagor Chowdhury, included thin-layer chromatography (TLC), mass spectrometry, nuclear magnetic resonance (NMR), electron spin resonance (ESR) and absorption spectroscopy. Hereafter we present spectra associated

with the two latter characterization techniques. TLC and mass spectrometry will be addressed later in the Chapter.

## 2.b Electron spin resonance

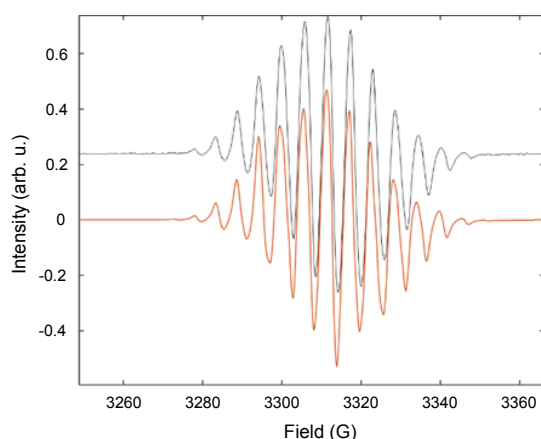
The presence of an unpaired electron can easily be revealed by electron spin resonance (ESR) measurements. ESR (also known as electron paramagnetic resonance, EPR) relies on the Zeeman effect. An electron has a spin quantum number  $s = \frac{1}{2}$ , with magnetic components  $m_s = +\frac{1}{2}$  or  $m_s = -\frac{1}{2}$ . Under an external magnetic field with strength  $B_0$ , the electron's magnetic moment aligns either antiparallel ( $m_s = -\frac{1}{2}$ ) or parallel ( $m_s = +\frac{1}{2}$ ) to the field, where each alignment is associated with the energy:

$$E = m_s g_e \mu_B B_0 \quad (\text{VI.1})$$

$g_e$  and  $\mu_B$  are constants:  $g_e$  is the electron spin g-factor ( $g_e = 2.0023$  for a free electron), and  $\mu_B$  is the Bohr magneton ( $\mu_B = 9.2740 \cdot 10^{-24} \text{ J.T}^{-1}$ ).

As a result, the Zeeman splitting  $\Delta E = g_e \mu_B B_0$  is proportional to  $B_0$  and an unpaired electron can go from one energy level to the other by either absorbing or emitting a photon of energy  $h\nu = \Delta E$ . In practice, a microwave excitation is provided under an increasing external magnetic field. As the strength of the external magnetic field increases, the Zeeman splitting increases, until it matches the energy of the microwave. Since there are typically more electrons in the lower state (due to the Maxwell–Boltzmann distribution) there is a net absorption of energy. This absorption of energy is monitored and its derivative is converted into a spectrum.

ESR spectra for the TMOV and DOBV compounds were recorded by our chemist colleagues at room-temperature in dichloromethane. For TMOV (Figure VI.10), the signal features multiple ESR lines indicative of a hyperfine structure. The spacing between the ESR spectral lines depends on the degree of interaction between the unpaired electron and the nearby nuclear spins. The hyperfine structure observed for the TMOV compound is attributed to the coupling of the spin of the unpaired electron with the nitrogen and hydrogen atoms associated to the verdazyl ring [261]. The simulated ESR spectrum matches well the experimental one (Figure VI.10). The hyperfine coupling constants obtained from the simulated spectrum reveal that the unpaired electron is preferentially localized on N3 and N5.



*Figure VI.10: Simulated (red) and experimental (black) ESR spectra of the TMOV compound.* The experimental curve has been recorded in dichloromethane at room temperature. Courtesy of Shagor Chowdhury.

The radical character of the DOBV compound was also revealed by ESR spectroscopy (not shown). The simulated spectrum suggests that the hyperfine coupling involves only the four N atoms of the verdazyl ring (and no H atom). It should be mentioned that the ESR spectrum of the DOBV compound

is similar to that of the compound 1,1'-5,5'-tetramethyl-6,6'-dioxo-3,3'-biverdazyl reported in Ref. [262]. This compound is the analogue of DOBV with methyl- rather than dodecyl-substituted N atoms.

## 2.c UV-visible spectroscopy

UV-visible spectroscopy (UV-vis) is a technique widely used in chemistry labs. It allows identifying certain substituents and their associated concentrations, as well as determining the kinetics of a chemical reaction. UV-vis relies on the excitation of the compound (in diluted solution) *via* UV-visible light ( $\simeq 200\text{-}800\text{ nm}$ ). The intensity of the light before ( $I_0$ ) and after ( $I$ ) passing through the sample is measured with a spectrophotometer. The absorbance of a compound is defined as  $-\log(I/I_0)$ . For a compound which presents only one absorbing species, the absorbance is related to the concentration of the absorbing species through the Beer-Lambert law:

$$A = \epsilon c L \quad (\text{VI.2})$$

where  $c$  is the concentration of the absorbing species,  $L$  is the path length through the sample and  $\epsilon$  is the molar attenuation coefficient (also known as the molar extinction coefficient or molar absorptivity) of the absorbing species. The latter is a constant (it is an intrinsic property of the absorbing species) and is a measure of how strongly a chemical species absorbs light at a given wavelength.

It was previously shown that the substituent introduced at position 3 on the verdazyl ring strongly affects the absorbance spectrum of verdazyl radicals [263]. The absorbance spectrum of the TMOV compound diluted in dichloromethane was recorded by Shagor Chowdhury (Figure VI.11, black). It shows a very intense band centered at 250 nm and a weak band at 413 nm. This data is fully consistent with the one previously reported by Gilroy *et al.* for compound A1 (Figure VI.11, orange) [249].

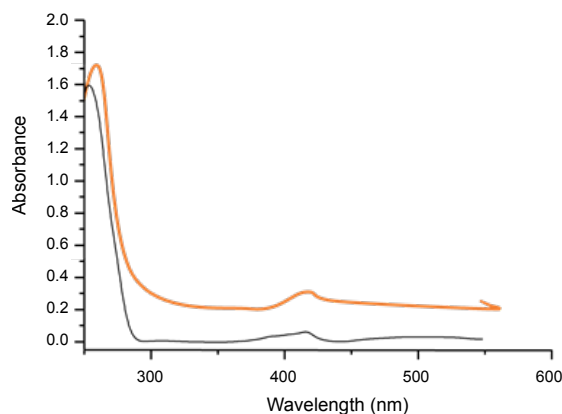


Figure VI.11: UV-visible absorbance spectra of the TMOV compound (black) and compound A1 (orange) [249]. Both experimental curves have been recorded in dichloromethane at room temperature using conventional 1 mm-long quartz cells. Courtesy of Shagor Chowdhury.

The absorption spectrum recorded for DOBV compound (not shown) features three bands at 250 nm, 287 nm and 344 nm.

## 2.d Raman spectroscopy

Besides the chemical analyses performed in Lyon by our chemist colleagues, we performed in Néel Institute Raman spectroscopy on as-prepared DOBV molecules (powder). To our knowledge, no Raman spectrum of a verdazyl radical has been reported so far (in particular, none can be found in the Spectral Database for Organic Compounds, SDBS).



Numerous peaks are visible at a laser excitation wavelength of 797 nm (Figure VI.12). An incomplete Raman peak assignment was made with use of the table provided in Ref. [264]. The N,N'-substituted dodecyl chains correspond to CC aliphatic chains (an aliphatic compound is a non-aromatic compound) and give a Raman signal at about 250-400  $\text{cm}^{-1}$ . Other Raman peaks, appearing between 600 and 1300  $\text{cm}^{-1}$  are observed and can be ascribed to CC alicyclic or aliphatic chains (an alicyclic compound is both an aliphatic and a cyclic compound). No CC alicyclic compound is present in the DOBV compound, so these peaks can be again assigned to the dodecyl chains. The intense Raman peaks observed at 449 and 521  $\text{cm}^{-1}$  cannot be assigned based on the table provided in Ref. [264]. They may correspond to the vibration modes of the verdazyl rings. A Raman band at  $\simeq 1586 \text{ cm}^{-1}$  (close to the G band value for graphene) is observed, and could be assigned to some of the C – C bonds present in the molecule. Finally, peaks in the 1610-1680  $\text{cm}^{-1}$  range are visible and are attributed to vibration modes of the C = N bonds in the DOBV compound. Surprisingly, it seems that no peak related to C = O bonds (1680-1820  $\text{cm}^{-1}$  range) is present at our excitation wavelength, although the DOBV compound presents two C = O bonds.

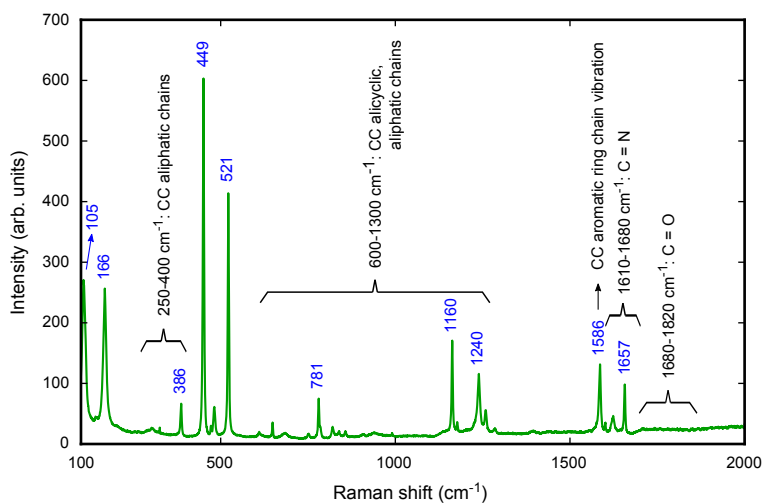


Figure VI.12: **Raman spectrum of the DOBV compound** (laser excitation wavelength = 797 nm). The wavenumbers associated with the most intense Raman peaks are indicated in blue. An incomplete Raman peak assignment is given, based on the table provided in Ref. [264].

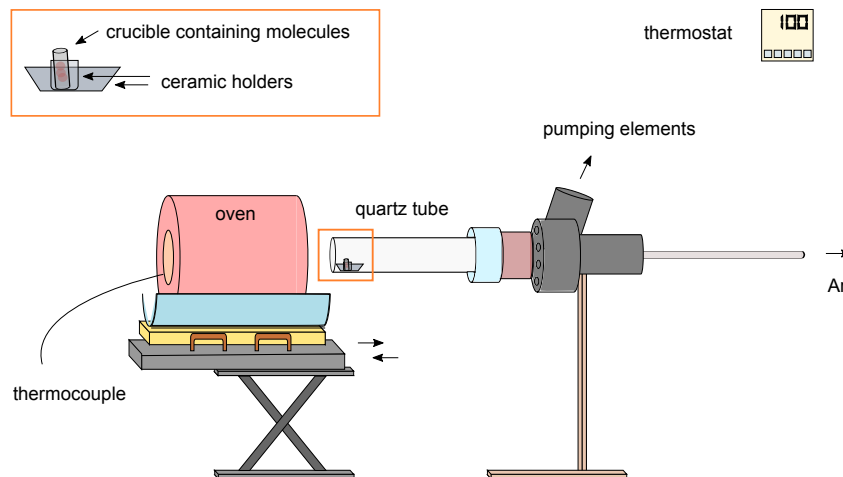
At the moment, the installation of a UHV-Raman spectroscopy apparatus is ongoing. Such set-up will allow performing Raman spectroscopy on samples kept in UHV. Comparing Raman spectra acquired on as-prepared molecules (powder) with Raman spectra acquired after deposition would be very insightful. It would help determining whether the sublimation/deposition process has modified the vibration modes of the molecules of interest. In particular, one could determine whether the molecule is degraded. As we will see in the following sections, this is a critical information, as the TMOV and DOBV molecules are degraded at relatively low temperatures.

### 3 Sublimation temperature and stability

#### 3.a Protocol

The sublimation temperature of the molecules is expected to strongly depend on the pressure. In order to estimate the sublimation temperature and to assess the temperature stability of the molecules in a close-to-UHV environment, two socket ovens were used: one was made available by Gérard Lapertot and Christophe Marin (IRIG) (see Figure VI.13), the other by Richard Haettel (Institut Néel). The idea is to determine at which temperature the molecular evaporator has to be heated so that the molecules sublime and deposit on surfaces. A socket oven consists of a tubular oven that wraps a tube in which

the elements to be resistively annealed are contained. In the case of the IRIG system (S1), the oven is slid around the tube, whereas in the case of the Institut Néel system (S2) the quartz is slid inside the oven. Both systems are maintained under a secondary vacuum:  $10^{-6} - 10^{-7}$  mbar for S1 and  $10^{-8}$  mbar for S2, and the temperature of the ovens are regulated with a thermostat. It is important to note that, for both systems, the thermocouple measures the temperature in the resistance of the oven, not inside the tube where the sample is placed.



*Figure VI.13: General sketch of the socket oven system in IRIG (S1).* The temperature of the socket oven is regulated with a thermostat. Once the desired temperature is reached, the socket oven is slid and wraps the quartz tube in which the molecule-containing quartz crucible is. The quartz tube is maintained at  $10^{-6} - 10^{-7}$  mbar with a turbo pump and a backing pump.

The preparation of the ovens/cleaning of the elements is made as follows:

1. The quartz tube and the ceramic elements are degassed at high temperature: the temperature is increased from room temperature up to 1170 K within 4 hours, and it is maintained at this temperature for 5 hours. Then, the ensemble is cooled down to room temperature within an hour. After the degassing, the pressure is in the low  $10^{-7}$  mbar.
2. The system is left under vacuum for a few days. After that, the pressure is around  $10^{-7}$  mbar down to  $5 \cdot 10^{-8}$  mbar.
3. Ultrasonic cleaning of the quartz crucible is performed using acetone and ethanol, followed by a  $N_2$  drying. The system is vented with Ar and the quartz crucible is introduced alongside the ceramic elements inside the quartz tube. The system is then placed under vacuum again.
4. The empty quartz crucible is degassed at 570 K during 24 hours: the pressure goes approximately from the low  $10^{-6}$  mbar down to the high  $10^{-8}$  mbar.
5. The system is left under vacuum for a few days.

Once this procedure has been followed and the system is clean, the quartz crucible is filled with molecules using a folded aluminium foil and is positioned in a quasi-vertical configuration (see inset of Figure VI.13). The ceramic holders containing the quartz crucible are then placed in the quartz tube. The ensemble is pumped again and left under vacuum for a few days. It is then ready for a thermal treatment. During the thermal treatment and once the desired temperature is reached, the oven/tube is slid and positioned so that the sample stands in the middle of the oven. After the thermal treatment, the product that remains in the quartz crucible is sent to Christophe Bucher and Shagor Chowdhury for chemical analysis. To determine whether the molecules have been degraded during the thermal treatment,

they perform EPR, NMR, TLC, mass spectrometry and ultraviolet-visible spectroscopy measurements. Repeating cycles of thermal treatments and post-treatment chemical analysis allows us to determine (if it exists!) the range of temperature in which the molecules are sublimated without being degraded. Note that since the thermocouple measures the temperature at the level of the resistance oven, the range of temperature that corresponds to a degradation-free sublimation of the molecules is lower than the measured range by approximately 40 K. Please also note that a comparison between a temperature measured in a socket oven and a temperature measured in the molecular evaporator described in Section 1.e should be made with caution. Generally speaking, comparing temperatures should be done with caution, especially when the temperatures are measured in different systems. The fact that the pressure is not exactly the same in the socket ovens and in the UHV system makes any comparison even more questionable, since the evaporation temperature is expected to depend on pressure in a non trivial way. It prevents us from making straightforward conclusions concerning the temperature at which the molecular evaporator should be heated in order to sublimate and deposit the molecules of interest. Still, the sublimation tests proved to be very useful in giving some insight on the relevant temperature ranges for further deposition in UHV, as is explained in the following.

### 3.b TMOV molecules

The sublimation tests with the TMOV molecules are summed up in Figure VI.14. Here, the first and second sublimation tests (TMOV-1 and TMOV-2) were made in S1 whereas the third one was made in the UHV system using the molecular evaporator. As a result, one must take particular care when comparing temperatures.

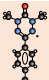


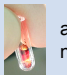




	TMOV-1	TMOV-2	TMOV-3
<b>System</b>	S1	S1	UHV
<b>Initial pressure</b>	$\approx 10^{-6}$ mbar	$3.0 \cdot 10^{-6}$ mbar	$10^{-9} - 10^{-10}$ mbar
<b><math>T_{\max}</math></b>	563 K	440 K	2 consecutive treatments T1 = 443 K T2 = 393 K
<b>Consumed quantity</b>	?	?	?
<b>Post-treatment visual aspect</b>	 black not a powder	 reddish not a powder	 after T1: reddish not a powder
<b>Deposition on the quartz tube ?</b>	433 K: whitish 513 K: rainbow	433 K: whitish	—
<b>Molecules intact after the treatment ?</b>		 	

Figure VI.14: Summary of TMOV sublimation tests. TMOV molecules are found to degrade before the temperature reaches 393 K in the thermocouple.

For the first two sublimation tests, the aspect of the molecules was monitored at several stages: the temperature was increased up to  $T_{\max}$  in different steps and the aspect of the molecules could be observed at each step simply by retracting the oven. The molecules are initially in the form of a dark red powder.

Around 420 K-440 K, this powder turns into a more reddish liquid and starts covering the lateral walls of the crucible. At 433 K, a whitish deposit is observed on the quartz tube, outside the region that is wrapped by the oven i.e in a colder part of the tube. This deposition either corresponds to solvents or pollution that have evaporated and then re-condensed on the colder parts of the quartz tube, or it corresponds to the molecules of interest (TMOV) that experienced the same process. After such an annealing (TMOV-2), the product that remains in the crucible exhibits both the signature of the TMOV molecules and the signature of a different molecule. TMOV molecules are therefore starting to degrade before 433 K. This is confirmed by the third sublimation test. This last test was performed in two steps: first, the temperature was risen up to 443 K; then, without cleaning the crucible, new molecules were added. The only thermal treatment that these second-round molecules experienced is the bake-out of the chamber. During the bake-out, the temperature of the chamber is increased up to 393 K and the temperature is 20 K to 40 K less in the molecular evaporator and close to it. Still, such a low temperature treatment was enough to degrade the second-round molecules since the signature of TMOV was not observed in the remaining product of TMOV-3. The molecules therefore degrade before or around 350 K-370 K. At higher temperatures, around 450 K, the powder dries and it later becomes darker around 500 K. As is expected from TMOV-3, after an annealing up to 563 K maximum (TMOV-1), the signature of TMOV is not found in the remaining product. At 513 K, a deposit having a different aspect from the one obtained at 433 K was observed on the quartz tube. This deposit presented a color gradient (referred to as "rainbow" in Figure VI.14). This gradient may be due to differences in thicknesses. Whatever this deposit corresponds to, it for sure cannot be the initial molecule since TMOV degrades before or around 350 K-370 K.

Considering that TMOV molecules degrade during the bake-out, before or around 350 K-370 K, their study was discounted.

### 3.c DOBV molecules

Instead, the rest of the studies was made using DOBV molecules. These molecules being larger than TMOV molecules, their sublimation temperature is expected to be higher.

The sublimation test results concerning DOBV molecules are shown in Figure VI.15. As one might expect, the visual aspect of the molecules seems to be correlated with the degraded/preserved character of the initial molecule. Indeed, the only sublimation test after which the signature of DOBV molecules - and only DOBV molecules! - is found is the one for which the visual aspect of the powder remains the same after the thermal treatment (DOBV-2). This sublimation test indicates that the temperature range in which the molecules experience a degradation-free sublimation is around 395 K. To determine whether the temperature range extends much higher than 395 K, a third sublimation test (DOBV-3) was performed: after 40 minutes at 423 K, the DOBV molecules signature was not found in the remaining product. This means that, if the temperature range of sublimation extends higher than 395 K, it for sure does not extend up to 423 K. This is supported by the fact that the sublimation rate in the second sublimation test is quite high. The oven temperature was risen from room temperature up to 393 K within 12 minutes and maintained at this temperature (up to 395 K max) during 11 minutes. After this treatment, three quarters of the initial mass was lost. It is therefore very likely that the sublimation temperature range extends lower than 393 K but not much higher. Taking into account the fact that the thermocouple temperature is higher by approximately 20 K to 40 K than the temperature in the vicinity of the molecules, the effective sublimation temperature range is expected to be of the order of 350 K-370 K.

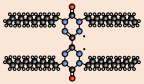

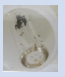




	DOBV-1	DOBV-2	DOBV-3
<b>System</b>	S1	S1	S2
<b>Initial pressure</b>	$6.2 \cdot 10^{-8}$ mbar	$6.7 \cdot 10^{-7}$ mbar	$\approx 10^{-8}$ mbar
<b>Tmax</b>	443 K	393 K	423 K
<b>Consumed quantity</b>	63% to 76% of the initial mass	62% to 72% of the initial mass	$\approx 42\%$ of the initial mass
<b>Post-treatment visual aspect</b>	 reddish not a powder	 black powder, same as before the treatment	 reddish not a powder
<b>Deposition on the quartz tube ?</b>	No	No	No
<b>Molecules intact after the treatment ?</b>			

Figure VI.15: **Summary of DOBV sublimation tests.** DOBV molecules sublime when the temperature is lower or of the order of 395 K in the thermocouple.

## 4 DOBV deposition on metals

### 4.a Experimental adjustments

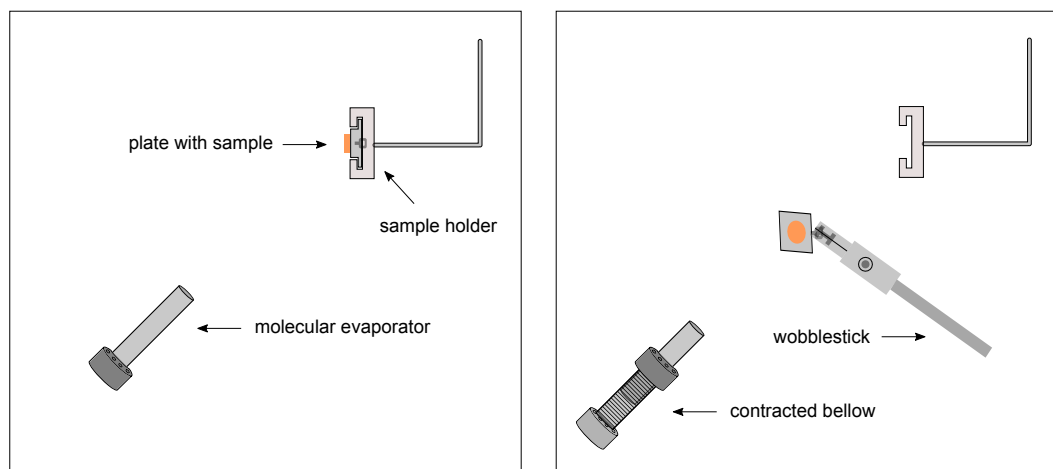
As seen in the previous section, the degradation-free sublimation range of temperature of DOBV molecules is of the order of 350 K-370 K. During the bake-out, since the molecular evaporator is not isolated from the chamber and the temperature can go up to 403 K in the chamber (and slightly less in the vicinity of the molecular evaporator), ensuring that the molecules do not sublime during the bake-out required some adjustments. An axis-translator equipped with a bellow was mounted between the flange of the molecular evaporator and the flange of the UHV chamber: it authorizes to retract the molecular evaporator during the bake-out so that the local temperature in the vicinity of the molecular evaporator is lower. When the temperature of the chamber is around 403 K, the temperature measured by the thermocouple of the retracted molecular evaporator - which is at the level of the molecule-containing crucibles - is approximately 335 K to 345 K.

After every new loading of molecules in the dedicated crucible, particular care is given to the temperature during the bake-out of the chamber. During the bake-out, the molecular evaporator is completely retracted using the axis translator and the heating tape that covers its exterior parts is chosen so that it heats at relatively low temperatures, approximately 350 K. The temperature inside the molecular evaporator is expected to be less, which ensures that DOBV molecules do not sublime. Following the bake-out of the chamber, the built-in bake-out of the molecular evaporator is performed: the temperature of the molecular evaporator inner parts (excluding the crucibles) is risen up to 375 K within an hour and maintained at this temperature overnight. During this process, the water cooling system is running. The crucibles are then degassed (with the water cooling system still running): the temperature is increased up to the sublimation temperature of the molecules and maintained at this temperature for 30 minutes. Following this procedure ensures recovering a satisfying pressure within 10

days in the chamber while preserving the integrity of the molecules.

However, the adding of the axis translator comes with a major drawback. During the bake-out, the bellow is fully extended. After the bake-out, the molecular evaporator is introduced in the chamber (the bellow is contracted). The problem is that the (contracted) bellow does not allow to recover the initial configuration: the molecular evaporator is approximately 10 cm further away from the sample holder than it was before. This far-off configuration was used for some time but it did not provide any signs of successful deposition on any of the various surfaces that were placed on the sample holder. Since successful depositions had previously been observed with fullerenes in the initial configuration, it was concluded that the origin of the unsuccessful depositions was the larger distance between the sample holder and the molecular evaporator. The working distance specified by the manufacturer (Kentax) ranges from 7 cm to 12 cm. In the far-off configuration, the sample was more than 15 cm away from the sample. Since the elementary surface of a sphere of radius  $r$  increases with  $r^2$  and the molecules sublimate along a sublimation cone, if we assume that the sublimation is isotropic, then the number of molecules at a distance  $r$  of the source decays with  $r^2$ . As a result, the distance between the sample and the molecular evaporator is crucial and should not be much larger than the recommended working distance.

In order to solve this issue, the next deposition tests were performed by approaching the plate on which the sample is fixed close to the molecular evaporator using the wobblestick (see Figure VI.16). This new configuration is not ideal since the position of the sample is not well controlled. It also prevents us from either heating or cooling down the sample on which the molecules are deposited as the deposition occurs. Indeed, the heating and cooling down of the sample take place on the sample holder. Nevertheless this new configuration rapidly gave hints of successful depositions in both RHEED and STM.



*Figure VI.16: Sketch of the initial (left) and final (right) deposition configurations.* The mounting of the axis translator has pulled back the molecular evaporator from the sample holder with respect to the initial configuration. In order to recover a smaller distance between the sample holder and the molecular evaporator, the plate is approached using the wobblestick. The diagrams are not to scale.

#### 4.b RHEED monitoring

To make sure that the new configuration was indeed a satisfying one for depositing molecules on surfaces, we monitored the deposition process by means of RHEED measurements. This way, we could check the metal surface state, and progressively increase the temperature at which the molecular evaporator was held when there was no evidence that we deposited molecules. The first metal substrate that was used for

such deposition trials was Pt(111), as it is a quite reactive surface. Using Pt(111) helps being sensitive to the deposition of any compound on the surface in relatively shorter time scales than for other surfaces.

Figure VI.17 shows RHEED patterns taken along the  $[01\bar{1}0]$  and  $[11\bar{2}0]$  incident azimuths, before and after exposing the Pt(111) surface to the DOBV molecular flux, with the DOBV-containing crucible held at 388 K. The RHEED patterns of clean Pt(111) in both highest-symmetry directions exhibit intense streaks. After exposing the surface to the molecular flux for 15 minutes, these streaks are much less intense, indicating that something has indeed covered the Pt(111) surface.

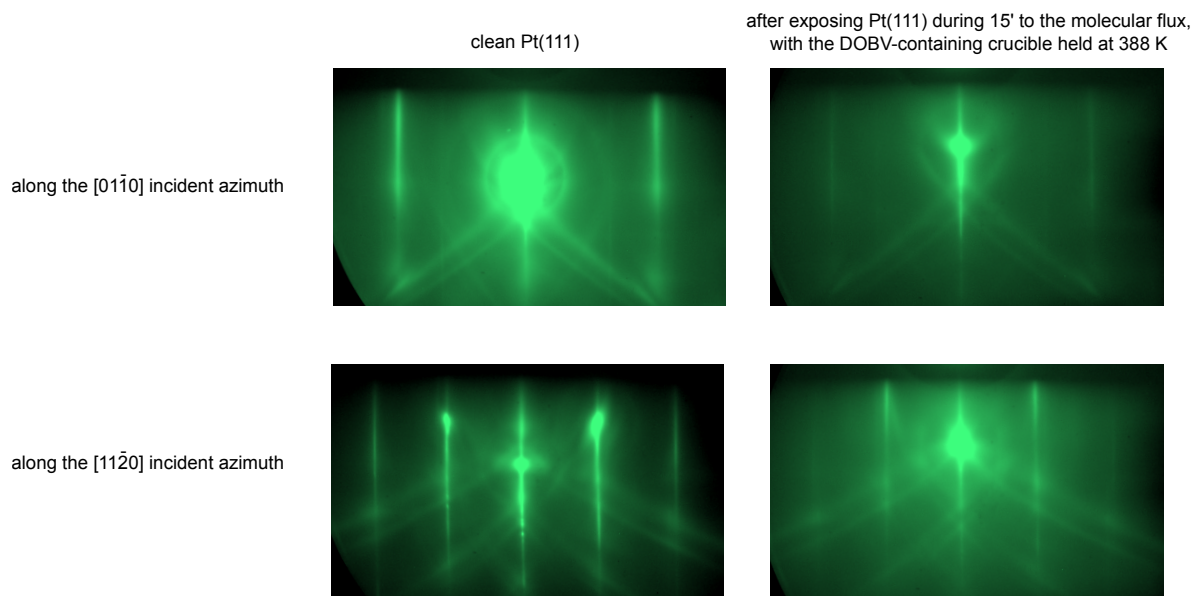


Figure VI.17: RHEED patterns taken along the  $[01\bar{1}0]$  and  $[11\bar{2}0]$  incident azimuths before and after exposing the Pt(111) surface to the DOBV molecular flux, with the DOBV-containing crucible held at 388 K. The Pt(111) surface was exposed to the DOBV flux for 15 minutes.

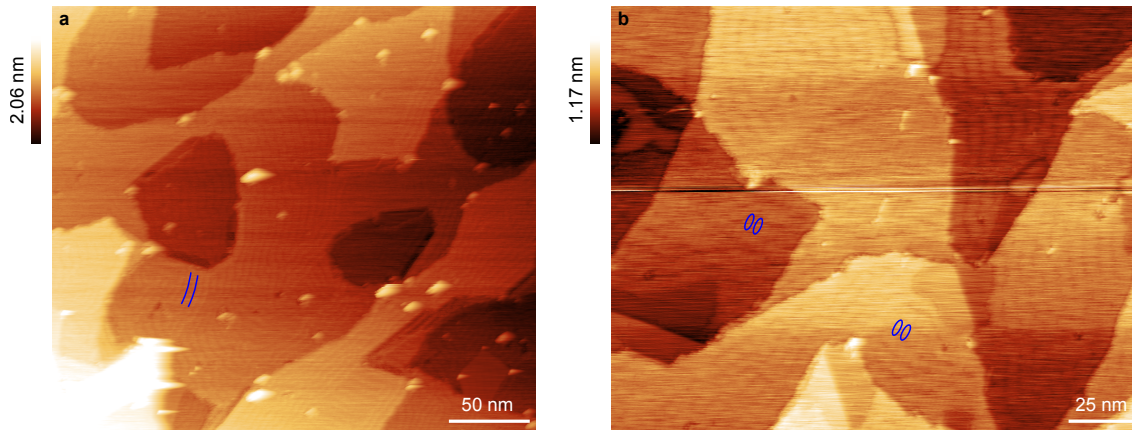
#### 4.c DOBV molecular assemblies on Cu(111)

Before trying to deposit DOBV molecules on quasi-free standing superconducting graphene, we performed several deposition trials on a more simple system, namely the (111) surface of copper. One STM measurements campaign (measurements campaign 1) carried out during summer 2018, gave promising results.

Figure VI.18 shows typical STM images obtained after exposing the clean Cu(111) surface to the DOBV molecular flux during 10 minutes, with the DOBV-containing crucible held at 353 K. These images display periodic arrangements ascribed to the molecules. 5-6 nm-wide chains covering almost the whole Cu(111) surface are visible (these chains were absent from the clean Cu(111) surface). Some of these chains are indicated with blue lines in Figure VI.18(a). The chains seem to follow Cu(111) step-edges. Features resolved at the intrachain scale are visible in Figure VI.18(b). Indeed, the molecular chains seem to be formed by 2.5-3 nm-long and 5-6 nm-wide objects (presumably individual or few molecules), indicated with blue oval shapes. Individual DOBV molecules are approximately 3.4 nm-wide and 1.2 nm-long, hence one can assume that each molecular chain comprises, for instance, two chains of interdigitated DOBV molecules. Unfortunately, no smaller scale STM image with intramolecular resolution could be acquired, hence the exact structure of the observed molecular assemblies could not be resolved.

Following the measurements campaign 1, chemical analyses performed by our chemist colleagues on the product remaining in the DOBV-containing crucible indicated that the DOBV molecules were still present but not pure. Unfortunately, these analyses were not performed immediately after the





*Figure VI.18: Measurements campaign 1: STM images of Cu(111) after exposing the surface to DOBV molecular flux during 10 minutes, with the DOBV-containing crucible held at 353 K. Both STM images were taken at 300 K with the following tunneling parameters:  $I_t = 1$  nA,  $V_b = -1$  V. (a) Large scale STM image. Some of the 5-6 nm-wide molecular chains are indicated with blue lines. (b) Smaller scale STM image. The molecular chains are formed by 2.5-3 nm-long and 5-6 nm-wide objects, indicated with blue oval shapes.*

measurements campaign 1 was over, but after several bake-outs of the UHV chamber. For this reason, we cannot conclude whether the molecules were already degraded at the time when the STM images shown in Figure VI.18 were acquired.

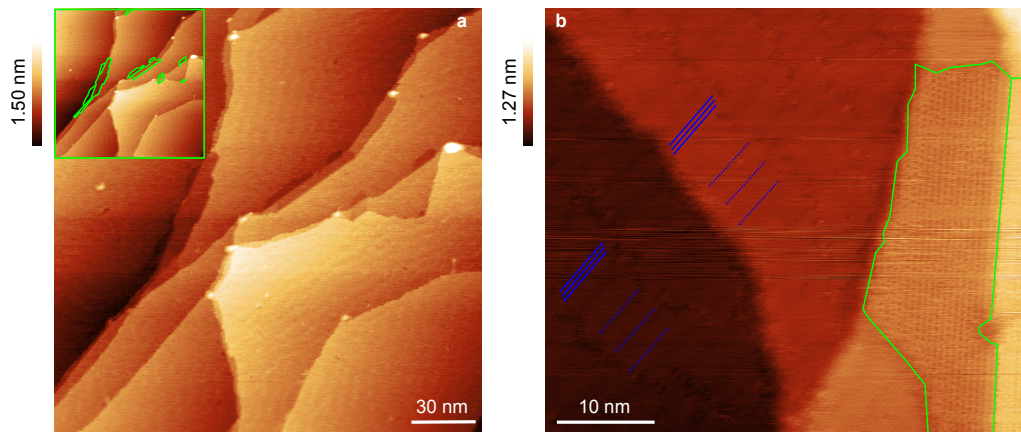
An other STM measurements campaign (measurements campaign 2) was carried out during summer 2019. We used the same deposition parameters as the ones used for the measurements campaign 1 but observed different features from the ones presented in Figure VI.18. Indeed, instead of observing a relatively homogeneous surface covered with 5-6 nm-wide chains, we observed two types of regions:

- 7 nm- up to 10 nm-wide chains made of filaments (parallel lines) separated by  $\simeq 0.5$  nm.
- few tens of nanometers-large triangular arrangements (with unit cell dimensions of  $0.8 \times 0.8$  nm<sup>2</sup>), appearing close to the Cu(111) step-edges.

These observations cannot correspond to pristine DOBV molecules, as the latter are approximately 3.4 nm-wide and 1.2 nm-long.

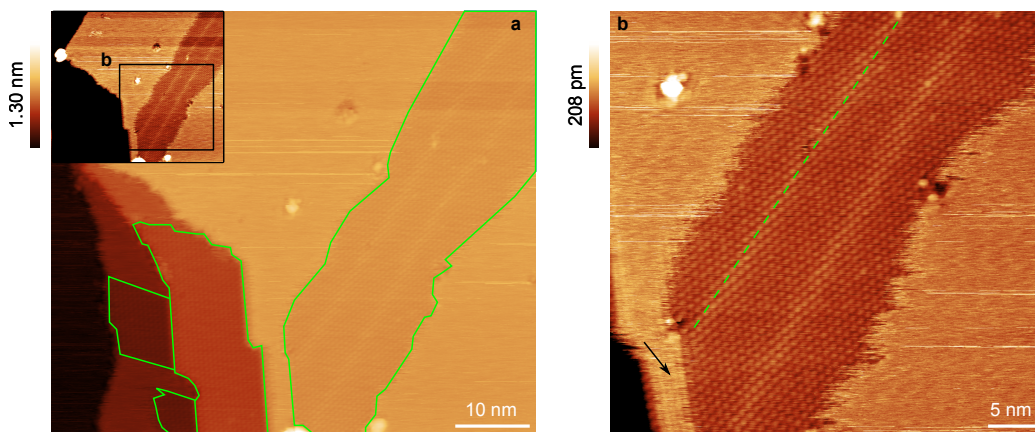
Filaments belonging to the former type of region are visible in the left part of Figure VI.19(b). A modulation in apparent topography with associated periodicity of  $\simeq 3$  nm along the chains of filaments is highlighted with blue dotted lines. Whether this modulation in apparent topography corresponds to the 2.5-3 nm-long and 5-6 nm-wide objects previously observed during the measurements campaign 1 cannot be decided. The chains observed here seem wider than the ones observed in the measurements campaign 1, but the poor precision we had before (as we only acquired relatively large scale images) prevents us from making any definite statement. Within the chains, parallel lines (filaments) that were not observed before are visible. Again, it is hard to conclude whether these filaments were present before and not resolved. We propose that the filaments observed here correspond to alkyl chains detached from DOBV molecules. The length of the filaments (7 nm up to 10 nm) suggests that dodecyl chains have reacted and formed longer chains (each DOBV molecule contains four 0.6 nm-long dodecyl chains).

Triangular patterns forming few tens of nanometers-large domains whose boundaries are indicated with green lines are observed in Figure VI.19. They are confined close to Cu(111) step-edges and sometimes extend on both sides of a Cu(111) step-edge, as seen in Figure VI.19(a). We propose that such regions correspond to assemblies of 6-oxoverdazyl rings of DOBV molecules. Overall, the thermal treatment (or the deposition process) could be held responsible for the breaking of the DOBV molecules into smaller compounds. These compounds would then diffuse and self-assemble in different regions of the Cu(111)



*Figure VI.19: Measurements campaign 2: STM images of Cu(111) after exposing the surface to DOBV molecular flux during 10 minutes, with the DOBV-containing crucible held at 353 K. Both STM images were taken at 300 K with the following tunneling parameters:  $I_t = 1$  nA,  $V_b = -0.5$  V. (a) Large scale STM image. Inset: The domains displaying triangular arrangements are indicated with green lines. They are confined close to Cu(111) step-edges. (b) Smaller scale STM image. The filaments (parallel lines) separated by  $\simeq 0.5$  nm, and the associated modulation in apparent topography are highlighted with solid blue lines and dotted blue lines, respectively. Domains with triangular arrangements (right part of the image) are indicated with green lines.*

surface, forming chains of filaments with dodecyl substituents and triangular patterns with the core of DOBV molecules.



*Figure VI.20: Measurements campaign 2: STM images of Cu(111) after exposing the surface to DOBV molecular flux during 10 minutes, with the DOBV-containing crucible held at 353 K. Both STM images were taken at 300 K with the following tunneling parameters:  $I_t = 1.2$  nA,  $V_b = 0.9$  V. (a) Large scale STM image. The domains displaying triangular arrangements are indicated with green lines. Inset: Same STM image with a different contrast. The triangular pattern in the topmost terrace is better seen. (b) Close-up view at the region framed in the inset of (a). The triangular arrangement is clearly seen. The modulation in apparent topography is highlighted with a green dashed line and is attributed to lateral confinement. A region displaying triangular shapes beyond the well-defined embedded region is pointed with a black arrow.*

A closer view at a region exhibiting triangular patterns is shown in Figure VI.20. Figure VI.20(a) shows Cu(111) terraces partly covered with domains showing triangular arrangements. Similarly to Figure VI.19, the boundaries of such domains are indicated with green lines. In the topmost terrace (right part of Figure VI.20(a)), the region covered with a triangular pattern extends over a few tens of nanometers and displays a modulation in apparent topography. This modulation is highlighted with a dashed green line in the close-up view shown in Figure VI.20(b). This kind of modulation was observed in many different regions of the sample, in triangular domains which were relatively large (few tens of nanometers-large). When having a look at the boundaries of such domains, one notices that instead of observing filaments, triangular shapes extending slightly beyond the well-defined triangular domains can be observed (see

region pointed with a black arrow in Figure VI.20(b)). This observation seems to indicate that the whole surface of Cu(111) is covered, but that for some reason, most of the surface appears featureless and only a few regions exhibit well-defined triangular patterns. These well-defined regions appear less high than the surrounding regions, as if they were somehow embedded. We propose that the regions displaying well-defined triangular patterns are confined regions, where the positions of the objects forming the patterns are fixed due to lateral confinement. We speculate that the surrounding regions are covered with parts broken up from DOBV molecules (including core parts of DOBV molecules). We propose that such objects are free to diffuse at room temperature, and become observable in confined regions only. We also attribute the modulation in apparent topography to the lateral confinement. We believe that the lateral constraints exerted on the molecular assemblies result in the buckling of the assemblies.

## Conclusion

Verdazyl radicals are promising candidates for realizing spin molecular systems on quasi-free standing superconducting graphene. We have determined the sublimation temperature of two verdazyl compounds synthesized by our chemist colleagues in a close-to-UHV environment. We have shown that 3-(p-tolyl)-1,5-dimethyl-6-oxoverdazyl (TMOV) molecules degrade before or around 350 K-370 K, and 1,1'-5,5'-tetradodecyl-6,6'-dioxo-3,3'-biverdazyl (DOBV) molecules degrade at about 350 K-370 K. Only the latter verdazyl compound was considered for UHV depositions on surfaces as its sublimation temperature is slightly higher. Experimental adjustments were made to ensure that DOBV molecules do not sublime during the bake-out of the UHV chamber containing the molecular evaporator. Preliminary results were obtained with DOBV molecules on a model system, namely Cu(111). We could not draw any definite conclusion on the structure of the molecular assemblies observed on Cu(111), but it seems reasonable that, for the measurements campaign 2, these assemblies do not correspond to pristine DOBV molecules. Further investigations are needed to conclude on whether it is possible to deposit DOBV molecules in UHV conditions without degrading them. Other verdazyl compounds such as 1,3,5-triphenyl-6-oxoverdazyl and 1,3,5-triphenyl-6-thioxoverdazyl radicals could be considered in future works, as it was shown that they can be deposited on Au(111) [258]. Only after that can we consider depositing verdazyl radicals on quasi-free standing superconducting graphene.



In this thesis, we undertook the realization of a graphene-based system consisting of a quasi free-standing graphene platform with induced superconducting character and in close vicinity to magnetic impurities. The fabrication of such a sample was motivated by recent theoretical articles predicting unconventional Yu-Shiba-Rusinov (YSR) states in superconducting graphene [4, 5]. Although the targeted graphene-based system was not fabricated yet, all three ingredients (quasi-free standing graphene, induced superconducting character and proximity to magnetic impurities) have been addressed in the manuscript.

As previously demonstrated in Ref. [3], growing graphene on a Re(0001) substrate results in induced superconductivity in graphene. Structural aspects related to graphene grown on Re(0001) were addressed in Chapters III and IV. In particular, we showed in Chapter III that increasing the number of annealing cycles positively contributes to growing high-quality extended graphene domains. The structure of a surface rhenium carbide was studied as well, and three atomic models were proposed. Density functional theory calculations should soon inform us on the stability of the proposed models and on a possible hierarchy (in energy) between them. In Chapter IV a widely observed defect in the nanorippled structure of graphene on strongly interacting metals such as Re(0001) and Ru(0001) was ascribed to stacking faults either in graphene or in the metal substrate. These studies (Chapters III and IV) contribute to grasping a little better the richness of graphene grown on metallic substrates.

Although rhenium provides the required induced superconducting character, growing graphene directly on top of such a strongly interacting metal results in a major limitation: the two-dimensional character of pristine graphene is lost. In order to recover a quasi-free standing character (which constitutes one of the three requirements we have identified), graphene was decoupled from its initial substrate *via* intercalation of gold atoms. The results supporting this claim were presented in Chapter V. Our data showed that besides the recovery of a quasi-free standing character, gold-intercalated graphene on Re(0001) presents a high density of defects. The latter was attributed to the formation of defects upon intercalation. We believe that the Raman spectroscopy-based methods used in this study to assess the density of defects should be routinely used in studies related to intercalated graphene to unveil the often underestimated impact of intercalation on the quality of graphene. Additionally, we showed that rhenium-induced superconductivity in graphene is not altered by gold intercalation, hence the two first requirements for realizing the targeted system are fulfilled.

The regained two-dimensional character of graphene should allow observing a few nanometers-extended YSR states [130], provided that we bring magnetic impurities in close proximity to graphene. Preliminary results involving two original magnetic verdazyl compounds were presented in Chapter VI. The sublimation temperatures of the two compounds in a close-to-ultra-high vacuum environment were determined. Although we did not deposit these compounds on quasi-free standing superconducting graphene yet, preliminary results obtained on a model system, Cu(111), were presented. We could not resolve the precise structure of the molecular assemblies covering the Cu(111) surface yet, and the thermal stability of the compounds was discussed. The deposition of other compounds should probably be explored.

Before shifting to quasi-free standing superconducting graphene as a hosting material for magnetic impurities, further investigations on model systems are needed. One promising perspective could rely on the use of Au(111). Indeed, it was shown that 1,3,5-triphenyl-6-oxoverdazyl and 1,3,5-triphenyl-6-thioverdazyl can be successfully deposited on Au(111) under ultra-high vacuum conditions [258]. Additionally, Au(111) presents an opportunity for cross-laboratory measurements, as it less easily oxidizes than Cu(111). In this prospect, a Au(111) single-crystal with dimensions compatible with both the

ultra-high vacuum system located in CNRS/Institut Néel and one of the two low temperature scanning tunneling microscopes of CEA/IRIG was purchased. Observing molecular assemblies on Au(111) at low temperature should help determining their structure. Besides, observing a Kondo effect could ascertain the radical character of the deposited molecules, as it was done in Ref. [258]. If the DOBV compound studied in this manuscript proves to be degraded in the temperature range corresponding to the bake-out of the ultra-high vacuum chamber used for molecular depositions, other verdazyl compounds could be envisaged, such as the ones used in Ref. [258].

---

## BIBLIOGRAPHY

---

- [1] C. Tonnoir. Scanning tunneling spectroscopy study of epitaxial graphene on superconducting rhenium. *Université Grenoble Alpes*, PhD thesis, 2013.
- [2] A. Artaud. Quasi-long-range order and topological defects in graphene on rhenium studied by scanning tunneling microscopy. *Université Grenoble Alpes*, PhD thesis, 2017.
- [3] C. Tonnoir, A. Kimouche, J. Coraux, L. Magaud, B. Delsol, B. Gilles and C. Chapelier. Induced superconductivity in graphene grown on rhenium. *Phys. Rev. Lett.*, 111(24):246805, 2013.
- [4] T. O. Wehling, H. P. Dahal, A. I. Lichtenstein and A. V. Balatsky. Local impurity effects in superconducting graphene. *Phys. Rev. B*, 78(3):035414, 2008.
- [5] J. L. Lado and J. Fernández-Rossier. Unconventional Yu–Shiba–Rusinov states in hydrogenated graphene. *2D Mat.*, 3(2):025001, 2016.
- [6] A. H. Castro Neto, F. Guinea, N. M. R. Peres, K. S. Novoselov and A. K. Geim. The electronic properties of graphene. *Rev. Mod. Phys.*, 81(1):109–162, 2009.
- [7] K. S. Novoselov, A. K. Geim, S. V. Morozov, D. Jiang, M. I. Katsnelson, I. V. Grigorieva, S. V. Dubonos and A. A. Firsov. Two-dimensional gas of massless Dirac fermions in graphene. *Nat.*, 438(7065):197–200, 2005.
- [8] L. Wang, I. Meric, P. Y. Huang, Q. Gao, Y. Gao, H. Tran, T. Taniguchi, K. Watanabe, L. M. Campos, D. A. Muller, J. Guo, P. Kim, J. Hone, K. L. Shepard and C. R. Dean. One-dimensional electrical contact to a two-dimensional material. *Science*, 342(6158):614–617, 2013.
- [9] A. K. Geim and K. S. Novoselov. The rise of graphene. *Nat. Mat.*, 6(3):183–191, 2007.
- [10] K. I. Bolotin, K. J. Sikes, Z. Jiang, M. Klima, G. Fudenberg, J. Hone, P. Kim and H. L. Stormer. Ultrahigh electron mobility in suspended graphene. *Nat. Mat.*, 146(9):351–355, 2008.
- [11] J.-H. Chen, C. Jang, S. Xtao, M. Tshigami and M. S. Fuhrer. Intrinsic and extrinsic performance limits of graphene devices on SiO<sub>2</sub>. *Nat. Nanotechnol.*, 3(4):206–209, 2008.
- [12] Y. Zhang, Y.-W. Tan, H. L. Stormer and P. Kim. Experimental observation of the quantum Hall effect and Berry’s phase in graphene. *Nat.*, 438(7065):201–204, 2005.
- [13] M. I. Katsnelson, K. S. Novoselov and A. K. Geim. Chiral tunnelling and the Klein paradox in graphene. *Nat. Phys.*, 2(9):620–625, 2006.
- [14] C. W. J. Beenakker. Colloquium : Andreev reflection and Klein tunneling in graphene. *Rev. Mod. Phys.*, 80(4):1337–1354, 2008.
- [15] A. Allard and L. Wirtz. Graphene on metallic substrates: Suppression of the Kohn anomalies in the phonon dispersion. *Nano Lett.*, 10(11):4335–4340, 2010.



- [16] C. Oshima, T. Aizawa, R. Souda, Y. Ishizawa and Y. Sumiyoshi. Surface phonon dispersion curves of graphite (0001) over the entire energy region. *Solid State Commun.*, 65(12):1601–1604, 1988.
- [17] S. Siebentritt, R. Pues, K.-H. Rieder and A. M. Shikin. Surface phonon dispersion in graphite and in a lanthanum graphite intercalation compound. *Phys. Rev. B*, 55(12):7927, 1997.
- [18] A. C. Ferrari and D. M. Basko. Raman spectroscopy as a versatile tool for studying the properties of graphene. *Nat. Nanotechnol.*, 8:235–246, 2013.
- [19] A. C. Ferrari, J. C. Meyer, V. Scardaci, C. Casiraghi, M. Lazzeri, F. Mauri, S. Piscanec, D. Jiang, K. S. Novoselov, S. Roth and A. K. Geim. Raman spectrum of graphene and graphene Layers. *Phys. Rev. Lett.*, 97(18):187401, 2006.
- [20] S. Piscanec, M. Lazzeri, F. Mauri, A. C. Ferrari and J. Robertson. Kohn anomalies and electron-phonon interactions in graphite. *Phys. Rev. Lett.*, 93(18):185503, 2004.
- [21] A. Eckmann, A. Felten, I. Verzhbitskiy, R. Davey and C. Casiraghi. Raman study on defective graphene: Effect of the excitation energy, type, and amount of defects. *Phys. Rev. B*, 88(3):035426, 2013.
- [22] L. M. Malard, M. A. Pimenta, G. Dresselhaus and M. S. Dresselhaus. Raman spectroscopy in graphene. *Phys. Reports*, 473(5–6):51–87, 2009.
- [23] A. C. Ferrari and J. Robertson. Resonant Raman spectroscopy of disordered, amorphous, and diamondlike carbon. *Phys. Rev. B*, 64(7):075414, 2001.
- [24] M. M. Lucchese, F. Stavale, E. H. Martins Ferreira, C. Vilani, M. V. O. Moutinho, R. B. Capaz, C. A. Achete and A. Jorio. Quantifying ion-induced defects and Raman relaxation length in graphene. *Carbon*, 48(5):1592–1597, 2010.
- [25] L. G. Cançado, A. Jorio, E. H. Martins Ferreira, F. Stavale, C. A. Achete, R. B. Capaz, M. V. O. Moutinho, A. Lombardo, T. Kulmala and A. C. Ferrari. Quantifying defects in graphene via Raman spectroscopy at different excitation energies. *Nano Lett.*, 11(8):3190–3196, 2011.
- [26] M. Lazzeri and F. Mauri. Nonadiabatic Kohn anomaly in a doped graphene monolayer. *Phys. Rev. Lett.*, 97(26):266407, 2006.
- [27] S. Pisana, M. Lazzeri, C. Casiraghi, K. S. Novoselov, A. K. Geim, A. C. Ferrari and F. Mauri. Breakdown of the adiabatic Born–Oppenheimer approximation in graphene. *Nat. Mater.*, 6(3):198–201, 2007.
- [28] J. Yan, Y. Zhung, P. Kim and A. Pinczuk. Electric field effect tuning of electron-phonon coupling in graphene. *Phys. Rev. Lett.*, 98(16):166802, 2007.
- [29] A. Das, S. Pisana, S. Piscanec, B. Chakraborty, S. K. Saha, U. V. Waghmare, R. Yiang, H. R. Krishnamurthy, A. K. Geim, A. C. Ferrari and A. K. Sood. Electrochemically top gated graphene: Monitoring dopants by Raman scattering. *Nat. Nanotechnol.*, 3(4):210–215, 2008.
- [30] D. M. Basko, S. Piscanec and A. C. Ferrari. Electron-electron interactions and doping dependence of the two-phonon Raman intensity in graphene. *Phys. Rev. B*, 80(16):165413, 2009.
- [31] W. Zhao, P. H. Tan, J. Liu and A. C. Ferrari. Intercalation of few-layer graphite flakes with  $\text{FeCl}_3$ : Raman determination of Fermi level, layer decoupling and stability. *J. Am. Chem. Soc.*, 133(15):5941–5946, 2011.
- [32] L. Pietronero and S. Strässler. Bond-length change as a tool to determine charge transfer and electron-phonon coupling in graphite intercalation compounds. *Phys. Rev. Lett.*, 47(8):593–596, 1981.

- [33] M. Huang, H. Yan, C. Chen, D. Song, T. F. Heinz and J. Hone. Phonon softening and crystallographic orientation of strained graphene studied by Raman spectroscopy. *PNAS*, 79(20):205433, 2009.
- [34] T. M. G. Mohiuddin, A. Lombardo, R. R. Nair, A. Bonetti, G. Savini, R. Jalil, N. Bonini, D. M. Basko, C. Galiotis, N. Marzari, K. S. Novoselov, A. K. Geim and A. C. Ferrari. Uniaxial strain in graphene by Raman spectroscopy: G peak splitting, Grüneisen parameters, and sample orientation. *Phys. Rev. B*, 79(20):205433, 2009.
- [35] F. Ding, H. Ji, Y. Chen, A. Herklotz, K. Dörr, Y. Mei, A. Rastelli and O. G. Schmidt. Stretchable graphene: A close look at fundamental parameters through biaxial strain. *Nano Lett.*, 10(9):3453–3458, 2010.
- [36] J. Zabel, R. R. Nair, A. Ott, A. Georgiou, A. K. Geim, K. S. Novoselov and C. Casiraghi. Raman spectroscopy of graphene and bilayer graphene under biaxial strain: Bubbles and balloons. *Nano Lett.*, 12(2):617–621, 2012.
- [37] J. Wintterlin and M.-L. Bocquet. Graphene on metal surfaces. *Surf. Sci.*, 603(10–12):1841–1852, 2009.
- [38] A. Dahal and M. Batzill. Graphene–nickel interfaces: a review. *Nanoscale*, 6(5):2548–2562, 2014.
- [39] H. Tetlow, J. Posthuma de Boer, I. J. Ford, D. D. Vvedensky, J. Coraux and L. Kantorovich. Growth of epitaxial graphene: Theory and experiment. *Phys. Rep.*, 542(3):195–295, 2014.
- [40] A. Ya. Tontegode. Carbon on transition metal surfaces. *Prog. Surf. Sci.*, 38(3–4):201–429, 1991.
- [41] W. J. Arnoult and R. B. McLellan. The solubility of carbon in rhodium ruthenium, iridium and rhenium. *Scripta Metallurgica*, 6(10):1013–1018, 1972.
- [42] J. C. Shelton, H. R. Patil and J. M. Blakely. Equilibrium segregation of carbon to a nickel (111) surface: A surface phase transition. *Surf. Sci.*, 43(2):493–520, 1974.
- [43] X. S. Li, W. W. Cai, J. H. An, S. Kim, J. Nah, D. X. Yang, R. Piner, A. Velamakanni, I. Jung, E. Tutuc, S. K. Banerjee, L. Colombo and R. S. Ruoff. Equilibrium segregation of carbon to a nickel (111) surface: A surface phase transition. *Science*, 324(5932):1312–1314, 2009.
- [44] E. Miniussi, M. Pozzo, A. Baraldi, E. Vesselli, R. R. Zhan, G. Comelli, T. O. Mendes, M. A. Niño, A. Locatelli, S. Lizzit and D. Alfè. Thermal Stability of corrugated epitaxial graphene grown on Re(0001). *Phys. Rev. Lett.*, 106(21):216101, 2011.
- [45] E. Miniussi, M. Pozzo, T. O. Mendes, M. A. Niño, A. Locatelli, E. Vesselli, G. Comelli, S. Lizzit, D. Alfè and A. Baraldi. The competition for graphene formation on Re(0001): A complex interplay between carbon segregation, dissolution and carburisation. *Carbon*, 73:389–402, 2014.
- [46] T. A. Land, T. Michely, R. J. Behm, J. C. Hemminger and G. Comsa. STM investigation of single layer graphite structures produced on Pt(111) by hydrocarbon decomposition. *Surf. Sci.*, 264(3):261–270, 1992.
- [47] K. Hermann. Periodic overlayers and moiré patterns: Theoretical studies of geometric properties. *J. Phys.: Condens. Matter*, 24(31):314210, 2012.
- [48] P. Zeller and S. Günther. What are the possible moiré patterns of graphene on hexagonally packed surfaces? Universal solution for hexagonal coincidence lattices, derived by a geometric construction. *New J. Phys.*, 16(8):083028, 2014.

- [49] A. Artaud, L. Magaud, T. Le Quang, V. Guisset, P. David, C. Chapelier and J. Coraux. Universal classification of twisted, strained and sheared graphene moiré superlattices. *Sci. Rep.*, 6(1):25670, 2016.
- [50] P. Zeller, X. Ma, S. Günther. Indexing moiré patterns of metal-supported graphene and related systems: Strategies and pitfalls. *New J. Phys.*, 19(1):013015, 2017.
- [51] B. Wang, M.-L. Bocquet, S. Marchini, S. Günther and J. Wintterlin. Chemical origin of a graphene moiré overlayer on Ru(0001). *Phys. Chem. Chem. Phys.*, 10(24):3530–3534, 2008.
- [52] C. Busse, P. Lazic, R. Djemour, J. Coraux, T. Gerber, N. Atodiresei, V. Caciuc, R. Brako, A. T. N'Diaye, S. Blügel, J. Zegenhagen and T. Michely. Graphene on Ir(111): Physisorption with chemical modulation. *Phys. Rev. Lett.*, 107(3):036101, 2011.
- [53] I. Pletikosić, M. Kralj, P. Pervan, R. Brako, J. Coraux, A. T. N'Diaye, C. Busse and T. Michely. Dirac cones and minigaps for graphene on Ir(111). *Phys. Rev. Lett.*, 102(5):056808, 2009.
- [54] H. Zi-Pu, D. F. Ogletree, M. A. van Hove and G. A. Somorjai. LEED theory for incommensurate overlayers: application to graphite on Pt(111). *Surf. Sci.*, 180(2–3):433–459, 1987.
- [55] P. Sutter, J. T. Sadowski and E. Sutter. Graphene on Pt(111): Growth and substrate interaction. *Phys. Rev. B*, 80(24):245411, 2009.
- [56] L. Gao, J. R. Guest and N. P. Guisinger. Epitaxial graphene on Cu(111). *Nano Lett.*, 10(9):3512–3516, 2010.
- [57] E. N. Voloshina and Y. S. Dedkov. General approach to understanding the electronic structure of graphene on metals. *Mat. Res. Express*, 1(3):035603, 2014.
- [58] B. Kiraly, E. V. Iski, A. J. Mannix, B. L. Fisher, M. C. Hersam and N. P. Guisinger. Solid-source growth and atomic-scale characterization of graphene on Ag(111). *Nat. Commun.*, 4(1):2804, 2013.
- [59] S. Nie, N. C. Bartelt, J. M. Wofford, O. D. Dubon, K. F. McCarty and K. Thürmer. Scanning tunneling microscopy study of graphene on Au(111): Growth mechanisms and substrate interactions. *Phys. Rev. B*, 85(20):205406, 2012.
- [60] M. Papagno, P. Moras, P. M. Sheverdyeva, J. Doppler, A. Garhofer, F. Mittendorfer, J. Redinger and C. Carbone. Hybridization of graphene and a Ag monolayer supported on Re(0001). *Phys. Rev. B*, 88(23):235430, 2013.
- [61] L. Gao, Y. Liu, R. Shi, T. Ma, Y. Hu and J. Luo. Influence of interface interaction on the moiré superstructures of graphene on transition-metal substrates. *RSC Adv.*, 7(20):12179–12184, 2013.
- [62] S. Marchini, S. Günther and J. Wintterlin. Scanning tunneling microscopy on graphene on Ru(0001). *Phys. Rev. B*, 76(7):075429, 2007.
- [63] P. W. Sutter, J.-I. Flege and E. A. Sutter. Epitaxial graphene on ruthenium. *Nat. Mater.*, 7(5):406–411, 2008.
- [64] E. Sutter, D.-P. Acharya, J. T. Sadowski and P. Sutter. Scanning tunneling microscopy on epitaxial bilayer graphene on ruthenium(0001). *Appl. Phys. Lett.*, 94(13):133101, 2009.
- [65] B. Wang, S. Günther, J. Wintterlin and M. Bocquet. Periodicity, work function and reactivity of graphene on Ru(0001) from first principles. *New J. Phys.*, 12(4):043041, 2010.
- [66] Y. Gamo, A. Nagashima, M. Wakabayashi, M. Terai and C. Oshima. Atomic structure of monolayer graphite formed on Ni(111). *Surf. Sci.*, 374(1–3):61–64, 1997.

- [67] D.-e. Jiang, M.-H. Du and S. Dai. First principles study of the graphene/Ru(0001) interface. *J. Chem. Phys.*, 130(7):074705, 2009.
- [68] M. Vanin, J. J. Mortensen, A. K. Kelkkanen, J. M. Garcia-Lastra, K. S. Thygesen and K. W. Jacobsen. Graphene on metals: A van der Waals density functional study. *Phys. Rev. B*, 81(8):081408, 2010.
- [69] P. A. Khomyakov, G. Giovannetti, P. C. Rusu, G. Brocks, J. van den Brink and P. J. Kelly. First-principles study of the interaction and charge transfer between graphene and metals. *Phys. Rev. B*, 79(19):195425, 2009.
- [70] A. L. Hsu, R. J. Koch, M. T. Ong, W. Fang, M. Hofmann, K. K. Kim, T. Seyller, M. S. Dresselhaus, E. J. Reed, J. Kong and Tomás Palacios. Surface-induced hybridization between graphene and titanium. *ACS Nano*, 8(8):7704–7713, 2014.
- [71] G. Giovannetti, P. A. Khomyakov, G. Brocks, V. M. Karpan, J. van den Brink and P. J. Kelly. Doping graphene with metal contacts. *Phys. Rev. Lett.*, 101(2):026803, 2008.
- [72] J. Sánchez-Barriga, A. Varykhalov, D. Marchenko, M. R. Scholz and O. Rader. Minigap isotropy and broken chirality in graphene with periodic corrugation enhanced by cluster superlattices. *Phys. Rev. B*, 85(20):201413, 2012.
- [73] M. Kralj, I. Pletikosić, M. Petrović, P. Pervan, M. Milun, A. T. N’Diaye, C. Busse, T. Michely, J. Fujii and I. Vobornik. Graphene on Ir(111) characterized by angle-resolved photoemission. *Phys. Rev. B*, 84(7):075427, 2011.
- [74] D. Usachov, A. Fedorov, O. Vilkov, V. K. Adamchuk, L. Y. Yashina, L. Bondarenko, A. A. Saranin, A. Grüneis and D. V. Vyalikh. Experimental and computational insight into the properties of the lattice-mismatched structures: Monolayers of *h*-BN and graphene on Ir(111). *Phys. Rev. B*, 86(15):155151, 2012.
- [75] E. Wang, X. Lu, S. Ding, W. Yao, M. Yan, G. Wan, K. Deng, S. Wang, G. Chen, L. Ma, J. Jung, A. V. Fedorov, Y. Zhang, G. Zhang and S. Zhou. Gaps induced by inversion symmetry breaking and second-generation Dirac cones in graphene/hexagonal boron nitride. *Nat. Phys.*, 12:1111–1115, 2016.
- [76] T. Ohta, J. T. Robinson, P. J. Feibelman, A. Bostwick, E. Rotenberg and T. E. Beechem. Evidence for interlayer coupling and moiré periodic potentials in twisted bilayer graphene. *Phys. Rev. Lett.*, 109(18):186807, 2012.
- [77] H. Selig and L. B. Ebert. Graphite intercalation compounds. *Adv. Inorg. Chem. Radiochem.*, 23:281–327, 1980.
- [78] M. S. Dresselhaus and G. Dresselhaus. Intercalation compounds of graphite. *Adv. Phys.*, 30(2):139–326, 1981.
- [79] S. Basu, C. Zeller, P. J. Flanders, C. D. Fuerst, W. D. Johnson and J. E. Fischer. Synthesis and properties of lithium-graphite intercalation compounds. *Mater. Sci. Engineer.*, 38(3):275–283, 1979.
- [80] R. Niess and E. Stumpp. Graphit einlagerungsverbindungen mit thallium(III) bromid. *Carbon*, 16(4):265–268, 1978.
- [81] J. G. Hooley, M. W. Bartlett, B. V. Liengme and J. R. Sams. A Mössbauer study of graphite iron chloride compounds. *Carbon*, 6(5):681–685, 1968.
- [82] R. Mu, Q. Fu, L. Jin, L. Yu, G. Fang, D. Tan and X. Bao. Visualizing chemical reactions confined under graphene. *Angew. Chem. Int. Ed.*, 51(20):4856–4859, 2012.

- [83] A. Ya. Tontegode and F. K. Yusifov. Superefficient diffusion of cesium atoms into rhenium covered by a 2D graphite film. *Appl. Surf. Sci.*, 90(2):185–190, 1995.
- [84] J. Xu, Y. Dou, Z. Wei, J. Ma, Y. Deng, Y. Li, H. Liu and S. Dou. Recent progress in graphite intercalation compounds for rechargeable metal (Li, Na, K, Al)-ion batteries. *Adv. Sci.*, 4(10):1700146, 2017.
- [85] J. Coraux, A. T. N’Diaye, N. Rougemaille, C. Vo-Van, A. Kimouche, H.-X. Yang, M. Chshiev, N. Bendiab, O. Fruchart and A. K. Schmid. Air-protected epitaxial graphene/ferromagnet hybrids prepared by chemical vapor deposition and intercalation. *J. Phys. Chem. Lett.*, 3(15):2059–2063, 2012.
- [86] Z. Y. Al Balushi, K. Wang, R. K. Ghosh, R. A. Vilá, S. M. Eichfeld, J. D. Caldwell, X. Qin, Y.-C. Lin, P. A. DeSario, G. Stone, S. Subramanian, D. F. Paul, R. M. Wallace, S. Datta, J. M. Redwing and J. A. Robinson. Two-dimensional gallium nitride realized via graphene encapsulation. *Nat. Mater.*, 15(11):1166–1171, 2016.
- [87] M. Sicot, P. Leicht, A. Zusan, S. Bouvron, O. Zander, M. Weser, Y. S. Dedkov, K. Horn and M. Fonin. Size-selected epitaxial nanoislands underneath graphene moiré on Rh(111). *ACS Nano*, 6(1):151–158, 2012.
- [88] M. Petrović, I. Š Rakić, S. Runte, C. Busse, J. T. Sadowski, P. Lazić, I. Pletikosić, Z.-H. Pan, M. Milun, P. Pervan, N. Atodiresei, R. Brako, D. Šokčević, T. Valla, T. Michely and M. Kralj. The mechanism of caesium intercalation of graphene. *Nat. Commun.*, 4(1):2772, 2013.
- [89] S. Vlaic, A. Kimouche, J. Coraux, B. Santos, A. Locatelli and N. Rougemaille. Cobalt intercalation at the graphene/iridium(111) interface: Influence of rotational domains, wrinkles, and atomic steps. *Appl. Phys. Lett.*, 104(10):101602, 2014.
- [90] P. Sutter, J. T. Sadowski and E. A. Sutter. Chemistry under cover: Tuning metal-graphene interaction by reactive intercalation. *J. Am. Chem. Soc.*, 132(23):8175–8179, 2010.
- [91] S. Vlaic, N. Rougemaille, A. Kimouche, B. Santos Burgos, A. Locatelli and J. Coraux. Intercalating cobalt between graphene and iridium (111): Spatially dependent kinetics from the edges. *Phys. Rev. Mater.*, 1(5):053406, 2017.
- [92] S. Vlaic, N. Rougemaille, A. Artaud, V. T. Renard, L. Huder, J.-L. Rouviere, A. Kimouche, B. Santos, A. Locatelli, V. Guisset, P. David, C. Chapelier, L. Magaud, B. Canals and J. Coraux. Graphene as a mechanically active, deformable two-dimensional surfactant. *J. Phys. Chem. Lett.*, 9(10):2523–2531, 2018.
- [93] L. Huang, Y. Pan, L. Pan, M. Gao, W. Xu, Y. Que, H. Zhou, Y. Wang, S. Du and H.-J. Gao. Intercalation of metal islands and films at the interface of epitaxially grown graphene and Ru(0001) surfaces. *Appl. Phys. Lett.*, 99(16):163107, 2011.
- [94] M. Sicot, Y. Fagot-Revurat, B. Kierren, G. Vasseur and D. Malterre. Copper intercalation at the interface of graphene and Ir(111) studied by scanning tunneling microscopy. *Appl. Phys. Lett.*, 105(19):191603, 2014.
- [95] D. A. Estyunin, I. I. Klimovskikh, V. Y. Voroshin, D. M. Sostina, L. Petaccia, G. Di Santo and A. M. Shikin. Formation of a quasi-free-standing graphene with a band gap at the Dirac point by Pb atoms intercalation under graphene on Re(0001). *J. Exp. Theo. Phys.*, 125(5):762–767, 2017.
- [96] A. Varykhalov, M. R. Scholz, T. K. Kim and O. Rader. Effect of noble-metal contacts on doping and band gap of graphene. *Phys. Rev. B*, 82(12):121101, 2010.

- [97] D. Marchenko, A. Varykhalov, M. R. Scholz, G. Bihlmayer, E. I. Rashba, A. Rybkin, A. M. Shikin and O. Rader. Giant Rashba splitting in graphene due to hybridization with gold. *Nat. Commun.*, 3(1):1232, 2012.
- [98] A. M. Shikin, A. G. Rybkin, D. Marchenko, A. A. Rybkina, M. R. Scholz, O. Rader and A. Varykhalov. Induced spin-orbit splitting in graphene: the role of atomic number of the intercalated metal and  $\pi$ -d hybridization. *New J. Phys.*, 15(1):013016, 2013.
- [99] E. N. Voloshina, A. Generalov, M. Weser, S. Böttcher, K. Horn and Y. S. Dedkov. Structural and electronic properties of the graphene/Al/Ni(111) intercalation system. *New J. Phys.*, 13(11):113028, 2011.
- [100] B. Premalal, M. Cranney, F. Vonau, D. Aubel, D. Casterman, M. M. De Souza and L. Simon. Surface intercalation of gold underneath a graphene monolayer on SiC(0001) studied by scanning tunneling microscopy and spectroscopy. *Appl. Phys. Lett.*, 94(26):263115, 2009.
- [101] I. Gierz, T. Suzuki, R. T. Weitz, D. S. Lee, B. Krauss, C. Riedl, U. Starke, H. Höchst, J. H. Smet, C. R. Ast and K. Kern. Electronic decoupling of an epitaxial graphene monolayer by gold intercalation. *Phys. Rev. B*, 81(23):235408, 2010.
- [102] C. Enderlein, Y. S. Kim, A. Bostwick, E. Rotenberg and K. Horn. The formation of an energy gap in graphene on ruthenium by controlling the interface. *New J. Phys.*, 12(3):033014, 2010.
- [103] X. Fei, L. Zhang, W. Xiao, H. Chen, Y. Que, L. Liu, K. Yang, S. Du and H. J. Gao. Structural and electronic properties of Pb-intercalated graphene on Ru(0001). *J. Phys. Chem. C*, 119(18):9839–9844, 2015.
- [104] P. Leicht, L. Zielke, S. Bouvron, R. Moroni, E. Voloshina, L. Hammerschmidt, Y. S. Dedkov and M. Fonin. *In situ* fabrication of quasi-free-standing epitaxial graphene nanoflakes on gold. *ACS Nano*, 8(4):3735–3742, 2014.
- [105] F. Calleja, H. Ochoa, M. Garnica, S. Barja, J. J. Navarro, A. Black, M. M. Otrokov, E. V. Chulkov, A. Arnau, A. L. Vázquez de Parga, F. Guinea and R. Miranda. Spatial variation of a giant spin-orbit effect induces electron confinement in graphene on Pb islands. *Nat. Phys.*, 11(1):43–47, 2015.
- [106] I. I. Klimovskikh, M. M. Otrokov, V. Y. Voroshnin, D. Sostina, L. Petaccia, G. Di Santo, S. Thakur, E. V. Chulkov and A. M. Shikin. Spin-orbit coupling induced gap in graphene on Pt(111) with intercalated Pb monolayer. *ACS Nano*, 11(1):368–374, 2017.
- [107] A. Varykhalov, J. Sánchez-Barriga, A. M. Shikin, C. Biswas, E. Vescovo, A. Rybkin, D. Marchenko and O. Rader. Electronic and magnetic properties of quasifreestanding graphene on Ni. *Phys. Rev. Lett.*, 101(15):157601, 2008.
- [108] M. N. Nair, M. Cranney, F. Vonau, D. Aubel, P. Le Fèvre, A. Tejada, F. Bertran, A. Taleb-Ibrahimi and L. Simon. High van Hove singularity extension and Fermi velocity increase in epitaxial graphene functionalized by intercalated gold clusters. *Phys. Rev. B*, 85(24):245421, 2012.
- [109] M. N. Nair, M. Cranney, F. Vonau, D. Aubel, P. Le Fèvre, A. Tejada, F. Bertran, A. Taleb-Ibrahimi and L. Simon. Surface intercalation of gold underneath a graphite monolayer on Ni(111) studied by angle-resolved photoemission and high-resolution electron-energy loss spectroscopy. *Phys. Rev. B*, 85(24):245421, 2000.
- [110] S. Datta and B. Das. Electronic analog of the electro-optic modulator. *Appl. Phys. Lett*, 56(7):665–667, 1990.

- [111] M. M. Otrokov, I. I. Klimovskikh, F. Calleja, A. M. Shikin, O. Vilkov, A. G. Rybkin, D. Estyunin, S. Muff, J. H. Dil, A. L. Vázquez de Parga, R. Miranda, H. Ochoa, F. Guinea, J. I. Cerdá, E. V. Chulkov and A. Arnau. Evidence of large spin-orbit coupling effects in quasi-free-standing graphene on Pb/Ir(111). *2D Mater.*, 5(3):035029, 2018.
- [112] Y Dedkov and E Voloshina. Comment on "Spin-orbit coupling induced gap in graphene on Pt(111) with intercalated Pb monolayer". *ACS Nano*, 11(11):10627–10629, 2017.
- [113] I I Klimovskikh, M M Otrokov, V Y Voroshnin, D Sostina, L Petaccia, G Di Santo, S Thakur, E V Chulkov and A M Shikin. Reply to "Comment on "Spin-orbit coupling induced gap in graphene on Pt(111) with intercalated Pb monolayer"". *ACS Nano*, 11(11):10630–10632, 2017.
- [114] M. Krivenkov, E. Golias, D. Marchenko, J. Sánchez-Barriga, G. Bihlmayer, O. Rader and A. Varykhalov. Nanostructural origin of giant Rashba effect in intercalated graphene. *2D Mater.*, 4(3):035010, 2017.
- [115] J. Sławińska and J. I. Cerdá. Spin-orbit proximity effect in graphene on metallic substrates: decoration vs intercalation with metal adatoms. *New J. Phys.*, 21(7):073018, 2019.
- [116] I. Gierz, C. Riedl, U. Starke, C. R. Ast and K. Kern. Atomic hole doping of graphene. *Nano Lett.*, 8(12):4603–4607, 2008.
- [117] H. E. Romero, P. Joshi, A. K. Gupta, H. R. Gutierrez, M. W. Cole, S. A. Tadigadapa and P. C. Eklund. Adsorption of ammonia on graphene. *Nanotechnology*, 20(24):245501, 2009.
- [118] D. B. Farmer, R. Golizadeh-Mojarad, V. Perebeinos, Y.-M. Lin, G. S. Tulevski, J. C. Tsang and P. Avouris. Chemical doping and electron-hole conduction asymmetry in graphene devices. *Nano Lett.*, 9(1):388–392, 2009.
- [119] X. Dong, D. Fu, W. Fang, Y. Shi, P. Chen and L.-J. Li. Doping single-layer graphene with aromatic molecules. *Small*, 5(12):1422–1426, 2009.
- [120] J. Moser, A. Verdaguer, D. Jiménez, A. Barreiro and A. Bachtold. The environment of graphene probed by electrostatic force microscopy. *Appl. Phys. Lett.*, 92(12):123507, 2008.
- [121] Y. Sato, K. Takai and T. Enoki. Electrically controlled adsorption of oxygen in bilayer graphene devices. *Nano Lett.*, 11(8):3468–3475, 2011.
- [122] Light-driven reversible modulation of doping in graphene. M. Kim, N. S. Safron, C. Huang, M. S. Arnold and P. Gopalan. *Nano Lett.*, 12(1):182–187, 2012.
- [123] H. González-Herrero, J. M. Gómez-Rodríguez, P. Mallet, M. Moaied, J. J. Palacios, C. Salgado, M. M. Ugeda, J.-Y. Veuillen, F. Yndurain and I. Brihuega. Atomic-scale control of graphene magnetism by using hydrogen atoms. *Science*, 352(6284):437–441, 2016.
- [124] Y. Zhang, S.-Y. Li, H. Huang, W.-T. Li, J.-B. Qiao, W.-X. Wang, L.-J. Yin, K.-K. Bai, W. Duan and L. He. Scanning tunneling microscopy of the  $\pi$  magnetism of a single carbon vacancy in graphene. *Phys. Rev. Lett.*, 117(16):166801, 2016.
- [125] H. Shiba. Classical spins in superconductors. *Prog. Theor. Phys.*, 40(3):435–451, 1968.
- [126] W. J. de Haas, J. de Boer and G. J. van den Berg. The electrical resistance of gold, copper and lead at low temperatures. *Physica*, 1(7–12):1115–1124, 1934.
- [127] J. Kondo. Resistance minimum in dilute magnetic alloys. *Prog. Theor. Phys.*, 32(1):37–49, 1964.



- [128] J. Bardeen, L. N. Cooper and J. R. Schrieffer. Theory of superconductivity. *Phys. Rev.*, 108(5):1175–1204, 1957.
- [129] A. Yazdani, B. A. Jones, C. P. Lutz, M. F. Crommie and D. M. Eigler. Probing the local effects of magnetic impurities on superconductivity. *Science*, 275(5307):1767–1770, 1997.
- [130] G. C. Ménard, S. Guissart, C. Brun, S. Pons, V. S. Stolyarov, F. Debontridder, M. V. Leclerc, E. Janod, L. Cario, D. Roditchev, P. Simon and T. Cren. Coherent long-range magnetic bound states in a superconductor. *Nat. Phys.*, 11(12):1013–1016, 2015.
- [131] S. Andrieu and P. Müller. Les surfaces solides: concepts et méthodes. Ch.4: Techniques de diffraction de surface LEED et RHEED. *CNRS Editions*, 204–220, 2005.
- [132] A. Kimouche. Toward novel hybrid materials based on epitaxial graphene: Controlling the formation of defects and using them for intercalation. *Université Grenoble Alpes*, PhD thesis, 2013.
- [133] Kentax GmbH. Operating instructions for Evaporator HE-SC-2-cell and variable power supply unit, 2017.
- [134] C. N. Berglund and W. E. Spicer. Photoemission studies of copper and silver: Theory. *Phys. Rev.*, 136(4A):A1030–A1044, 1964.
- [135] J. Bardeen. Tunnelling from a many-particle point of view. *Phys. Rev. Lett.*, 6(2):57–59, 1961.
- [136] J. Tersoff and D. R. Hamann. Theory of the scanning tunneling microscope. *Phys. Rev. B*, 31(2):805–813, 1985.
- [137] G. Froehlicher. Etude par spectroscopie Raman de monocouches de graphène intégrées dans des transistors à effet de champ. *Ecole Normale Supérieure de Cachan*, Master report, 2013.
- [138] P. Hohenberg and W. Kohn. Inhomogeneous electron gas. *Phys. Rev.*, 136(3B):B864–B871, 1964.
- [139] W. Kohn and L. J. Sham. Self-consistent equations including exchange and correlation effects. *Phys. Rev.*, 140(4A):A1133–A1138, 1965.
- [140] J. P. Perdew, J. A. Chevary, S. H. Vosko, K. A. Jackson, M. R. Pederson, D. J. Singh and C. Fiolhais. Atoms, molecules, solids, and surfaces: Applications of the generalized gradient approximation for exchange and correlation. *Phys. Rev. B*, 46(11):6671–6687, 1992.
- [141] G. Kresse and J. Hafner. Ab initio molecular dynamics for liquid metals. *Phys. Rev. B*, 47(1):568–561, 1993.
- [142] G. Kresse and D. Joubert. From ultrasoft pseudopotentials to the projector augmented-wave method. *Phys. Rev. B*, 59(3):1758–1775, 1999.
- [143] G. Cresse and D. Joubert. J. P. Perdew, K. Burke and M. Ernzerhof. Generalized gradient approximation made simple. *Phys. Rev. Lett.*, 77(18):3865–3868, 1996.
- [144] S. Grimme. Semiempirical GGA-type density functional constructed with a long-range dispersion correction. *J. Comput. Chem.*, 27(15):1787–1799, 2006.
- [145] D. W. Brenner. Empirical potential for hydrocarbons for use in simulating the chemical vapor deposition of diamond films. *Phys. Rev. B*, 42(15):9458–9471, 1990.
- [146] P. Merino, M. Švec, A. L. Pinardi, G. Otero and J. A. Martín-Gago. Strain-driven moiré superstructures of epitaxial graphene on transition metal surfaces. *ACS Nano*, 5(7):5627–5634, 2011.

- [147] E. Loginova, S. Nie, K. Thürmer, N. C. Bartelt and K. F. McCarty. Defects of graphene on Ir(111): Rotational domains and ridges. *Phys. Rev. B*, 80(8):085430, 2009.
- [148] H. Hattab, A. T. N'Diaye, D. Wall, G. Jnawali, J. Coraux, C. Busse, R. van Gastel, B. Poelsema, T. Michely, F.-J. Meyer zu Heringdorf and M. Horn-von Hoegen. Growth temperature dependent graphene alignment on Ir(111). *Appl. Phys. Lett.*, 98(14):141903, 2011.
- [149] G. C. Dong, D. W. van Baarle, M. J. Rost and J. W. M. Frenken. Graphene formation on metal surfaces investigated by *in-situ* scanning tunneling microscopy. *New J. Phys.*, 14(5):053033, 2012.
- [150] Y. Qi, C. Meng, X. Xu, B. Deng, N. Han, J. Zhao, M. Liu, Q. Fu, M. Hong, Y. Li, Y. Zhang, Z. Liu, Y. Ning and K. Liu. Unique transformation from graphene to carbide on Re(0001) induced by strong carbon-metal interaction. *J. Am. Chem. Soc.*, 139(48):17574–17581, 2017.
- [151] J. Lahiri, T. Miller, L. Adamska, I. I. Oleynik and M. Batzill. Graphene growth on Ni(111) by transformation of a surface carbide. *Nano Lett.*, 11(2):518–522, 2011.
- [152] R. B. Levy and M. Boudart. Platinum-like behavior of tungsten carbide in surface catalysis. *Science*, 181(4099):547–549, 1973.
- [153] S. T. Oyama. Preparation and catalytic properties of transition metal carbides and nitrides. *Catalysis Today*, 15(2):179–200, 1992.
- [154] J. Bansmann, L. Lu, V. Senz, A. Bettac, M. Getzlaff and K. H. Meiwes-Broer. Structure and magnetism of self-organized Co islands. *Eur. Phys. J. D*, 9(1):461–466, 1999.
- [155] A. Varykhalov, O. Rader and W. Gudat. Self-organization of one-dimensional Au nanowires on a surface carbide and lateral electron quantization. *Phys. Rev. B*, 72(24):241404, 2005.
- [156] R. S. Zimmer and W. D. Robertson. A carbon structure on the Re(0001) surface. *Surf. Sci.*, 29:230–236, 1972.
- [157] D. R. Lide. CRC Handbook of Chemistry and Physics, 88th edition. *Taylor and Francis Group*, 12–201, 2008.
- [158] N. Blanc, F. Jean, A. V. Krasheninnikov, G. Renaud and J. Coraux. Strains induced by point defects in graphene on a metal. *Phys. Rev. Lett.*, 111(8):085501, 2013.
- [159] A. Artaud, L. Magaud, K. Ratter, B. Gilles, V. Guisset, P. David, J. I. Martínez, J. A. Martín-Gago, C. Chapelier and J. Coraux. Size-selective carbon clusters as obstacles to graphene growth on a metal. *Nano Lett.*, 18:4812–4820, 2018.
- [160] A. Artaud, E. Mazaleyrat, G. D. Förster, C. Tonnoir, L. Magaud, F. Calvo, C. Chapelier and J. Coraux. Depressions by stacking faults in nanorippled graphene on metals. *submitted*, 2019.
- [161] J. Grant and T. Haas. A study of Ru(0001) and Rh(111) surfaces using LEED and Auger electron spectroscopy. *Surf. Sci.*, 21(1):76–85, 1970.
- [162] A. Van Bommel, J. Crombeen and A. Van Tooren. LEED and Auger electron observations of the SiC(0001) surface. *Surf. Sci.*, 48(2):463–472, 1975.
- [163] M. Corso, W. Auwärter, M. Muntwiler, A. Tamai, T. Greber and J. Osterwalder. Boron nitride nanomesh. *Science*, 303(5655):217–220, 2004.
- [164] R. Laskowski, P. Blaha, T. Gallauner and K. Schwarz. Single-layer model of the hexagonal boron nitride nanomesh on the Rh(111) surface. *Phys. Rev. Lett.*, 98(10):106802, 2007.

- [165] D. Kim, D. Sun, W. Lu, Z. Cheng, Y. Zhu, D. Le, T. S. Rahman and L. Bartels. Toward the growth of an aligned single-layer MoS<sub>2</sub> film. *Langmuir*, 27(18):11650–11653, 2011.
- [166] S. G. Sørensen, H. G. Füchtbauer, A. K. Tuxen, A. S. Walton and J. V. Lauritsen. Structure and electronic properties of *in situ* synthesized single-layer MoS<sub>2</sub> on a gold surface. *ACS Nano*, 8(7):6788–6796, 2014.
- [167] S. Altenburg and R. Berndt. Local work function and STM tip-induced distortion of graphene on Ir(111). *New J. Phys.*, 16(5):053036, 2014.
- [168] S. Altenburg, J. Kröger, B. Wang, M.-L. Bocquet, N. Lorente, and R. Berndt. Graphene on Ru(0001): Contact formation and chemical reactivity on the atomic scale. *Phys. Rev. Lett.*, 105(23):, 2010.
- [169] M. P. Boneschanscher, J. van der Lit, Z. Sun, I. Swart, P. Liljeroth and D. Vanmaekelbergh. Quantitative atomic resolution force imaging on epitaxial graphene with reactive and nonreactive AFM probes. *ACS Nano*, 6(11):10216–10221, 2012.
- [170] E. N. Voloshina, E. Fertitta, A. Garhofer, F. Mittendorfer, M. Fonin, A. Thissen and Y. S. Dedkov. Electronic structure and imaging contrast of graphene moiré on metals. *Sci. Rep.*, 3(1):1072, 2013.
- [171] P. Yi, S. Dong-Xia and G. Hong-Jun. Formation of graphene on Ru(0001) surface. *Chin. Phys.*, 16(11):3151, 2007.
- [172] A. L. Vázquez de Parga, F. Calleja, B. Borca, M. C. G. Passeggi, Jr., J. J. Hinarejos, F. Guinea and R. Miranda. Periodically rippled graphene: Growth and spatially resolved electronic structure. *Phys. Rev. Lett.*, 100(5):056807, 2008.
- [173] Y. Pan, H. Zhang, D. Shi, J. Sun, S. Du, F. Liu and H.-j. Gao. Highly ordered, millimeter-scale, continuous, single-crystalline graphene monolayer formed on Ru(0001). *Adv. Mater.*, 21(27):2777–2780, 2009.
- [174] E. Sutter, D.-P. Acharya, J. T. Sadowski and P. Sutter. Scanning tunneling microscopy on epitaxial bilayer graphene on ruthenium(0001). *Appl. Phys. Lett.*, 94(13):133101, 2009.
- [175] K. Donner and P. Jakob. Structural properties and site specific interactions of Pt with the graphene/Ru(0001) moiré overlayer. *J. Chem. Phys.*, 131(16):164701, 2009.
- [176] W. Feng, S. Lei, Q. Li and A. Zhao. Periodically modulated electronic properties of the epitaxial monolayer graphene on Ru(0001). *J. Phys. Chem. C*, 115(50):24858–24864, 2011.
- [177] S. Günther, S. Dänhardt, M. Ehrensperger, P. Zeller, S. Schmitt and J. Winterlin. High-temperature scanning tunneling microscopy study of the ordering transition of an amorphous carbon layer into graphene on ruthenium (0001). *ACS Nano*, 7(1):154–164, 2013.
- [178] F. Natterer, S. Rusponi, M. Papagno, C. Carbone and H. Brune. Optimizing long-range order, band gap, and group velocities for graphene on close-packed metal surfaces. *J. Phys.: Condens. Matter*, 24(31):314203, 2012.
- [179] J. Lu, A. H. C. Neto and K. P. Loh. Transforming moiré blisters into geometric graphene nanobubbles. *Nat. Commun.*, 3(1):823, 2012.
- [180] B. Wang, X. Ma, M. Caffio, R. Schaub and W.-X. Li. Size-selective carbon nanoclusters as precursors to the growth of epitaxial graphene. *Nano Lett.*, 11(2):424–430, 2011.
- [181] Y. Pan, M. Gao, L. Huang, F. Liu and H.-J. Gao. Directed self-assembly of monodispersed platinum nanoclusters on graphene Moiré template. *Appl. Phys. Lett.*, 95(9):093106, 2009.

- [182] M. Sicot, S. Bouvron, O. Zander, U. Rüdiger, Y. S. Dedkov and M. Fonin. Nucleation and growth of nickel nanoclusters on graphene Moiré on Rh(111). *Appl. Phys. Lett.*, 96(9):, 093115.
- [183] Q. Liao, H. Zhang, K. Wu, H. Li, S. Bao and P. He. Nucleation and growth of monodispersed cobalt nanoclusters on graphene moiré on Ru(0001). *Nanotechnology*, 22(12):125303, 2011.
- [184] A. K. Engstfeld, H. E. Hoster, R. J. Behm, L. D. Roelofs, X. Liu, C.-Z. Wang, Y. Han and J. W. Evans. Directed assembly of Ru nanoclusters on Ru(0001)-supported graphene: STM studies and atomistic modeling. *Phys. Rev. B*, 86(8):085442, 2012.
- [185] K. Wu, H. Zhang, Y. Wang, Y. Lu, Y. Cai, J. Song, H. Li, S. Bao and P. He. Templating ultra-small manganese isomers with preference for adsorption sites and narrow distribution tuned by different moiré periodicities of monolayer graphene on Ru(0001). *Nanotechnology*, 24(21):215302, 2013.
- [186] D. Teng, L. B. Vilhelmsen and D. S. Sholl. Investigating energetics of Au<sub>8</sub> on graphene/Ru(0001) using a genetic algorithm and density functional theory. *Surf. Sci.*, 628:98–103, 2014. could not find the issue number
- [187] X. Wen-Yan, H. Li, Q. Yan-De, L. Xiao, W. Ye-Liang, D. Shi-Xuan and G. Hong-Jun. Effects of graphene defects on Co cluster nucleation and intercalation. *Chin. Phys. B*, 23(8):088108, 2014.
- [188] G. Förster, F. Rabilloud and F. Calvo. Atomistic modeling of epitaxial graphene on Ru(0001) and deposited ruthenium nanoparticles. *Phys. Rev. B*, 92(16):165425, 2015.
- [189] J. Coraux, A. T. N’Diaye, C. Busse and T. Michely. Structural coherency of graphene on Ir(111). *Nano Lett.*, 8(2):565–570, 2008.
- [190] To build the network of lines constituting the grid, we adjust the orientation of each individual line so they pass through the atomic positions. This triangulation procedure improves the reliability on the determination of the atomic positions, and can only be applied in regions where the carbon lattice is close-to-ideal.
- [191] E. Cockayne, G. M. Rutter, N. P. Guisinger, J. N. Crain, P. N. First and J. A. Stroscio Grain boundary loops in graphene. *Phys. Rev. B*, 83(19):195425, 2011.
- [192] M. Ugeda, D. Fernández-Torre, I. Brihuega, P. Pou, A. Martínez-Galera, R. Pérez and J. Gómez-Rodríguez. Point defects on graphene on metals. *Phys. Rev. Lett.*, 107(11):116803, 2011.
- [193] S. Standop, O. Lehtinen, C. Herbig, G. Lewes-Malandrakis, F. Craes, J. Kotakoski, T. Michely, A. V. Krasheninnikov and C. Busse. Ion impacts on graphene/Ir(111): Interface channeling, vacancy funnels, and a nanomesh. *Nano Lett.*, 13(5):1948–1955, 2013.
- [194] N. Krane, C. Lotze, J. M. Lager, G. Reecht and K. J. Franke. Electronic structure and luminescence of quasi-freestanding MoS<sub>2</sub> nanopatches on Au(111). *Nano Lett.*, 16(8):5163–5168, 2016.
- [195] P. Sutter, M. Hybertsen, J. Sadowski and E. Sutter. Electronic structure of few-layer epitaxial graphene on Ru(0001). *Nano Lett.*, 9(7):2654–2660, 2009.
- [196] J. Lu, P. S. E. Yeo, C. K. Gan, P. Wu and K. P. Loh. Transforming C<sub>60</sub> molecules into graphene quantum dots. *Nat. Nanotechnol.*, 6(4):247–252, 2011.
- [197] Y. Cui, Q. Fu, H. Zhang and X. Bao. Formation of identical-size graphene nanoclusters on Ru(0001). *Chem. Commun.*, 47(5):1470–1472, 2011.
- [198] E. Starodub, S. Maier, I. Stass, N. Bartelt, P. Feibelman, M. Salmeron and K. McCarty. Graphene growth by metal etching on Ru(0001). *Phys. Rev. B*, 80(23):235422, 2009.

- [199] P. Simonis, C. Goffaux, P. Thiry, L. Biro, P. Lambin and V. Meunier. STM study of a grain boundary in graphite. *Surf. Sci.*, 511(1–3):319–322, 2002.
- [200] J. S. Alden, A. W. Tsen, P. Y. Huang, R. Hovden, L. Brown, J. Park, D. A. Muller and P. L. McEuen. Strain solitons and topological defects in bilayer graphene. *Proc. Nat. Ac. Sci. USA*, 110(28):11256–11260, 2013.
- [201] J. Lin, W. Fang, W. Zhou, A. R. Lupini, J. C. Idrobo, J. Kong, S. J. Pennycook and S. T. Pantelides. AC/AB stacking boundaries in bilayer graphene. *Nano Lett.*, 13(7):3262–3268, 2013.
- [202] J. Lahiri, Y. Lin, P. Bozkurt, I. I. Oleynik and M. Batzill. An extended defect in graphene as a metallic wire. *Nat. Nanotechnol.*, 5(5):326–329, 2010.
- [203] J.-H. Chen, G. Autès, N. Alem, F. Gargiulo, A. Gautam, M. Linck, C. Kisielowski, O. Yazyev, S. Louie and A. Zettl. Controlled growth of a line defect in graphene and implications for gate-tunable valley filtering. *Phys. Rev. B*, 89(12):121407, 2014.
- [204] O. Lehtinen, S. Kurasch, A. Krasheninnikov and U. Kaiser. Atomic scale study of the life cycle of a dislocation in graphene from birth to annihilation. *Nat. Commun.*, 4(1):2098, 2013.
- [205] F. Banhart, J. Kotakoski and A. V. Krasheninnikov. Structural defects in graphene. *ACS Nano*, 5(1):26–41, 2011.
- [206] Y.-C. Lin, T. Björkman, H.-P. Komsa, P.-Y. Teng, C.-H. Yeh, F.-S. Huang, K.-H. Lin, J. Jadcak, Y.-S. Huang, P.-W. Chiu, A. V. Krasheninnikov and K. Suenaga. Three-fold rotational defects in two-dimensional transition metal dichalcogenides. *Nat. Commun.*, 6(1):6736, 2015.
- [207] B. Wang, M. König, C. J. Bromley, B. Yoon, M.-J. Treanor, J. A. Garrido Torres, M. Caffio, F. Grillo, F. Früchtl, N. V. Richardson, F. Esch, U. Heiz, U. Landman and R. Schaub. Ethene to graphene: Surface catalyzed chemical pathways, intermediates, and assembly. *J. Phys. Chem. C*, 121(17):9413–9423, 2017.
- [208] K. F. McCarty, P. J. Feibelman, E. Loginova and N. C. Bartelt. Kinetics and thermodynamics of carbon segregation and graphene growth on Ru(0001). *Carbon*, 47(7):1806–1813, 2009.
- [209] Y. Qi, C. Meng, X. Xu, B. Deng, N. Han, M. Liu, M. Hong, Y. Ning, K. Liu, J. Zhao, Q. Fu, Y. Li, Y. Zhang and Z. Liu. Unique transformation from graphene to carbide on Re(0001) induced by strong carbon–metal interaction. *J. Am. Chem. Soc.*, 139(48):17574–17581, 2017.
- [210] E. Koren, E. Sutter, S. Bliznakov, F. Ivars-Barcelo and P. Sutter. Isolation of high quality graphene from Ru by solution phase intercalation. *Appl. Phys. Lett.*, 103(12):121602, 2013.
- [211] T. G. Pedersen, C. Flindt, J. Pedersen, N. A. Mortensen, A.-P. Jauho and K. Pedersen. Graphene antidot lattices: Designed defects and spin qubits. *Phys. Rev. Lett.*, 100(13):136804, 2008.
- [212] J. Li, L. Kong and B. Liu. Proposed definition of microchemical inhomogeneity and application to characterize some selected miscible/immiscible binary metal systems. *J. Phys. Chem. B*, 108(41):16071–16076, 2004.
- [213] H. Vita, St. Böttcher, P. Leicht, K. Horn, A. B. Shick and F. Máca. Electronic structure and magnetic properties of cobalt intercalated in graphene on Ir(111). *Phys. Rev. B*, 90(16):165432, 2014.
- [214] D. W. Boukhvalov and M. I. Katsnelson. Destruction of graphene by metal adatoms. *Appl. Phys. Lett.*, 95(2):023109, 2009.
- [215] S. Namsani and J. K. Singh. Dewetting dynamics of gold film on graphene: Implications for nanoparticle formation. *Farad. Disc.*, 186:153–170, 2016.

- [216] M. Klimenkov, S. Nepijko, H. Kuhlenbeck, M. Bäumer, R. Schögl and H.-J. Freund. The structure of Pt-aggregates on a supported thin aluminum oxide film in comparison with unsupported alumina: a transmission electron microscopy study. *Surf. Sci.*, 391(1–3):27–36, 1997.
- [217] G. D’Agostino, A. Pinto and S. Mobilio. Simulated gold clusters and relative extended x-ray-absorption fine-structure spectra. *Phys. Rev. B*, 48(19):14447–14453, 1993.
- [218] D. Franz, S. Runte, C. Busse, S. Schumacher, T. Gerber, T. Michely, M. Mantilla, V. Kilic, J. Zegenhagen and A. Stierle. Atomic structure and crystalline order of graphene-supported Ir nanoparticle lattices. *Phys. Rev. Lett.*, 110(6):065503, 2013.
- [219] D. Franz, N. Blanc, J. Coraux, G. Renaud, S. Runte, T. Gerber, C. Busse, T. Michely, P. J. Feibelman, U. Hejral and A. Stierle. Atomic structure of Pt nanoclusters supported by graphene/Ir(111) and reversible transformation under CO exposure. *Phys. Rev. B*, 93(4):045426, 2016.
- [220] N. Rougemaille, S. Vlaic, L. Aballe, M. Foerster and J. Coraux. Confined step-flow growth of Cu intercalated between graphene and a Ru(0001) surface. *2D Mater.*, 6(3):035004, 2019.
- [221] H. Hibino, H. Kageshima and M. Nagase. Epitaxial few-layer graphene: towards single crystal growth. *J. Phys. D: Appl. Phys.*, 43(37):374005, 2010.
- [222] J. I. Paredes, A. Martínez-Alonso and J. M. D. Tascón. Triangular versus honeycomb structure in atomic-resolution STM images of graphite. *Carbon*, 39(3):476–479, 2001.
- [223] Y. Wang, Y. Ye and K. Wu. Simultaneous observation of the triangular and honeycomb structures on highly oriented pyrolytic graphite at room temperature: An STM study. *Surf. Sci.*, 600(3):729–734, 2006.
- [224] H. S. Wong, C. Durkan and N. Chandrasekhar. Tailoring the local interaction between graphene layers in graphite at the atomic scale and above using scanning tunneling microscopy. *ACS Nano*, 3(11):3455–3462, 2009.
- [225] P. Xu, Y. Yang, S. D. Barber, J. K. Schoelz, D. Qi, M. L. Ackerman, L. Bellaiche and P. M. Thibado. New scanning tunneling microscopy technique enables systematic study of the unique electronic transition from graphite to graphene. *Carbon*, 50(12):4633–4639, 2012.
- [226] C. Riedl and U. Starke. Structural properties of the graphene-SiC(0001) interface as a key for the preparation of homogeneous large-terrace graphene surfaces. *Phys. Rev. B*, 76(24):245406, 2007.
- [227] V. W. Brar, Y. Zhang, Y. Yayon, T. Ohta, J. L. McChesney, A. Bostwick, A. Rotenberg, K. Horn and M. F. Crommie. Scanning tunneling spectroscopy of inhomogeneous electronic structure in monolayer and bilayer graphene on SiC. *Appl. Phys. Lett.*, 91(12):122102, 2007.
- [228] G. M. Rutter, N. P. Guisinger, J. N. Crain, E. A. A. Jarvis, M. D. Stiles, T. Li, P. N. First and J. A. Stroscio. Imaging the interface of epitaxial graphene with silicon carbide via scanning tunneling microscopy. *Phys. Rev. B*, 76(23):235416, 2007.
- [229] P. Mallet, F. Varchon, C. Naud, L. Magaud, C. Berger and J.-Y. Veillen. Electron states of mono- and bilayer graphene on SiC probed by scanning-tunneling microscopy. *Phys. Rev. B*, 76(4):041403, 2007.
- [230] F. Hiebel, P. Mallet, L. Magaud and J.-Y. Veillen. Atomic and electronic structure of monolayer graphene on 6H-SiC(000 $\bar{1}$ )(3 $\times$ 3): A scanning tunneling microscopy study. *Phys. Rev. B*, 80(23):235429, 2009.

- [231] S. Schumacher, F. Huttmann, M. Petrović, C. Witt, D. F. Förster, C. Vo-Van, J. Coraux, A. J. Martínez-Galera, V. Sessi, I. Vergara, R. Rückamp, M. Grüninger, N. Schleheck, F. Meyer zu Heringdorf, P. Ohresser, M. Kralj, T. O. Wehling and T. Michely. Europium underneath graphene on Ir(111): Intercalation mechanism, magnetism, and band structure. *Phys. Rev. B*, 90(23):235437, 2014.
- [232] J. Sławińska, P. Dabrowski and I. Zasada. Doping of graphene by a Au(111) substrate: Calculation strategy within the local density approximation and a semiempirical van der Waals approach. *Phys. Rev. B*, 83(24):245429, 2011.
- [233] D. Marchenko, A. Varykhalov, J. Sánchez-Barriga, Th. Seyller and O. Rader. Rashba splitting of 100 meV in Au-intercalated graphene on SiC. *Appl. Phys. Lett.*, 108(17):172405, 2016.
- [234] S. Reich, J. Maultzsch and C. Thomsen. Tight-binding description of graphene. *Phys. Rev. B*, 66(3):035412, 2002.
- [235] P. Leicht, J. Tesch, S. Bouvron, F. Blumenschein, P. Erler, L. Gagnaniello and M. Fonin. Rashba splitting of graphene-covered Au(111) revealed by quasiparticle interference mapping. *Phys. Rev. B*, 90(24):241406, 2014.
- [236] Z. Klusek, P. Dabrowski, P. Kowalczyk, W. Olejniczak, P. Blake, M. Szybowicz and T. Runka. Graphene on gold: Electron density of states studies by scanning tunneling spectroscopy. *Appl. Phys. Lett.*, 95(11):113114, 2009.
- [237] M. H. Kang, S. C. Jung and J. W. Park. Density functional study of the Au-intercalated graphene/Ni(111) surface. *Phys. Rev. B*, 82(8):085409, 2010.
- [238] J. Kliewer, R. Berndt, E. V. Chulkov, V. M. Silkin, P. M. Echenique, S. Crampin. Dimensionality effects in the lifetime of surface states. *Science*, 288(5470):1399–1402, 2000.
- [239] S. M. Hollen, G. A. Gambrel, S. J. Tjung, N. M. Santagata, E. Johnston-Halperin and J. A. Gupta. Modification of electronic surface states by graphene islands on Cu(111). *Phys. Rev. B*, 91(19):195425, 2015.
- [240] I. Pocsik, M. Hundhausen, M. Koos and L. Ley. Origin of the D peak in the Raman spectrum of microcrystalline graphite. *J. Non-Cryst. Solids*, 227–230(2):1083–1086, 2008.
- [241] E. B. Barros, H. Son, Ge. G. Samsonidze, A. G. Souza Filho, J. Mendes Filho, G. Dresselhaus and M. S. Dresselhaus. Laser-energy-dependent Raman scattering studies of graphitic foams. *Phys. Rev. B*, 76(3):035444, 2007.
- [242] C. Zacherl, J. Saal, Y. Wang and Z. K. Liu. First-principles calculations and thermodynamic modeling of the Re-Y system with extension to the Ni-Re-Y system. *Intermetallics*, 18(12):2412–2418, 2010.
- [243] T. Dubouchet. Ph.D thesis, Université Grenoble Alpes, 2010.
- [244] U. Stark and W. Müller-Warmuth. Hydrogen bond formation and molecular motion in solutions of aniline with nitroxide free radicals. *Ber. Bunsenges. Phys. Chem.*, 94(2):168–172, 1990.
- [245] D. Bardelang, M. Hardy, O. Ouari and P. Tordo. Spin labels and spin probes. *Encyclopedia of Radicals in Chemistry, Biology and Materials*, 2012.
- [246] B. Pilawa. New concepts for molecular magnets. *Ann. Phys.*, 8(3):191–254, 1999.
- [247] C. J. Hawker, A. W. Bosman and E. Harth. New polymer synthesis by nitroxide mediated living radical polymerizations. *Chem. Rev.*, 101(12):3661–3688, 2001.



- [248] G. N. Lipunova, T. G. Fedorchenko and O. N. Chupakhin. Verdazyls: synthesis, properties, application. *Russ. Chem. Rev.*, 82(8):701–734, 2013.
- [249] J. B. Gilroy, S. D. J. McKinnon, B. D. Koivisto and R. G. Hicks. Electrochemical studies of verdazyl radicals. *Org. Lett.*, 9(23):4837–4840, 2007.
- [250] B. D. Koivisto and R. G. Hicks. The magnetochemistry of verdazyl radical-based materials. *Coord. Chem. Rev.*, 249(23):2612–2630, 2005.
- [251] A. Rajca. Organic diradicals and polyradicals: From spin coupling to magnetism? *Chem. Rev.*, 94(4):871–893, 1994.
- [252] D. J. R. Brook, H. H. Fox, V. Lynch and M. A. Fox. Structural indicators of electronic interaction in the 1,1',5,5'tetramethyl-6,6'-dioxo-3,3'-biverdazyl diradical. *J. Phys. Chem.*, 100(6):2066–2071, 1996.
- [253] D. E. Williams. Crystal structure of 2,4,6-triphenylverdazyl. *Acta. Cryst.*, B29(1):96–102, 1973.
- [254] N. Azuma, J. Yamauchi, K. Mukai, H. Ohya-Nishiguchi and Y. Deguchi. The magnetic properties of verdazyl free radicals. III. The anomalous magnetic behaviour of symmetrical triphenylverdazyl. *Bull. Chem. Soc. Jpn.*, 46(9):2728–2734, 1973.
- [255] K. Takeda, H. Deguchi, T. Hoshiko, K. Konishi, K. Takahashi and J. Yamauchi. Magnetic behavior of organic free radicals with localized and delocalized electrons. *J. Phys. Soc. Jpn.*, 58(9):3361–3370, 1989.
- [256] S. Tomiyoshi, T. Yano, N. Azuma, M. Shoga, K. Yamada, and J. Yamauchi. Weak ferromagnetism and antiferromagnetic ordering of 2p electrons in the organic radical compound 2,4,6-triphenylverdazyl. *Phys. Rev. B*, 49(22):16031, 1994.
- [257] F. A. Neugebauer, H. Fischer and C. Krieger. Verdazyls. Part 33. EPR and ENDOR studies of 6-oxo- and 6-thioxoverdazyls. X-Ray molecular structure of 1,3,5-triphenyl-6-oxoverdazyl and 3-tert-butyl-1,5-diphenyl-6-thioxoverdazyl. *J. Chem. Soc. Perkin Trans. 2*, 535–544, 1993.
- [258] J. Liu, H. Isshiki, K. Katoh, T. Morita, B. K. Breedlove, M. Yamashita and T. Komeda. First observation of a Kondo resonance for a stable neutral pure organic radical, 1,3,5-triphenyl-6-oxoverdazyl, adsorbed on the Au(111) surface. *J. Am. Chem. Soc.*, 135(2):651–658, 2013.
- [259] M. Bancercz, B. Youn, M. V. DaCosta and M. K. Georges. A hydrazine- and phosgene-free synthesis of tetrazinanones, precursors to 1,5-dialkyl-6-oxoverdazyl radicals. *J. Org. Chem.*, 77(5):2415–2421, 2012.
- [260] P. Hui and R. Chandrasekar. Light propagation in high-spin organic microtubes self-assembled from shape persistent macrocycles carrying oxo-verdazyl biradicals. *Adv. Mater.*, 25(21):2963–2967, 2013.
- [261] J. B. Gilroy, S. D. J. McKinnon, P. Kennepohl, M. S. Zsombor, M. J. Ferguson, L. K. Thompson and R. G. Hicks. Probing electronic communication in stable benzene-bridged verdazyl diradicals. *J. Org. Chem.*, 72(21):8062–8069, 2007.
- [262] R. M. Fico Jr., M. F. Hay, S. Reese, S. Hammond, E. Lambert and M. A. Fox. Electronic interactions in verdazyl biradicals. *J. Org. Chem.*, 64(26):9386–9392, 1999.
- [263] G. Rayner, T. Smith, W. Barton, M. Newton, R. J. Deeth, I. Prokes, G. J. Clarkson and D. M. Haddleton. A comparison of verdazyl radicals modified at the 3-position as mediators in the living radical polymerisation of styrene and n-butyl acrylate. *Polym. Chem.*, 3(8):2254–2260, 2012.
- [264] Horiba. Raman data and analysis - Raman bands.  
<https://www.horiba.com/fileadmin/uploads/Scientific/Documents/Raman/bands.pdf>.

# Estelle Mazaleyrat

57 rue du Vercors  
38000 Grenoble  
estelle.mazaleyrat@neel.cnrs.fr



---

## Work experience

- 10/2016 – Now **PhD work**, *CEA/IRIG & CNRS/Institut Néel*, Grenoble.  
Growth, structure and electronic properties of epitaxial graphene on rhenium, towards a two-dimensional superconducting platform.
- 02/2019 – 03/2019 **ARPES measurements campaign**, *LPEM/ESPCI*, Paris, group of Sergio Vlaic.  
Gold intercalation of graphene on Re(0001) monitored by ARPES, LEED and Auger spectroscopy.
- 01/2017 – 04/2017 **Sessional lecturer**, *Université de Grenoble*.  
Tutorial and practical classes in optics, 1st year Bachelor.
- 02/2016 – 08/2016 **M2 internship**, *CEA/IRIG & CNRS/Institut Néel*, Grenoble.  
Training and first results related to gold intercalation of graphene on Re(0001).
- 09/2015 – 02/2016 **M2 project**, *Ecole Polytechnique Fédérale de Lausanne*, Switzerland, group of Oleg Yazyev.  
Numerical calculation of graphene's band structure (monolayer/bilayer/nanoribbons).
- 05/2015 – 08/2015 **M1 internship**, *Institut Fresnel*, Marseille.  
Improvement of the scanning system of optical microscopes: realization of an opto-mechanical diagnosis and implementation of technical solutions.
- 06/2014 – 08/2014 **Worker internship**, *ST Microelectronics*, Crolles (38).  
Clean-room operator: night shifts (8:30pm - 5am) in the dry etching workshop.

---

## Education

- In progress **Doctoral thesis in Physics**, *Université Grenoble Alpes*.
- 2015 – 2016 **Erasmus semester**, *Ecole Polytechnique Fédérale de Lausanne*, Switzerland.  
Solid state physics, superconductivity, semiconductor physics, experimental techniques.
- 2013 – 2016 **Engineering school**, *Phelma (Grenoble INP)*.  
Solid state physics, semiconductor physics, nanoscience, experimental techniques, optics.
- 2011 – 2013 **“Classe prépa” (MPSI-MP)**, *Lycée Champollion*, Grenoble.  
Two-year classes in maths, physics and chemistry to prepare for the selective “Grandes Ecoles” entrance exam.

---

## Languages

- English Proficient (BULATS: 89/100)  
Spanish Intermediate  
Italian Basics

*I have lived 1 year ½ close to Milan.*

---

## Computer skills

- Languages Python, C, Matlab, LabView  
Softwares Inkscape  
Others Latex

---

## Interests

- Sports Rock climbing, hiking.  
Others First aid certificate.

---

## List of publications

- to be submitted Defective, hole-doped and superconducting quasi free-standing graphene on Re(0001) obtained by gold intercalation. **E. Mazaleyrat**, S. Vlaic, A. Artaud, L. Magaud, A. C. Gómez Herrero, S. Lisi, P. Singh, N. Bendiab, V. Guisset, P. David, S. Pons, D. Roditchev, C. Chapelier and J. Coraux.
- to be submitted Structure of graphene and a surface carbide grown on the (0001) surface of rhenium. **E. Mazaleyrat**, A. Artaud, L. Magaud, A. C. Gómez Herrero, S. Lisi, V. Guisset, P. David, C. Chapelier and J. Coraux.
- submitted Depressions by stacking faults in nanorippled graphene on metals. A. Artaud, **E. Mazaleyrat**, G. D. Förster, C. Tonnoir, B. Gilles, P. David, V. Guisset, L. Magaud, F. Calvo, C. Chapelier and J. Coraux.
- to be submitted Clockwise and anti-clockwise rotational epitaxy confined under a graphene layer. S. Lisi, **E. Mazaleyrat**, A. C. Gómez Herrero, V. D. Nguyen, V. Guisset, P. David and J. Coraux.
- submitted Decoupling molybdenum disulfide from its substrate by cesium intercalation. R. Sant, S. Lisi, V. D. Nguyen, **E. Mazaleyrat**, A. C. Gómez Herrero, O. Geaymond, V. Guisset, P. David, A. Marty, M. Jamet, C. Chapelier, L. Magaud, Y. J. Dappe, M. Bianchi, P. Hofman, G. Renaud and J. Coraux.
- to be submitted Stepwise oxidation, reorganisation, and bonding strength of a hexahydroxyl-triphenylene on a copper surface. A. C. Gómez Herrero, C. Sánchez-Sánchez, F. Chérioux, J. I. Martínez, J. Abad, L. Floreano, A. Verdini, A. Cossaro, **E. Mazaleyrat**, V. Guisset, P. David, S. Lisi, J. A. Martín-Gago and J. Coraux.

